Spatial Mechanical Behaviour of Skin

THESIS SUBMITTED IN PARTIAL FULFILLMENT OF THE REQUIREMENTS
OF THE DEGREE OF DOCTOR OF PHILOSOPHY

FEBURARY 2016

BY

ALEXANDER PETER KAO

SCHOOL OF ENGINEERING AND MATERIALS SCIENCE

QUEEN MARY, UNIVERSITY OF LONDON

MILE END ROAD, LONDON, E1 4NS

Statement of Originality

I, Alexander Peter Kao, confirm that the research included within this thesis is my own work or that where it has been carried out in collaboration with, or supported by others, that this is duly acknowledged below and my contribution indicated. Previously published material is also acknowledged below.

I attest that I have exercised reasonable care to ensure that the work is original, and does not to the best of my knowledge break any UK law, infringe any third party's copyright or other Intellectual Property Right, or contain any confidential material.

I accept that the College has the right to use plagiarism detection software to check the electron version of the thesis.

I confirm that this thesis has not been previously submitted for the award of a degree by this or any other university.

Alexander Peter Kao

Abstract

Skin is a complex biological composite system that serves as the outermost barrier to the environment and is mechanically robust. Understanding the mechanical properties of skin is important to improve and compare current in vitro experiments to the physiological conditions as the mechanical properties have a crucial role in determining cell behaviour. The mechanical behaviour of skin at the cellular level is expected to be dominated by the collagen fibre network within the dermis, which displays an anisotropic mechanical response to macroscopic loading. However, the three dimensional mechanical properties of skin at the nanoscale are not well understood. The aim of this work is to examine the mechanical properties of skin at the nanoscale in three dimensions and explore the links between the nanoscale and the macroscopic behaviour. Multiple sample preparation techniques are employed to expose the different layers of skin for mechanical testing and the elastic modulus of skin is evaluated by using atomic force microscopy (AFM) nanoindentation. The effect of freezing skin to cryogenic temperatures on the mechanical properties is evaluated and found to have no impact on the mechanical response of skin, indicating that the composition and structure of skin are robust enough to withstand the cryosectioning sample preparation methods used to expose the transverse layers of skin. AFM indentation was used to evaluate the elastic modulus of the dermis depending on the orientation of the sample and found to have an isotropic mechanical response. This result is opposite to anisotropy observed in macroscopic skin due to small scale mechanical testing ignoring collagen fibril orientation during strain. The variations in the elastic modulus of skin are also evaluated by AFM indentation at high spatial resolution to construct a composite model of the mechanical behaviour of skin at the nanoscale to predict the macroscopic response. The AFM nanoindentation

technique was extended to evaluate the mechanical properties of a cell derived matrix deposited on an electrospun nanofibre scaffold, where the results indicate increasing the nanofibre diameter produces a cell derived matrix with an increased elastic modulus for more effective scaffolds. This work highlights the use of AFM mechanical testing to evaluate the nanoscale mechanical behaviour of skin, treated as a composite biological system, and determine the influence of the length scale and sample orientation on the observed mechanical response.

Acknowledgements

First, I would like to thank my supervisor Professor Asa H. Barber for giving me the opportunity to embark upon my PhD studies and his continued support and guidance throughout. I would also like to thank my second supervisor Dr John Connelly for his support and valuable insight. The work in this thesis could not have been completed without the support of the people at the NanoVision Centre, particularly Dr Zofia Luklinska and Russell Bailey. I would also like to acknowledge the support of the group members within both the Barber and Connelly research groups particularly, Dr Urszula Stachewicz, Dr Filipe Almeida, Dr Yiran An, Fengfeng Zhang, Wenjun Sun, Fiona Kenny and Georgios Theocharidis.

I would also like to thank Dr Andrew Kao for always providing thought provoking discussion and helping me approach challenges from a different perspective.

Lastly, I would like to thank Queen Mary, University of London for providing the funding for my research and my parents for providing unconditional support throughout my studies.

Publications Arising from this Work

A. P. Kao, J. Connelly, and A. H. Barber. (2016). 3D nanomechanical evaluations of dermal structures in skin. Journal of the Mechanical Behavior of Biomedical Materials. 57. 14-23. doi:10.1016/j.jmbbm.2015.11.017

G. Theocharidis, Z. Drymoussi, A. P. Kao, A. H. Barber, D. Lee, K. Braun, and J. Connelly. (2015). Type VI collagen regulates dermal matrix assembly and fibroblast motility. The Journal of Investigative Dermatology. 136. 74-83. doi:10.1038/jid.2015.352

Table of Contents

List of Figures

List of Tables

Chapter 1 – Introduction

1.1 Background

Skin is a complex biological composite material with multiscale structure, as shown in Figure 1.1. The composition of skin is well understood, and predominantly comprises of the collagenous dermal layer and the cellular epidermal layer. Each constituent layer of skin contributes to the overall composite material properties. However, the complexity of skin due to a structural hierarchy ranging from small scale constituents to larger macroscopic features makes the link between skin composition and resultant mechanical performance challenging. The aim of this thesis is to therefore explore the small scale mechanical properties of skin, such as elucidating the layered and sub-layer structure, and provide a relationship to the material properties of the whole tissue. An experimental and theoretical approach is taken using small scale experimental mechanical testing combined with analytical and computational modelling to solve this demanding problem.

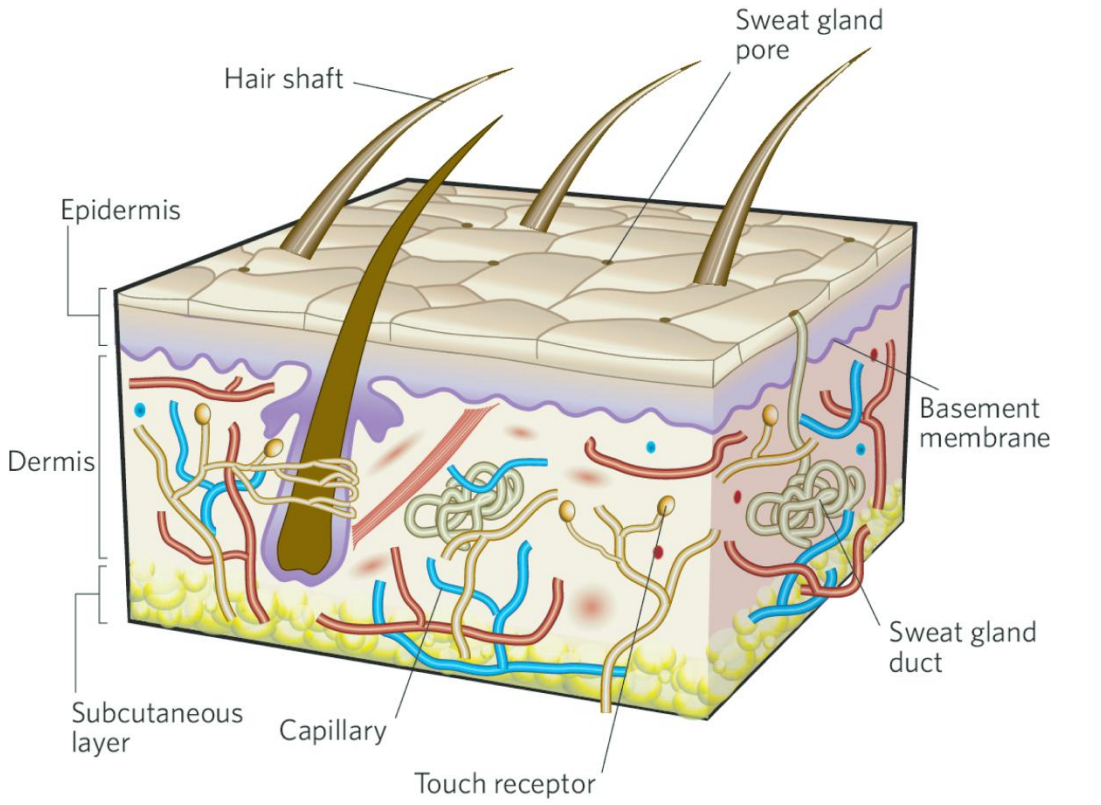

Figure 1.1. Illustration of whole skin showing the constitute biological components, adapated from (MacNeil, 2007).

General large scale macroscopic mechanical behaviour has been extensively investigated through the use of conventional mechanical testing apparatus such has uniaxial tension and indentation (Jachowicz et al., 2007; Ottenio et al., 2014). The structural complexity of skin makes it difficult to draw significant conclusions from the mechanical analysis of individual components or layers to the overall mechanical response of skin, whereas large volume testing is ideal for examining the macroscopic response of skin. The structure-property relationships at the macroscale are well defined with large scale deformations of whole skin displaying highly anisotropic behaviour (Gahagnon et al., 2012; Ní Annaidh et al., 2012b; Ottenio et al., 2014).

To a lesser degree, the nano/microscale mechanical properties of skin have been evaluated using atomic force microscopy (AFM) and other microindentation techniques through measurements of the constituent layers of skin. The nanoscale mechanical response of whole skin and the relationship to the macroscopic response along with the structure-property relationships are unknown. This thesis aims to explore the spatial changes in the mechanical properties of skin at the nanoscale and establish a link between nanoscale mechanical response and the macroscopic mechanical behaviour in three dimensions. The need to understand spatial mechanical properties specifically addresses the aim of evaluating the complexity of skin, and indeed other biological structures that exploits compositional variations in space to achieve mechanical function. The evaluation of skin at the nanoscale is additionally considered as critical in understanding the complex microenvironment required for the construction of engineered *in vitro* environments that are representative of the *in vivo* condition, which have applications in the development of tissue scaffolds for skin.

1.2 Thesis Outline

In this work the mechanical properties of skin are investigated at the nanoscale using atomic force microscopy (AFM) indentation measurements. Several sample preparation methods are evaluated to ensure the individual components of skin can be accurately measured at the nanoscale using AFM. The spatial variation in skin mechanical properties is determined and used to develop a finite element model. The macroscopic mechanical behaviour of skin is predicted from the nanoscale

mechanical measurements and a working link between the two length scales is established.

The second chapter of this thesis reviews the existing literature focusing on the composition, structure, and mechanical properties of skin at macroscopic and microscopic length scales. This chapter also details the understanding and importance of mechanical properties and how these properties can be investigated using AFM. The third chapter outlines the experimental methods employed to isolate the skin samples and expose the individual layers of skin. The *in situ* AFM mechanical testing method is developed and validated. The fourth chapter explores the effects of the sample preparation methods on the mechanical response of skin to establish that treatments applied to skin are not influencing the mechanical measurements being performed. With the sample preparation method validated, the microscopic mechanical properties and the positional variations in mechanical properties of skin could be measured. The fifth chapter therefore provides insight into the effect of sample structure, particularly the influence of structural orientation, on mechanical response at the nanoscale and comparisons to the observations in bulk skin samples are discussed. The potential effect of the orientation of individual components with respect to the applied load is investigated and an explanation for the variations in mechanical response is established. The sixth chapter correlates the nano/microscale mechanical properties to macroscopic mechanical measurements conducted on whole skin samples. A link between the nanoscale and macroscale mechanics is established by applying theoretical composite material theories to the nanoscale mechanical properties. The complex spatial mechanical properties evaluated in Chapter 5 are also used to develop a finite element analysis to predict the macroscopic mechanical response of whole skin.

The seventh chapter combines the experimental techniques applied to skin samples to a cell derived matrix deposited on an electrospun tissue scaffold to evaluate the spatial changes in the mechanical properties and investigate if changes in the mechanical properties of the constituent components effect the overall mechanical response of the cell derived matrix. The composite mechanical properties of the engineered biocomposite are predicted and suitability as a mechanical analogue to skin is discussed. Finally, the eighth chapter summarises the findings of this thesis and future studies are proposed.

Chapter 2 – Literature review

2.1 Introduction

This chapter aims to review the existing literature on skin structure, function, and mechanical properties. Particular focus will be placed on the mechanical behaviour of skin at different length scales and the importance of understanding the mechanical behaviour of skin with respect to the cellular microenvironment.

2.2 The structure of skin

Skin is a complex composite material consisting of various components that combine to form the outermost structure of the body. The skin is the largest organ in the human body covering the entire surface area. The skin is approximately 2 mm in thickness and covers more than 2 m^2 in surface area of an adult human (Shimizu, 2007). At the most basic level, skin provides a physical barrier between the interface of the human body and the outside environment. The skin also regulates the internal

temperature of the body through a sweating system and provides environmental information through a vast neural network. Structurally, the skin is made up of two main layers, with the overall structure illustrated in Figure 2.1. The first layer at the surface of skin is the stratified epithelium, or the epidermis, which is roughly between 75 and 150 μm in thickness (Shimizu, 2007) but considerably thicker on the palms and soles where the thickness can be up to 0.6 mm (Shimizu, 2007). Beneath the epidermis lies a much denser fibrous connective tissue known as the dermis. The dermis is much thicker than the epidermis and provides the majority of the structural stability and is where the majority of the mass in the skin is located (Shimizu, 2007). The dermis houses a large amount of the vascular and neural networks for the skin and many specialised glands related to the excretion and secretion of biological structures (Goldsmith, 1991).

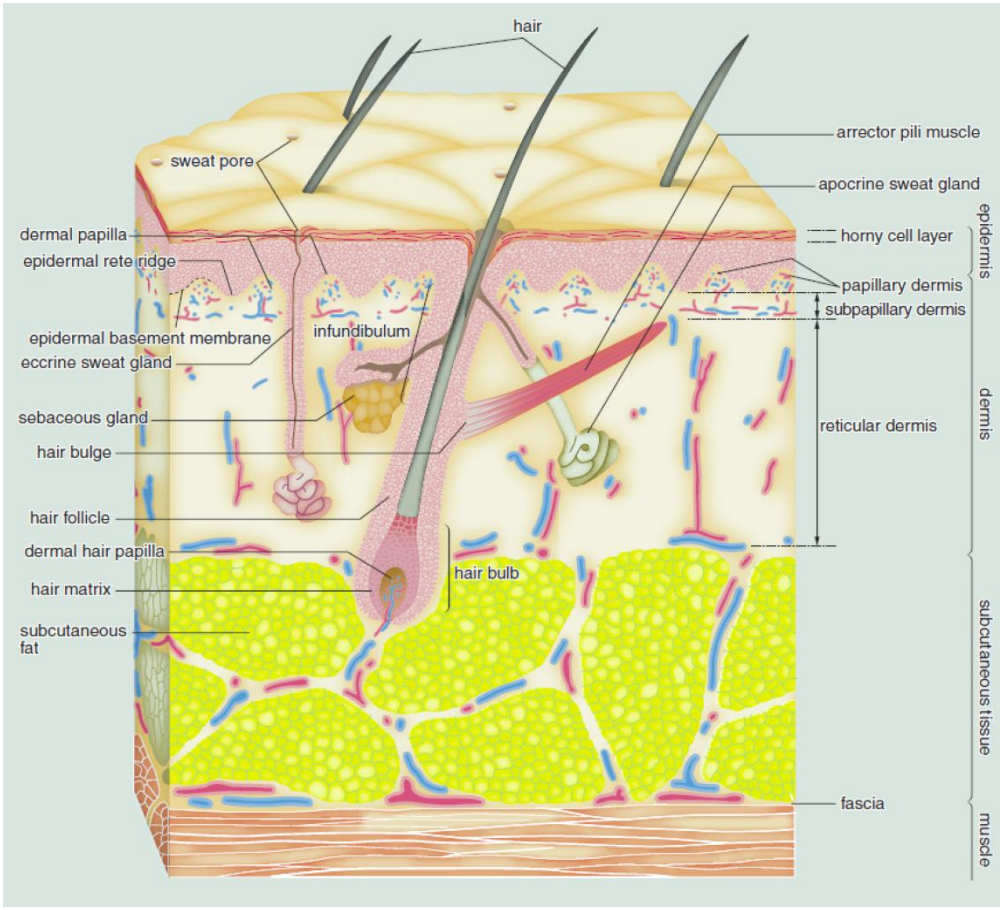

Figure 2.1. Illustration of the structure of skin, showing all the components and layers present in the structure. Adapted from, Shimizu 2007.

2.2.1 Epidermis

The epidermis can be described as a continuous sheet of epithelial cells known as keratinocytes, identified by the specific production of keratin proteins which form intermediate fibres contained within the cell cytoskeleton (Fuchs and Green, 1980a), but the epidermis also contains pores for glandular structures and hair follicles (Goldsmith, 1991). The epidermis is a layered structure made up of four main layers, as illustrated in Figure 2.2, with each layer identified by specific stage of keratinocyte proliferation and the expression of specific proteins (Candi et al., 2005).

The bottom layer of the epidermis is known as the basal cell layer. The basal cell layer contains the subpopulation of epidermal stem cells, also known as basal cells, and is the germinative layer for the epidermis (Fuchs and Raghavan, 2002). Basal cells proliferate and remain attached to the basal layer with some of the basal cells moving into the spinous layer, sometimes referred to as the stratum spinosum, of the epidermis (Simpson et al., 2011). This transition from basal layer to spinous layer is marked by a specific change in protein expression by the keratinocyte. Specifically, basal cells readily expressing keratin 5 (K5) and keratin 14 (K14) as the intermediate filaments which contribute to the cytoskeleton of the cell (Blanpain and Fuchs, 2009). This protein expression switches from K5/K14 to the expression of keratin 1 (K1) and keratin 10 (K10) when the basal cells proliferate into the spinous region (Simpson et al., 2011). The expression of K1 and K10 forms a more robust network of intermediate filaments that reinforce the cytoskeleton and result in a structure that can better withstand mechanical stresses (Blanpain and Fuchs, 2009). Above the spinous layer lies the stratum granulosum, or granular cell layer, which contains flattened keratinocytes. The granular layer is named because of the granules of proteins and lipids, called keratohyalin granules, that form within the cytoplasm of the cell (Wickett and Visscher, 2006).

Keratinocytes increasingly undergo a transformation into corneocytes moving upwards within the granular layer. Corneocytes are mechanically robust as their nucleus is digested and the cytoplasm replaced with a crosslinked network of keratin microfibrils and lipids that begin the formation of the cornified envelope. This cornification process utilises the proteins and lipids contained within the keratohyalin granules (Wickett and Visscher, 2006) and produces the cornified envelope of a enzymatically crosslinked insoluble layer of proteins and lipids surrounding the

corneocytes that acts as physical and chemical barrier protecting the body from the environment but also retaining liquid within the body (Candi et al., 2005). Corneocytes that have a fully developed cornified envelope make up the outermost layer of the epidermis known as the cornifed layer, also referred to as the stratum corneum or horny cell layer, and is approximately 15-20 cell layers in thickness but substantially larger on the palms and soles (Shimizu, 2007).

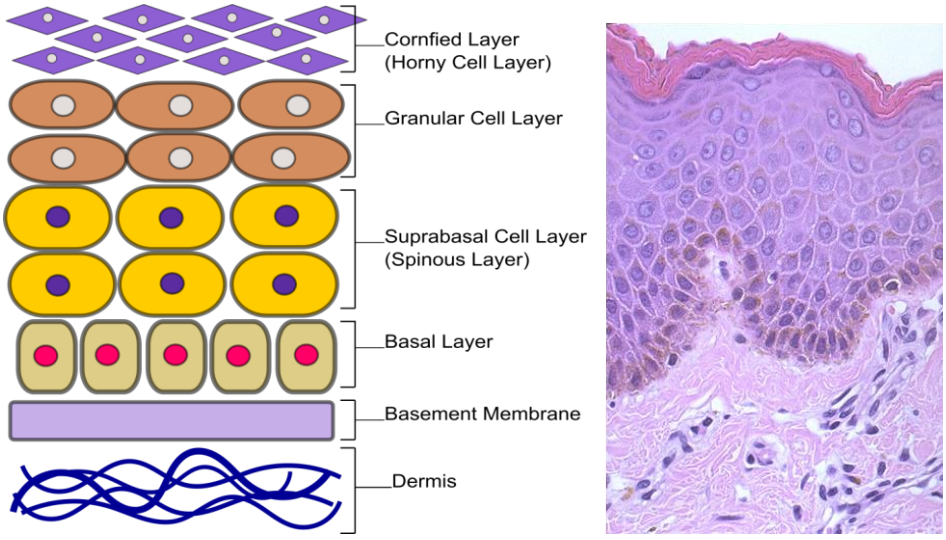

Figure 2.2. (Left) Illustration of the layers of the epidermis from the basal layer to the cornified layer at the surface of the skin.(Right) Histology image of the through thickness skin showing the different regions of the epidermis adapted from Kierszenbaum et al. (Kierszenbaum and Tres, 2015)

2.2.2 Epidermal-Dermal Junction

The epidermal-dermal junction, or the epidermal basement membrane, lies between the epidermis and the dermis of the skin and is a critical component to the structure of skin as it provides structural support for the monolayer of cells that begin the formation of the basal layer in the epidermis (LeBleu et al., 2007). The basement

membrane is a continuous structural element of the skin and consists of four major components; type IV collagen, laminin, nidogen/entactin, and perlecan (LeBleu et al., 2007). Type IV collagen is the most abundant component of the basement membrane making up approximately 50% of the composition. Type IV collagen is a nonfibrillar collagen and is secreted from keratinocytes and fibroblasts in the form of protomer units that self-assemble into a network structure present in basement membranes (Burgeson and Christiano, 1997). The second component of the basement membrane is laminin that, in terms of composition, represents the most abundant noncollagenous protein within the basement membrane structure. Laminin is a heterotrimer formed of a α-chain, β-chain, and γ-chain. The epidermal basement membrane contains laminin α3, β3 and γ2 chains that assemble into laminin-332, also known as laminin 5 (Burgeson and Christiano, 1997). This basement membrane assembles through the joining of both the collagen and laminin networks (LeBleu et al., 2007). The interaction between collagen and laminin is stabilised by nidogen and perlecan components found in the basement membrane. Nidogen and perlecan make up the minor composition of the basement membrane and are responsible for binding the collagen IV and laminin networks together (LeBleu et al., 2007). Nidogen is a glycoprotein that has been shown to bind to type IV collagen, perlecan and laminin among other protein structures. Perlecan is a heparin sulphate proteoglycan that is not specific to the basement membrane but provides protein binding sites for nidogen, type IV collagen and integrins. Together with nidogen, the perlecans are integrated into the type IV collagen and laminin networks and cause additional binding of the collagen and laminin (LeBleu et al., 2007).

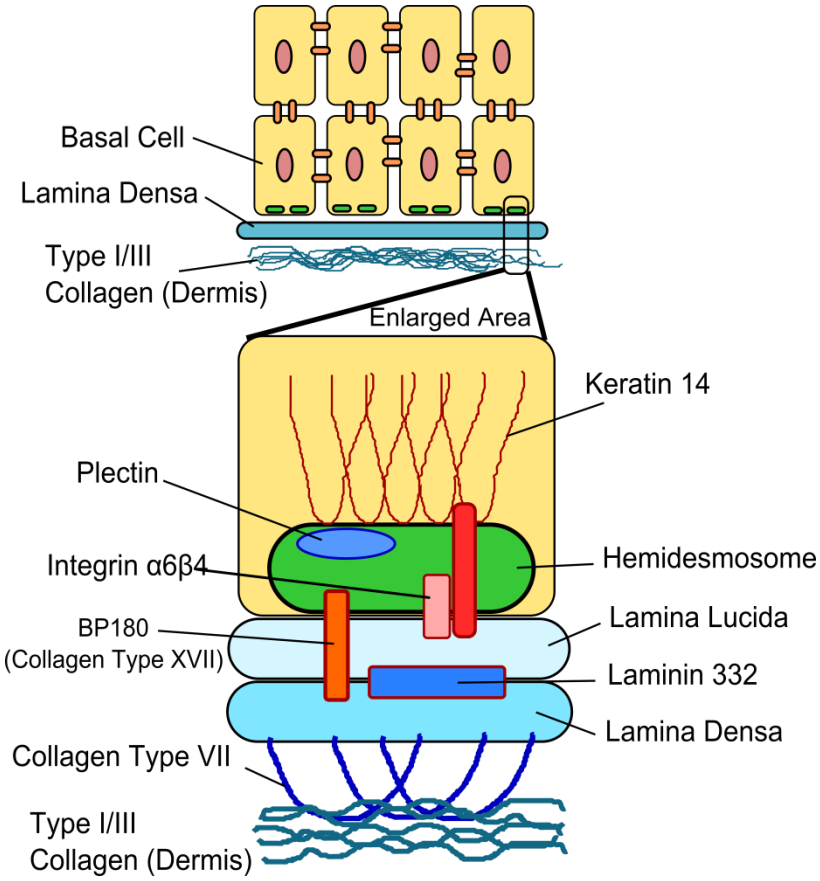

Figure 2.3. Illustration of the epidermal basement membrane with enlarged image of basal cell attachment to the basement membrane

At a larger scale, the basic structure of the basement membrane is separated into two lamellae of lamina lucida and the lamina densa, as shown in Figure 2.3. The layer directly below the basal cells of the epidermis is the lamina lucida, which is electron-lucent and separates the basal cells from the electron dense lamina densa that connects to the dermis below (Burgeson and Christiano, 1997). One of the major functions of the epidermal basement membrane is to join the epidermis to the dermis and therefore provides a clear mechanical role. The epidermis is attached to the basement membrane through hemidesmosomes within the basal cells, which attach, through the lamina luicda to the lamina densa by integrin binding sites and anchoring

fibrils (Pulkkinen and Uitto, 1998). The anchoring fibrils are comprised of collagen XVII, which is a form of collagen commonly referred to as bullous pemphigoid antigen 2 or BP180 because the protein structure is 180 kDa in length (Zillikens and Giudice, 1999). Integrin α6β4 is located within the hemidesmosomes and causes basement membrane binding through to the lamina lucida (Burgeson and Christiano, 1997). The lamina luicda is a continuous amorphous region mainly comprised of laminin glycoproteins with anchoring filaments oriented around hemidesomes. The lamina densa is also a continuous amorphous region containing mainly laminin glycoproteins, collagen IV, proteoglycans, and fibronectin (Andriani et al., 2003). Beneath the lamina densa is a region referred to as the reticular layer which contains mainly fibrous components such as anchoring fibrils, dermal microfibril bundles and collagen fibres (Shimizu, 2007). The epidermal basement membrane is bound to the dermis through anchoring fibrils composed of collagen type VII (Osawa et al., 2003). These fibrils penetrate down from the lamina densa into the upper layers of the dermis and then either loop back up to the lamina densa or terminate in the dermis (Burgeson and Christiano, 1997).

The primary role of the epidermal basement membrane is the adherence of the epidermis to the dermis through the structures described above in Figure 2.3. This adhesion role includes providing structural stability to the monolayer of basal cells that make up the base of the epidermis. The basement membrane also plays a role as a specialised extra cellular matrix, by providing growth factors to influence cell behaviour, manage cell proliferation, differentiation and migration. Typically, the epidermal basement membrane will be approximately 100 nm in thickness (Osawa et al., 2003) but is unevenly made up of the lamina lucida and the lamina densa.

2.2.3 Dermis

The dermis represents the largest structural constituent of human skin. The dermis is largely composed of collagen fibres, elastin fibres, and a matrix substance of glycosamino-proteoglycans also known as the ground substance. These components are controlled and regulated by dermal fibroblasts, which are the primary cells that live within the dermis (Goldsmith, 1991). The major structural component of the dermis is collagen which makes up 77% of the dry weight in skin (Shimizu, 2007). Two main forms of collagen are present within the dermis; type I, type III, and type V with traces of type VI (Tobin, 2006). Collagens are formed of three polypeptide chains that are composed of repeating amino acid structures, for each collagen type the three chains combine to form a triple-helical structure (Kadler et al., 1996).

Collagen type I, III, V present in the dermis readily self-assemble to form fibrils. The fibrils are made up of 300 nm length triple helix collagen molecules that are spaced approximately 40 nm apart. The spacing between the collagen molecules leads to the characteristic periodic d-spacing, which leads to the periodic banding structure (Chakravarti et al., 1998; Kadler et al., 1996). The nanometre sized fibrils combine to form fibril bundles which occur at the micrometre length scale and are referred to as collagen fibres (Gelse et al., 2003). The collagen fibres combine to form a mesh structure within the dermis (Fang et al., 2012; Lavker et al., 1987). This network of collagen fibres forms the basis for the robust mechanical properties of the dermis (Silver et al., 2003). Observation of the structure of the dermis by transmission electron microscopy, shown in Figure 2.4 (Lavker, 1979), highlights the network nature of the collagen fibres present. The collagen network within the dermis forms a lattice network structure which displays a preferential orientation (Noorlander et al., 2002). The lattice network is composed of two collagen fibre

families each exhibiting a preferential angle of alignment within the tissue. The overall orientation direction has been shown to be consistent with the orientation of the Langer's lines observed in vivo (Ottenio et al., 2014). The Langer's lines are observed at the macroscopic level on the surface of the skin and represent the predominant direction of the collagen fibrils parallel to the surface of the skin. Ní Annaidh et al. have shown that the collagen within the dermis preferentially aligns at two angles equidistant from the overall direction of the Langer's line (Ní Annaidh et al., 2012a).

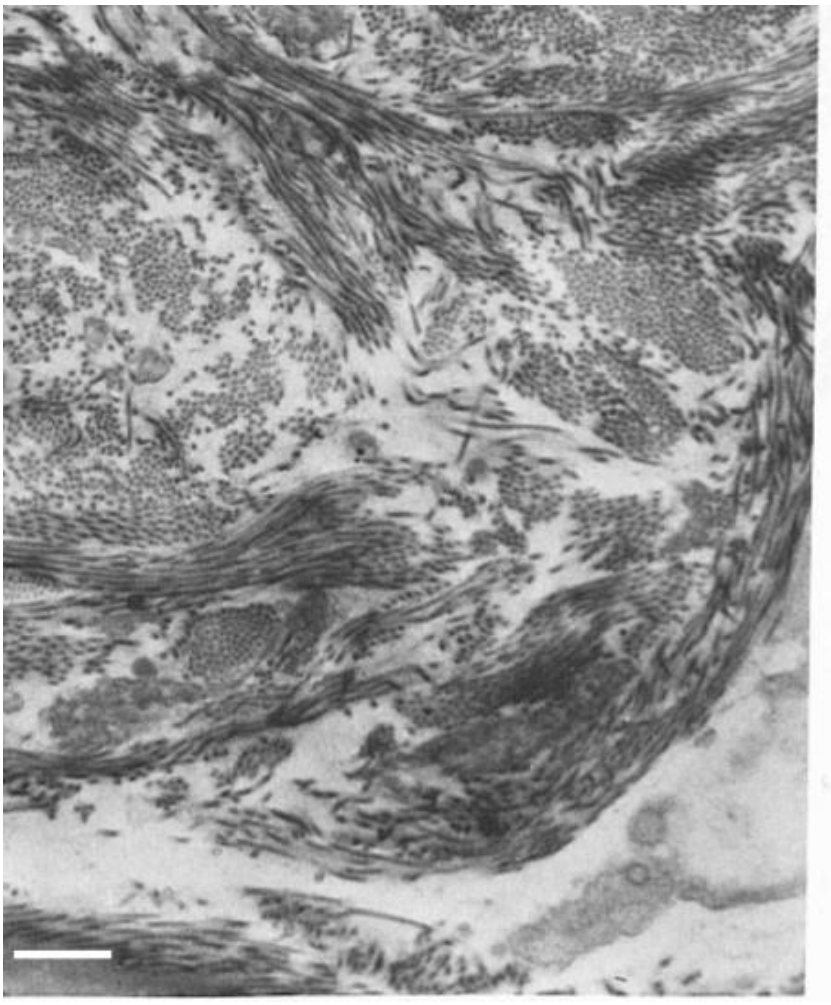

Figure 2.4. Transmission electron micrograph of the dermis of human skin highlighting the orientation of the collagen fibres, scale bar 1 µm, (Lavker, 1979)

Within the dermis, elastic fibres are woven within the bundles of collagen fibres and are responsible for restoring the morphology of the collagen fibres after any deformation (Tobin, 2006). The elastic fibres form a three dimensional network mainly consists of elastin, fibrillins and microfibrillar associated glycoproteins (Silver et al., 2003; Tobin, 2006) that spans the entire dermis . The network of elastic fibres organises within the collagen network and near the epidermal-dermal junction the elastic fibres are aligned vertically in relation to the surface of the skin and cylindrical in shape (Lavker et al., 1987). The elastic fibres become more branched within the papillary dermis and become larger and ribbon-like in morphology in the reticular dermis (Lavker et al., 1987).

At a macromolecular level the collagen fibrils observed are mainly collagens type I and V and are coated with type III, as illustrated in Figure 2.5 (Silver et al., 2003). Glycosaminoglycans and proteoglycans link between the collagen fibrils and form the extrafibrillar matrix of the dermis (Tobin, 2006).

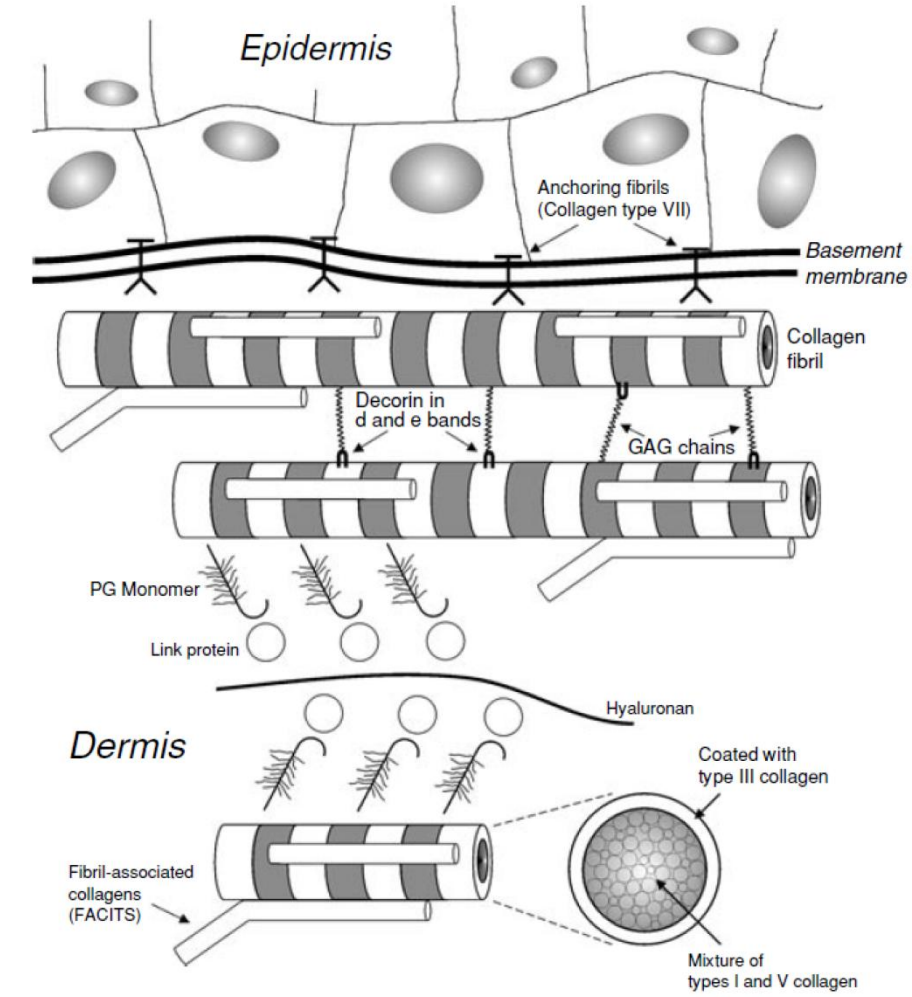

Figure 2.5. The macromolecular structure of the dermis with the collagen fibrils, comprised of collagen type I and V coated with type III. Glycosaminoglycans and proteoglycans form the extrafibrillar matrix of the dermis. The dermis is linked to the epidermis by collagen type VII anchoring fibrils, (Silver et al., 2003).

The dermis is also divided into two separate regions, the papillary dermis and the reticular dermis. The reticular dermis is much larger in volume than the papillary dermis and comprises the majority of the dermis. The papillary dermis is present

directly beneath the epidermal basement membrane and occupies the space between dermal papillae (Evans et al., 2013). As a result, the papillary layer contains smaller concentrations of collagen and elastic fibre bundles to maintain a higher concentration of ground substance (Shimizu, 2007). Beneath the papillary dermis is the denser reticular dermis layer and larger diameter collagen and elastin fibres with a reduced concentration of ground substance. The reticular dermis accounts for the majority of the mechanical properties of human skin as it is the largest volume within skin (Silver et al., 2003).

2.2.4 Force Transduction in Skin

Skin is a particularly interesting candidate for studying the mechanical properties of a tissue because of its complex structure, the large volume of skin present within the human body and the important role the skin plays in daily function (Shimizu, 2007). One of the major functions of the skin is to withstand the interaction forces that are applied to the surface of the body. The skin should be able to withstand substantial forces without failure and also transmit these forces to the body while reducing the impact on the fragile cells and environment contained beneath the skin (Silver et al., 2003). The dermis provides the major region of skin and is therefore expected to define the mechanical properties of skin. However, the transfer of forces through all layers of the skin needs to be achieved and structural integrity of the skin material maintained. The process of understanding how force is transferred through skin requires evaluation of both the components of skin as well as the interfaces formed between each phase. A simple mechanism can be developed by considering that external forces are applied to the skin through the epidermis. The keratinocytes

joined through desmosomes in the epidermis transfer forces mainly from binding through keratin and actin filaments in the cytoskeleton at keratinocyte-keratinocyte junctions down through the epidermis (Silver et al., 2003). These forces can then be transferred through hemidesmosomes bringing across the basement membrane to integrin binding sites within the basement membrane and then down through collagen anchoring fibrils into the dermis, as shown in Figure 2.3 (Silver et al., 2003). A composite model considering the epidermis, basement membrane and dermis is therefore expected to define the overall mechanical properties of skin material. However, determination of the mechanical properties of the various layers of skin at the submicrometre length scale requires suitable experimental techniques.

2.3 Mechanics

2.3.1 Basic mechanics

A solid material of a specified geometry subjected to an external force will deform in response to the force. Elastic behaviour occurs when the material returns to the original geometry upon removal of the force. The most common method for studying this elastic behaviour is applying a force along a single axis that causes expansion (stretching) along this axis, referred to as a tensile test. The basic tensile test is shown in Figure 2.6, with the initial geometry and the deformation under load illustrated. The two fundamental quantities used to describe the deformation behaviour of materials are stress, σ, and strain, ε, where stress and strain can be related to the load and deformation by (Courtney, 2005),

$$\sigma = \frac{F}{A_0}$$ Equation 2.1

$$\varepsilon = \frac{\Delta l}{l_0}$$ Equation 2.2

where F is the force applied to the material that deforms the material, of initial cross sectional area of A_0 and length l_0, to a length l. The deformation of the material is described by this change in the length of the material geometry, Δl, is equivalent to $\Delta l = l - l_0$. Examining the mechanical behaviour of materials using stress and strain provide quantities that are in a normalised form and provide material properties that are independent of the specimen geometry (Courtney, 2005).

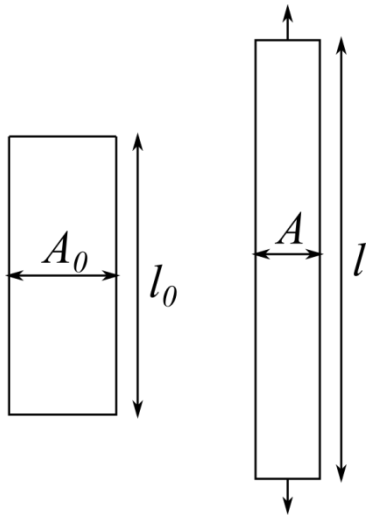

Figure 2.6. Schematic representation of a uniaxial tensile test with the cross sectional area of the sample A_0 contracting to A under the applied load and the extension of the initial length of the sample l_0 to the final length l.

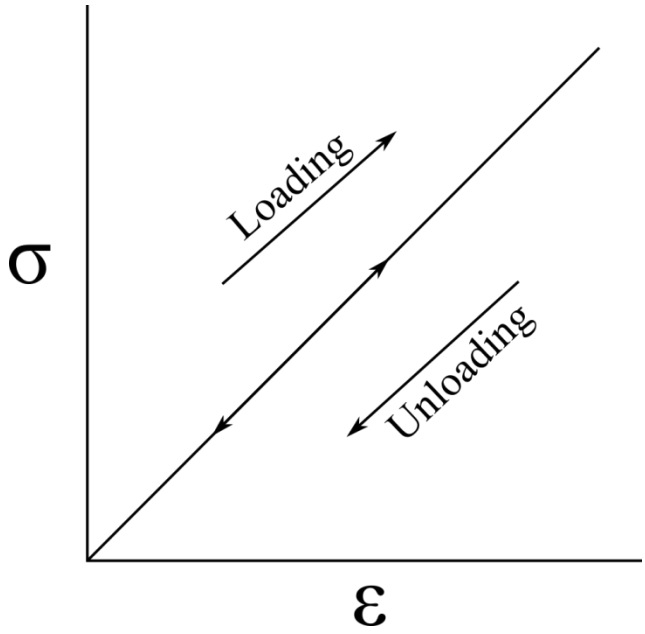

Figure 2.7. Schematic representation of a linear elastic stress versus strain curve with the unloading curve retracing the loading curve.

Elastic behaviour is observed in all classes of materials and represents the deformation response corresponding to the reversible deformation of the interatomic bonds within the material. The reversible deformation is a linear relationship between the stress and the strain and is illustrated in Figure 2.7. The slope of this response, σ versus ε, is represented as the elastic modulus, E, of the material. The linear elasticity of a material can also be described by the force and deformation relationship which is related to Hooke's law by (Courtney, 2005),

$$F = k \cdot \Delta l \qquad \text{Equation 2.3}$$

where, k also referred to as the spring constant, is the slope of the linear force-deformation curve. The spring constant of the material can be related to the elastic modulus through a relationship including the geometry of the specimen (Courtney, 2005),

$$k = \frac{EA}{l_0}$$ Equation 2.4

The material properties have thus far been described for a material being stretched under a tensile load. When the force is applied the material extension occurs along the longitudinal axis of the material. Under elastic deformation there is a contraction of the material along the transverse axis. The relationship between the axial strain and transverse strain is through the Poisson's ratio such that (Callister and Rethwisch, 2007),

$$v = -\frac{\varepsilon_t}{\varepsilon_a}$$ Equation 2.5

where, ε_t is the transverse strain and ε_a the axial strain. The transverse strain is typically a contraction of the material leading to a negative value in most materials and the axial strain is positive, all of which result in a positive value for the Poisson's ratio for most materials. The elastic modulus and Poisson's ratio provide a comprehensive description of the elastic behaviour of a material (Callister and Rethwisch, 2007). The description of the elastic mechanical properties can be extended to form a three dimensional mechanical response if the material is homogenous and the stress-strain response is equal in all directions. If this is the case and the material properties are equal in all three principal directions then the material is considered isotropic (McClintock and Argon, 1966). If an applied load in any direction results in an independent elastic response then the material is anisotropic (McClintock and Argon, 1966). Anisotropic behaviour is common in single crystals and composite materials, where the structure of the material influences the mechanical response significantly.

The uniaxial tensile test is often used to characterise the mechanical properties of materials because of the simplicity of the testing set up. However, difficulties arise in utilising this testing method with decreasing length scale (Oyen and Cook, 2009). Standard uniaxial tensile testing involves gripping a large volume of sample and applying a load, where the measured volume of the sample contributing to the stress-strain measurements is expected to be the total sample volume. Indentation based mechanical testing controllably measures smaller volume of the whole sample volume using contact of a probe of known geometry into the material sample to be investigated (McKee et al., 2011). The small measured volume using indentation allows for characterisation of the variations in the mechanical properties across a sample surface. Effectively observing the local changes in mechanical properties due to changes in structure or composition using indentation is an advantage over tensile testing where mechanical properties are averaged over the whole sample volume. The ability to measure small volumes is of particular interest when considering composite materials, which may have multiple components that result in variations in the local mechanical properties that would not be measured using large volume testing methods. The large volume testing methods, such as tensile testing, often load a sample to complete failure, whereas indentation based testing subjects the sample to a loading and unloading cycle that can avoid failure. Throughout the loading and unloading cycle, the force applied to the indenter is recorded along with the displacement of the indenter and the duration of the testing cycle. The data is then represented as a force-displacement curve for analysis, which is analogous to the force-deformation curves previously described for the tensile testing.

Indentation testing experiments critically require a complete description of the probe used to indent the sample. As the contact area between the probe tip and the sample

surface are used to describe the mechanical response, the probe geometry is often selected to be either a flat cylindrical punch, conical, spherical, or pyramidal geometries as these tip shapes are well established and have well defined experimental methods (Oyen and Cook, 2009). The main difference between the flat punch tip shape and the conical/spherical/pyramidal geometries is the variation of contact area with increasing indentation depth. With the flat punch, the contact area remains constant through the testing process to give force-deformation curves that are similar to the large volume testing methods, where the elastic response produces a linear force-deformation curve. Conical/spherical/pyramidal tip shapes provide contact area changes with indentation depth that result in non-linear force-deformation curve behaviour. This work considers the use of a sharp conical indenter geometry, which is representative of the tip of an atomic force microscopy probe able to evaluate nanometre structural features found within skin structures.

The solution for a rigid cone indenter in contact with an elastic half-space, with Figure 2.8 illustrating the indenter tip shape and surface deformation from the indentation load, was established by Sneddon and is given by the following relationship (Love, 1939; Sneddon, 1948),

$$F = \frac{2E \tan \alpha}{\pi\left(1 - \nu^2\right)} h^2 \qquad \text{Equation 2.6}$$

where F is the force applied to move the indenter a distance, h, into the sample surface, α is the half-tip opening angle of the cone, E the elastic modulus of the surface, and ν the Poisson's ratio of the surface. Equation 2.6 highlights the non-linear relationship between the applied force and the indentation depth. The solution stated here is applicable for indentations that are completely elastic in behaviour. For indentation measurements the elastic behaviour is described as the trace of the

force-displacement curve during the loading is the same as the force-displacement behaviour when the load is removed (Oyen and Cook, 2009).

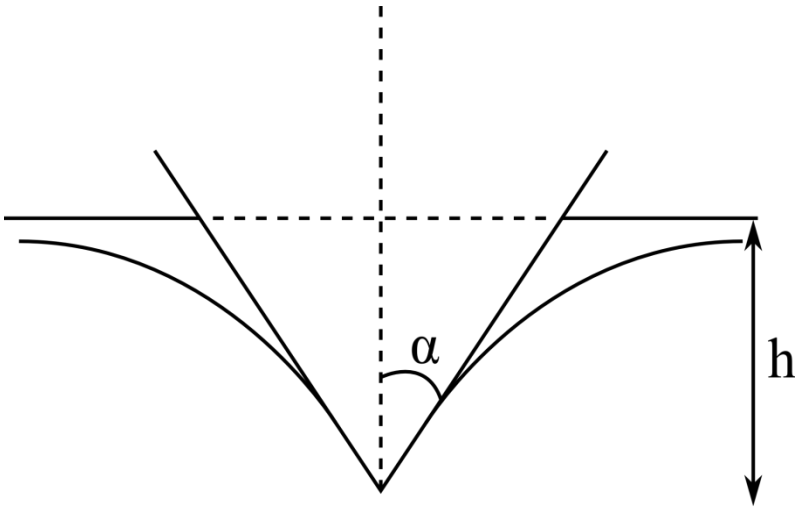

Figure 2.8. A schematic representation of the conical indenter tip indenting the sample surface, represented as an elastic half-space. The indentation depth, h, and the half-tip opening angle, α, are shown.

More commonly the application of indentation loading will lead to permanent deformation of the sample. Permanent deformation within the loading and unloading curves is characterised by the lack of complete recovery of the displacement. The elastic-plastic deformation behaviour is most readily analysed using the Oliver-Pharr method, which has become synonymous with the analysis of nanoindentation data.

The Oliver-Pharr analysis builds upon the initial work by Doerner and Nix, which established that the initial unloading region of the force-displacement curve is described as a linear elastic response (Doerner and Nix, 1986). According to Oliver and Pharr (1992), the elastic modulus is extracted from the unloading data of the force-displacement curve where the initial unloading is fit to the following power-law expression (Oliver and Pharr, 1992),

$$F = a\left(h - h_f\right)^m \qquad \text{Equation 2.7}$$

where a, h_f and m are curve fitting parameters. These parameters are then used to calculate the stiffness at the maximum load, where the stiffness is defined as the slope of the unloading curve and given by $S = dF/dh$. Computation of the stiffness allows for evaluation of the contact depth, h_c, which is the vertical distance where contact is made between the sample and the indenter. The contact depth is computed at the maximum point of the unloading curve (F_{max},h_{max}) and is given by (Oliver and Pharr, 1992)

$$h_c = h_{\max} - e\frac{F_{\max}}{S} \qquad \text{Equation 2.8}$$

where e is a dimensionless geometric parameter related to the shape of the indenter, e = 0.72 for a conical indenter, e = 0.75 for a paraboloid of revolution, and e = 1 for a flat punch geometry (Oliver and Pharr, 1992). The contact depth is used to define the contact area between the indenter and the sample through the use of a calibration function $A_c(h_c)$. The calibration function is determined by indenting a material of known elastic modulus to several different depths and using linear regression to fit a function to describe how the contact area of the indenter varies with indentation depth. The reduced elastic modulus, E_r, can be extracted by analysing the stiffness and the contact area which are related through the following expression (Oliver and Pharr, 1992),

$$E_r = \frac{S\sqrt{\pi}}{2\sqrt{A_c}} \qquad \text{Equation 2.9}$$

The reduced elastic modulus is used here to account for the contribution of a non-rigid indenter to force-displacement curve and is defined by (Oliver and Pharr, 1992)

$$\frac{1}{E_r} = \frac{\left(1 - {\nu_s}^2\right)}{E_s} + \frac{\left(1 - \nu_i^2\right)}{E_i} \qquad \text{Equation 2.10}$$

with E_s and ν_s being the elastic modulus and Poisson's ratio of the sample and E_i and ν_i the same parameters for the indenter. In practice the elastic modulus of the indenter is several orders of magnitude higher than that of the sample, especially in the case of biological materials and the reduced elastic modulus is taken as the plane strain modulus of the sample (Sirghi et al., 2008),

$$\frac{1}{E_r} = \frac{\left(1 - \nu^2\right)}{E} \qquad \text{Equation 2.11}$$

For example a silicon nitride indenter will have an approximate elastic modulus of 280 GPa with a Poisson's ratio of 0.2 (Khan et al., 2004) and polydimethylsiloxane substrate with an elastic modulus of 2 MPa and an assumed Poisson's ratio of 0.5 (Sirghi and Rossi, 2006), the contribution from the indenter to the calculated elastic modulus according to Equation 2.10 would be less than 0.001%. Therefore, Equation 2.11 is suitable for calculating the elastic modulus from the reduced elastic modulus value with low elastic modulus materials. It should be noted that throughout this thesis whenever elastic modulus, or *E*, is stated it refers to the linear isotropic elastic modulus.

2.4 Atomic Force Microscopy

The characterisation and mechanical testing of sample surfaces at small length scales by indentation can be conducted using atomic force microscopy (AFM). AFM falls into the class of scanning probe microscopy (SPM). SPM is a microscopy technique that is based around using a probe to measure a specific interaction between a sample

surface and the SPM probe. The interaction varies depending on the application, for example scanning tunnelling microscopy uses the tunnelling current between the probe and the sample surface.

In order to reconstruct an image from the measured interaction force, the probe is scanned across the sample surface in a predetermined rectangular pattern in the x and y directions, also known as raster scanning. The value of the interaction force at each point during the scan is recorded along with the z coordinate of the probe. As the interaction force between the probe and the sample surface changes, the z coordinate is changed in order to maintain a predefined set point. The set point is a specified value of the interaction force that the SPM system maintains throughout the raster scan. A feedback loop is used to maintain the set point by comparing the value of the interaction to the predefined set point value and adjusting the z coordinate in order to return from the measured interaction value to the set point value. The x, y and z coordinates at each point during the scan are recorded so a three dimensional reconstruction can be performed (Binnig et al., 1986).

The AFM monitors the repulsive or attractive atomic forces between the probe and the sample surface. The net force acting between the probe and sample surface will be repulsive or attractive depending on the distance between the probe and the sample surface. Contact between the probe and the sample surface is defined by a repulsive force, resulting in the probe being pushed away from the sample surface (Cappella and Dietler, 1999). The force acting between the probe and sample away from hard contact becomes attractive and is caused by long range interaction through van der Waals forces, which will pull the probe towards the surface (Weisenhorn et al., 1989). The characterisation of the forces between the probe and the sample surface can be described by a Lennard – Jones potential curve, shown in Figure 2.9.

As the distance between the two decreases the force is attractive between the two until a stable minimum is reached, decreasing the distance further results in a repulsive interaction between the two bodies (Cappella and Dietler, 1999).

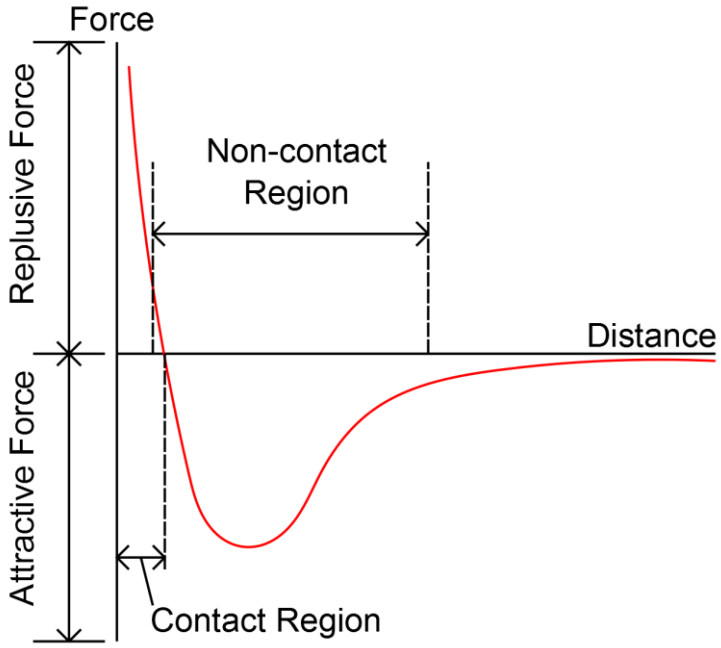

Figure 2.9. The Lennard - Jones potential curve describing the interaction forces between two atoms as a function of distance between the two atoms.

The AFM was originally developed by Binnig *et al.* in 1986 as a method for measuring forces on the order of 10^{-16} N (Binnig et al., 1986). The initial AFM system utilised a diamond probe mounted on a gold foil cantilever with an STM system as the feedback mechanism, where the tunnelling current was used to control the z coordinate of the probe (Binnig et al., 1986). In the modern AFM system, shown schematically in Figure 2.10, the probe is often mounted on a cantilever, which is often made of silicon or silicon nitride. A cantilever system is used in order to measure small attractive and repulsive forces between the probe and the sample

surface. The interaction forces are measured by monitoring the cantilever deflection, which is a result of the force applied to the AFM probe. An optical lever system, where laser light is reflected off the back of the cantilever onto a photodiode, is used to monitor the cantilever deflection (Lévy and Maaloum, 2001). The photodiode is separated into quadrants to allow for measurement of cantilever deflection in the z direction but also lateral deflection of the cantilever. The raster scanning elements are piezoelectric positioners in the x, y and z directions. Individual piezo scanners allow for high spatial resolution and control of the z position of the probe. Depending on the AFM system, the piezo scanners can be mounted to the cantilever system or beneath the sample. This mounting allows for raster scanning by moving the stage or moving the probe. The cantilever itself is additionally fixed to a piezoelectric generator, which allows oscillation of the cantilever for dynamic operation as discussed below.

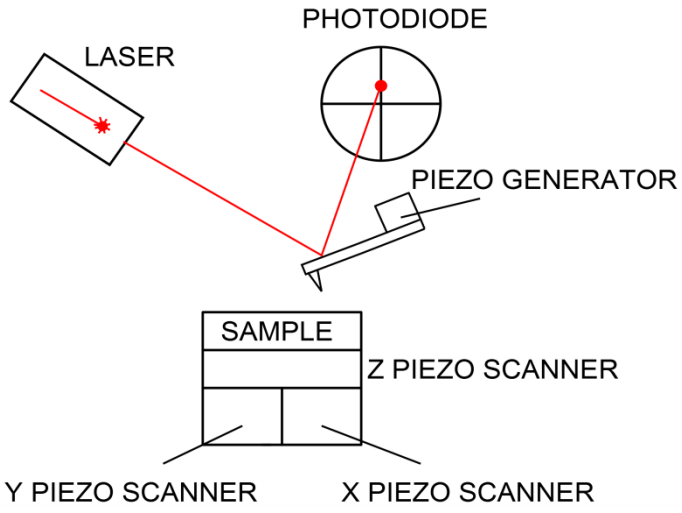

Figure 2.10. Schematic of conventional AFM setup with optical lever method for detecting cantilever deflections.

Contact mode and semi contact mode are the two principal imaging operation modes for the AFM. Each mode corresponds to a different region of the Lennard – Jones potential. Contact mode operates in the repulsive region of the potential, as shown in Figure 2.9, and corresponds to the probe moving into physical contact with the surface of the sample, with the resultant repulsive force between the probe and the surface causing cantilever deflection away from the sample surface. In contact mode, the set point is a predefined amount of cantilever deflection, with a constant degree of cantilever deflection corresponding to a constant force being applied to the sample surface. As the probe is scanned across the surface, topographical features will cause an increase in decrease in cantilever deflection, which will trigger the set point to adjust the height of the probe to return to the set point value of cantilever bending (García and Perez, 2002). Placing the probe in contact with the sample surface has the potential to damage both the sample surface and the probe tip as the applied force between the probe in contact with the sample acts over a relatively small contact area.

Semi contact mode, also known as non-contact or intermittent contact mode, operates in the attractive force region of the Lennard – Jones potential as shown in Figure 2.9. In semi contact mode, the cantilever is oscillated by a piezoelectric generator at the resonant frequency of the cantilever. The resonant frequency provides a stable amplitude of oscillation that can be measured by the optical lever system (Drake et al., 1989). The attractive force applied through van der Waals interactions between the probe and the sample surface reduces the amplitude of the oscillation of the cantilever (Weisenhorn et al., 1989). Reducing the distance between the probe and the sample surface increases the attractive force and further decreases the amplitude of the oscillation of the cantilever (Weisenhorn et al., 1992). The set point in semi

contact mode is specified as the magnitude of the cantilever oscillation. Low values of the set point can result in a high attractive force between the probe and the sample surface, resulting in probe coming into intermittent contact with the sample surface during oscillation and scanning.

Within semi contact mode, phase imaging can be used to measure the material properties of the sample surface in addition to collecting topographical information with semi contact mode. The piezoelectric generator induces an oscillation at a known phase angle and the interactions between the probe and the sample surface result in a phase lag between the cantilever and the generator. Phase imaging measures the phase shift between the phase angle of the piezoelectric generator and the measured phase angle of the cantilever (García and Perez, 2002). The oscillations of the cantilever provide intermittent contact between the probe and sample surface with the resulting attractive interaction between the probe and the sample causing a phase lag, or phase shift, between the phase angle of the driving force and the cantilever (Bar et al., 1997). The magnitude of the phase shift depends on the stiffness of the material, where low stiffness materials will produce larger phase shifts because of higher attractive interactions (Bar et al., 1998). The phase shift information can be collected in conjunction with the topographical height information measured with standard semi contact mode imaging to compare the height information with qualitative material property information (Magonov and Reneker, 1997). However, changing probe contact areas with a sample surface due to changes in topography restrict the use of phasing imaging as a quantitative method for evaluating material mechanical properties. Advantages of semi contact mode and phase imaging are based on the probe requiring only intermittent contact with the sample surface during operation, which reduces the risk of damaging the probe tip

and the sample surface during imaging (Giessibl, 2003). Indeed, the integrity of the probe tip is extremely important when studying the surface of a material as the radius of curvature of the probe tip determines the ultimate achievable resolution with the AFM (Jandt, 2001). The geometry of the AFM tip introduces convolution into the final reconstructed image such that large tip radii of curvature cause broadening of the lateral dimensions of features in the reconstruction of a sample's surface, whereas a blunted or damage tip can introduce additional error into the final reconstructed image (García and Perez, 2002).

One of the major benefits of the AFM is the operation in a liquid environment (Drake et al., 1989; Hansma et al., 1994; Weisenhorn et al., 1992, 1989). The ability to immerse the entire AFM system in a liquid allows for the imaging and characterisation of many materials that would be otherwise impossible to measure in air or a vacuum (Alsteens et al., 2012; Kurland et al., 2012). This operation is particularly important when studying biological materials such as cells or proteins, as they require specific imaging environments (Bastatas et al., 2012; Cross et al., 2008; Ge et al., 2007; Haga et al., 2000; Heinisch et al., 2012; Kurland et al., 2012; Lulevich et al., 2010; Sen et al., 2005; Sirghi et al., 2008; Wu et al., 1998).

2.4.1 Contact Mechanics

The local mechanical properties of a material are commonly measured using AFM based indentation, which requires an understanding of the contact forces that are involved between the two interacting bodies of the AFM tip and sample surface. Specifically, force applied by the AFM tip will cause mechanical contact deformation of the sample (García and Perez, 2002). The deformation and contact

mechanics between the probe and sample can be described by continuum elasticity theories. These theories describe the forces between two interacting bodies through both the contact and adhesive forces. Numerous theories have been developed that can be applied to studying contact mechanics depending on the type of contact that is taking place between the bodies. These theories relate the contact and adhesive forces to the material properties of the system and are therefore considered here.

The interaction between two bodies in contact was initially studied by Hertz in 1882 (Notbohm et al., 2012). The work conducted by Hertz applied to linear elastic spheres contacting planar surfaces at small displacements and assumed that there were no surface or shear forces between the sample and contacting sphere. This work was also applied to the contact between a sphere and a planar surface, referred to as the linear elastic half space. Two other methods proposed more complete theories that incorporate the adhesive forces into the description of the contact mechanics. The Derjaguin-Muller-Toporov (DMT) theory generally applies to stiff contacts with low adhesive forces and small tip interactions (García and Perez, 2002). The final main contact mechanics theory is described by the Johnson-Kendell-Roberts (JKR) model, which can be used to describe low stiffness contact with large adhesive forces and large tip interactions (García and Perez, 2002). The major differences between the DMT and JKR theories lie in the adhesion force between the sphere and the elastic half space. Specifically, JKR accounts for the initial deformation that occurs within the half space because of the applied adhesive force with the contacting sphere (Greenwood, 2007). Figure 2.11 illustrates this initial contact between a sphere mounted on an AFM cantilever and an elastic half space as modelled by each theory. The Hertz model exhibits no initial adhesion between the two surfaces, DMT displays an initial adhesive force between the two surfaces, whereas JKR accounts

for the tensile force that is applied to the half space drawing it up into adhesive contact with the sphere.

Figure 2.11. Illustration of the initial contact of Hertz, DMT, and JKR theories.

Maugis showed that DMT and JKR theories represent the upper and lower bounds of the same contact behaviour and can be related through the Tabor parameter, μ_T (Greenwood, 2007, 1997).

$$\mu_T = \left(\frac{R\Delta\gamma^2}{E_r{}^2 \varepsilon_0^3} \right)^{\frac{1}{3}} \qquad \text{Equation 2.12}$$

Where R is the radius of the sphere, $\Delta\gamma$ the work of adhesion, ε the equilibrium spacing, and E_r the reduced modulus defined in Equation 2.10 (Johnson and Greenwood, 1997).

The Tabor parameter is instructive in defining which theory to apply when measuring the contact behaviour between the sphere and sample surface. A Tabor parameter of less than 0.1 indicates that elastic deformation is negligible, which warrants use of DMT theory. Conversely a Tabor parameter of greater than 5 indicates that there is significant adhesive interaction so that JKR theory can be applied. Additionally, these DMT and JKR theories can also be compared by the elasticity parameter, λ, as proposed by Maugis (Greenwood, 1997).

$$\lambda = 2\sigma_0 \left(\frac{9R}{16\pi\Delta\gamma E_r^{\ 2}} \right)^{\frac{1}{3}} \qquad \text{Equation 2.13}$$

Where R is the radius of the sphere, $\Delta\gamma$ the work of adhesion, σ_0 the maximum adhesion stress, and E_r the reduced modulus. The elasticity parameter, Equation 2.13 can again be used to select which theory describes the contact and is equal to $1.16\mu_T$. With $\lambda = 0$ the Hertz theory applies, $\lambda < 0.1$ DMT, and $\lambda > 5$ JKR applies. The region between $\lambda = 0.1$ and 5 indicates a transition region between the DMT and JKR theories (Johnson, 1997).

Magius also proposed a set of equations to define the contact in the region of $0.1 > \lambda > 5$ in addition to the elasticity parameter used to describe the transition between the DMT and JKR theories. However, despite these equations, which were experimentally verified by Lantz et al., the material properties of the elastic modulus and the adhesive force cannot be directly determined from a simple force distance curve (Butt et al., 2005). Despite these shortcomings, methods can be used to model experimental data and extract material properties such as the elastic modulus, but difficulties mainly lie in selecting the appropriate theory that applies to the experimental conditions. Lin et al. have shown that these theories can be applied to model the contact interactions of soft materials, mainly polyvinyalcohol gels and tissue engineered cartilage, with and without adhesive forces and comparing the results to macroscopic measurements with good agreement (Lin et al., 2007a, 2007b). The theories described above are generally used to evaluate the forces involved in the adhesion and separation of two bodies, and are not generally suited to the evaluation of material properties.

The adhesive interactions between the AFM probe tip and the sample surface during an indentation curve can be incorporated into the analysis of force-displacement curves and a simple model was put forward by Sirghi and Rossi. The model proposes that the total force applied to the cantilever during the unloading curve is a sum of the elastic force of the sample, F_E, and the adhesive force of the AFM tip-sample contact, F_A, via,

$$F = F_E + F_A \qquad \text{Equation 2.14}$$

The elastic force, for a conical indenter, is equal to Sneddon's solution for the indentation of a purely elastic half-space, described in Equation 2.6. The adhesive forces will result in a remnant indentation depth, h_f, which can be incorporated into the expression for the elastic force during the unloading of the indenter such that the expression becomes (Sirghi and Rossi, 2006),

$$F_E = \frac{2E\tan\alpha}{\left(1-\nu^2\right)\pi}\left(h-h_f\right)^2 \qquad \text{Equation 2.15}$$

The contribution of the adhesive interaction between the AFM probe and the sample surface the work of adhesion is first considered. Where the energy of adhesion, W_a, for the contact is described as (Sirghi and Rossi, 2006)

$$W_a = -\gamma_a A_c \qquad \text{Equation 2.16}$$

where γ_a is the thermodynamic work of adhesion and A_c is the function describing the contact area between the AFM probe and the sample surface. The contact area of the AFM probe, modelled as a sharp conical tip, is given by (Sirghi and Rossi, 2006),

$$A_c = \frac{\pi\tan\alpha}{\cos\alpha}h_c^2 \qquad \text{Equation 2.17}$$

The adhesive contact energy can then be rewritten in terms of the indentation depth, *h*, as (Sirghi and Rossi, 2006)

$$W_a = -\frac{\gamma_a 4\tan\alpha}{\pi\cos\alpha}h^2 \qquad \text{Equation 2.18}$$

The adhesive force can then be expressed as (Sirghi and Rossi, 2006)

$$F_a = -\frac{\gamma_a 8\tan\alpha}{\pi\cos\alpha}h \qquad \text{Equation 2.19}$$

which, for a remnant indentation imprint at a displacement, h_f, modifies Equation 2.19 to give (Sirghi and Rossi, 2006)

$$F_a = -\frac{\gamma_a 8\tan\alpha}{\pi\cos\alpha}\left(h - h_f\right) \qquad \text{Equation 2.20}$$

The above equation leads to the total force being applied to the AFM probe tip to be expressed via (Sirghi and Rossi, 2006)

$$F(h) = \frac{2E\tan\alpha}{\left(1-\nu^2\right)\pi}\left(h - h_f\right)^2 - \frac{\gamma_a 8\tan\alpha}{\pi\cos\alpha}\left(h - h_f\right) \qquad \text{Equation 2.21}$$

Equation 2.21 can then be applied to fit the unloading curve of an AFM force-displacement curve where the adhesive interaction is present.

The adaptation of atomic force microscopy (AFM) systems to explore biomaterials and native biological materials has become increasingly popular because the AFM provides an accessible method for measuring the mechanical properties of biological materials by applying forces to different points at a sample surface (Jandt, 2001). The force sensitivity and high spatial resolution of the AFM allows for mechanical measurements to be made on the nanoscale and accurately determine the material properties of these small volumes (Mathur et al., 2001). Mathur *et al*. were able to use the low force sensitivity of the AFM to accurately probe endothelial, cardiac

muscle and skeletal muscle cells using AFM force distance curves and report the measured elastic modulus; approximately 100 kPa for cardiac muscle, 25 kPa for skeletal, and between 2 kPa and 7 kPa for endothelial cells (Mathur et al., 2001). Similarly, Cross *et al* have shown that cancerous cells show a change in overall cell stiffness and this has been extensively studied using AFM. Cancerous tumour cells showed a statistically significant decrease, over 80% reduction, in the overall stiffness when compared to benign cells (Cross et al., 2008). Charras et al. utilised the high spatial resolution of the AFM to map the mechanical properties over the surface of osteoblasts and develop a finite element model for the examining the strains experienced throughout a cell (Charras and Horton, 2002). Such a method of exploiting AFM to identify local mechanical properties across a surface is of potential interest in exploring structure-mechanical function relationships in skin to address the aims of this thesis.

2.4.2 Calibration of AFM Cantilevers

The AFM is a powerful technique able to both image a sample's surface as well as investigate surface mechanics, both with high spatial resolution. Mechanical measurements at the surface of a material are typically quantified by recording the interactions between the AFM probe and the surface of interest. The AFM probe is the most important component of the system and directly interacts with the surface of the material, which makes it extremely important to understand the behaviour of the material. AFM probes are designed and fabricated as cantilever systems and generally take two forms, a rectangular design or v-shaped design. The cantilever design allows for direct application of Hooke's law to the system and quantification

of the interactions forces. In order to utilize Hooke's law, the normal spring constant of the cantilever must be known.

Numerous methods for calculating the spring constant of AFM cantilevers have been developed, both analytical and experimental, but many require the input of cantilever dimensions. However, accurately determining cantilever dimensions is non-trivial and can lead to significant errors in the resultant spring constant value. In order to understand the effect of the cantilever dimensions on the calculated spring constant, a rectangular cantilever can be modelled as a simple beam with a rectangular cross section and one fixed end, as shown in Figure 2.12 (Cleveland et al., 1993). The stiffness of the rectangular beam can be defined as

$$k = \frac{F}{\delta} = \frac{Ewt^3}{4L^3}\delta \qquad \text{Equation 2.22}$$

Where k is the normal spring constant, F the force applied to the AFM probe that causes cantilever bending, δ the deflection of the cantilever beam and E is the elastic modulus of the beam material. Equation 2.22 shows a dependence of the stiffness on the cube of the thickness of the beam, indicating that uncertainty in the measurement of the thickness could result in a large error in the calculation of the spring constant value.

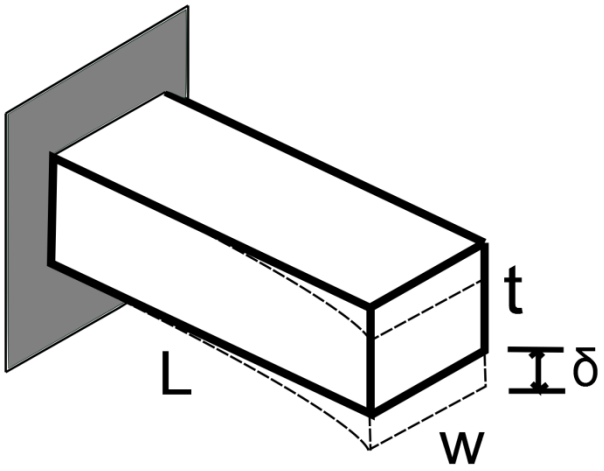

Figure 2.12. Simple beam bending diagram used to represent the geometric approximations applied to the AFM rectangular cantilevers when calculating the cantilever spring constant by the Sader method.

Initially Sader *et al.* developed a method for calibrating AFM cantilevers that required knowledge of the mass and the dimensions of the cantilever (Sader et al., 1995). However, the difficulties of measuring the mass and the dimensions, particularly the cantilever thickness, made this impractical for standard laboratory use. Sader *et al*. further outlined an analytical method that required knowledge of the cantilever resonant frequency, quality factor and plan view dimensions shown in Equation 2.23 (Sader et al., 1999).

$$k = 0.190\rho_f w^2 L Q_f \Gamma_i \omega^2 \qquad \text{Equation 2.23}$$

Where ρ_f is the density of the fluid environment, usually air, w is the width of the cantilever, L the length of the cantilever, Q_f the quality factor of the cantilever in the fluid environment, Γ_i the hydrodynamic function and ω the resonant frequency of the cantilever.

Critically, all of the parameters in Equation 2.23 can be measured easily experimentally. The plan view dimensions can be measured with high accuracy optically or with an electron microscope and the resonant frequency and quality factor can be measured using a standard AFM set up. Liquid density and the hydrodynamic function, which described the motion of the cantilever in liquid, are also assumed based on tables and mechanics calculations respectively. The spring constant using Equation 2.23 is therefore easily measurable. The only drawback of the Sader method is that cantilevers with rectangular plan view dimensions only are considered (Sader et al., 1999).

For v-shaped cantilevers, the most basic approach is to use the parallel beam approximation (PBA) (Sader, 1995). The PBA models the cantilever as two rectangular beams joined at one end. The stiffness for this model can be defined as (Albrecht et al., 1990)

$$k = \frac{Ewt^3}{2L^3}\left(1+\frac{b^2}{4L^2}\right)^{-2} \qquad \text{Equation 2.24}$$

Equation 2.24 shows a strong dependence between the measured thickness and the calculated spring constant value in the model. In addition, PBA describes the v-shaped cantilever shown in Figure 2.13a only and does not accurately model additional v-shaped cantilever designs shown in Figure 2.13b-d.

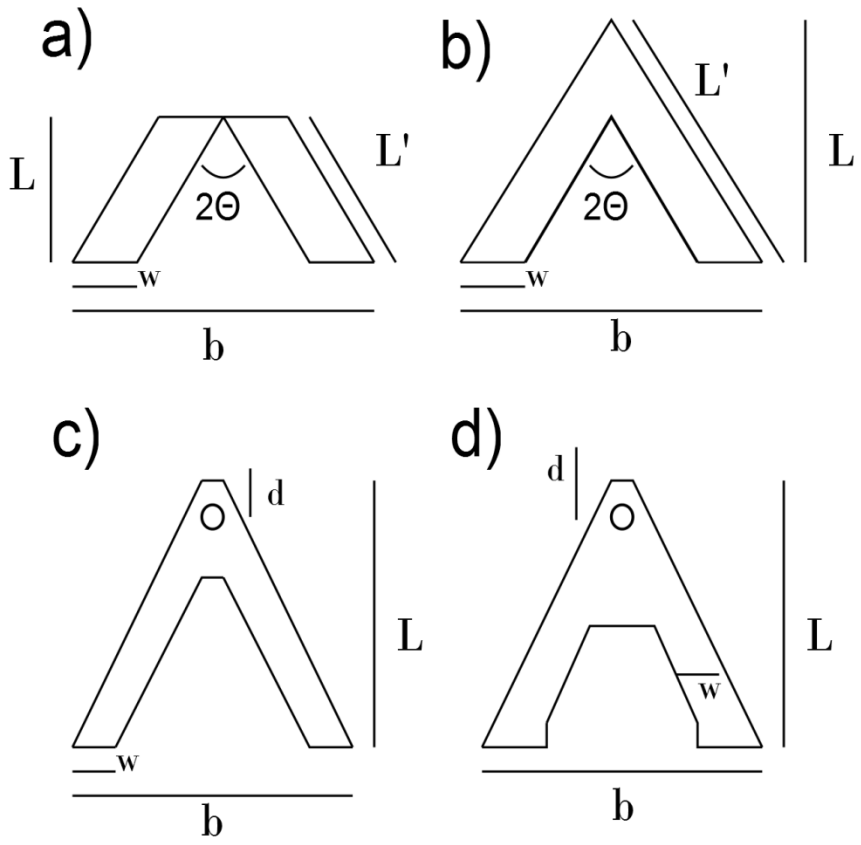

Figure 2.13. The variations in cantilever designs illustrated in a) and b) represent the geometries used for theoretical calculations of the cantilever spring constant. Cantilevers c) and d) display the actual geometry of v-shaped AFM cantilevers. Different geometries of v-shaped cantilevers, illustrating the potential variations in cantilever designs and highlighting the non-ideal geometries where the spring constant cannot be evaluated by simplifying the geometry for an analytical estimations.

The result of multiple v-shaped cantilever geometries has produced a range of equations that aim to model the cantilever and calculate the spring constant value (Clifford and Seah, 2005). The different analytical models are outlined in Equation 2.23-Equation 2.26 where the dimensions are shown in Figure 2.13a-b. Equation

2.23 and Equation 2.24 consider the cantilever geometry a) from Figure 2.13 and are different results for the parrallel beam approximation. The model described by Equation 2.26 is applied to the idealised cantilever geometry shown in Figure 2.13b. It should be noted that all of the models show a dependence on the elastic modulus and the thickness of the cantilever.

(Sader and White, 1993)

$$k = \frac{Ewt^3}{2L^3}\left(1+\frac{4w^3}{b^3}\right)^{-1} \qquad \text{Equation 2.25}$$

(Sader, 1995)

$$k = \frac{Ewt^3}{2L^3}\cos\theta\left(1+\frac{4w^3}{b^3}\left(3\cos\theta-2\right)\right)^{-1} \qquad \text{Equation 2.26}$$

These methods also assume the cantilevers are perfect in shape and free of any internal defects or stresses that can alter the spring constant.

For rectangular shaped cantilevers, the method for calculating the spring constant can be achieved through dimensional or experimental analysis and are well defined using the Sader method (Sader et al., 1999) or finite element analysis (Clifford and Seah, 2005). However, calculating the spring constant for v-shaped cantilevers can be more complex due to non-perfect v-shaped cantilevers that are fabricated from multiple materials with varying elastic modulus or additional layers deposited on the surface of the cantilever. Heterogeneous cantilever materials are commonly found due to the application of a thin film of gold sputtered onto the back surface of the cantilever to improve laser reflection from the back of the cantilever to the photodiode detector. The use of multiple layers in a cantilever complicates the use of established spring constant calculations based on the dimensions of the cantilever using beam bending theory. Therefore, a method that does not require the measurement of the cantilever dimensions is beneficial.

The measurement of thermal fluctuations is considered the current state-of-the-art and allows for a dynamic experimental method for calculating the normal spring constant of any shape cantilever using an existing AFM set up. This method was originally outlined by Hutter and Bechhoefer and has been expanded on by others. The thermal fluctuation method models the cantilever as a harmonic oscillator in equilibrium with the surrounding environment and therefore any changes in the thermal environment will cause fluctuations in the oscillator (Hutter and Bechhoefer, 1993). The system can be described using the mass, resonant angular frequency, deflection and temperature of the oscillator in the general form

$$H = \frac{p^2}{2m} + \frac{1}{2} m\omega_0^2 \delta^2 \qquad \text{Equation 2.27}$$

Equation 2.27 represents the Hamiltonian of a harmonic oscillator at equilibrium where p is the momentum, m the mass, ω_0 the resonant angular frequency, and δ the deflection of the oscillator. The deflections of the oscillator, in the case of an AFM cantilever, are caused by thermal gradients in the environment. The deflections of the cantilever due to the changes in the thermal environment can also be called thermal fluctuations (Hutter and Bechhoefer, 1993). Each term in the Hamiltonian can be described by utilising the equipartition theorem which states that the average value of each term is $k_bT/2$, where k_b is Boltzmann's constant and T is the temperature (Hutter and Bechhoefer, 1993). Knowing the value of each term in the Hamiltonian allows for the establishment of a relationship between the motion of the oscillator and the average value from the equipartition theorem, shown in Equation 2.28.

$$\left\langle \frac{1}{2} m\omega_0^2 \delta^2 \right\rangle = \frac{k_b T}{2} \qquad \text{Equation 2.28}$$

Further, the angular resonant frequency is defined as

$$\omega_0^2 = \frac{k}{m} \qquad \text{Equation 2.29}$$

with the relationship from Equation 2.29 the normal spring constant can be related to the deflection of the oscillator by

$$k = \frac{k_b T}{\langle \delta^2 \rangle} \qquad \text{Equation 2.30}$$

where $\langle \delta^2 \rangle$ is the mean square deflection of the oscillator. Equation 2.30 directly relates the deflections of a harmonic oscillator to the normal spring constant. The relationship shows that the value of the spring constant increases as the mean square deflections of the oscillator decreases. Measurement of thermal fluctuations of a cantilever at room temperature have given AFM cantilever deflections of approximately 3 Å for a cantilever spring constant of 0.05 $N.m^{-1}$ (Hutter and Bechhoefer, 1993). The relationship between mean square deflection and spring constant from Equation 2.30 is therefore useful for quantifying the spring constant of any cantilever shape based on knowing the deflections of the oscillator if additional environment noises are removed. In order to remove additional noise, the deflections must be analysed in the frequency domain at the resonant frequency of the oscillator as other contributions to noise are unlikely to have a resonance at the resonant frequency of the oscillator. The behaviour of the deflections of the oscillating cantilever around its resonant frequency can be described by a power spectral density (PSD) (Hutter and Bechhoefer, 1993). A PSD describes how the power of a signal, which is the deflection signal in the case of the oscillator, changes over a range of frequencies. The PSD for the deflections of the oscillator can be described by a

Lorentzian line shape and the integral of a PSD describes the power of the deflections and represents the mean square deflections over the range of frequencies sampled. Using this information, Equation 2.30 can be rewritten as

$$k = \frac{k_b T}{P_{PSD}} \qquad \text{Equation 2.31}$$

where P_{PSD} is the value of the integral of the Lorentzian fit for the PSD of deflection vs frequency data. In practice, measurements of the thermal fluctuations of the AFM cantilever are taken over a range of frequencies away from the cantilever resonance in order to observe any additional noise, which can be subtracted from the system, so only the thermal fluctuations of the system are being analysed for the calculation of the spring constant.

2.5 Skin Mechanics

The macroscopic mechanical behaviour of skin has been studied extensively using traditional mechanical testing methods, such as uniaxial tension or indentation and other less conventional methods such as suction (Diridollou et al., 2000; Jachowicz et al., 2007; Ní Annaidh et al., 2012b). These testing methods provide a direct measurement of the bulk mechanical properties of skin at a large scale and can be used to describe the macroscopic mechanical environment. Uniaxial tensile testing is also used to determine the strength of skin in terms of the ultimate tensile strength or understand the failure behaviour of skin on a large scale. However, the extreme stresses and strains applied to skin in these testing environments are rarely experienced in vivo and simply serve as a method to fully understand skin as a

material. The elastic modulus of skin, sampled from human and mouse models, from several previous studies as determined by the use of different macroscopic mechanical testing methods are assembled and displayed in Table 2.1. These results show that the macroscopic elastic modulus value of skin lies between approximately 4 kPa and 160 MPa. Such a large range of reported values for the elastic modulus indicates that the mechanical response of the skin is highly variable between sample donors and that there is an effect of the testing method on the measured response. The effect of the testing method on the elastic modulus is most evident when subjecting a skin sample to a uniaxial tensile test. Whole skin displays a non-linear stress-strain relationship under tensile loading, with an initial linear region, characterised by a small slope of the curve occurring at small strains ($\varepsilon<0.1$), transitioning to another linear region with a higher slope, as illustrated in Figure 2.14 (Ní Annaidh et al., 2012b).

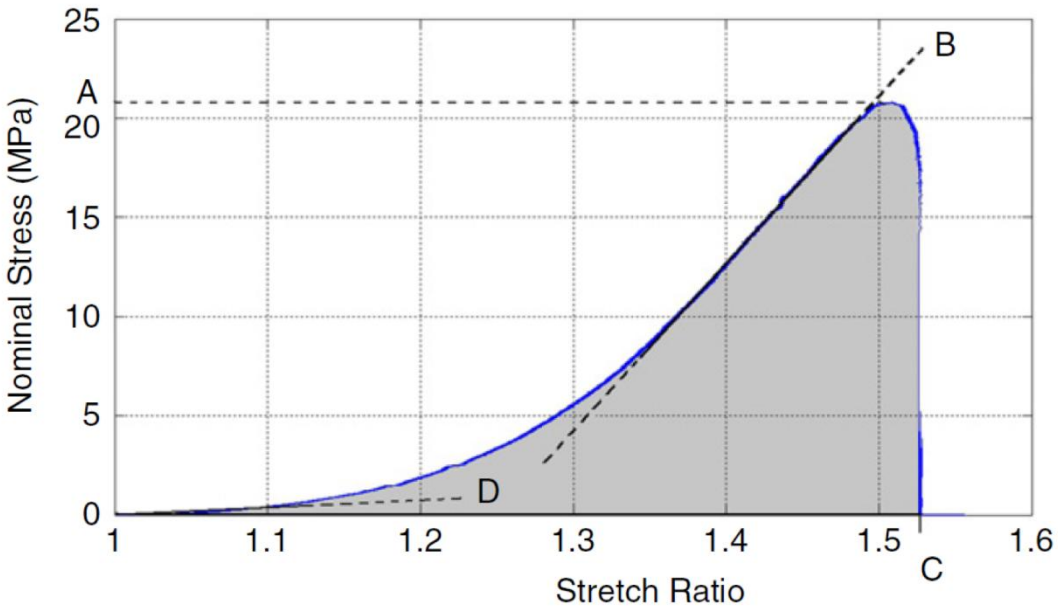

Figure 2.14. Stress vs stretch for a uniaxial tensile test of full thickness human back skin. (A) showing the maximum tensile stress, (B) the upper slope showing the increased elastic modulus as a result of the load transfer to the aligned collagen fibres, (C) the stretch ratio at which failure of the sample occurred, and (D) the initial lower slop region showing the low elastic modulus response. Adapted from (Ní Annaidh et al., 2012b).

The initial slope of the stress-strain curve results in an elastic modulus between 0.54 MPa and 1.95 MPa whereas the slope of the upper region results in an elastic modulus of 37.66 MPa to 112.47 MPa (Ní Annaidh et al., 2012b). The low strain elastic modulus region is attributed to the contribution of the elastic fibres within the dermis to the mechanical response and the high strain elastic modulus is the result of the stressing of the collagen fibres (Silver et al., 2001). The ability of the collagen fibres to realign within the matrix should also be considered when analysing the behaviour of the stress-strain curves as it is established that despite being a

preferentially aligned network, the collagen fibres will go through a reorientation process to align with the direction of the strain leading to the overall non-linear stress-strain behaviour (Purslow et al., 1998).

Uniaxial tensile testing provides unique insight into the dependence of the mechanical response to the direction of the applied load, displaying the anisotropic behaviour of skin that is well established (Corr et al., 2009; Gąsior-Głogowska et al., 2013; Melling et al., 2000; Ní Annaidh et al., 2012a, 2012b). The mechanical anisotropy arises from the preferential alignment of the collagen fibres within the dermis, where applying the load parallel to the fibre direction results in a high elastic modulus between 112 MPa and 160 MPa and applying the load perpendicular to the fibre direction reduces the elastic modulus to between 37.6 MPa and 70.6 MPa (Ní Annaidh et al., 2012b; Ottenio et al., 2014).

The effect of the collagen fibre network can be simplified by representing skin as a two-phase composite material where the collagen fibres represent continuous aligned fibre reinforcement within a matrix. Applying a load parallel the fibre direction results in a higher elastic modulus compared to when the load is perpendicular to the fibre direction that results in a lower elastic modulus. The stress-strain curve behaviour for both the parallel and perpendicular sample alignment is similar with a low elastic modulus initial region transitioning to a higher elastic modulus region. The anisotropic effect under uniaxial tension is independent of the applied strain with the anisotropic response of the elastic modulus evident at across all strain levels under tensile loading (Melling et al., 2000). These experimental results consider macroscopic scale testing and applying a large strain to skin with the assumption that the collagen fibres will be exposed to the loading conditions. However, no studies currently report on the effect of the direction of the applied load on the mechanical

properties of the skin at the nanoscale, where directionality could have an effect on the microenvironment experienced by cells within the skin.

Investigations into the mechanical properties of skin have also been conducted at the submicron length scale with the major findings tabulated in the second half of Table 2.1. A large range of reported elastic modulus values for skin and the constituent components is observed that is similar to the measurements at the macroscale. Submicron scale measurements techniques, such as AFM indentation and microprobe indentation, allow for characterisation of the isolated constituent layers of skin. However, the through thickness spatial variation of the mechanical properties of skin has yet to be investigated. The analysis of the through thickness mechanical properties would provide a comprehensive mechanical description without disrupting the constitute components by separating the layers. Skin is a three dimensional microenvironment and by performing through thickness mechanical testing it would be possible to observe any location dependent changes in the mechanical properties. The potential spatial variations in the mechanical properties that could exist through thickness would provide a better understanding of the cell microenvironment existing within the skin. As skin is a complex biological composite material, the spatial variations through the thickness also provides an avenue to investigate the contribution of the individual layers to the overall mechanical properties.

Table 2.1. Elastic modulus values from literature of skin and skin components determined by various mechanical testing methods at a range of length scales. Elastic modulus values are represented as the average value or the range of values reported.

Location	Testing Method		Elastic Modulus (MPa)	Notes	Reference
Macroscopic			**Average or Range**		
Full thickness	Indentation	*in vivo*	0.00567		(Delalleau et al., 2006)
Stratum Corneum	Indentation	*in vitro*	2.6		(Geerligs et al., 2011)
Epidermis	Indentation	*in vitro*	1.1		
Full thickness	Indentation	*in vivo*	0.007-0.033		(Jachowicz et al., 2007)
Full Thickness	Indentation	*in vivo*	0.0083		(Zahouani et al., 2009)
Full thickness	Indentation	*in vitro*	0.0045-0.008		(Pailler-Mattei et al., 2007)
Full thickness	Uniaxial tension	*in vivo*	12	Parallel direction	(Gąsior-Głogowska et al., 2013)
			2	Perpendicular direction	
Full thickness	Uniaxial tension	*in vitro*	112.47	Parallel direction	(Ní Annaidh et al., 2012b)
			37.66	Perpendicular direction	
Full thickness	Uniaxial tension	*in vitro*	160.8	Parallel direction	(Ottenio et al., 2014)
			70.6	Perpendicular direction	
Full thickness	Uniaxial tension	*in vitro*	0.1	Low strain region	(Silver et al., 2001)
			18.8	High strain region	
Full thickness	Extension	*in vivo*	0.657	Parallel direction	(Khatyr et al., 2004)
			0.13	Perpendicular direction	
Full thickness	Suction	*in vivo*	0.129		(Diridollou et al., 2000)

Micro/nanoscale				**Probe Size (μm)**	
Dermis	AFM indentation	*in vitro*	0.322	Sharp cone	(Grant et al., 2012)
Dermis	AFM nanoindentation Mouse	*in vitro*	0.006427	Sharp cone	(Petrie et al., 2012)
Dermis	AFM nanoindentation	*in vitro*	0.0001-0.01	5	(Achterberg et al., 2014)
Stratum Corneum	AFM nanoindentation	*in vitro*	1.033	6.62	(Crichton et al., 2011)
	Mouse		2.346	1.9	
Epidermis	AFM nanoindentation	*in vitro*	0.751	6.62	
	Mouse		2.42	1.9	
Dermis	AFM nanoindentation	*in vitro*	11.62	6.62	
	Mouse		32.1	1.9	
Full thickness	Microprobe indentation	*in vitro*	29.7	0.5	(Crichton et al., 2013)
	Mouse		11.15	1	
			8.19	2.5	
			3.26	5	
			1.31	10	
			0.86	20	

2.6 Scaffolds for Tissue Engineering of Skin

Tissue engineering is the research and development of engineered systems that mimic native biological tissue and can be used to replace, repair, or improve the local tissue environment (Howard et al., 2008). There are two main approaches to tissue engineering, with the first approach being the fabrication of a porous scaffold, which can be used as a support structure for the in vitro disposition of cells (Yang et al., 2004). The cells are then able to remodel the scaffold by producing their own extra cellular matrix materials (Howard et al., 2008). The second approach to tissue engineering also utilises a porous scaffold to act as a growth factor reservoir or drug

delivery vessel. The growth factors, or drugs, are then used to stimulate the surrounding cells to populate the scaffold and generate the tissue (Howard et al., 2008).

Tissue engineered scaffolds in function should be representative of the native ECM which is being replicated (Liao et al., 2006). Therefore there are several functions that must be considered for a scaffold for use in tissue engineering. The scaffold material should provide a porous structure that the cells can attach to, grow and differentiate both in vitro and in vivo (Chan and Leong, 2008). A scaffold with a porous structure provides binding sites for the cells and allows cells to freely migrate within; the porous design also allows for the diffusion of nutrients to promote cell growth and remodelling of the scaffold (Blackwood et al., 2008). The biomaterial selected for the scaffold system should degrade over time (Nair and Laurencin, 2007). The degradation of the scaffold should be tailored so the implanted cells can remodel the scaffold system by depositing their own extra cellular matrix and ultimately completely replacing the scaffold with native tissue (O'Brien, 2011). In addition to the biodegradation of the scaffold material, the biomechanical cues provided by the scaffold are important in regulating cell behaviour (Engler et al., 2006), therefore the scaffold system should provide a mechanical environment that is analogous to the native tissue. The scaffold must also be robust enough to withstand the handling that occurs in vitro (Zhu et al., 2008). This section will focus on fabrication and properties of porous scaffolds used as support structures for the in vitro study of cellular behaviour.

2.6.1 Fabrication of Tissue Scaffolds

There are many different fabrication methods for producing scaffolds for tissue engineering. The types of scaffolds can therefore be generalised into the different categories of, prefabricated porous scaffolds, decellularised extracellular matrix, cell derived matrix, or hydrogels (Chan and Leong, 2008). Each of these approaches results in a porous scaffold where cells can reside. The focus of this section will be on the prefabricated porous scaffolds, which are often constructed using natural or synthetic biomaterials (Chan and Leong, 2008). Natural biomaterials are materials that can be derived from the native tissues and then processed to produce porous scaffolds (Hubbell, 1995). Natural biomaterials such as, proteins, polysaccharides, lipids, and inorganic ceramics provide high levels of biocompatibility therefore providing an platform for cell attachment and growth with limited surface modification (Nair and Laurencin, 2007). Synthetic biomaterials are generally classified into bioglasses or synthetic polymers, these materials provide controlled material properties when compared to the natural biomaterials allowing for the design of specific physical, chemical and mechanical properties of the scaffold (Yang et al., 2004). However, the main drawback of some synthetic biomaterials is the biocompatibility, leading to difficulty in maintaining cell attachment to the scaffold and limiting cell growth (Chan and Leong, 2008). Surface modifications are often implemented to improve cell attachment and biocompatibility. One example of surface modification is the coating of the scaffold with natural biomaterials such as, collagen, fibronectin or other biopolymers through adsorption (Cipitria et al., 2011). The mechanical environment has been shown to significantly affect cell behaviour (Engler et al., 2006), this is an important property that is considered during the selection of a material for a tissue engineering scaffold. The selected material system

should mimic the native environment thus providing the correct biomechanical cues for the cells to produce the ECM required for the tissue. Natural biomaterial scaffolds alone often do not provide mechanical properties that are representative of the native material but also robust enough to be handled throughout the tissue engineering process (Chan and Leong, 2008). Composites of natural and synthetic biomaterials are often used to provide the necessary biomechanical cues while giving the scaffold overall mechanical stability.

Fabrication of polymer based scaffolds is generally achieved through several different methods. These methods include: stereolithography, selective laser sintering, 3D printing, fused deposition modelling, and electrospinning (Cipitria et al., 2011; Hollister, 2005). These methods, apart from electrospinning, are often referred to as rapid prototyping methods (Hutmacher, 2001). Rapid prototyping methods take advantage of computer aided design to develop a 3D model of the desired scaffold, which can then be produced layer-by-layer using synthetic biomaterials (Hollister, 2005). Electrospinning is a technique of producing randomly oriented non-woven fibre mats (Bhardwaj and Kundu, 2010). The electrospinning process involves applying a high voltage between a conductive polymer solution and collector substrate. The polymer solution forms a thin jet region which is drawn towards the collector, and as the jet moves towards the collector the solvent of the polymer solution evaporates producing solid polymer fibres. The solid polymer fibres, which can be on the order of nanometers in diameter, are then deposited on the collector substrate (Doshi and Reneker, 1995).

Electrospun scaffolds have been widely used when trying to replicate the microenvironment and physical properties of skin (Chandrasekaran et al., 2011; Franco et al., 2011; Gümüşderelioğlu et al., 2011; Kumbar et al., 2008; Powell et al.,

2008; Venugopal et al., 2006; Zhou et al., 2008). The randomly oriented nanofibres are often used to represent the collagen fibre matrix of the dermis and the overall flexibility of the non-woven mats mimic the behaviour of skin (Pan et al., 2006). The polymer systems used to produce scaffolds for skin analogues often includes composites of natural and synthetic biomaterials such as, collagen and polycaprolactone (PCL) (Gümüşderelioğlu et al., 2011; Powell and Boyce, 2009) or poly(L-lactic acid)-co-PCL and gelatin (Chandrasekaran et al., 2011), as these systems provide the mechanical stability required of a skin analogue and the necessary biocompatibility for cells to adhere and populate the scaffold. The mechanical properties of electrospun nanofibre scaffolds generally fall within the megapascal range, for example a collagen/PCL electrospun scaffold resulted in an elastic modulus of 82.08 MPa when tested under uniaxial tension (Gümüşderelioğlu et al., 2011). Additionally, a poly(L-latic acid) scaffold resulted in an elastic modulus between 30.25 MPa and 37.95 MPa (Cui et al., 2013), which is similar to the elastic modulus values of skin when tested by uniaxial tension, as shown in Table 2.1. Based on the literature, the bulk mechanical properties of electrospun scaffolds appear to replicate the bulk mechanical response of skin under tension, however there has been no investigation into the nanoscale mechanical properties of these scaffolds or how the mechanical properties of these scaffolds change with the introduction of cellular material. The contribution of each of the components of a scaffold, fibre and cellular material, to the overall mechanical properties is unknown, and investigation of these components could provide an understanding of the mechanical cellular microenvironment that exists within these scaffolds.

2.7 Conclusions

This chapter provides an introduction to the structure and function of skin. The basic mechanical properties of materials and testing methods are discussed. The mechanical properties at the nanoscale can provide understanding into the mechanical microenvironment that exists within skin at the cellular length scale. The current state of research tends to investigate individual regions, isolated layers or macroscopic behaviour whereas a comprehensive analysis linking nanoscale mechanical behaviour to whole skin is lacking. This thesis attempts to evaluate the spatial variations of the mechanical properties through the thickness of whole skin and establish a composite model that can be used to predict the macroscopic mechanical properties from the measurement of micrometre length scale volumes.

Chapter 3 – Materials and Methods

3.1 Introduction

This chapter aims to provide an overview of the materials and methods used throughout the thesis. Skin can be considered as a multilayer composite system containing components with nanoscale dimensions. Several techniques are therefore required in order to expose the multiple layers at the nanometre length scale and conduct mechanical characterisation at this length scale. The techniques used to expose the individual layers of skin include a combination of mechanical peeling and cryosectioning. Atomic force microscopy (AFM) was used for mechanical characterisation at the nanoscale. The methods described here are used throughout the thesis and therefore described in detail for reference in subsequent chapters.

3.2 Sample preparation

The aim of the sample preparation process was to expose the individual layers of skin for mechanical characterisation. Two sample types were produced, the first exposed the dermal surface by mechanically peeling the epidermis from the dermis, and the second was a cross section through the thickness of the skin

Mouse skin samples used for mechanical peeling were taken from freshly excised wild type C57BL/6 mouse tails and were prepared in the matter described by Braun et al. (Braun et al., 2003) This protocol disrupts the binding, using a chelating agent, of the epidermis to the dermis at the junction between the lamina lucida and the basal lamina. The separation exposes the surface of the basement membrane and the dermis. After mouse tails were harvested, animals were sacrificed according to Home Office regulations (license PPL 70/7166), and the skin cut lengthwise along the tail. The tail skin was then peeled off of the tail using forceps. The bulk sample was sectioned using a surgical scalpel into samples approximately 0.5 x 0.5 cm in size. The sectioned whole skin samples were incubated in 0.005 M Ethylenediaminetetraacetic acid (EDTA) in Dubelco's phosphate buffered saline (DPBS) at 37°C for approximately four hours. The EDTA solution acts as a chelation agent disrupting the cation mediated joining of the epidermal layers to the dermis, and allows for separation of the epidermis from the dermis. The epidermis was gently peeled away from the dermis using forceps, rinsed with phosphate buffered saline (PBS) to remove any excess EDTA solution that may be still present on either the epidermis or the dermis and then stored in a PBS solution with 0.2% sodium azide and 0.05% protease inhibitor. The process of removing the epidermis was conducted while the skin samples were submerged in PBS to prevent any dehydration of the tissue. Sodium azide was added to the solution in order to prevent infection or the growth of bacteria, and the addition protease inhibitor slowed down the degradation of the extra cellular matrix. The sections of dermis were stored at 4°C until use.

Cryosections of mice tails where produced in order to expose the individual layers of skin. The skin was obtained from the same C57BL/6 mice used to prepare the dermal

surfaces previously. The whole skin was peeled away from the tail and then cut into 0.5 cm x 0.5 cm sections in the same manner as described when preparing the dermal explants. The whole skin was then embedded in water soluble cutting compound (OCT Tissue-tek, Sakura, EU) and frozen over dry ice. The skin samples were aligned vertically within the embedding mould to ensure that the layers of skin were exposed during the cryosectioning. Frozen samples were maintained by transferring to a -80˚C freezer until sectioned. Transverse sections were cut using a Lieca CM1860 cryostat (Lieca Biosystems, UK) using a cutting temperature of -20˚C. Whole skin sections were cut to 5 µm in thickness and then transferred to Superfrost Plus glass slides (Thermoscientific, UK). During the sectioning process the samples were kept at -20˚C in order to prevent the samples from dehydrating.

3.3 Atomic force microscopy

The characterisation and mechanical testing of the sample surfaces was conducted using an AFM (NTegra, NT-MDT, Rus.). AFM imaging conducted within this work generally used low set point contact mode applied to the sample contained in a phosphate buffered saline (PBS) environment. PBS was selected as it provides an environment that will maintain the hydration levels within the excised mouse tail tissue. The range of samples studied required a number of AFM configurations as shown in Figure 3.1. Different AFM configurations were required depending on the sample preparation method. For example, tissue samples could be placed into a stainless steel liquid cell as is illustrated in Figure 3.1a,c. Samples prepared on glass slides could not be loaded into the liquid cell therefore in order to access the sample

surface with the AFM the glass slide was mounted directly to the AFM stage, as shown in Figure 3.1b,d.

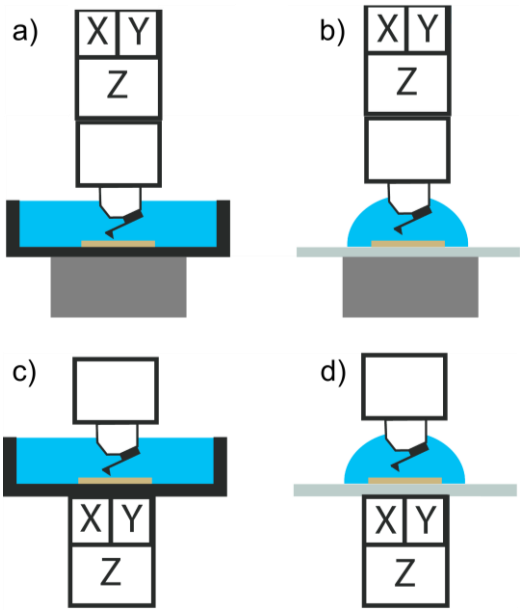

Figure 3.1. AFM/sample configurations used with a) steel liquid cell with piezoelectric actuators located above the AFM cantilever. b) Configuration for samples deposited on glass slides with the piezoelectrics located above the AFM cantilever. With c) and d) the piezoelectric actuators are located beneath the sample. For all configurations the cantilever is mounted to a quartz crystal and the laser is reflected through the quartz onto the photodiode. The liquid cell has a diameter of 3 cm and a depth of 0.5 cm.

3.3.1 Calibration of AFM Cantilevers

Multiple frequencies scans are taken near the resonant frequency of the AFM cantilever and averaged to produce a representative Lorentzian curve for the cantilever deflection. The curve fitting the cantilever deflection versus oscillating frequency can then be integrated and the spring constant calculated using Equation

2.31. A sample plot of the frequency scans fit to a Lorentzian for the thermal fluctuation method is shown in Figure 3.2.

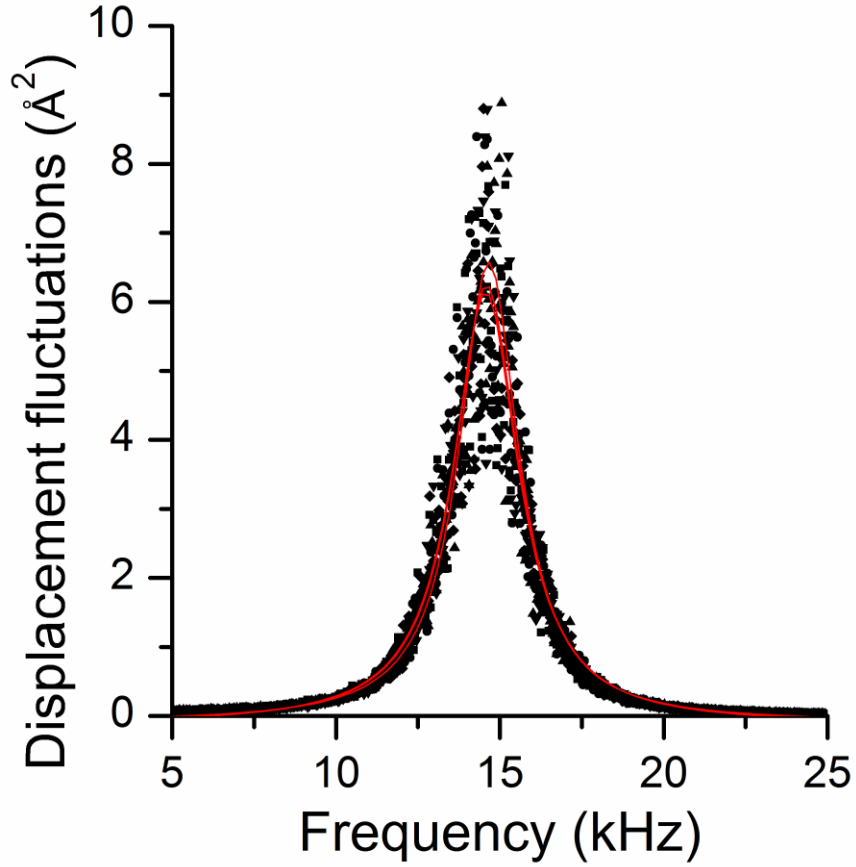

Figure 3.2. Plot of the fluctuations in the displacement of the tip of the cantilever vs the oscillating frequency. Three frequency scans of the same cantilever are plotted and the red curves show the fit of the Lorentzian, which is used to calculate the spring constant of the cantilever.

The one major drawback of the approach put forward by Hutter and Bechhoefer is the lack of contribution of additional vibration modes leading to errors of up to 20% in the value of the spring constant (Lévy and Maaloum, 2001). Therefore, Equation

2.31 only represents the contribution of the first vibration mode. However, AFM cantilevers oscillate through multiple vibration modes due to thermal fluctuations. When measuring the cantilever deflection data from only the first vibrational mode, represented by the first resonant peak, Equation 2.31 must be corrected to account for this, and is then rewritten as (Butt et al., 2005)

$$k = \beta \frac{k_b T}{\langle \delta^2 \rangle} \qquad \text{Equation 3.1}$$

Where $\beta = 0.965$ represents the correction factor for measuring only the contributions from the first vibration mode of v-shaped cantilevers (Lévy and Maaloum, 2001). The method of measuring the deflections of the oscillating cantilever must also be considered when calculating the spring constant of the cantilever. An optical lever method is commonly employed by the AFM system to measure the deflection of the cantilever. This method does not actually directly measure the physical deflection of the cantilever but simply measures the inclination of the cantilever. Equation 3.1 above must be further modified to calculate the normal spring constant by incorporating the effective deflection, which is actually measured by the AFM system, and the contribution of measuring only a single vibration mode using.

$$k = \beta^* \frac{k_b T}{\langle \delta^2 \rangle} = \beta^* \frac{k_b T}{P} \qquad \text{Equation 3.2}$$

Where β^* is 0.764, this value was determined using finite element analysis (Butt et al., 2005; Lévy and Maaloum, 2001). The correction factor simply adjusts for the difference in the inclination measured by the optical lever system and the actual deflection of the cantilever. The method of using thermal fluctuations is beneficial because the evaluation of the cantilever response to the thermal environment only is

required and not direct measurements of cantilever geometry, with associated errors and potential handling damage, using electron microscopy. The thermal fluctuation method also has relatively low uncertainty, reported to be between 5-10% by Burnham et al., when compared to other calibration methods with typical uncertainty values as high has 25% (Burnham et al., 2002). Additionally, as no dimensional measurements of the cantilever are required, this method can be applied to any AFM cantilever including rectangular and v-shaped.

3.3.2 AFM indentation

AFM is able to provide mechanical evaluation of the surface of a material in conjunction with corresponding surface imaging (Dimitriadis et al., 2002). Mechanical probing is often achieved by performing force-displacement curves on an area of interest by pushing the AFM probe into the sample and then removing. Force-displacement curves, schematically shown in Figure 3.3, are similar to traditional indentation techniques used to measure the hardness and elastic modulus of solid materials because the AFM probe is moved a fixed distance into the sample surface and the force and displacement of the probe are measured (Lin and Horkay, 2008). The raw data measured from the AFM produces cantilever deflection and z-piezo displacement but this data can be converted to measure applied force and indentation distance. The AFM force-displacement curve is illustrated in Figure 3.3, highlighting key interactions occurring during the measurement.

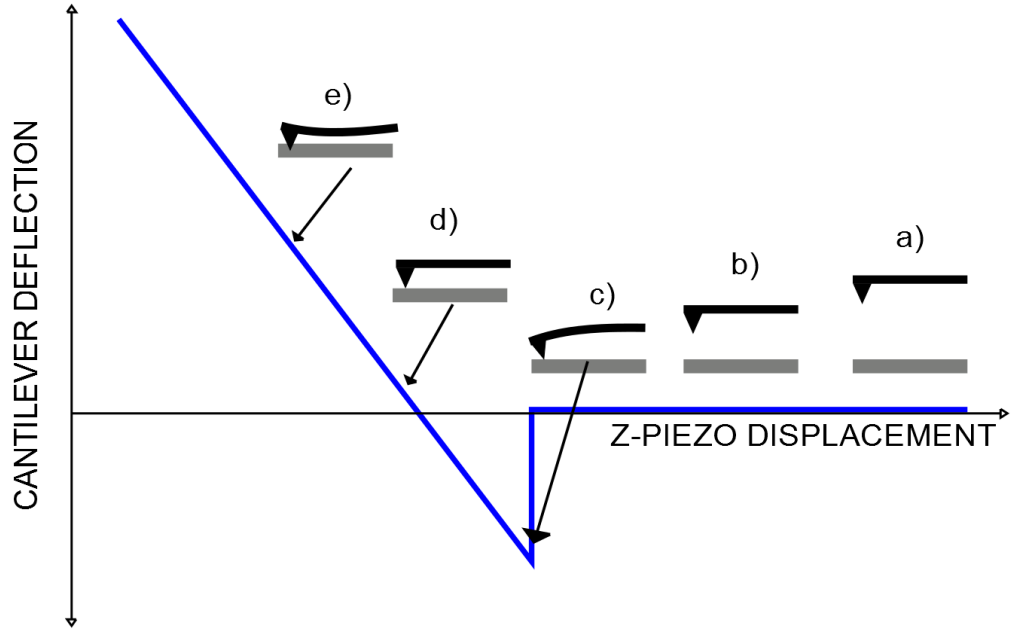

Figure 3.3. Schematic AFM force - distance curve: Steps a - b) show the approach of the probe to the sample surface, c) initial contact between probe and sample, d) zero force and deflection point, e) indentation into the sample surface.

The elastic moduli of the samples used in this work were mechanically characterised using AFM indentation. The AFM system (Ntegra, NT-MDT, Russia) utilised several different piezoelectric scanners configurations but the method for conducting the force-displacement curves is generalised for the configuration with the piezoelectric scanners situated beneath the sample stage. Force-displacement curves were conducted by moving the sample a specified distance and recording the resulting cantilever deflection signal, which is recorded in nA. The output curve from the AFM system is therefore a curve describing the cantilever deflection signal vs the displacement of the z-piezo. This data has to be translated to a curve representing the applied force vs the indentation depth into the sample. To perform this analysis a force-displacement measurement conducted on a sapphire sheet. The sapphire is

treated as a non-deformable sample and the force-displacement curve provides the relationship between the cantilever deflection signal (nA) and the total amount of cantilever bending (nm). Using the relationship of nm/nA the cantilever deflection signal can be converted to the total cantilever bending where cantilever bending = (cantilever deflection signal) · (ratio of nm/nA from sapphire sample). From the amount of cantilever bending the indentation depth into the sample by the AFM probe can be calculated by the indentation depth = (total z-piezo displacement) – (cantilever bending).

The applied force for the indentation can be calculated from the cantilever bending by utilising Hooke's Law,

$$F = kd \qquad \text{Equation 3.3}$$

where F is the applied force, k is the spring constant of the cantilever and d is the cantilever bending.

Extracting the elastic modulus as a characteristic mechanical property of the sample requires curve fitting of the force-displacement curve by first identifying the contact point between the AFM probe and the sample surface. The identification of the contact point is a critical step in the data analysis and can be influenced by any adhesive interactions between the AFM probe and the sample during the indentation process. For the samples analysed throughout this work, the initial adhesive "snap in" was not observed, allowing for the use of the Hertzian analysis of the contact. Additionally, minimal hysteresis between the loading and unloading curves was observed, which indicates a primarily elastic response of the sample to the indentation loading. The method for identifying the contact point was adapted from a strategy initially outlined by Lin et al for automating indentation curve analysis and

was applied to the recorded AFM cantilever deflection vs z-piezo height data prior to the adjustment to a force-displacement curve (Lin et al., 2007a, 2007b). The contact point is identified by fitting a linear function to the noncontact region of the curve and a quadratic to the indentation region of the curve and searching for the point on the curve where the mean square error between the two regions is at a minimum. The curve fitting applied to each region of the raw cantilever deflection vs z-piezo height curve is shown in Figure 3.4. The point on the curve where the mean square error between the two functions is a minimum is taken as the contact point. The force-displacement curve is then translated so that the contact point represents the start of the indentation curve. The process of locating the contact point and applying the curve fitting is conducted manually using a custom script in MS Excel.

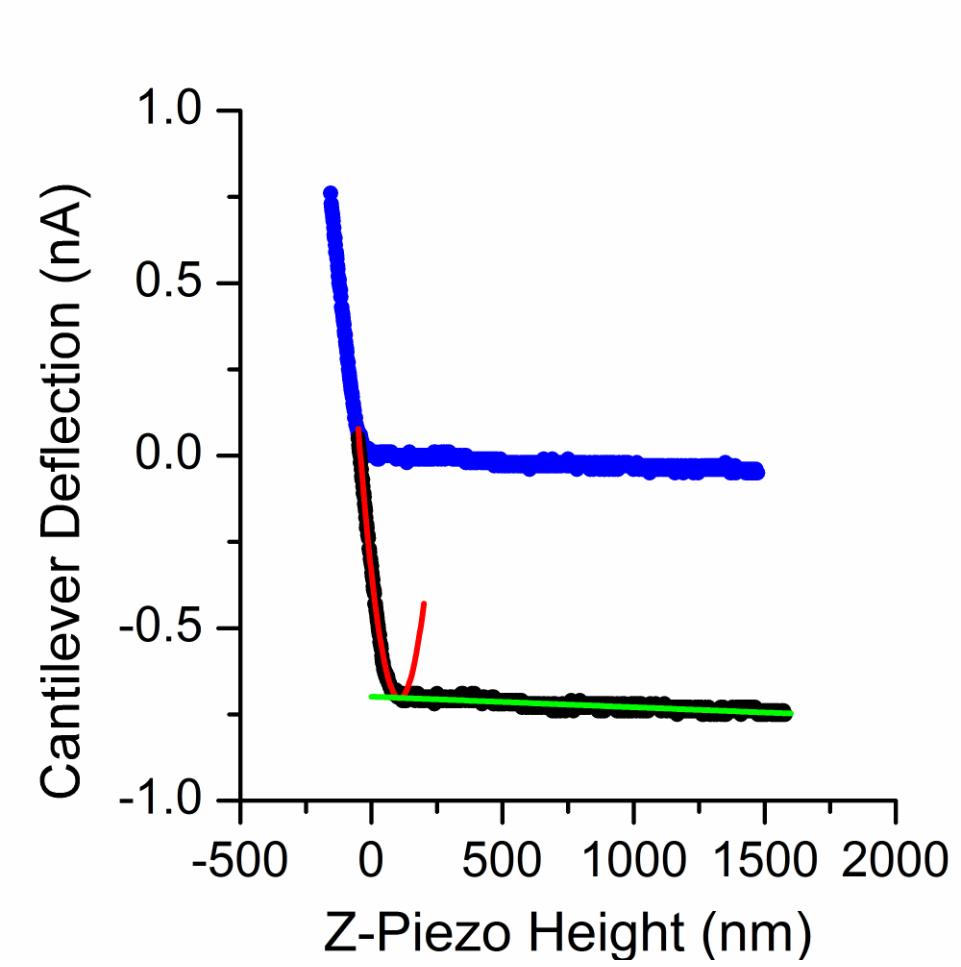

Figure 3.4. Plot of the cantilever deflection vs piezo height showing the curve fitting applied to each region. The non-contact region is fitted to a linear curve shown in green and the contact/indentation region is fitted to a quadratic shown in red. The curve adjusted to the contact point is plotted in blue.

Following Sneddon's solution for the Hertzian contact between a cone and an elastic half space, a parabolic fit can be applied to the force-displacement curve of the form (Sirghi and Rossi, 2006)

$$F = B \cdot d^2 \qquad \text{Equation 3.4}$$

where B represents the curve fitting parameter. The elastic modulus can then be extracted from the following relationship (Sirghi and Rossi, 2006)

$$E = \frac{B\pi\left(1-\nu^2\right)}{2\tan\alpha}$$ Equation 3.5

3.3.3 Indentation of agarose gels

Biological materials are complex systems and often comprised of heterogeneous structures with varying mechanical properties. In order to evaluate the testing methodology being employed throughout this work, a homogenous agarose gel was selected for initial analysis. Agarose gels can be produced with varying mechanical properties that are similar in order of magnitude to biological tissues. The agarose gels can be mechanically tested using different techniques and the resulting elastic modulus values can be compared to validate the experimental methodologies. Agarose gels were produced at two different weight percent compositions by dissolving the dry agarose (Agarose, low gelling temperature, Sigma-Aldrich, UK) in PBS overnight at 70˚C and casting the gels at room temperature in tissue culture plastic petri dishes. Gels were then stored at 4˚C overnight in PBS prior to testing. 50 force-displacement measurements were conducted on each gel and the elastic modulus was calculated. A typical force-displacement curve conducted on an agarose gel is shown in Figure 3.5. The force-displacement curves were analysed using the Hertz method previously outlined in this chapter. AFM force-displacement measurements resulted in an elastic modulus of 27.26 ± 6.785 kPa (mean ± standard deviation) for the 1.5 wt% gel and 45.18 ± 9.712 kPa for the 2.0 wt% gel.

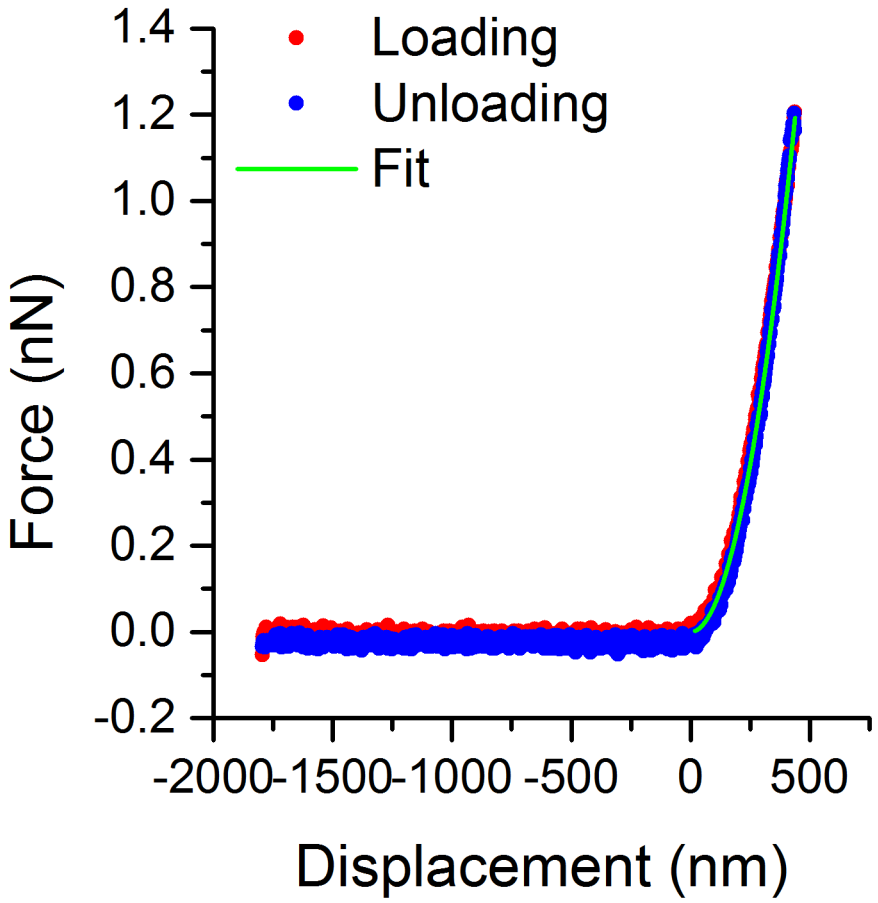

Figure 3.5. Typical AFM force-displacement curve conducted on an agarose gel. The loading curve (red) is retraced by the unloading curve (blue) indicating an elastic response of the gel. The green line shows the fit of Equation 2.6 to the unloading data set.

The elastic modulus of 1.5 wt% and 2.0 wt% agarose gels were independently measured by Dr. Robin Delaine-Smith using unconfined compression (Delaine-Smith et al., 2016). The elastic modulus was calculated from the initial slope of the stress vs strain curve, resulting in a mean elastic modulus of 24.66 kPa for the 1.5 wt% gel and 43.49 kPa for the 2.0 wt% gel, details of the experimental setup can be found in the Appendix. The elastic modulus results from both experimental

techniques are plotted in Figure 3.6 and show good agreement between the measurement techniques with a significant difference between the two gel weight percentages. The agreement between the AFM force-displacement curves and the unconfined compression measurements indicates that the methodology being applied to measure the elastic modulus using AFM is both accurate and precise.

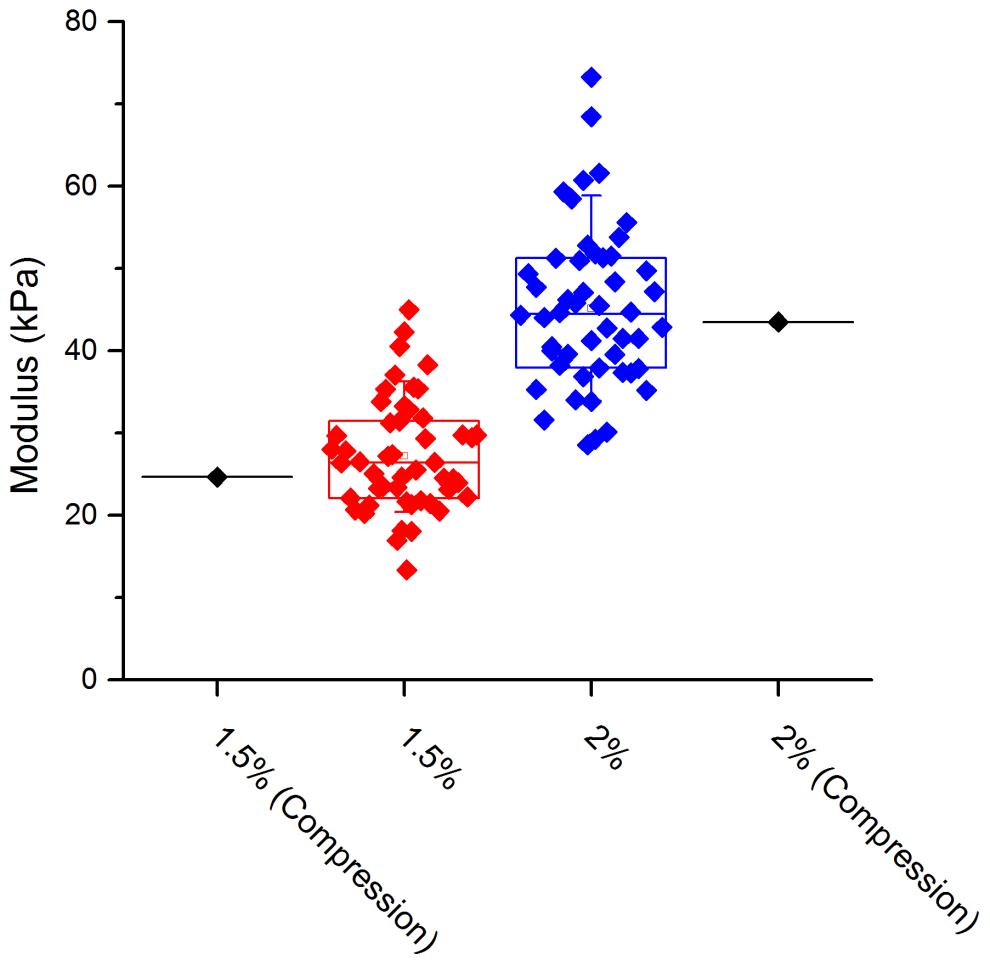

Figure 3.6. Elastic modulus data for agarose gels used for validation of the AFM force-displacement measurements. The box within the plot represents the interquartile range and the whiskers the 10th and 90th percentile. With * indicating significant difference between the two data sets (Student's T-test, $p < 0.01$, n = 50)

3.4 Statistical Analysis

The statistical tests described in this section were used to evaluate the significance of the experimental data obtained throughout the thesis. The D'Agostino Pearson Omnibus Test was used to test if the distribution of the sample data could be

considered Gaussian, or normal, in shape (D'Agostino et al., 1990). The overall shape of the distribution is used in determining what statistical significance tests can be employed. In the case where the distribution of the data was interpreted as normal, the Student's T-test was used. The two sample Student's T-test evaluates if the means of the sample distributions are equal. When the result of the D'Agostino Pearson Omnibus Test indicated the sample distribution deviated from a normal distribution, sample transformations were employed or non-parametric significance tests were utilised. Non-parametric significance tests are applied when the distribution of the sample data is significantly non-normal and are used to evaluate if two sample distributions can be considered to be taken from the same distribution or not. The non-parametric significance test used throughout this work was the Mann-Whitney U-Test, which evaluates if two independent samples are derived from the same distribution (Nachar, 2008). All statistical tests were conducted using OriginLabs 8 Pro (OriginLabs, USA).

Probability density functions were constructed using MATLAB to visualise the sample data distributions. Lognormal probability density functions were fit to the distributions using the following equation (Limpert et al., 2001).

$$f\left(x \mid \mu,\sigma\right) = \frac{1}{x\sigma\sqrt{2\pi}} \exp\left(\frac{-\left(\ln x - \mu\right)^2}{2\sigma^2}\right) ; x > 0 \qquad \text{Equation 3.6}$$

The mean of the lognormal probability distribution is defined as,

$$mean = \exp\left(\mu + \frac{\sigma^2}{2}\right) \qquad \text{Equation 3.7}$$

And the variance as,

$$\text{var} = \exp\left(2\mu + \sigma^2\right)\left(\exp\left(\sigma^2\right) - 1\right) \qquad \text{Equation 3.8}$$

Where μ and σ are fitting parameters and are used when comparing between different distributions.

Throughout this work standard deviation and standard error of mean are used. Standard deviation is stated to interpret the overall variation within the data set, whereas standard error of mean is stated to highlight the location of the mean within the data set.

3.5 Conclusions

This chapter describes the methods used to expose the individual layers of skin so that the surfaces of these layers can be analysed at the nanoscale. AFM indentation techniques were described as the primary method for conducting mechanical analysis at a submicron length scale. These methods are described in this chapter such that they can be referred to in subsequent chapters.

Chapter 4 – Effect of freezing on the elastic modulus of skin

4.1 Introduction

The layered structure of skin poses numerous challenges when attempting to analyse the mechanical properties of the constituent components. Specifically, layers such as the epidermis can be easily removed through mechanical peeling, as described in Chapter 3, but only result in a single surface of the dermis being exposed. Exposing the constituent layers of skin while maintaining the physiological state of skin is a proposed strategy in this chapter to allow analysis of mechanical properties throughout the volume of skin. Such exposure is typically achieved by freezing of the skin samples to cryogenic temperatures and applying mechanical cross sectioning at this low temperature. The low temperature should aim to minimize or remove sample damage from the sectioning by suppressing plastic deformation of the sample during the sectioning process. However, understanding physiologically relevant mechanical properties of skin requires an increase of sample temperature, with this

temperature change requiring no induced change in the resultant mechanical performance of skin.

Some of the steps required in the temperature cycling of samples from freezing to thawing as well as mechanical sectioning have been considered in the literature, although mechanical effects are less well understood. The freezing of cells and biological tissues have been shown to have a detrimental effect on the structure and viability of those tissues and cells (Coutinho et al., 2007; Elmoazzen et al., 2005; Janz et al., 2012; Shi et al., 2008; Zieger et al., 1996). The formation of intracellular and extracellular ice crystals is believed to be the main cause of tissue and cell damage (Karlsson and Toner, 1996). The extracellular ice formation presents mechanical and biochemical effects to the cells and their environment. As ice crystals nucleate and grow, the cell becomes confined and mechanically deformed by the crystal growth leading to cell damage (Zieger et al., 1997). Additionally, ice crystal grow within the surround solution and are ejected from the crystal causing the cell to release water in order to maintain homeostasis that leads to cellular dehydration (Karlsson and Toner, 1996). The formation of intracellular ice during the freezing process can lead to mechanical deformation and damage to the cell, for example at the cell membrane (Karlsson and Toner, 1996). Addition of cryoprotective agents or additives (CPA) attempts to reduce the cellular damage during the freezing and thawing process. The process of cryopreservation is mainly focussed on maintaining cell integrity during the freezing and thawing (Fuller, 2004). The cryopreservation of tissues poses challenges that require specific protocols to preserve the cellular activity within the tissue (Zieger et al., 1997). CPAs can be classified into two different categories, intracellular and extracellular, with each category providing a different role to mitigate the potential damage from cryostorage

(Karlsson and Toner, 1996). The role of an extracellular CPA, such as sucrose, is to stabilise the extracellular spaces and minimise the formation and growth of ice crystals and structurally maintain the cellular environment (Fuller, 2004). Intercellular CPAs, such as dimethyl sulfoxide (DMSO), aim to stabilise the internal structure of the cell and prevent cellular damage from dehydration (Fuller, 2004). However, the mechanisms by which CPAs act on the system is still not completely understood (Bakhach, 2009). Many of the damaging effects of freezing can be managed by controlling the rate of cooling, such as rapid cooling rates restrict the formation of intracellular ice (Baust et al., 2009).

The many different methods used when cryopreserving tissue are often dependant on the tissue type and the aim of the cryopreservation process (Fuller, 2004). The cryopreservation of skin and skin equivalents involve the use of a range of CPAs including propane-1,2-diol, glycerol, DMSO and trehalose (Bakhach, 2009; Chen et al., 2011; Devireddy et al., 2003; Neidert et al., 2004; Newton et al., 1998; Pasch et al., 1999; Suhodolčan et al., 2013; Verbeken et al., 2012; Villalba et al., 1996; Wang et al., 2010). Similar protocols have also been used to cryopreserve keratinocyte monolayers (Pasch et al., 1999), collagen based tissue equivalents (Neidert et al., 2004), and full thickness porcine skin (Zieger et al., 1997). The previous work investigating the effect of CPA on skin mainly examines the cell viability after thawing, which is improved in the presence of a CPA (Bravo et al., 2000; Pasch et al., 1999), but the effect of the freezing process on the mechanical properties is less well understood. One of the few studies indicating no detrimental effect of freezing on the mechanical properties of skin was provided by Foutz et al. but this work investigated whole skin at the macroscopic level using uniaxial tension.

Consideration of effects at the nanoscale level of the dermis (Foutz et al., 1992) is therefore largely ignored.

Several other tissue types, including arteries and tendons (Giannini et al., 2008; Venkatasubramanian et al., 2006) have been thoroughly investigated to understand the effects of cryostorage on the mechanical properties. Venkatasubramanian et al. showed that freezing resulted in an increased elastic modulus of the arteries in the physiological regime but this change was not observed in the presence of a CPA. Suhodolcan et al. presented similar results in patellar tendon ligaments (Suhodolčan et al., 2013) and Giannini et al. showed that decreased collagen fibril density accompanied by decreased mechanical performance occurred within posterior tibial tendons after the freezing and thawing (Giannini et al., 2008). These previous works highlight the importance of investigating the effects of freezing and thawing on the mechanical properties of a biological material, but only take into consideration the macroscopic deformations and characteristics, such as strain to failure and ultimate tensile strength. Investigations on the effects of freezing and thawing on the nanoscale mechanical properties of complex biological tissues, such as the dermis, is lacking.

This chapter aims to investigate the potential changes in the nanoscale mechanical properties of the dermis as a result of the freezing and thawing process and whether the addition of a CPA during the process can mitigate any changes in the mechanical properties. The results presented in this chapter will also provide validation for the sample preparation and testing techniques used throughout this work.

4.2 Materials and Methods

4.2.1 Patterning of dermal samples

Dermal explant samples were prepared from C57BL/6 wild type mice as previously detailed in Chapter 3 with the addition of a patterned grid deposited on the sample surface. The orientation of the dermal explants samples relative to the whole mouse tail is shown in Figure 4.1. The position of the AFM measurements was critical for assessing the effects of freezing and thawing on the mechanical behaviour of the dermal explant sample and required a method for relocating a previously measured area of the sample.

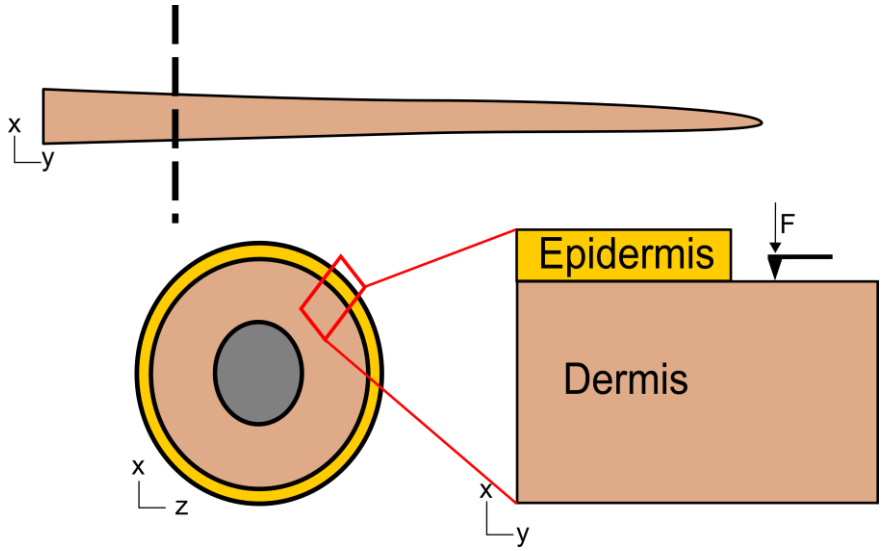

Figure 4.1. Dermal explants sample orientation relative to the whole mouse tail. The location of the AFM applied load is denoted by the arrow marked F.

The dermal explants produced by the mechanical peeling process do not have any definable surface features that can be used to accurately relocate a specific location on the sample surface. A coordinate system was established by patterning a micron scale grid onto the sample surface using a TEM grid (Agar Scientific, UK) as a

negative lithography pattern where the spacing between the lines of the TEM grid formed a specific pattern. The bar width of the TEM grid is 40 μm. The patterning process is illustrated in Figure 4.2, where the TEM grid was first attached to the dermal surface by mechanical clips and the surface water is removed from the sample using laboratory wipes. Waterproof ink was deposited over the area of the sample covered by the grid and the grid then removed from the surface, resulting in a microscopic grid pattern on the surface of the dermal explant. The results of this patterning process are shown in Figure 4.3. The grids produced using this method are robust, and remain visible and well defined throughout the imaging and measurement process in a liquid environment. The grids also remain well defined after the freezing and thawing process, making this patterning process a convenient method for locating a specific location on a sample that does not have any easily definable surface features.

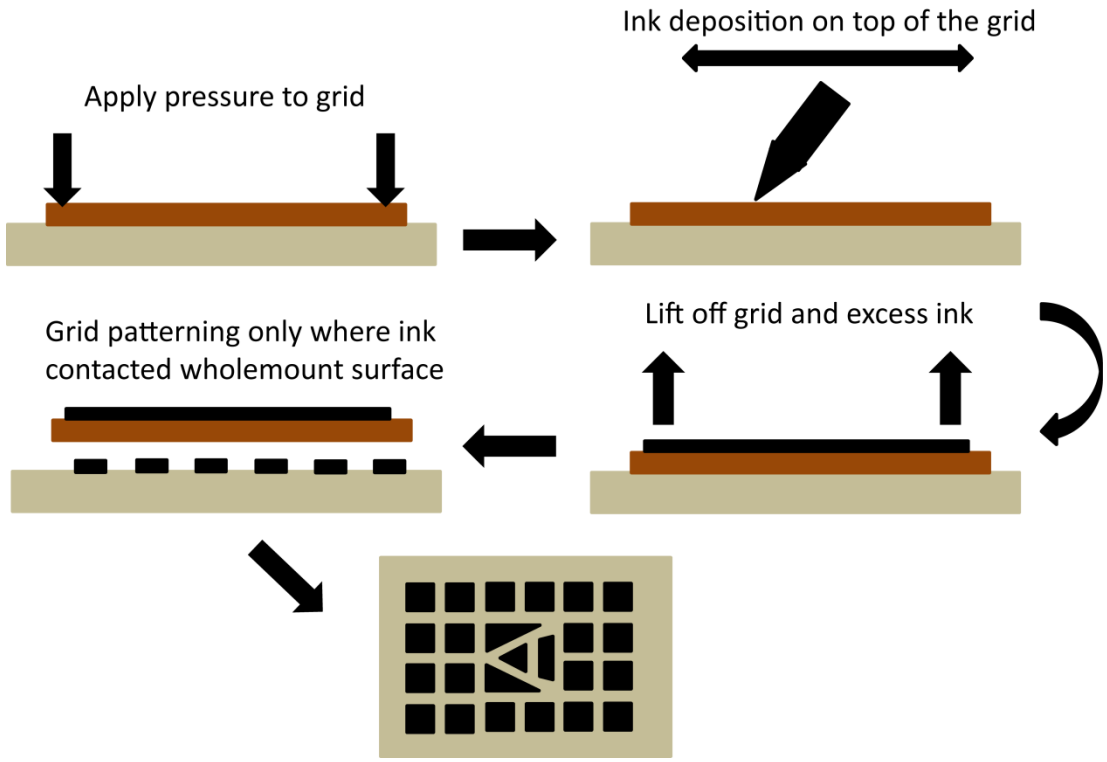

Figure 4.2. Illustration outlining the patterning process: a) TEM grid is attached to the sample surface by mechanical spring clips, b) after removal of surface water by blotting with laboratory wipes, waterproof ink is applied to the surface, c) the mechanical clips are removed and the TEM gird is lifted off of the surface resulting in d-e) a patterned surface that provides both orientation of the sample and location on the sample.

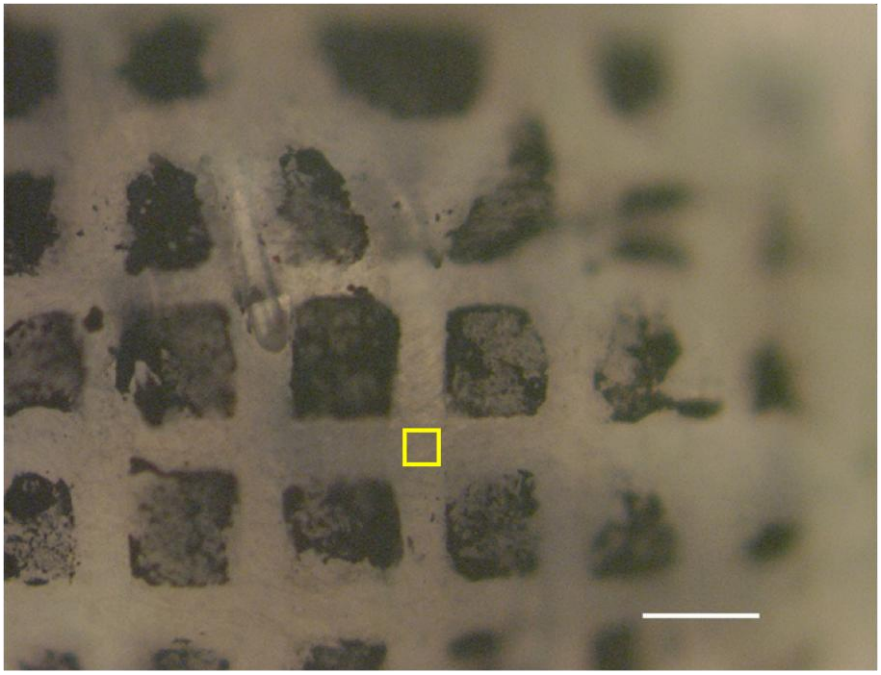

Figure 4.3. Optical microscopy image of a patterned grid on a dermal explant sample displaying clear features allowing for identification of location on the sample and the orientation of the sample relative to the AFM probe. The AFM scan area is indicated by the yellow box. Scale bar = 100 µm.

4.2.2 Mechanical Analysis

Small scale mechanical measurements were conducted on skin samples using an AFM (Ntegra AFM system, NT-MDT, Russia) with a sample stage mounted on piezoelectric positioners. The Si_3N_4 AFM probe was positioned away from any remaining hair follicles on the dermal surface using in situ optical microscopy and AFM force displacement curves were collected over a 20 µm x 20 µm area. AFM indentation measurements were conducted within a non-patterned region of the sample using the patterned surface as reference for the orientation of the sample. The AFM probe tip was positioned over a specific grid location on the dermal explant samples to ensure the AFM probe could be returned to the same location.

The force-displacement measurements were carried out while the AFM probe and dermal explant sample were completely submerged in phosphate buffered saline (PBS) within a stainless steel liquid cell. The dermal explant samples were mechanically coupled to the bottom of the liquid cell using spring clips, and the liquid cell was magnetically attached to the AFM stage. Dermal samples were imaged in contact mode using a low cantilever set point value. AFM height images were taken over a 20 µm x 20 µm area. AFM indentations were conducted using a Si_3N_4 cantilever with a spring constant between 0.19 $N.m^{-1}$ and 0.5 $N.m^{-1}$, determined by the thermal fluctuation method described in Chapter 3. 400 displacement controlled indentations were performed within the imaged area in a raster scan pattern with an indentation velocity of 2 $\mu m.s^{-1}$ and an indentation depth up to 500 nm. The minimum indentation depth was at least 100 nm, which is greater than the radius of curvature for the AFM probe, to ensure that the conical estimation for the AFM probe tip geometry could be applied to the analysis of the force-displacement curves (Radmacher et al., 1995). The duration of the indentation raster scan to complete 400 indentations was approximately 25 minutes. The z-piezo feedback loop was turned off and then back on again after completing the indentation scan to return the piezoelectric positioners to the initial positions, and the 400 indentations were repeated over the same 20 µm x 20 µm area originally imaged. These indentation measurements were conducted on 11 individual dermal explant samples from three mouse tails.

The elastic modulus of the skin at each spatial location was determined using the curve fitting method described in Chapter 3. The force-displacement curves recorded for the dermal explant samples increased probe-sample adhesion during the unloading portion of the force-displacement curve, illustrated in Figure 4.4, which

led to a modification of the indentation analysis based on the method put forward by Sirghi and Rossi (Sirghi and Rossi, 2006). The purely elastic response during unloading the force-displacement interaction of a cone in contact with an elastic half-space was originally described by Sneddon and is defined by (Sneddon, 1948),

$$F = \frac{2E\tan\alpha}{\left(1-\nu^2\right)\pi}h^2 \qquad \text{Equation 4.1}$$

The additional contribution of the adhesive forces to the total force being measured by the AFM probe can be represented by (Sirghi and Rossi, 2006),

$$F(h) = \frac{2E\tan\alpha}{\left(1-\nu^2\right)\pi}h^2 - \frac{\gamma_a 8\tan\alpha}{\pi\cos\alpha}h \qquad \text{Equation 4.2}$$

where the second term of Equation 4.2 representing the contribution of the probe-surface adhesion to the applied force during the unloading portion of the force-displacement curve. Figure 4.4 displays a typical force-displacement curve carried out on a dermal explant sample and it should be highlighted that there was no remnant indentation on the sample surface leading to the exclusion of h_f from Equation 4.2. The Poisson's ratio, ν, here is assumed to be 0.5, consistent with an incompressible material and with values previously used in the literature (Petrie et al., 2012). Equation 4.2 can therefore be fit to the unloading curve of the force-displacement data and the elastic modulus data can be determined using the first term of Equation 4.2.

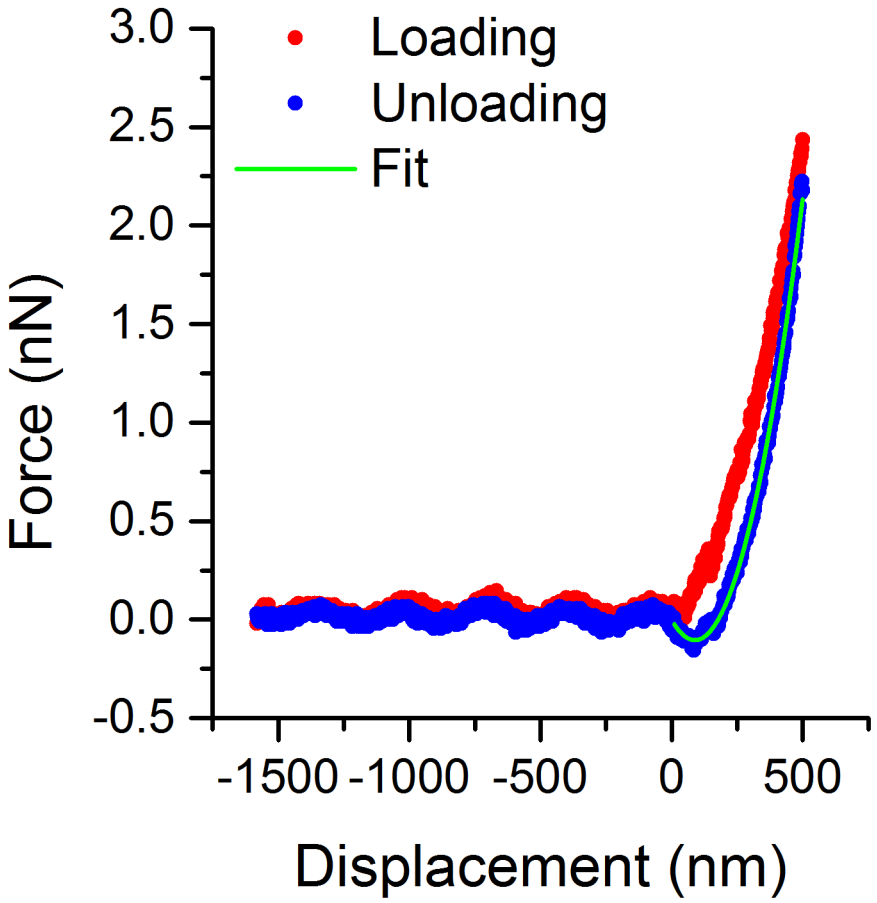

Figure 4.4. AFM force-displacement cantilever deflection vs z-piezo position data showing the loading (red) and unloading (blue) curves. The unloading curve shows the adhesive interaction occurring during the retraction of the cantilever from the sample surface. The adhesive interaction is represented by the negative force being applied to the cantilever during unloading. The green line shows the fit of Equation 4.2 to the unloading data set.

The elastic modulus data was reconstructed into a colour coded map using the AFM raster scan position as spatial coordinates for each elastic modulus value. The spatial coordinates provide positional indexing of the elastic modulus data which is

transformed into a matrix that was then represented as a colour coded image using Origin8 (OriginLabs, USA) software.

4.2.3 Procedure for freeze-thaw cycling

After the initial AFM mechanical measurements were taken, seven dermal explant samples were subjected to a freezing and thawing cycle. Prior to freezing, four samples were treated with a cryoprotective agent (CPA) and three samples were left untreated. The CPA was added in order to evaluate if there was any tissue damage that resulted in a change in the mechanical behaviour of the tissue as a consequence of the freezing and thawing process. The CPA used in this work consisted of a 1 M solution of sucrose with 10% v/v of dimethylsulfoxide (DMSO). DMSO is a commonly used intracellular CPA (Gaucher et al., 2012; Kubo and Kuroyanagi, 2004), and sucrose has been shown to perform as extracellular CPA (Chen et al., 2011; Fuller, 2004). Dermal explant samples were first placed in 10% v/v DMSO in PBS at 4˚C in individual 1 mL vials for 30 minutes. Samples were then transferred to a solution of 1 M sucrose with 10% v/v DMSO at 4˚C for 30 minutes. The vials containing the sample within the CPA solution were then placed in a -80˚C freezer for 20 hours, with untreated dermal samples in PBS also transferred to a -80˚C freezer. The vials were removed from the freezer and allowed to return to 4˚C, followed by CPA treated samples transferred into 10% v/v DMSO for 30 min. Further hydration in PBS for 30 min at 4˚C was followed by several rinses in PBS in order to ensure removal of CPA, while the untreated dermal samples were allowed to return to 4˚C. All the dermal explant samples were then stored in PBS at 4˚C until further use.

AFM indentations were performed at the same locations where the initial mechanical measurements were recorded using the grid referencing once the freeze thaw cycle was completed. The same indentation procedure over a 20 µm x 20 µm area was conducted at each of these locations.

4.2.4 Analysis of the effect of freeze thaw cycling

The AFM force-displacement curves recorded after freezing were analysed to determine the elastic modulus using the curve fitting method described in Chapter 3 with the modification accounting for the increased AFM probe-sample interactions. The data sets of elastic modulus after thawing were then compared to the elastic modulus values measured on the fresh samples. The data sets were treated in pairs for each sample; one data set describing the fresh mechanical behaviour and the second describing the behaviour after thawing. Each individual data set of AFM indentation measurements contained 400 points in a 20 by 20 matrix. The data set was reduced to a 10 by 10 matrix of 100 points by averaging over four neighbouring indentation values. This step was taken in an attempt to limit the experimental error in repositioning the AFM probe after the sample was treated. A local average of each data point should also allow for a better representation of the elastic modulus for a specific region of the selected area. No changes to the experimental setup with regards to the position of the sample or probe tip were used. Therefore the variation between the repeat measurements were quantified by calculating the root mean square (RMS) of the difference at each point of the measured area using the following equation

$$RMS = \sqrt{\frac{\sum_{1}^{i}\left(E_{N,i}{}^{2}\right)}{n}} \qquad \text{Equation 4.3}$$

where $E_{N,i}$ is the value representing the difference in the measured elastic modulus at each point, i, between the first set of measurements (fresh) and the second (thawed). The data was normalised to the largest value of elastic modulus contained within both data sets before calculating the difference between the two data sets. Calculating the RMS of the data set using Equation 4.3 allowed for a comparison between each data set, including the variation in the position of the measurements, as the difference between the two data sets is calculated for a specific point in the indentation scan. Boundary conditions for the RMS for elastic modulus data sets can be defined such that two data sets collected at exactly the same indentation point provides an RMS value of zero, whereas larger a differences between two data sets would return an increasing RMS value greater than zero. The RMS value incorporates all of the variables that could affect the measured elastic modulus, including any potential changes in the composition or structure of the dermal explant as a result of the freezing and the changes in the position of the AFM indentations as a result of removing the sample from the AFM stage during the freeze/thaw cycling.

4.3 Results and discussion

Force-displacement curves were conducted on the exposed patterned dermal surface of excised mouse tails and repeat measurements of a 20 μm by 20 μm area were taken to establish the variation of the elastic modulus values. The elastic modulus

values were constructed into a distribution map where each 1 µm by 1 µm pixel represented an individual AFM indentation measurement and the calculated elastic modulus at that point, shown in Figure 4.5, comparing the measured elastic modulus.

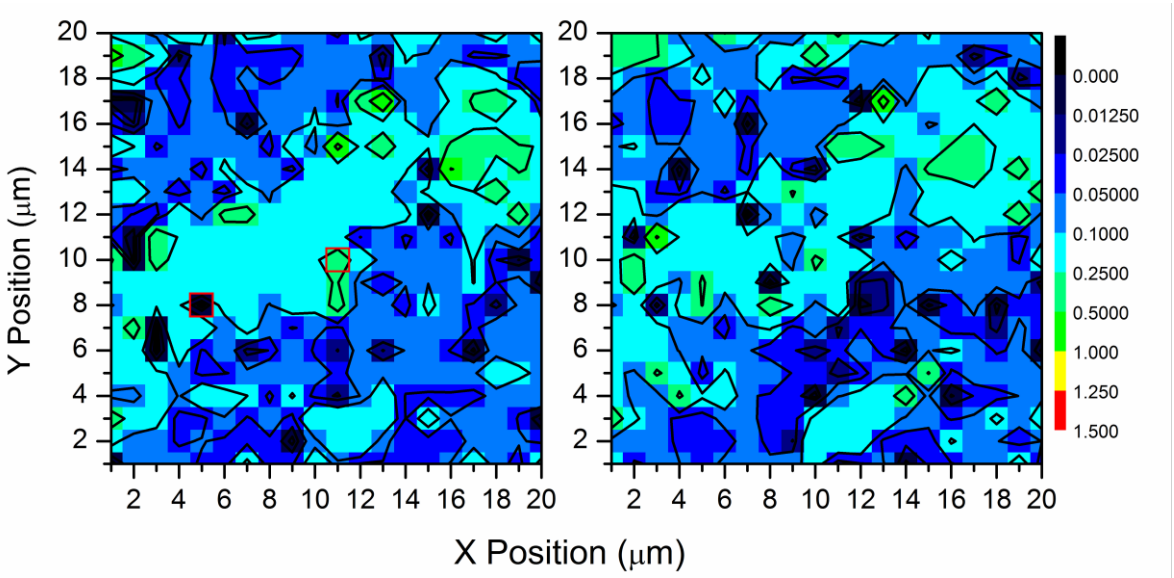

Figure 4.5. (Left) elastic modulus distribution of a fresh dermal explant sample. (Right) distribution plot of the repeat measurements conducted immediately after completion of the first set of AFM force-displacement curves. Colour scale represents elastic modulus in MPa. Force-displacement curves for the points highlighted by the red boxes are shown displayed within the Appendix.

The distribution maps of the elastic modulus above show that the surface of the dermis and basement membrane exhibit heterogeneous elastic modulus. The distribution maps also show that the repeat measurements provide the same indication of the elastic modulus at a given point, although this is a qualitative evaluation. In order to make a more rigorous evaluation, quantification of this variation was conducted. The quantification of this variation is represented by the

calculation of the RMS between the data sets using Equation 4.3. For the data set represented in Figure 4.5 the RMS value was calculated as 0.118. The repeat measurements were conducted on seven samples and the RMS was calculated for each set of repeat measurements. Conducting the repeat measurements over a set of samples produces a range of RMS values that represent the variation of the measurement of the elastic modulus due to the experimental set up because no alterations have been made to the position of the sample or the AFM probe. The range of RMS values calculated for the repeat measurements is from 0.102 to 0.291, indicating that the AFM measurements at a specified point are variable.

Of the seven dermal explant samples measured, four samples were treated with a CPA prior to freezing and thawing. Elastic modulus distribution maps were constructed for the CPA treated samples that were subjected to a freeze/thaw cycle and then remeasured, using the patterned grid as a reference to the position of the initial measurements. An example of the elastic modulus distribution map is shown in Figure 4.6.

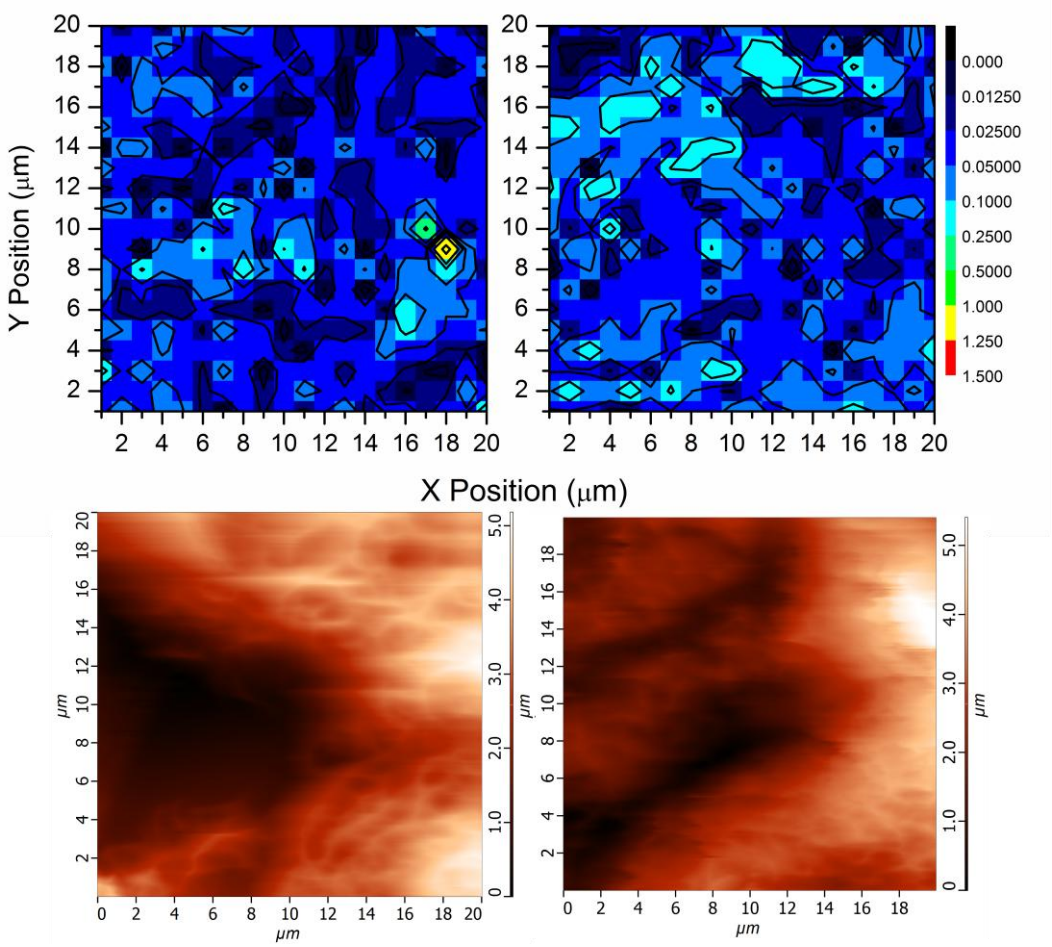

Figure 4.6. (Left) elastic modulus distribution of a fresh dermal explant sample. (Right) distribution plot of the repeat measurements conducted over the same area after the sample was frozen and thawed. Colour scale represents elastic modulus in MPa. (Bottom) AFM height images of the fresh (bottom left) and after thawing (bottom right).

Figure 4.6 again shows the heterogeneous distribution of the mechanical behaviour of the dermis. The large variation in elastic modulus is also evident through the presence of points in the image displaying elastic modulus values that are greater than 500 kPa when the majority of the points in the image display a modulus value in

the range of 10 to 50 kPa. The features of the distribution map of the initial measurements do not persist through to the distribution map of the thawed sample, therefore indicating some uncertainty in the repositioning of the AFM probe over a 20 µm by 20 µm area of the sample. Calculating the RMS value for all of the samples treated with a CPA provided a range between 0.125 and 0.249.

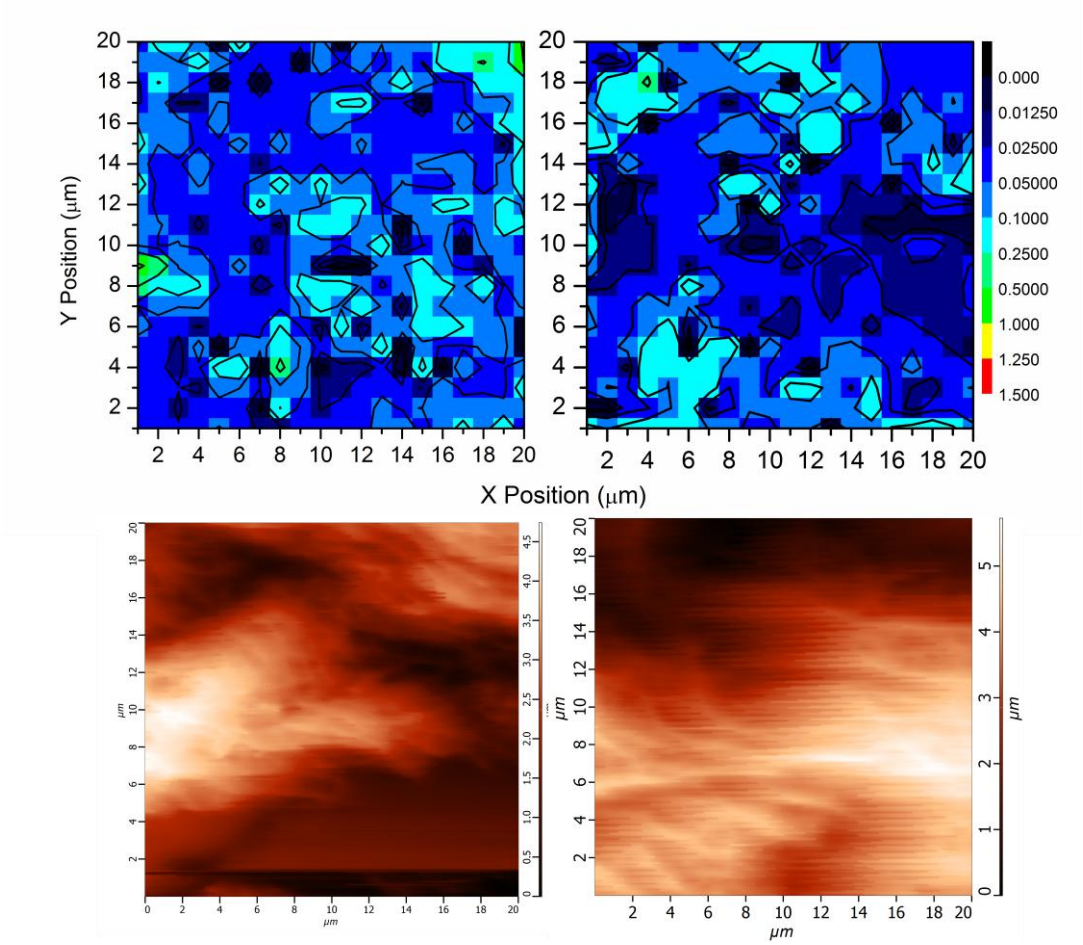

Figure 4.7. (Left) elastic modulus distribution of a fresh dermal explant sample. (Right) distribution plot of the repeat measurement of the area after the sample was treated with a CPA and subjected to freezing and thawing. Colour scale represents elastic modulus in MPa. (Bottom) AFM height images of the fresh (bottom left) and after thawing (bottom right).

Distribution maps were constructed for the untreated samples displaying the initial elastic modulus mapping of the fresh sample and after thawing of the sample, both distribution maps are shown in Figure 4.7. Similarly to the CPA treated samples, the features of the distributions maps for untreated samples vary between measurements. The heterogeneous material properties are observed before and after freezing including the large range of elastic modulus values measured, which is consistent with the previous images of Figure 4.5 and Figure 4.6. The RMS error was also calculated for the untreated samples and resulted in a range between 0.113 and 0.265. The summary of the RMS data for all three sample sets, repeat measurements, CPA treated and untreated, are shown in Figure 4.8a.

The distribution of elastic modulus values was also plotted as a frequency of counts histogram as shown in Figure 4.8b, which displays one sample from each condition with the corresponding distributions of elastic modulus values from the fresh measurements and the measurements taken after thawing. The distributions displayed in Figure 4.8b appear to be lognormal in shape, and fitting lognormal distributions to the data sets was used to quantify the differences, as described in Chapter 3. For the repeat measurements, initial lognormal distribution fitting parameters of $\mu = 4.464$ and $\sigma = 0.3871$ were fit and the repeat measurement resulted in parameters of $\mu = 4.460$ and $\sigma = 0.6254$. The sample treated with a CPA initially resulted in parameters of $\mu = 3.437$ and $\sigma = 0.6941$ with repeat measurements giving $\mu = 3.699$ and $\sigma = 0.6837$. For the untreated sample the fresh measurements the fitting resulted in $\mu = 3.916$ and $\sigma = 0.4996$ and after thawing parameters of $\mu = 4.059$ and $\sigma = 0.5059$. The lognormal fitting parameters provide little insight into any difference that may exist between the fresh measurements and repeat measurements. The distributions were

analysed using the D'Agostino-Pearson Omnibus test and indicated that none of the sample distributions were normal or lognormal in shape. The Paired-Sample Wilcoxon Ranked Sign test was used to test the significance between the pairs of distributions shown in Figure 4.8b. The test results for the distributions shown in Figure 4.8b returned corresponding p-values of 0.00398, 7.49E-5, and 2.069E-9 respectively, indicating that there is no consistent trend in the significance testing across the samples. This trend extended across all of the samples exposed to a freeze thaw cycling and measured with the AFM. With no consistent trend within the statistical analysis and the two-parameter distribution fitting, the RMS error calculation provides a method for evaluating the magnitude of the change between paired data sets using a single parameter.

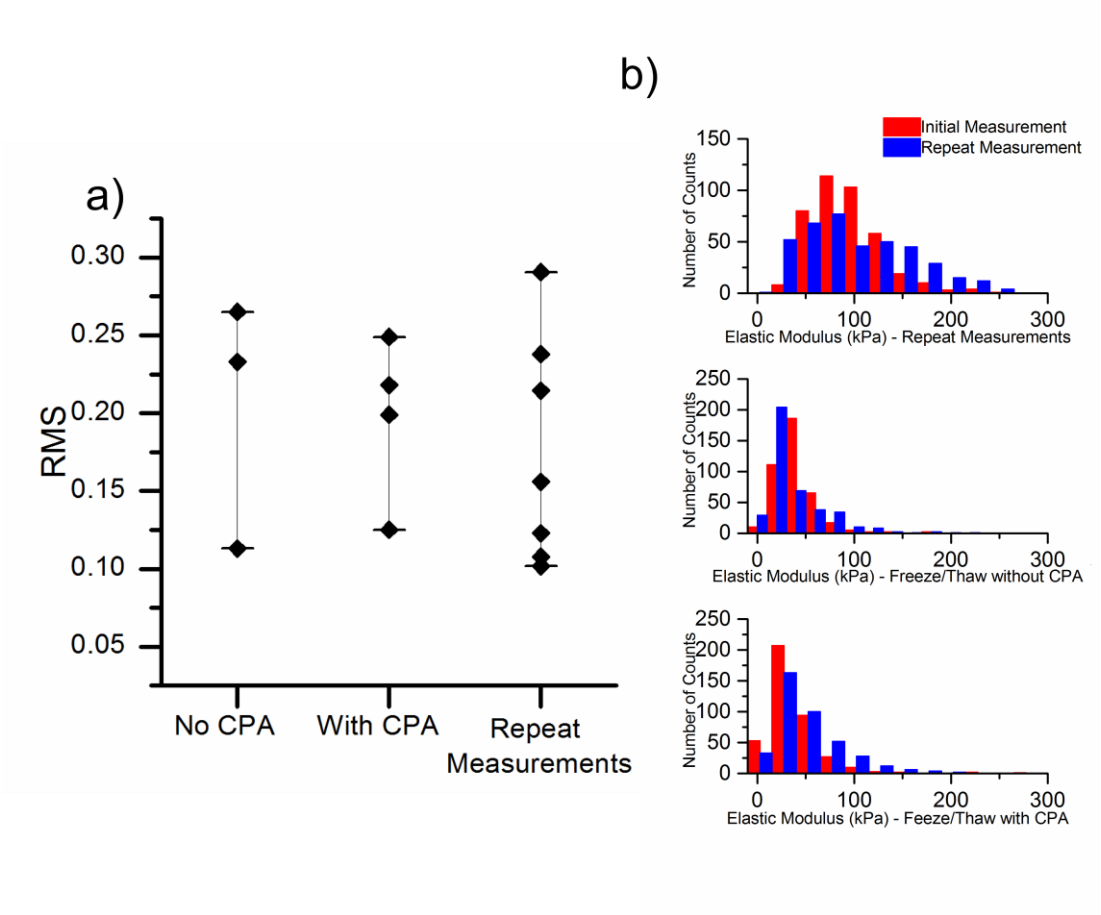

Figure 4.8. a) Plot of the RMS values for measurements of the elastic modulus before and after the freeze-thaw cycle for untreated, CPA treated samples and repeated measurements on fresh dermal explant samples. b) Histogram plots of the frequency of counts for the measured elastic modulus. Histograms are shown as paired samples with one histogram per condition of freezing and thawing.

Figure 4.8 shows that the addition of a CPA prior to the freezing and thawing cycle had no measurable effect on the mechanical behaviour of the dermal explant samples. The RMS values for samples treated with and without a CPA fall within the range of RMS values for the repeated measurements conducted on a fresh sample with no changes made to experimental set up. Potential error in the measurement of

the elastic modulus of the dermal explant samples after thawing is introduced through the repositioning of the sample relative to the AFM probe. Although a micron scale grid was used to locate a specific area, the positioning of the sample is confirmed through optical microscopy and it is unlikely that the exact position previously measured will be located again. The result of the RMS values of both the treated and untreated samples falling within the range of RMS values for the repeated measurements conducted on fresh samples tend to agree with the previous work by Foutz et al. that showed whole rat skin mechanical behaviour was unaffected by the freezing and thawing process, apart from the ultimate tensile strength, which was higher for the samples that had been frozen (Foutz et al., 1992). Previous studies observed similar behaviour in posterior tibial tendons, where the uniaxial tensile tests indicated a decrease in the ultimate tensile strength and ultimate tensile stress, which was attributed to the decrease in the collagen fibril density and total collagen content after freezing (Giannini et al., 2008). However, Giannini et al. observed no difference in the elastic modulus of the tendons that were tested fresh against tendons that had been frozen and thawed (Giannini et al., 2008). These previous observations are in agreement with the results of AFM indentation testing of dermal explant samples conducted in this work and indicate that the elastic modulus is unlikely to be effected by the process of freezing and thawing.

In addition to the observations made through mechanical measurement of the sample surface before and after the freeze thaw cycle, the AFM imaging throughout showed variations in the imaged areas, leading to a degree of uncertainty around the repositioning of the AFM probe after thawing of the samples. Low set point contact mode imaging of the dermal surfaces recorded surface height images that showed a continuous structure with indication of a fibrous network within the dermis. Figure

4.6 and Figure 4.7 show representative AFM height images recorded for a dermal explant samples used to image the area of where the force-displacement curves were to be measured. Imaging a similar region after the freeze/thaw cycle displayed similar surface height features. The height images both before and after thawing display a rough surface containing a fibril like structure within a continuous matrix. After removing the epidermis, the expected topography would be an undulating topography, corresponding to the epidermal ridges that protrude into the dermis. The topography shown in Figure 4.6 and Figure 4.7 are rough and displays fibrous structures. The observation of this fibrous structure indicates that the mechanical removal of the epidermis is possibly removing the basement membrane or a region of the upper dermis and exposing the underlying collagen fibre network embedded in the ground substance matrix.

The AFM images provide a method for observing any possible changes in the characteristics of the surface as a result of the freezing. However, no comments can be made on whether the freezing process has any effect on the composition of the tissue because the AFM imaging only measures the probe sample interactions to give sample height information.

Evaluation of the force-displacement curves of the dermal explant samples provided a range of elastic modulus values of a sample prepared by mechanically peeling the epidermis from the dermis. The elastic modulus values for all the initial measurements of the fresh dermal explants were combined and plotted as a histogram of the frequency of counts for the elastic modulus values, shown in Figure 4.9, which highlights the region of the distribution containing the majority of the counts. The resulting range of elastic modulus was from 0.148 kPa to 9.77 MPa. The large range of elastic modulus values for the dermal surface confirms the initial

observation of the heterogeneous nature of the dermis observed qualitatively through the distribution maps.

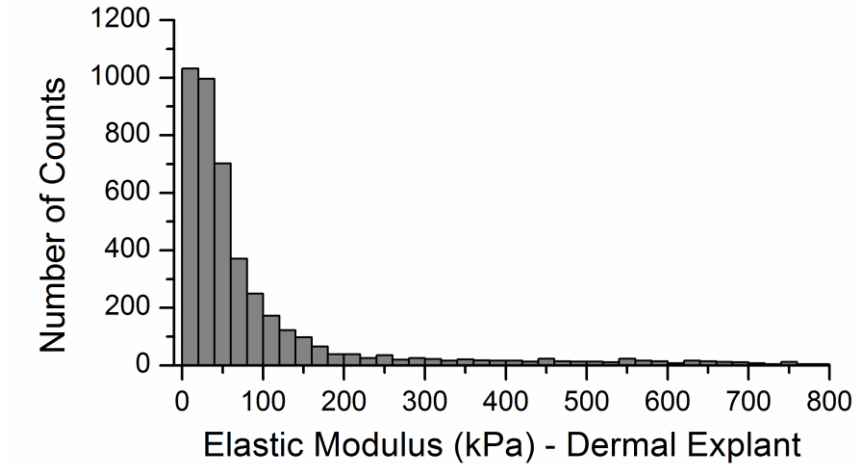

Figure 4.9. Histogram of the frequency of the measured elastic modulus values for the fresh dermal explants (both CPA and non-CPA treated samples prior to treatment and freezing). The range of measured elastic modulus was from 0.148 kPa to 9.77 MPa. This plot shows a range from 0 to 800 kPa in order to show in detail the peak of the distribution, total n = 4435.

Analysing the histogram provides a mean value of 137 kPa with a standard error of mean of 6.28 kPa and the median of the distribution at 44.3 kPa. The upper limit of the elastic modulus measurements, ~9.77 MPa, could potentially be due to the incomplete removal of the epidermal layer during the mechanical peeling process, where the elastic modulus is expected to be higher due to the cornified elements of the stratum corneum, with the elastic modulus value of the epidermis shown to be within the megapascal range (Beard et al., 2013; Crichton et al., 2013; Geerligs et al., 2011). Previous AFM and nanoindentation tests of mouse ear dermal explants in a

hydrated environment showed an elastic modulus range from 0.3 to 19.4 kPa (Petrie et al., 2012), although a different region of the skin with a different mouse type the magnitude of the measurements is consistent with the elastic modulus results presented in this work.

4.4 Conclusions

AFM indentation testing was performed at the nanoscale to measure the elastic modulus at the surface of dermal explant samples that were exposed to two different treatment conditions before freeze/thaw cycling. Although no previous work has investigated the elastic modulus of the dermis for mouse tail skin, the elastic modulus values measured here using small scale AFM based indentation techniques showed good agreement with previous literature on macroscopic specimens for measuring the elastic modulus of dermal tissue from mouse and human skin. This result shows that the AFM technique used throughout this thesis provides a method to measure the elastic modulus of skin at the nanoscale.

The dermal samples exposed to the freeze/thaw cycling with no CPA were expected to have a change in the elastic properties at the nanoscale based on the changes seen in previous work at the macroscale with collagenous tissues and collagen based tissue equivalents (Devireddy et al., 2003; Giannini et al., 2008). The changes in observed in the density and morphology of collagen fibre bundles as a result of freezing were expected to impact the nanoscale mechanical response observed in the dermis, but the AFM indentation results showed that the variability present within the experimental setup is greater than any change in the elastic modulus as a result of

the freeze thaw cycle. This result indicates that the structure and mechanics of the dermal explant surface are robust enough to withstand the biophysical changes that occur during the freezing and thawing cycle and that dermal samples subjected to cryogenic temperatures are mechanically analogous to freshly excised dermal explant samples. This conclusion allows the further examination of structure and mechanics of the different layers of skin by cryosectioning through the thickness of skin.

Chapter 5 – 3D nanomechanical mapping of skin

5.1 Introduction

The ability to measure the nanoscale mechanical properties of the dermal surface was established in the previous chapter. The effect of a freeze thaw cycling on the dermal tissue was also observed to show no significant impact on the elastic modulus of the tissue. The absence of significant variation in the elastic modulus as a result of freezing and thawing provides a clear avenue for exploration into the through thickness changes in mechanical properties of whole skin by cooling the tissue to cryogenic temperatures and sectioning through the thickness to expose the cross section of the different layers of skin. The ability to expose the through thickness surface from the dermis to epidermis without removing these layers from one another while maintaining the initial state allows for insight into how the mechanical properties of skin vary with respect to the spatial location within the tissue. The mechanical properties of cross sections of the dermis have been previously analysed in human tissue. However, no investigations that observe the variations in the

mechanical properties transitioning through the dermis into the epidermis exist although nanomechanical analysis of the dermis has been reported on cryosectioned tissue (Achterberg et al., 2014; Grant et al., 2012). The cross sectioning of whole skin samples will also provide a method for examining the changes in the mechanical properties of the dermis in response to a change in the directionality of the applied load. Previous work using transmission electron microscopy (TEM) to image the ultrastructure of the dermis in normal wild type mouse skin revealed that transverse sections are likely to reveal both the long axis of the collagen fibres and the axis perpendicular to the preferential direction of the collagen network. The collage fibre bundles are interwoven and not perfectly aligned, a reference image of wild type mouse skin is shown in Figure 5.1 from Tasheva et al. (2002). Areas within a transverse section of skin are expected to have regions that expose the long axis of the collagen fibres and regions that expose the cross section of the collagen fibres. Mechanical analysis of transverse sections may provide evidence of any contribution of the collagen fibre orientation on the mechanical properties at the subcellular level.

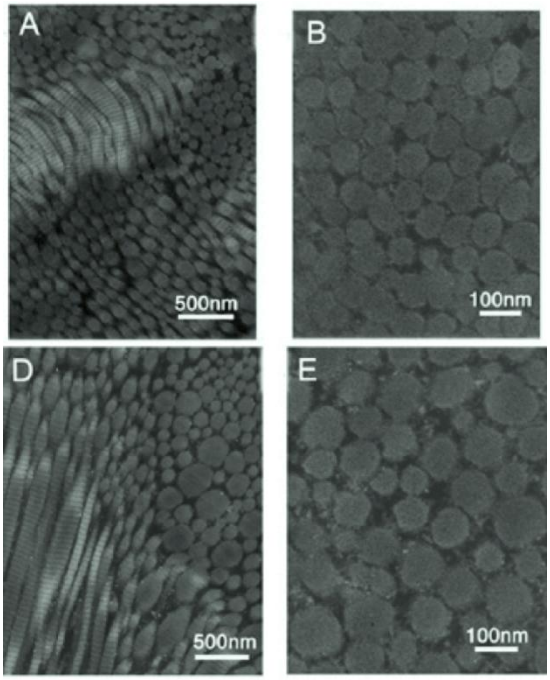

Figure 5.1. TEM micrograph of the collagen fibrils present in cross sections of wild type mouse tail skin showing fibril lengths and cross sections exposed at the tissue surface. (Tasheva et al., 2002)

The influence of the orientation of the collagen fibre network on the anisotropic behaviour of skin at the macroscopic level has been extensively studied (Gahagnon et al., 2012; Groves et al., 2013; Huang et al., 2010; Khatyr et al., 2004; Ní Annaidh et al., 2012a, 2012b; Sakai et al., 2011) but cellular or subcellular length scale investigations are lacking. The change in the direction of the applied load combined with the through thickness analysis will effectively allow for a three dimensional (3D) mechanical analysis of skin to be evaluated. The 3D mechanical properties of the dermis are important to understand as changes in the mechanical environment have a significant effect on the cells present within the microenvironment (Levy-Mishali et al., 2009). This chapter therefore aims to extend the mechanical analysis conducted on the dermal explant surface to observe the through thickness changes in

mechanical properties of whole skin and the potential variations that may exist due to the layered structure of the tissue.

5.2 Materials and Methods

5.2.1 Sample Preparation

Individual layers of skin were exposed using the cryosectioning method described in Chapter 3. Transverse sections were taken from tail skin harvested from the same mouse tails used in Chapter 4 to allow for a direct comparison of the sample preparation methods and the applied loading conditions. The cryosections were cut perpendicular to the long axis of the tail samples in order to include all the layers of skin within the cross section. The transverse cryosectioned samples produced a surface orthogonal to the dermal explant samples measured in Chapter 4, a schematic of the sample orientation and location of the mechanical measurements is shown in Figure 5.2. The exposed collagen fibre network of the transverse cryosectioned samples therefore provides a different orientation to the collagen fibre network examined within the dermal explant samples of Chapter 4. The sections were cut to a thickness of 5 μm to ensure that the maximum z-piezo scan distance of the AFM allowing for the entire height of the sample to be measured. Imaging from the sample surface down to the glass substrate, such as beyond the edge of the sample, allows for accurate measurement of the sample height after cryosectioning of the tissue.

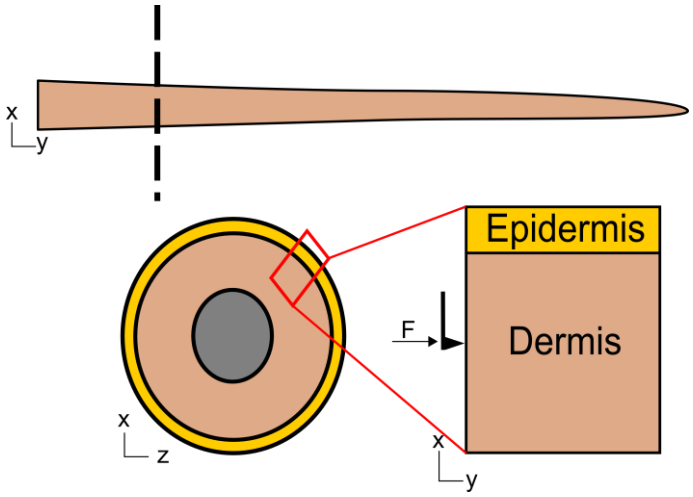

Figure 5.2. Schematic illustrating the sample orientation relative to the whole mouse tail. The location of the AFM indentations are indicated by the arrow marked F.

AFM imaging provides topographical information of the sample surface but is limited in giving compositional information required to understand the location of the sectioned sample relative to the whole skin. Histological staining was therefore exploited to determine the location of the individual layers of skin relative to the overall sample. Haematoxylin and eosin (H&E), as described in the Appendix, staining was used to stain the DNA within the nucleus and the connective tissue through the extracellular fibres. The H&E staining results in nuclei that are stained a blue/purple colour and the extracellular matrix fibres stained a red/pink. H&E staining provides a method where the sample composition can be observed using light microscopy (Suvarna et al., 2013). This staining method also provides a means to measure the thickness of the epidermal layer using optical microscopy due to the clarity of identifying this layer. Three cross sectional samples were prepared by H&E staining and observed using optical microscopy at 10x magnification (Olympus BX60). At least three images were captured using a CCD camera (MicroPublisher

3.3 RTV, QImaging, UK) for each sample and the epidermal thickness was measured using ImageJ (NIST, USA) by counting the number of pixels from the region defined by the basal layer to the edge of the cornified layers and converting the number of pixels to a length measurement using an image of a calibration slide captured at the same magnification. A total of 60 measurements were recorded to provide an average epidermal thickness for the whole mouse tail skin. In addition, H&E staining also distinguished the stratified layers of the epidermis allowing for measurement of the thickness of the different layers of skin.

5.2.2 Mechanical Analysis

Mechanical properties of the transverse cross sections of skin were determined by AFM indentation and analysis of subsequent AFM force-displacement curves. Glass slides containing the cross section samples were removed from the freezer and the tissue section was encircled using a hydrophobic barrier pen (ImmEdge, Vector Laboratories, USA). A 1 mL drop of PBS was then placed over the section of tissue to maintain the sample hydration. The glass slide was then mounted to a magnetic sample holder using double sided adhesive tape and placed on the AFM stage. Low-set point AFM contact mode imaging was conducted on regions of the sample where no evidence of tissue deformation or tearing from the cryosectioning process was observed by *in situ* optical microscopy. Cryosectioned samples were then imaged over 50 µm by 50 µm areas, to ensure the full thickness of the epidermis was included within the imaged area. Including the edge of the sample, which provided a height drop from the top of the cryosectioned tissue to the glass slide substrate for measurement of the section sample thickness. This sample height, determined by AFM height line scan shown in Figure 5.3, was used to determine the maximum

indentation depth for the AFM force-displacement measurements that can be utilised before the substrate stiffness influences the measurements (Gavara and Chadwick, 2012).

AFM indentations were performed over a region 5 μm in width along the x-axis with the y-axis being the length of the visible area of the sample within the imaged area. Figure 5.3 highlights an area represented by AFM indentations. AFM force-displacement curves were conducted at a spacing of 500 nm along the x-axis and at 100 nm spacing in the y-axis. A shorter interval for the force-displacement curves was used for the y-axis measurements as the variations in the mechanical properties of skin in the y-axis direction are more significant, for example a smaller interval may be able to observe the changes within the epidermis from layer to layer. AFM elastic modulus scans were conducted over three samples from three separate tail cryosections. The total number of AFM force-displacements curves for each scan was greater than 3500 for each cryosection measured. In total, three mouse tails were used and one section from each mouse tail was mechanically mapped.

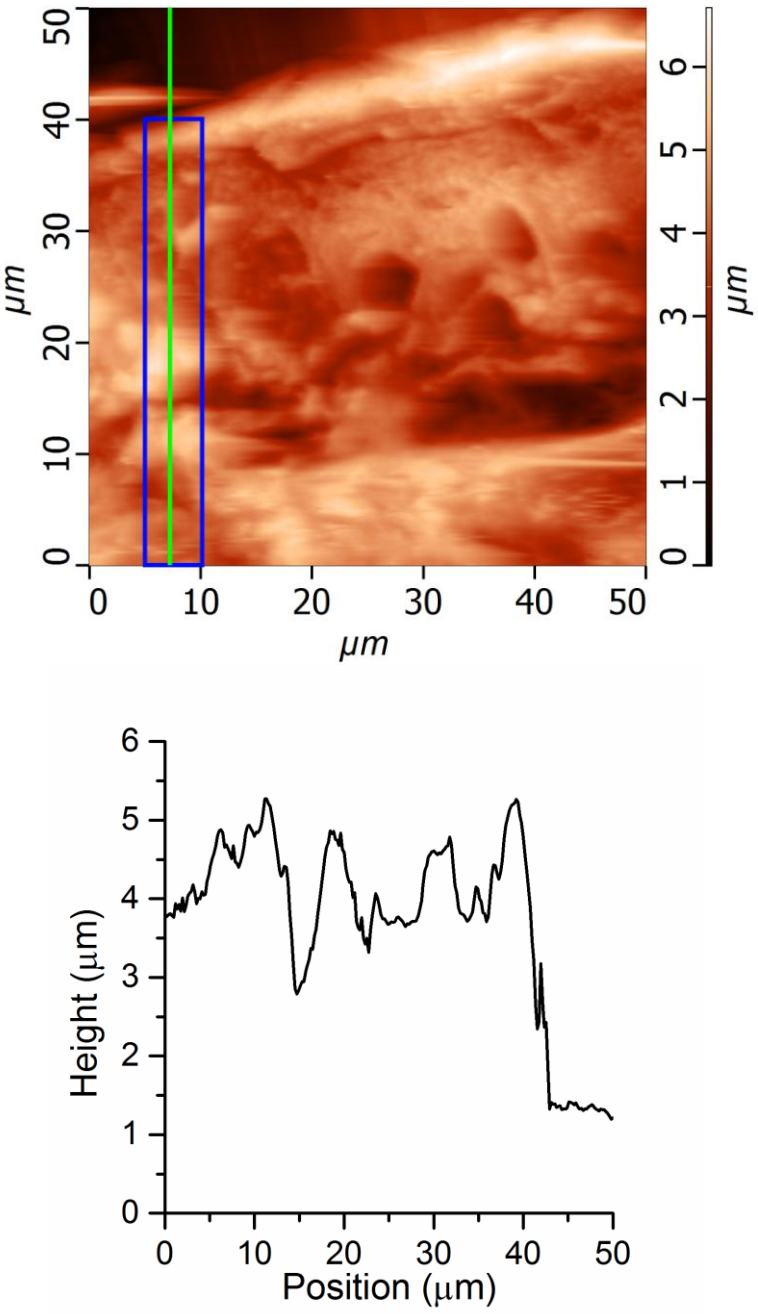

Figure 5.3. (Top) AFM height image of a through thickness cross section of mouse tail skin. Highlighted region (blue) represents the area measured by AFM indentation using force-displacement curves. (Bottom) Vertical line scan from within the highlighted region (green line) showing the drop off between the surface of the section to the glass slide.

The 100 nm spacing between force-displacement curves was selected for the y-axis to ensure the changes in mechanical properties between the different layers of skin were distinguished; because some of the layers of skin contain features that are approximately 100 nm in thickness, such as the basement membrane (Osawa et al., 2003). The force-displacement curves were carried out with v-shaped Si_3N_4 AFM probes (Bruker, EU) with a spring constant between 0.01 $N.m^{-1}$ and 0.5 $N.m^{-1}$, calibrated using the thermal fluctuation method outlined in Chapter 3 prior to performing any AFM imaging or force-displacement measurements. An AFM tip velocity of 2 $\mu m.s^{-1}$ was maintained throughout all force-displacement measurements. The force-displacement indentations where limited so that the final indentation depth of the raw cantilever deflection vs z-piezo displacement curve was less than 10% of the thickness of the cross section. The indentations were displacement controlled; limiting the final indentation depth to approximately 200 nm across all samples. This step was taken to avoid any contribution of the glass substrate to the measured elastic modulus (Gavara and Chadwick, 2012). The force-displacement curves recorded for the cryosections displayed elastic behaviour where the initial indentation loading curve was retraced by the subsequent unloading curve indicating elastic behaviour, with a representative force-displacement curve shown in Figure 5.4 below.

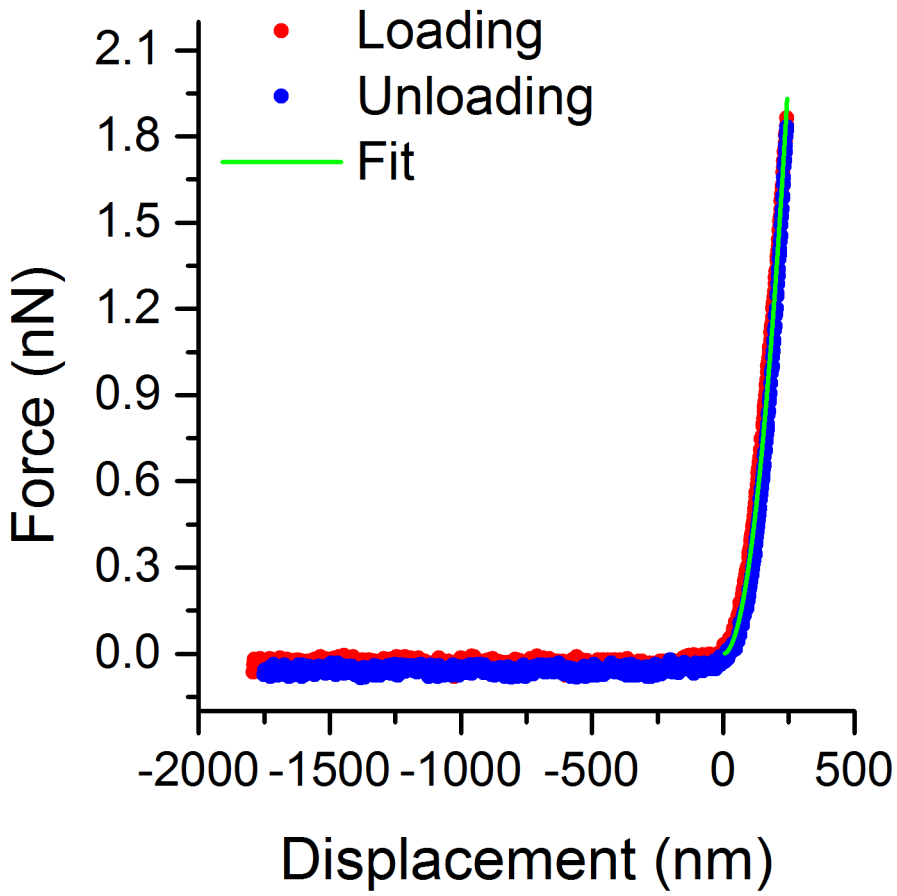

Figure 5.4. Force-displacement loading (red) and unloading (blue) curve data for the AFM indentation of a cross section sample of mouse skin. The retracing of the loading curve by the unloading curve shows the elastic response of the sample to the indentation load. The green line shows the fit of Equation 5.1 to the unloading data set.

The elastic behaviour of the unloading curve indicates that the analysis of the force-displacement curves is able to extract the elastic modulus using the approach previously described in Chapter 3 for the case where indentation loading and unloading can be modelled as Hertzian elastic contact. The following equation below

was fitted to the unloading curve assuming the AFM probe tip as a sharp conical indenter using Sneddon's approximation:

$$F = \frac{2E\tan\alpha}{\pi\left(1-\nu^2\right)}h^2 \qquad \text{Equation 5.1}$$

where F is the applied force, E the elastic modulus of the indented sample region, α the half tip opening angle of the AFM tip taken to be 17.5˚ from the manufacturer's specifications and confirmed by scanning electron microscopy (as shown in the Appendix), ν is the sample's Poisson's ratio was taken as 0.5 to be consistent with the previous measurements on the dermal explants, and h the displacement of the indenter into the sample. The calculated elastic modulus values were constructed into colour coded maps, using the location of each AFM force-displacement curve within the AFM scan to provide spatial coordinates using Origin8 (OriginLabs,USA) to illustrate the variations in the elastic modulus through the full thickness of the skin.

5.3 Results and Discussion

A representative optical microscopy image of the haematoxylin and eosin staining of cryosections from whole mouse tail skin is shown in Figure 5.5 and displays clear indications of the regions defining the stratum corneum, epidermis, and dermis. In Figure 5.5, the stratum corneum is identified as the outermost compressed layers, which are pink/brown in colour. The epidermis is defined in Figure 5.5 from the monolayer of blue nuclei to the beginning of the stratum corneum, and the dermis being the region below the epidermis with the pink colouration. Measurement of the thickness of the epidermis, including viable epidermis and stratum corneum, showed a total thickness of 23.3 μm ± 3.65 μm (mean ± standard deviation, n = 60). The

thickness of the stratum corneum and epidermis was taken into account when selecting the area of the cross section to examine using AFM.

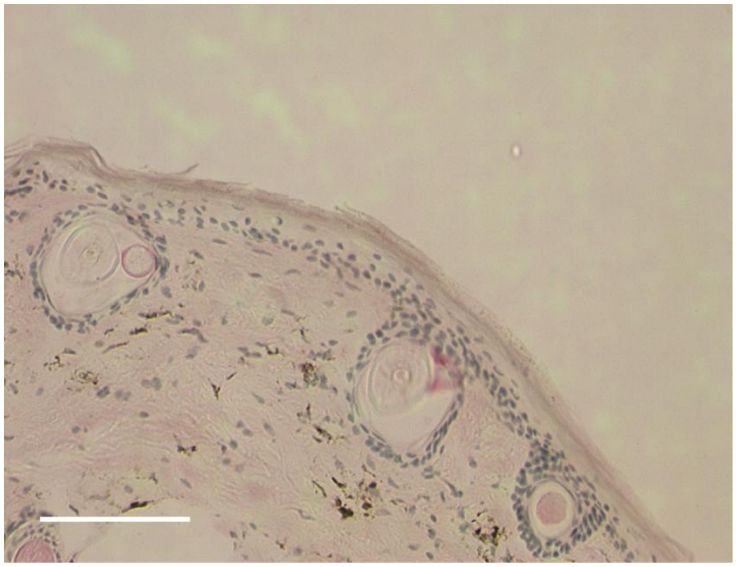

Figure 5.5. Optical microscopy image of H&E staining of cryosection of wild type mouse tail skin. All the regions of skin are present in the image. Circular regions just below the epidermal layer are hair follicles that were present within the tissue section. Scale bar is 100 µm.

AFM imaging of the transverse cryosections in Figure 5.6 revealed that the sectioning process did not yield a completely flat surface but one with varied height topography. The AFM height images also display height features that show the transition regions between the different layers of skin, although these transitions cannot be confirmed directly from the AFM images. The appearance of the defined layers could potentially arise from the different stiffness of the layers. The changes in stiffness in skin may change the sectioning processes using the microtome blade and the sample surface, causing heterogeneous sectioning that results in a variable

sample topography. The AFM height images for the imaged cryosections are shown in Figure 5.6

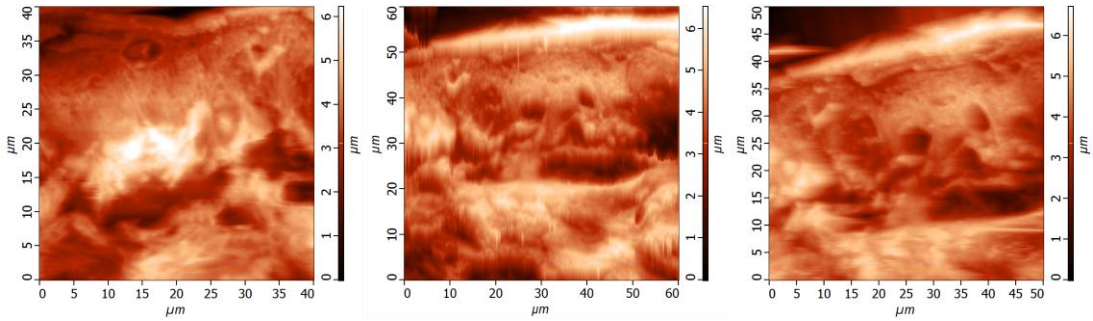

Figure 5.6. AFM height images with of the mouse tail cryosections. The clearest interface appears between the epidermis and the stratum corneum while the transition between the epidermis and the dermis is less clear.

Force-displacement curves measured over the region including the epidermis and dermis were used to derive an elastic modulus of the sample at each contact point. One transverse section from each of the three mouse tail samples used in Chapter 4 were analysed and the elastic modulus values were constructed into distribution maps with the colouration showing the range of elastic modulus as shown in Figure 5.7.

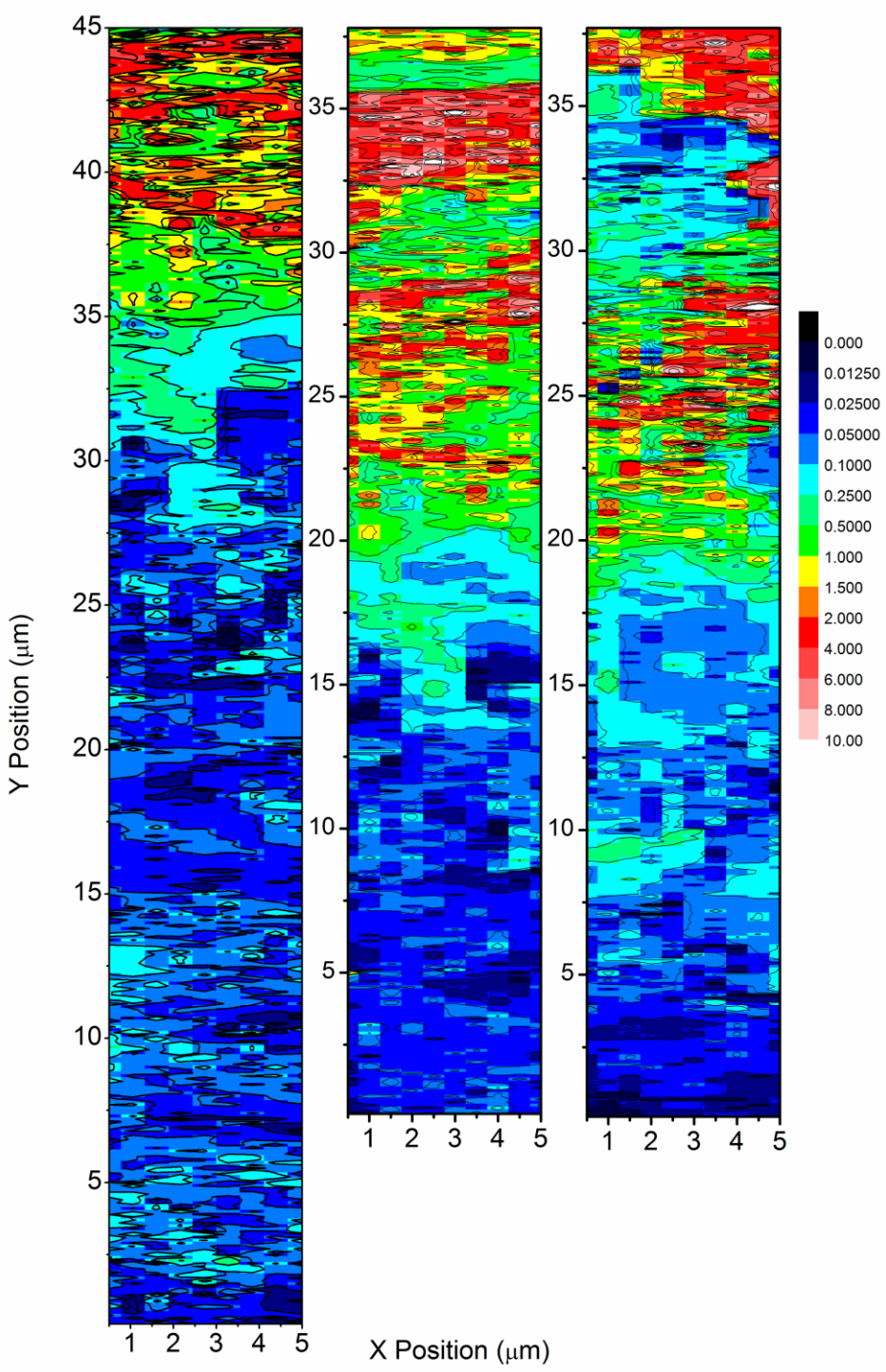

Figure 5.7. Elastic modulus distribution maps for three cryosection samples of wild type mouse tail skin showing the changes in elastic modulus within the skin with the epidermis at the top of the image and the dermis below. Elastic modulus measurements were conducted at 100 nm intervals in the Y direction and 500 nm intervals along the X direction. Scale of colouration is in MPa.

All three of the distribution maps shown in Figure 5.7 display a clear change in the elastic modulus with respect to the position within the skin. The dermis, starting at the bottom of the images, shows a lower elastic modulus than the epidermis located at the top of the images. The mechanical variations observed within the distribution maps are poorly defined and a gradient of elastic modulus values progressively increasing in stiffness as the position moves from within the dermis, starting at the bottom of Figure 5.7, towards the outer most layers of the epidermis is apparent. The gradient change in elastic modulus, particularly within the stratum corneum, can be explained by the terminal differentiation process of keratinocytes during the lifetime of the cell. Keratinocytes progress from basal stem cells and move upwards towards the skin surface while changing their internal cell composition. Initial changes switch of expression of K5 and K14 to K1 and K10, where K1/K10 fibres are more robust intracellular component and stiffen the cell (Fuchs and Green, 1980b; Poumay and Pittelkow, 1995). Keratinocytes will subsequently form the cornified envelope and the cell will become completely crosslinked. This crosslinking results in stiffening of the cell and can be represented by the high elastic modulus regions of the map distributions of Figure 5.7. The gradient of elastic modulus within the epidermis makes it difficult to perform any statistical analysis to provide a mean or median value of the elastic modulus for the epidermis Reporting a value for these quantities would therefore be unrepresentative due to the changing composition and stiffness of the epidermal structure.

The dermal region displays a narrower range of elastic modulus in line with the more consistent composition of the dermis as a collagen fibre network surrounded by a proteoglycan matrix. However, evidence of collagen fibres, which would be

characterised by a significantly higher elastic modulus, within the dermal regions of the distribution maps is lacking. Histograms of the elastic modulus values for the dermal region cross sections, at least 20 µm from the surface of the sample to avoid inclusion of measurements recorded for the epidermis, are shown in Figure 5.9b. Combining the dermal elastic modulus data from all three cryosections measured results in a mean elastic modulus of 60.9 kPa ± 0.721 kPa (standard error of mean, n = 6035 indentations), where the range of elastic modulus falls between a minimum of 20.4 Pa and 598 kPa. The range of elastic modulus indicates that no direct indentation of the AFM probe with collagen fibres is observed as direct indentation of a collagen fibre would result in a measured elastic modulus in the range of 1-2 MPa (Grant et al., 2008). The higher elastic modulus values measured could be influenced by the proximity of the indentation to the collagen network. The indentation probes a volume of material so it is possible that surrounding the collagen fibril network could influence the measured elastic modulus by stabilising the matrix ground substance.

The histogram in Figure 5.9b displays a long tail and a D'Agostino-Pearson omnibus test indicated that the data set was not taken from a normal distribution, based on this result the median was calculated for the data set to be 44.8 kPa. Previous AFM indentation of human skin reported an elastic modulus value of 1.0 kPa for the abdominal dermis using a 5 mm glass sphere attached to an AFM cantilever (Achterberg et al., 2014) and Grant et al. reported a mean of 322 kPa with a range of 25.8 kPa to 1.18 MPa for the normal human dermis using an AFM tip (Grant et al., 2012) indicating a large range of elastic modulus has been observed for the dermis for human samples, which is also a similar range to the values calculated for AFM indentation of the mouse tail dermal cryosections. Preparing skin samples by

cryosectioning provides a clear method for exposing the distinct layers of skin for mechanical characterisation and also for the mouse tail samples used here also provides a method for changing the orientation of the applied for relative to the dermal surface by sectioning in orthogonal planes. The dermal cryosections sampled from the same excised tails used in Chapter 4 allowed for a direct comparison of the measured elastic modulus. The change in sample orientation is illustrated in Figure 5.8 where the effective change is a rotation of the applied load by 90˚. Within Figure 5.8 the direction labelled 1 represents the loading condition applied to the dermal explant samples examined in Chapter 4. The direction labelled 2 in Figure 5.8 indicates the sample orientation and loading condition explored on the transverse cryosections. This comparison will provide evidence of anisotropic behaviour occurring at the nanoscale within the dermis.

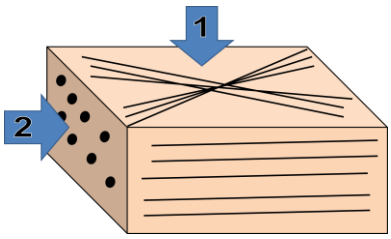

Figure 5.8. Illustration of the collagen fibre alignment within the dermis with respect to the two applied loading conditions. Arrow (1) represents the load applied during the indentation of the dermal explant samples and arrow (2) showing the potential orientation of the collagen fibres within the cryosections of whole skin.

The histograms for both the dermal explant samples and the dermal region of the cryosections are shown in Figure 5.9 for comparison. The two data sets have a median value in the 40 kPa range of elastic modulus, indicating that no orthotropic

behaviour occurring within these samples as the dermis has an isotropic response to the indentation loading at the nanoscale. An orthotropic response would produce a higher elastic modulus within one of the distributions. The isotropic response is characterised by the overlap of the elastic modulus distributions shown in Figure 5.9. Probability density functions were constructed for each data set using MATLAB (MathWorks, USA) and displayed in Figure 5.10. The binning conditions for each data set were the same and non-parametric distribution functions were fit to the data. The peak of the distribution function for the data from the elastic modulus of the cryosection is higher than the peak for the dermal explant samples. This result indicates that there is not complete agreement between the data sets when comparing the elastic modulus of the dermis. Statistical analysis of the histograms indicates that the distributions are neither normal nor lognormal using the D'Agostino-Pearson Omnibus test. However, fitting lognormal distributions to the dermal explant data set results in most likely estimate parameters of $\mu = 3.873$ and $\sigma = 1.337$ leading to a most likely value for the distribution of 48.09 kPa. For the cryosection, the lognormal most likely estimate parameters are $\mu = 3.822$ and $\sigma = 0.7670$, which provides a most likely value of 45.69 kPa for the cryosection data. The most likely value estimates indicate that there is similarity between the distributions of elastic modulus for the dermal explant and the cryosection samples. A Mann-Whitney U-test returned a p value of 0.747 when comparing the dermal explant data to the data from the cryosection, ($n = 4435$ for the dermal explant and $n = 6035$ for the dermal region of the cryosection) representing no significant difference between the two distributions and further indicating mechanical isotropy of the dermis at the nanoscale.

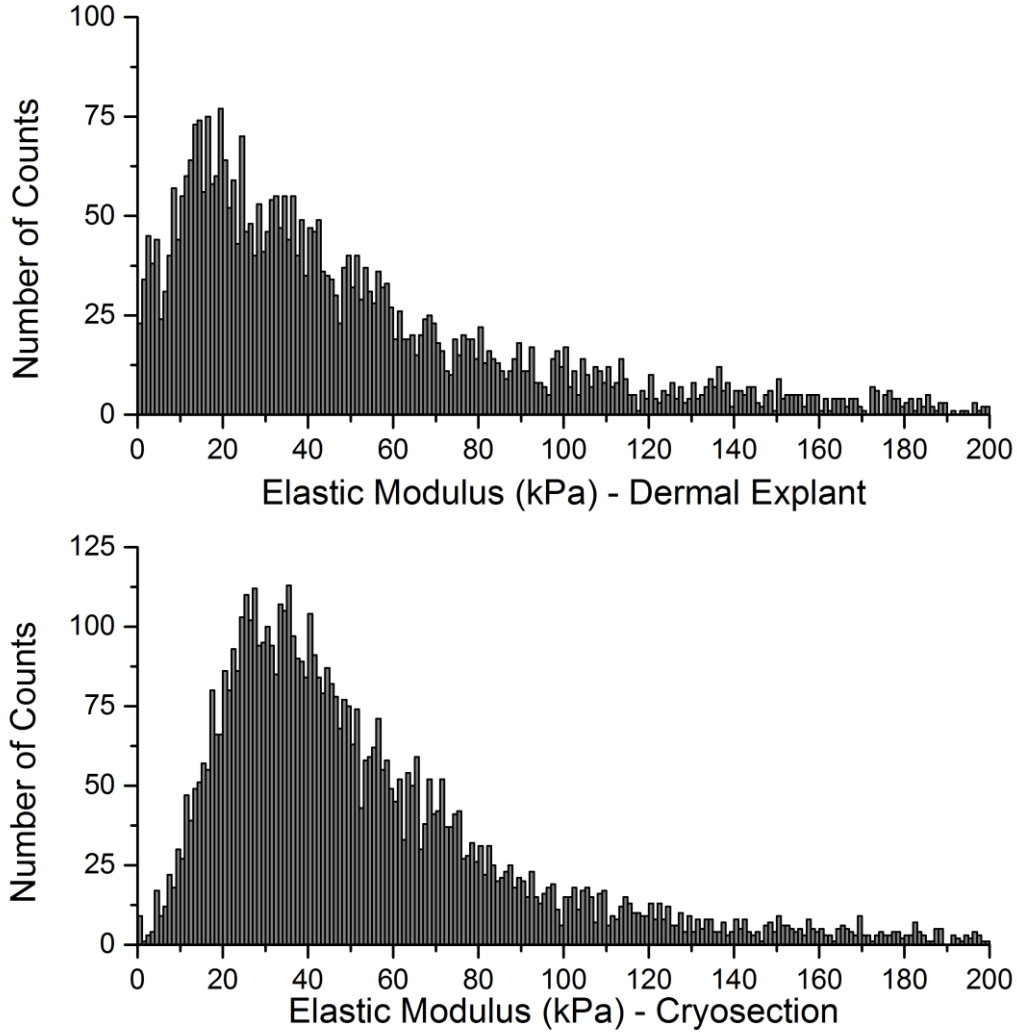

Figure 5.9. Histogram of the frequency of counts for the elastic modulus measurements recorded for dermal explants (n = 4435) and cryosection samples (n = 6035). Elastic modulus values shown between 0 and 200 kPa to highlight the shape of the distributions.

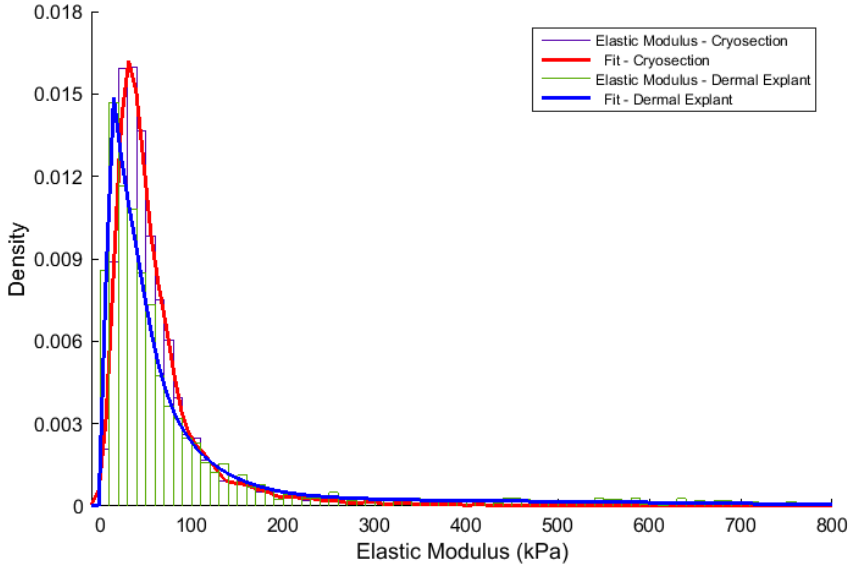

Figure 5.10. Probability density plots of the elastic modulus for the dermal explant (blue) and the cryosection (red).

The isotropic response of the dermis at the nanoscale suggests that the indentations are not directly applying a load to the individual components of the dermis and the mechanical response is not dominated by the stiff collagen fibre network. This result shows that the indentation forces are insufficient to directly strain the collagen network and the mechanical response is dominated by the matrix ground substance. Such a result is unexpected as previous work has shown at the macroscale that the orientation of the collagen network has an effect on the initial slope of a uniaxial tensile test, with the fibres aligned in the direction of the load giving a higher initial slope in a stress-strain plot (Groves et al., 2013; Ní Annaidh et al., 2012b). Therefore, the expectation was that some significant contribution of the orientation of the sample to the mechanical response would be measured but no significant change in the elastic modulus is observed at the nanoscale. The macroscopic anisotropy is a result of the alignment of the collagen fibres within the dermis where

the alignment of the collagen fibres has a significant effect on the mechanical properties, including the elastic modulus (Ní Annaidh et al., 2012b). The collagen fibres within the dermis form a lattice structure that has a preferential alignment along the Langer's lines. The lattice network of collagen fibres is also aligned parallel to the surface of the epidermis. In a uniaxial tension test conducted parallel to the preferred fibre orientation angle, the load will be applied along the long axis direction of the collagen fibres yielding an increased measurement of elastic modulus.

The initial AFM indentation measurements conducted on dermal explants in Chapter 4 applied a load perpendicular to the collagen fibre network, introducing a bending force to the fibres within the dermal matrix represented by the arrow marked 1 in Figure 5.8. The loading case for the transverse sections is therefore dependent on which orthogonal plane the section is taken from. If the section is taken from the plane perpendicular to the collagen alignment then the indentation loading of the transverse section would be along the axis of the collagen fibres as shown in Figure 5.8 by the arrow marked 2. A section taken parallel to the orientation angle may result in a loading condition similar to the dermal explant and be perpendicular to the long axis of the collagen fibres. AFM force-displacement measurements taken from sections perpendicular to the long axis of the fibres result in the collagen fibrils undergoing a buckling deformation where the contribution to the mechanical response would be minimal, which would potentially result in a reduced measured elastic modulus (Böl et al., 2015).

The mechanical response to indentation loading in transverse sections is expected to differ from the dermal explant samples as the orientation of the collagen network has changed due to collagen fibre bundles within the plane no longer aligned

perpendicular to the applied load. However, little difference in the elastic modulus between dermal explants and the transverse sections is observed as shown in Figure 5.9 and Figure 5.10, suggesting that the mechanical response at the nanoscale is not dependant on the structure or alignment of the collagen network of the dermis. The lack of a change in the mechanical response suggests that the length scale being observed is independent from the orientation of the collagen network contributing to the mechanical response of the dermis that is dominant at macroscopic length scales. This result of mechanical isotropy in the dermis indicates that the AFM indentation data from the dermal explant samples and the transverse sections can be combined to construct a three dimensional description of the elastic mechanical response of the dermis under nanometer deformations. This representation of the dermal mechanical environment potentially indicates that at small length scales, such as the cellular level where cells are applying small forces to the local microenvironment, the response of the surrounding material is independent of the direction of the applied force. The elastic modulus maps for the dermal explant and the transverse cross section are combined to illustrate that the elastic modulus of the dermis is independent of the orientation in Figure 5.11.

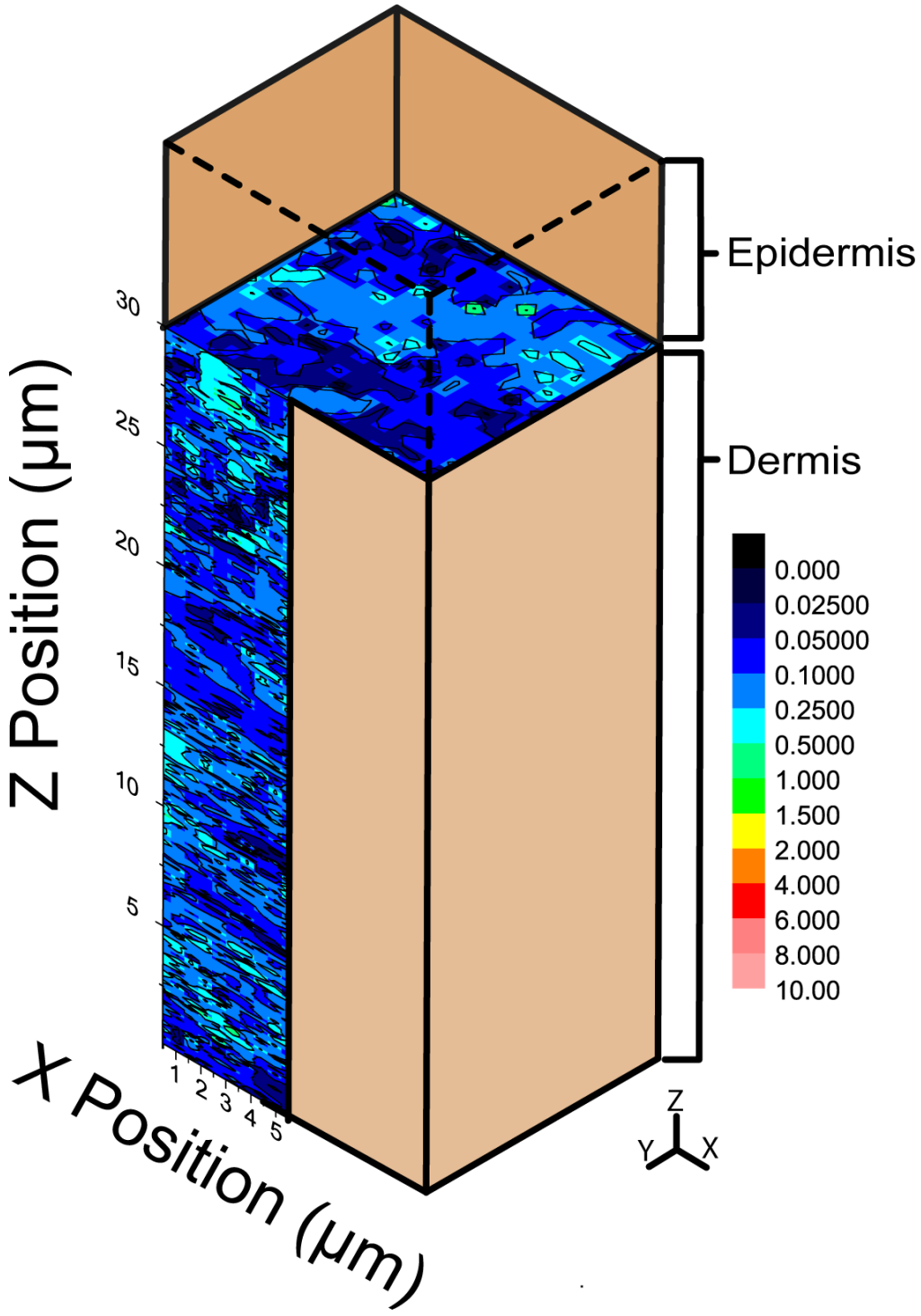

Figure 5.11. A 3D representation of the distribution of elastic modulus values for microscopic volumes of the dermis. The volume represented is proportional to the volume a cell may be exposed to in vivo or in vitro within a three dimensional environment. Scale for elastic modulus colouration in MPa.

The three dimensional representation of the mechanical behaviour of skin at the nanoscale, assuming the orientation of the collagen network is different between the samples, highlights the suggested isotropic nature of the dermis at this length scale, specifically as the elastic modulus in the xz plane in Figure 5.10 are the same, within error, as the elastic modulus values in the xy plane. The difficulty in producing dermal explant samples, due to the mechanical peeling required to remove the epidermis, indicates that mechanical properties of the dermis can be extracted from transverse sections, which are easier to prepare, due to the mechanical isotropy.

The mouse dorsal skin is a location often used studying the wound healing behaviour of skin (Ashcroft et al., 1999; Wu et al., 2007). However, separating the epidermis from the dermis at this location using the mechanical peeling method to analyse the mechanical properties of the dermis is difficult because of the significantly thinner epidermis present in the dorsal skin. The epidermal layer for the dorsal skin was thinner than the tail skin with a mean thickness of 8.31 μm ± 1.63 μm (mean ± standard deviation) when H&E staining images were quantified as previously described for the tail skin cryosections. Measuring the mechanical properties of transverse sections allows for analysis of the mechanical behaviour of the whole skin. Force-displacement curves were conducted on transverse cryosections of dorsal skin from two wild type mice over a region encompassing the epidermis and the dermis.

The elastic modulus values of the dermal region for the two cryosectioned dorsal skin mouse samples were combined into a histogram to visualise the distribution of elastic modulus values, as shown in Figure 5.12. The distribution for the elastic

modulus of these samples provides a range from 0.122 kPa to 167 kPa with a mean of 13.2 kPa ± 0.247 kPa (standard error of mean, n = 2606) and the median of the distribution falling at 9.65 kPa. The elastic modulus values presented here for the dermis are significantly lower than that of the dermis from the cryosectioned tail skin of the same breed of mice reported earlier in this chapter and displayed in Figure 5.9. This result suggests that there is a compositional change within the dermis depending on where the skin is located within the body, which results in variations in the skin elastic modulus.

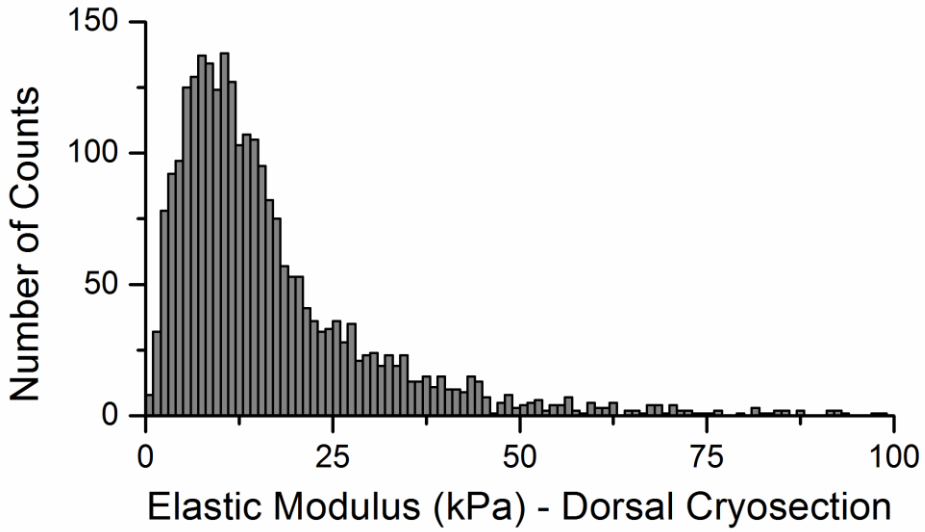

Figure 5.12. Frequency of counts for the elastic modulus measurements conducted on a dermis of dorsal cryosections of wild type mouse. Elastic modulus data shown between 0 and 100 kPa, total n = 2610

The variations in mechanical response of skin at the macroscopic level have been previously shown to vary with the anatomical region considered in the human body (Ryu et al., 2008; Smalls et al., 2006). The amino acid hydroxyproline is a major component of collagen and often used to quantify the collagen content within a tissue

(Maccarana et al., 2009; Prockop and Kivirikko, 1995). The biochemical composition of skin wild type mice was previously shown to vary through quantification of the hydroxyproline content of the skin, which was shown to significantly change based on the region of the skin that was sampled (Manne et al., 2013). Hydroxyproline is a component of collagen and a variation in the total content is expected to cause variability in mechanical performance, as collagen is an important stabilising component within the skin as established previously in this chapter. The biochemical analysis provides insight to the whole dermis and does not indicate special location for compositional changes within skin. However, collagen content varies depending on anatomical location and is thus likely to have an effect on the mechanical properties of the skin such as observed in elastic modulus variations between the tail skin and the dorsal skin here.

The variation in the total amount of collagen within the tissue and the resulting change in elastic modulus further indicate a potential stabilising effect of the collagen fibre network on the overall nanoscale mechanical response of skin. Decreasing collagen content and corresponding loss of collagen fibre density, which could be observed as a decrease in total hydroxyproline content within the dermis, is expected to result in a reduced elastic modulus. A region of the dermis with a higher density of collagen fibres will produce a higher elastic modulus due to a higher volume fraction of stiff collagen fibrils to reinforce the surrounding matrix ground substance. To understand this proposition further, the collagen fibres within the dermis are considered as the reinforcing material of a continuous fibre reinforced composite. A rule of mixtures, or the Voigt model, for the elastic modulus of a composite material (Wong and Bollampally, 1999) is applied using

$$E_c = (1 - V_f)E_m + V_f E_f \qquad \text{Equation 5.2}$$

where, E_c is the elastic modulus of the composite, V_f the volume fraction of the fibre reinforcement, E_m the elastic modulus of the matrix, and E_f the elastic modulus of the reinforcing fibres can be instructive in understanding the effect of increase collagen fibril content on dermis mechanics. Assuming $E_f > E_m$, the relationship shows that increasing reinforcing fibre volume fraction causes an increase in composite elastic modulus E_c. Therefore, increasing stiffer collagen content within a softer ground substance provides a similar effect of increasing the elastic modulus of the (composite) dermis. This composite approach would suggest that the collagen fibre network within the dermis is potentially stabilising the ground substance under deformations at the nanoscale and the degree of influence on the ground substance is dependent on the total amount of collagen present.

5.4 Conclusions

AFM force-displacement curves were used to measure the elastic properties of through thickness whole skin cryosections. The spatial distribution of the elastic modulus of skin was recorded to visualise the local variations in mechanical properties at the cellular length scale. The mechanical properties of the epidermis were shown to be significantly higher than the dermal region, with the epidermis also exhibiting a graded mechanical structure, which may be linked to the terminal differentiation and stratification of the keratinocytes present within the epidermal layers. The mechanical measurements of the dermal region of the cryosections resulted in elastic modulus values were comparable to the values of the mouse tail dermal explants. Similarity between the mechanical response of the dermis to two

different loading orientations suggests that the dermis may behave as an isotropic material at the nanoscale when probed by AFM nanoindentation.

Chapter 6 – Analytical modelling of skin using composite considerations

6.1 Introduction

The nanoscale mechanical properties of skin, with emphasis on the spatial variation through the thickness of skin, have been established in Chapter 5 along with the apparent isotropic mechanical response of the dermis at the nanoscale. The complex multicomponent structure of skin makes the evaluation of the individual components significantly challenging. However, the overall structure of skin can be simplified into a two phase composite system composed of the epidermis and the dermis. The ability to measure the spatial variations in the mechanical properties of whole skin provides the potential to estimate the mechanical response of a bulk sample under nanoscale loading conditions. Composite mechanical properties are generally estimated using the mechanical properties of two matrix and reinforcement phases, and the respective volume fraction of each phase present within the composite system. The orientation and structure of the reinforcement phase, as well as the loading conditions applied to the material, define the composite models that can be applied to estimate the overall composite mechanical properties. Here we consider established composite models but apply to skin where the mechanical properties have

been measured directly in the previous chapter. Thus, the relationship between nanoscale mechanical properties and the prediction of overall macroscopic tissue mechanical behaviour is considered.

The basic model of a composite considers two plates perfectly bonded and a tensile force applied such that each phase is exposed to an equal stress (isostress) or an equal strain (isostrain), as illustrated in Figure 6.1.

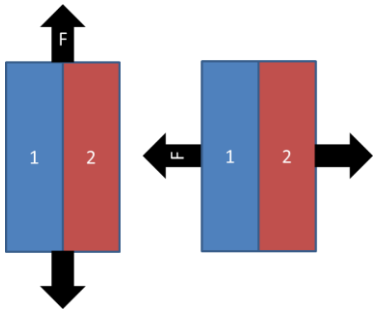

Figure 6.1. Illustration of the (left) isostrain and (right) isostress loading conditions for a two phase composite system.

The configuration where the applied strain is the same across both phases can be considered from the isostrain condition and the composite elastic modulus becomes a volume fraction weighted average of the elastic modulus of each component. The composite elastic modulus can be expressed as,

$$E_c = V_1 E_1 + V_2 E_2 \qquad \text{Equation 6.1}$$

where E_c represents the elastic modulus of the composite, V_2 the volume fraction of the reinforcement phase, E_2 the elastic modulus of the reinforcement, V_1 the volume fraction of the matrix, and E_1 the elastic modulus of the matrix. This representation of the isostrain conditions is also referred to as the rule-of-mixtures or the Voigt

composite model. The loading condition where the stress across both phases is equal, or isostress, can be represented by a similar volume fraction based expression given by,

$$\frac{1}{E_c} = \frac{V_1}{E_1} + \frac{V_2}{E_2} \qquad \text{Equation 6.2}$$

Equation 6.2 is often referred to as the inverse rule-of-mixtures or the Reuss composite model. The combined Voigt-Reuss (V-R) models represent the theoretical upper and lower bounds of the elastic modulus of a material. However, the practical applications of these models are often limited as the combination of reinforcement/matrix orientation and applied loading conditions are often not satisfied. The development of sophisticated volume fraction based composite models, particularly the Hashin-Shtrikman (H-S) model, attempts to eliminate the dependence of reinforcement geometry and loading conditions while providing tighter limits to the possible elastic modulus values. The H-S model considers a two phase composite system of matrix and reinforcement where the reinforcement is homogenous, isotropic, and of arbitrary geometry (Hashin and Shtrikman, 1963). The limits of the H-S model are calculated using the bulk modulus, shear modulus, and the volume fraction of each phase, with the upper bounds given by (Wong and Bollampally, 1999)

$$K_U = K_2 + (1 - V_2)\left(\frac{1}{(K_1 - K_2)} + \frac{3(V_2)}{3K_2 + 4G_2}\right)^{-1} \qquad \text{Equation 6.3}$$

$$G_U = G_2 + (1 - V_2)\left(\frac{1}{(G_1 - G_2)} + \frac{6(K_2 + 2G_2)(V_2)}{5G_2(3K_2 + 4G_2)}\right)^{-1} \qquad \text{Equation 6.4}$$

and the lower bounds via

$$K_L = K_1 + V_2\left(\frac{1}{(K_2 - K_1)} + \frac{3(1-V_2)}{3K_1 + 4G_1}\right)^{-1} \quad \text{Equation 6.5}$$

$$G_L = G_1 + V_2\left(\frac{1}{(G_2 - G_1)} + \frac{6(K_1 + 2G_1)(1-V_2)}{5G_1(3K_1 + 4G_1)}\right)^{-1} \quad \text{Equation 6.6}$$

where K is the bulk modulus and G the shear modulus. The bulk and shear moduli can be related to the elastic modulus through the following relationships (Hull and Clyne, 1996)

$$G = \frac{E}{2(1+\nu)} \quad \text{Equation 6.7}$$

$$K = \frac{E}{3(1-2\nu)} \quad \text{Equation 6.8}$$

Therefore, the upper and lower limits of the H-S model in terms of elastic modulus can be express respectively as (Lee, 1993)

$$E_U = \frac{9K_U G_U}{3K_U + G_U} \quad \text{Equation 6.9}$$

$$E_L = \frac{9K_L G_L}{3K_L + G_L} \quad \text{Equation 6.10}$$

The H-S bounds provide less variation between the upper and lower limits due to the more rigorous modelling of the composite, when compared to the V-R model, for the calculated elastic modulus of a two phase composite system. The H-S bounds potentially provide a more accurate estimation of the composite modulus depending on the volume fraction of reinforcement. The V-R and H-S models provide a theoretical limit on the elastic moduli of a composite material, and using these models provides an avenue to potentially predict the bulk mechanics of a complex composite system using nanoscale mechanical measurements of small volumes.

This chapter attempts to utilise the nanoscale mechanical description to define the mechanical properties of bulk skin as a composite system. Theoretical composite models used to describe engineering material composite systems are applied and evaluated against the macroscopic measurements of skin conducted at low strain levels. This chapter is also used to develop a finite element model based on the AFM nanomechanical measurements to be used as a platform for exploring the effects of the distribution of elastic modulus values, at the nanoscale, on the whole sample mechanical response under nanometer deformations at low strain levels.

6.2 Materials and Methods

6.2.1 Sample Preparation

The mouse tail samples used in this chapter were harvested from wild type CD1 mice and the tail samples were prepared in the same manner similar to the method described in Chapter 3. The animals were scarified according to Home Office regulations (license PPL 70/7166). Two tails were cut along the length of the tail and to isolate the whole skin was peeled away from the tendon. The whole skin sample was then cut into smaller sections approximately 3 cm x 3 cm in area.

Three whole skin tail samples were embedded in OCT and frozen down to -80°C for cryosectioning. The cryosectioning was carried out as previously described in Chapter 3 to produce transverse sections of the whole tail skin. Samples were fixed in methanol at -20°C for 15 minutes immediately after sectioning the. After fixation, the samples were rinsed three times in PBS at room temperature and then stored at 4°C in PBS until further use.

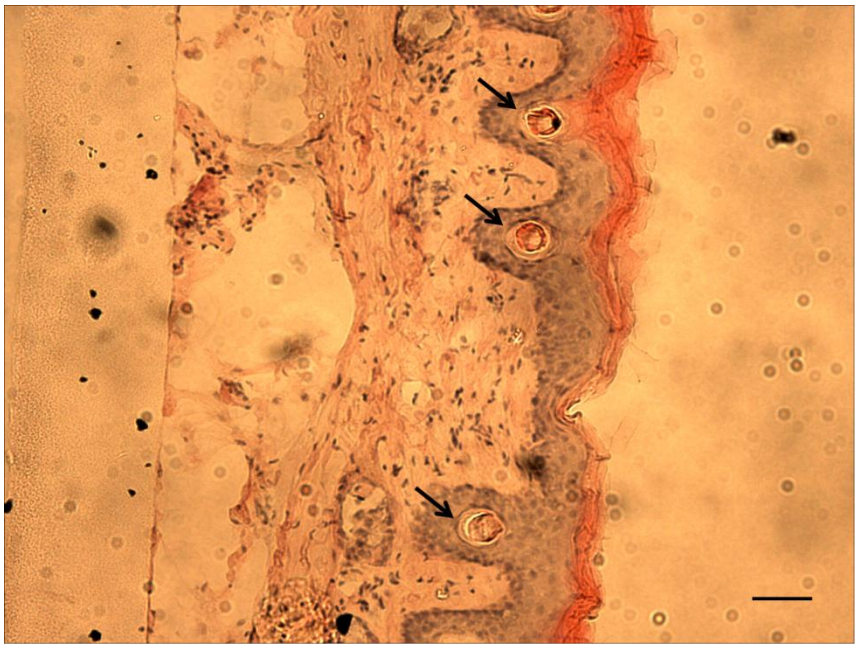

Figure 6.2. H&E staining of wild type CD1 mouse tail with the right edge showing the stratified layers highlighted by strong pink staining, the epidermal layers stained blue, and the dermal connective tissue showing light pink staining. Black arrows indicate locations where a hair follicle is present. Scale bar 20 μm.

Sample H&E staining was carried out using the protocol described in the Appendix to visualise the structure of the CD1 tail sections. The H&E staining was used to distinguish between the different layers of skin and the stained sections were then imaged using transmission optical microscopy (Olympus BX60) using a 10x objective lens. Images of a calibration grid were also captured using the same objective lens and camera settings. Optical images were captured using a CCD camera (Micropublisher 3.3 RTV, QImaging, UK). The epidermal thickness and whole sample thickness were quantified by importing the images into ImageJ alongside the calibration image. The epidermal thickness was manually measured using the draw line tool and converting the number of pixels to a length. The

epidermis was defined by the region from the layer of basal cells, which appear as a blue monolayer of nuclei within the image, to the edge of the stratum corneum, which is the edge of the sample. The thickness of the whole skin was also measured using the same quantification method. The whole skin thickness was only measured at points were the section was continuous and evidence of tearing or separation within the section was absent. The whole skin thickness was measured from the edge of the staining for the connective tissue within the skin to the edge of the stratum corneum. Four sections from two mouse tails were measured, and three images for each section and a minimum of ten measurements within each section were taken for each sample. The measurements of thickness for the whole skin and the epidermal layer were then used to calculate the volume fraction of epidermis and dermis. The volume fraction of the dermis was taken as

$$V_D = 1 - \frac{t_E}{t_W} \qquad \text{Equation 6.11}$$

$$V_D + V_E = 1 \qquad \text{Equation 6.12}$$

where, V_D is the fraction of dermis and V_E the fraction of epidermis within the CD1 tails, t_E is the thickness of the epidermis as measured by optical microscopy from the H&E stain, and t_W is the whole skin thickness. The fraction of epidermis and dermis are used later within this chapter as parameters for constructing a two phase composite model of skin.

6.2.2 Macroscopic mechanical analysis

Macroscopic indentation tests were performed using an MTS Bionix 100 (MTS, USA) equipped with a 1 mm cylindrical flat punch indenter and a 50 N load cell.

Whole skin samples were tested to 20% strain using displacement velocity of 0.01 $mm.s^{-1}$. Indentation of samples was held at 20% strain for 10 seconds prior to unloading at a rate of 0.01 $mm.s^{-1}$. For each mouse, three samples of whole skin were tested and three indents were conducted at least 0.5 cm apart on each sample. Indentation the time, load, and displacement were recorded throughout all of the indentation of skin experiments.

The indentation data for the skin samples was plotted as force vs displacement and the initial linear loading curve was fit assuming an elastic Hertzian contact condition. For a cylindrical flat punch indenter in contact with an elastic half space, the force is described by the following equation (Williams and Dwyer-Joyce, 2000),

$$F = \frac{2ER}{(1-v^2)}d \qquad \text{Equation 6.13}$$

where, F is the applied force, R the radius of the cylindrical punch, v the Poisson's ratio of the sample and E is the elastic modulus of the sample under the indenter. The whole skin samples were assumed to have a Poisson's ratio of 0.5 to be consistent with the values used for the nanoscale measurements conducted previously in Chapters 4 and 5. The initial loading region was only considered for analysis of the elastic modulus as the force-displacement curve became non-linear after 10% strain. As a result, 10% strain was selected as the threshold strain to which the elastic response to the indentation load could be applied.

6.2.3 Finite element Analysis

Finite element analysis (FEA) was conducted using commercially available software ABAQUS (Dassault Systèmes, FR). For all the FEA conducted in this work, the

ABAQUS standard/explicit modelling environment was used. The elastic modulus values measured in Chapter 5 for the transverse sections of mouse tail skin were used as the material data for the FEA models.

The AFM datasets of the elastic modulus values contain the spatial information of the measurements in addition to the mechanical properties and are constructed into a FEA mesh. The mesh was constructed by assigning each AFM data point an element number and corresponding nodes in the order in which the measurements were conducted. The element size was determined by the spacing between the AFM force-displacement measurements, with each element representing an area of 100 nm x 500 nm for the transverse cross section samples of skin. Each element was assigned the measured elastic modulus value from the AFM elastic modulus map according to the position within the raster scan and the Poisson's ratio defined as 0.499. Throughout the FEA modelling the elements and the sample system were considered to be homogenous and linear elastic isotropic. This assumption is based on the previous Chapters results of the linear elastic behaviour observed at the nanoscale but overall serves as a simplification of the bulk mechanical properties of skin. Therefore, the modelling results presented throughout this Chapter are only applicable to nanoscale deformations within the linear elastic response of skin.

The FEA conducted in this work considered the meshes produced from the cross section samples as an axisymmetric model. This method of analysis was selected to simplify the model definitions and analysis techniques required. The model therefore considered two dimensional 4-node bilinear axisymmetric solid continuum elements, CAX4, where the degrees of freedom are in the X-axis and Y-axis of a standard Cartesian coordinate system. A custom MATLAB script was used to automatically produce the mesh for importing into ABAQUS. A mesh was produced for each of the

transverse sections of mouse tail skin analysed by AFM indentation in Chapter 5. The MATLAB script assigned an element to each elastic modulus value from the AFM analysis arranged in the order the AFM force-displacement measurements were conducted. The resulting mesh contained the positional information of the AFM analysis alongside the mechanical description of the sample at that point. The unit system of time was seconds, distance in nanometres, and stress in GPa.

The boundary conditions applied to the individual mesh models are shown in Figure 6.3. Within the ABAQUS modelling environment the global directions and axes of a three dimensional system are defined such that the X-direction is U1, the Y-direction is U2, and the Z-direction is U3. Rotation around an axis is defined, for example about the X-axis, as UR1. The model is designed to simulate the unconfined compression of a bulk sample in response to a predefined level of strain. The compression loading condition was selected in order to ensure the entire sample measured by AFM indentation was included in the finite element analysis. The first boundary condition is applied to the axis of symmetry within the model, which for this analysis is represented as the Y-axis. The boundary conditions are such that there is no displacement in the X direction or rotation of the nodes lying along axis of symmetry (U1 = UR2 = UR3 = 0). The second boundary condition applies to the nodes representing the base of the sample where there is no displacement in the Y direction (U2 = UR1 = UR3 =0). The final boundary condition is applied to the top surface of the sample and represents the compression loading through a defined displacement of the nodes at the top surface where U2 = -25 nm. The displacement defined in this fashion represents a uniaxial loading condition where no end plates constrain the sample, so that the sample edges are free to deform in the U1 direction. The composite elastic modulus was determined from the model system through

analysis of the total internal energy of the system as a result of the deformation. The strain energy, *U*, of the deformation under uniaxial loading conditions can be defined through the deformation, Δ, and the initial dimensions of the sample by (Bowes et al., 1984)

$$U = \frac{EA_0\Delta^2}{2L_0} \qquad \text{Equation 6.14}$$

The strain energy of the whole model is considered and plotted against the deformation. The resulting plot of energy vs deformation is fitted to a second order polynomial and the elastic modulus extracted from the leading coefficient as the initial cross sectional area, A_0, and initial length, L_0, of the model are known. The axisymmetric FEA model is cylindrical in shape, so the cross sectional area of the model is calculated by using the width of the mesh in the X-direction as the radius.

Boundary conditions were defined in order to simulate the compression of an axisymmetric body. Meshes were defined that contained elements using a single value for the elastic modulus to give the compression condition and the FEA was conducted. The elements within these meshes also used CAX4 elements but had the dimensions of 100 nm by 100 nm with a total mesh size of 400 nm by 1000 nm. Elastic modulus values of 1 MPa and 10 kPa were used for this validation. Three additional meshes were produced with varying compositions of 1 MPa and 10 kPa elastic modulus elements. The compositions described by the volume fraction of 1 MPa elements within the mesh as V_{1MPa} = 0.2, 0.5, and 0.8, were used to understand the FEA description of a composite sample. The variation of the composition within the sample and the orientation of each phase is illustrated in Figure 6.3c. The verified boundary conditions were then applied to the meshes generated from the AFM data sets of the mouse tail skin cross section, which were analysed in Chapter 5.

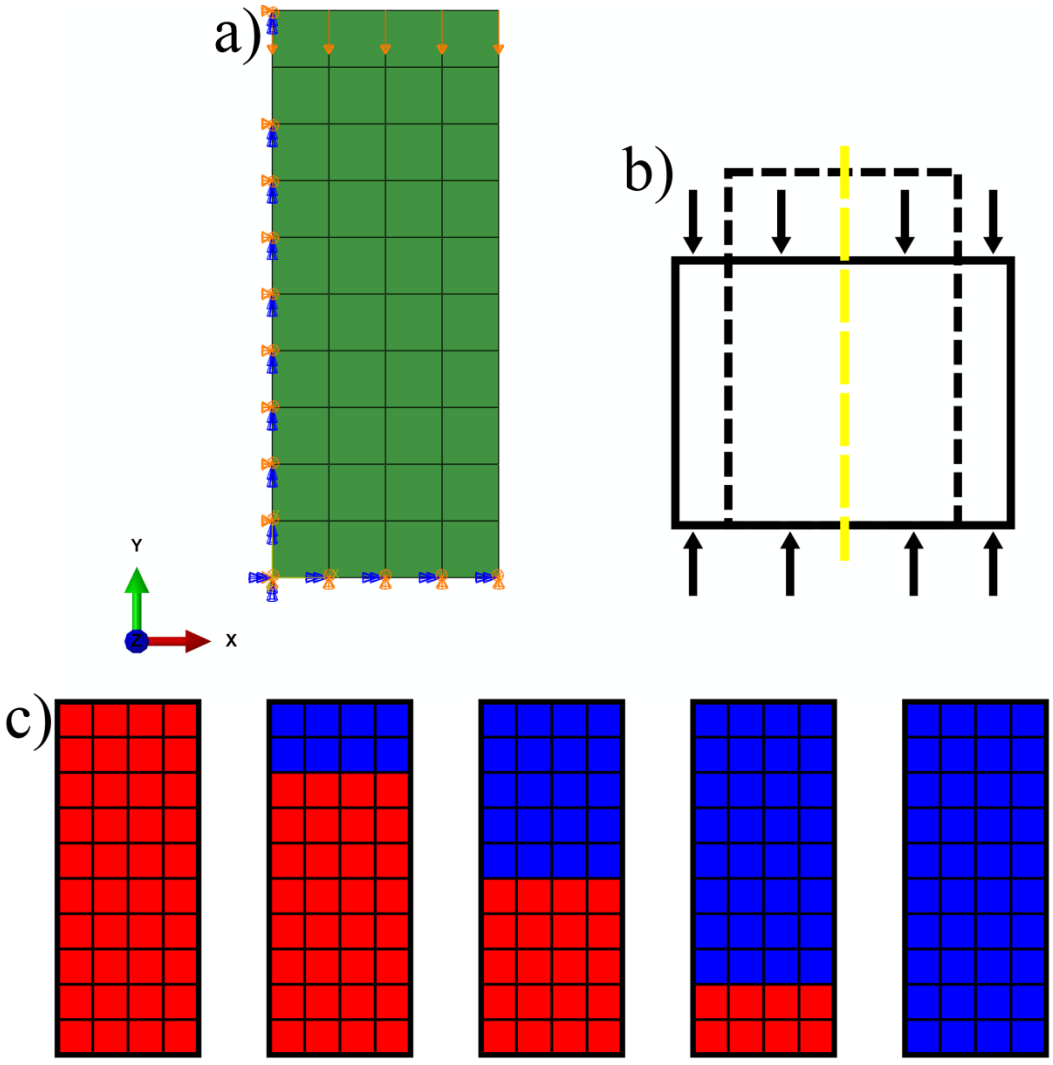

Figure 6.3. (a) ABAQUS representation of mesh used for validation of the illustrated boundary conditions. (b) Schematic of the applied deformation with the dashed yellow line representing the axis of symmetry for the model. (c) Illustration of the variation of the five constructed meshes used to observe the composite behaviour of the FEA with red representing the 10 kPa elements and blue the 1 MPa elements.

6.3 Results and Discussion

Indentation of whole skin mouse tail samples using a displacement controlled flat punch produced force-displacement measurements as shown in Figure 6.4. The cylindrical indenter contact area with the sample does not change with increasing indentation depth, indicating an expected linear force-displacement relationship. Figure 6.4 shows that the initial loading was linear followed by non-linear behaviour after a threshold strain in the loading force-displacement curve.

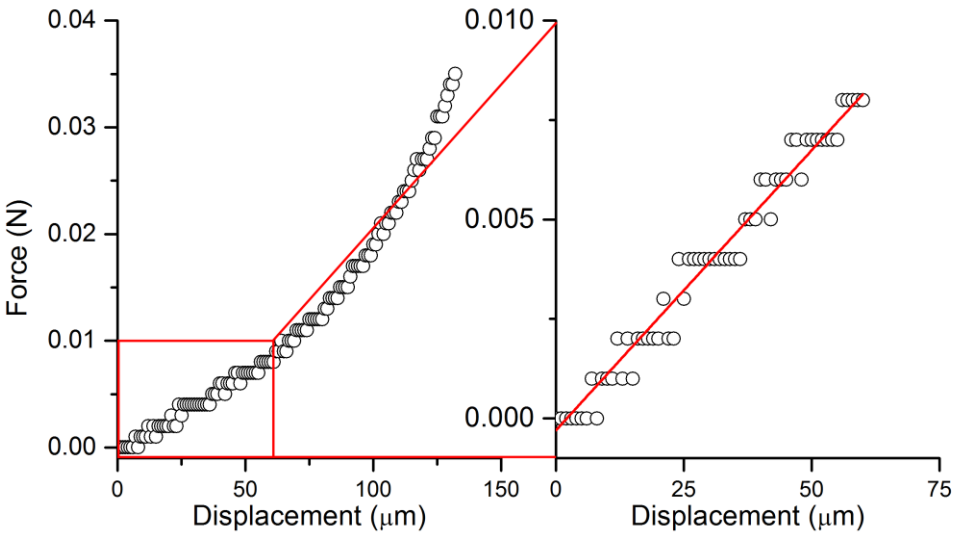

Figure 6.4. (a) Full force-displacement curve of whole skin using a 1 mm indenter showing non-linear behaviour beyond a threshold indentation depth between 50 μm and 75 μm. (b) Linear relationship within the highlighted region of the force displacement curve and linear fit line used to extract the elastic modulus using Equation 6.13.

The non-linear force-displacement behaviour observed when performing flat punch indentation is suggested as being due to the response of the collagen network to the applied load. Whole skin when subjected to a uniaxial tensile test responds with a non-linear stress-strain behaviour, which has been extensively reported (Gahagnon et al., 2012; Groves et al., 2013; Ní Annaidh et al., 2012b; Vexler et al., 1999). The non-linear behaviour leading to an increased linear stiffness has been associated with the alignment of the collagen network under loading (Groves et al., 2013; Ní Annaidh et al., 2012b). As the strain is increased, the collagen fibres within the dermis align with the applied load and thus increases the stiffness of the dermis (Eastwood et al., 1998; Groves et al., 2013; Ní Annaidh et al., 2012b). This non-linear behaviour also has an effect on the unloading behaviour of the force-displacement curve. In order to draw comparisons between the nanoscale mechanics measured in Chapters 4 and 5, and macroscopic skin mechanics, only initial loading is considered and the large strain behaviour is ignored. The small strain behaviour of the macroscopic test applies a similar loading condition to the AFM force-displacement measurements conducted in Chapters 4 and 5. The elastic modulus of the initial loading was calculated by fitting Equation 6.13 to the initial linear region of the force-displacement indentation curve as shown in Figure 6.4b. A resultant average elastic modulus of 78.36 kPa ± 8.338 kPa (standard error of mean, n = 17 indents across six samples from two mouse tails) was found using this approach. The standard deviation of the measurements was 34.38 kPa and the range of elastic modulus was from 35.81 kPa to 139.5 kPa. Both values are considered large compared to the mean, indicating a large amount of variability of the mechanical behaviour. This variability is also observed at the nanoscale in the measurements previously carried out in Chapter 4 and Chapter 5, suggesting that the variation in

mechanical properties is inherent in biological samples regardless of the length scale observed. A relationship between the nanoscale mechanical properties and macroscopic behaviour is thus suggested here and, indeed, expected.

The indentation uses a 1 mm diameter flat punch when contacting the skin and is an established macroscopic length scale measurement. The resulting elastic modulus recorded for the whole skin is anticipated as being derived from the mechanical properties of the dermis and the epidermis, with the elastic modulus value potentially a function of the contribution of each phase, or layer, to the overall mechanical response. The volume fraction of epidermis and dermis present must be determined in order to evaluate the individual contribution of each layer to the overall mechanical response. An approach is therefore used here to link the nanomechanical information, captured from AFM techniques in the last chapter, to macroscopic measurements by considering the structural composition of skin.

Histological techniques were used to analyse the structure of the skin samples used in this work. Analysis of the histological sections of the transverse CD1 mouse tail skin showed the whole skin to have an average thickness of 268.8 μm ± 29.99 μm (standard deviation, n = 20) with the epidermis having an average total thickness of 67.30 μm ± 13.17 μm (standard deviation, n = 40). Figure 6.2 shows a representative image of the H&E staining. The hair follicles of the tail skin are clearly visible within the section, denoted by black arrows in Figure 6.2. The regions of the skin where hair follicles were visible were not included in the measurements of the epidermal thickness because the region around the hair follicle is not representative of the thickness of the epidermis. The volume fraction of the epidermis within the whole skin was calculated using Equation 6.11 and Equation 6.12, using the average

values for the thickness of the whole skin and epidermis, and found to be V_E = 0.2503 or 25.03% of the whole skin volume is epidermis.

Several theoretical models for two phase composites have been previously discussed, specifically the Voigt-Reuss bounds, Equation 6.1 and Equation 6.2, and the Hashin-Shtrikman lower bound given by Equation 6.9 and Equation 6.10. These models were implemented to estimate the composite modulus but the elastic modulus of each component and the corresponding volume fraction of the components must be known. For the macroscopic indentation tests conducted, only the composite elastic modulus and the volume fraction of the dermis and epidermis are known. However, the previous chapter provides dermis and epidermis values that critically may provide a link between nanoscale mechanical behaviour of overall skin mechanics.

The modulus values obtained in Chapter 5 provide a unique approach to constructing a composite model for whole skin. Each data set for AFM indentations on transverse cross sections of skin contains elastic modulus values for both the dermis and the epidermis. Information about the fraction of each phase is therefore contained within the AFM data sets. The Voigt-Reuss model can be easily applied to each AFM data set by treating the individual elastic modulus values as individual components. The Voigt-Reuss model is modified to encompass all of the AFM data so that the Voigt model becomes

$$E_c = \sum_1^i \left(\frac{1}{n} E_i \right) \qquad \text{Equation 6.15}$$

and the Reuss model follows as

$$E_c = \left(\sum_1^i \frac{1/n}{E_i} \right)^{-1} \qquad \text{Equation 6.16}$$

where n is the total number of AFM indentations that were recorded, E_i is the individual elastic modulus value corresponding to a specific point within the data set, and E_c is the composite model. Equation 6.15 and Equation 6.16 are subsequently used to calculate the composite modulus of the whole skin and incorporates variations in mechanical behaviour across the measured area. The Voigt-Reuss bounds provide theoretical limits for the composite modulus of skin using a multi-phase composite model. The values of elastic modulus produced using Equation 6.15 and Equation 6.16 for each AFM data set are plotted in Figure 6.5 alongside the composite modulus value obtained from the macroscopic testing of whole skin.

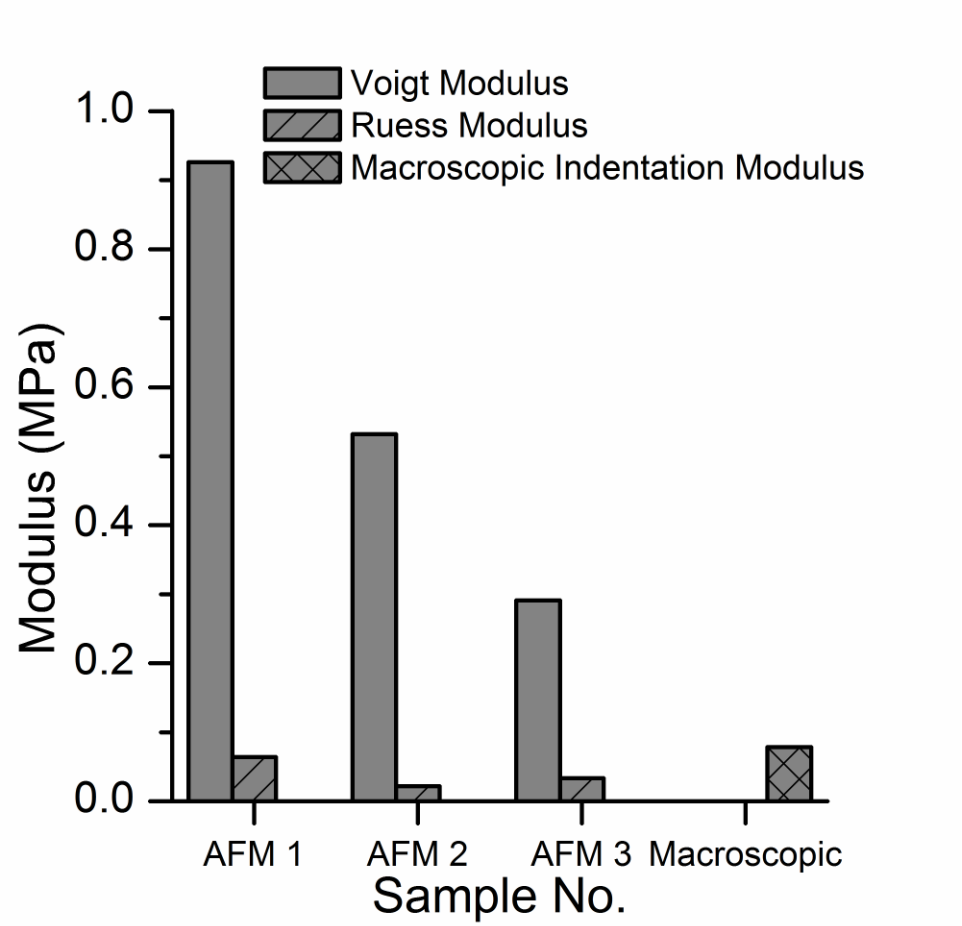

Figure 6.5. Bar chart of the composite elastic modulus calculated from the individual AFM measurements recorded from mouse cryosections. The Voigt model illustrates significantly higher predicted elastic modulus when compared to macroscopic measurements, while the Reuss model provides an improved estimation of the composite modulus.

Figure 6.5 indicates that the elastic modulus of skin is significantly overestimated using the Voigt model and consistently underestimated using the Reuss model when compared to the experimental macroscopic value. However, this simple approach fixed the epidermis and dermis volume fraction, which is unrealistic as different volume fractions of each phase are present throughout the tissue as shown in Figure

6.2 by the varying epidermal thickness throughout the cross section. An improvement to the approach is therefore to incorporate the volume fraction of each phase with the AFM mechanical data to provide a more accurate calculation of the composite skin elastic modulus. To achieve this, the elastic modulus data collected on the cryosections of mouse tail skin from Chapter 5 was plotted against the depth into the skin to evaluate the volume fraction of epidermis and dermis present within the measured area of the cryosection, as shown in Figure 6.6a, for one of the cryosection data sets.

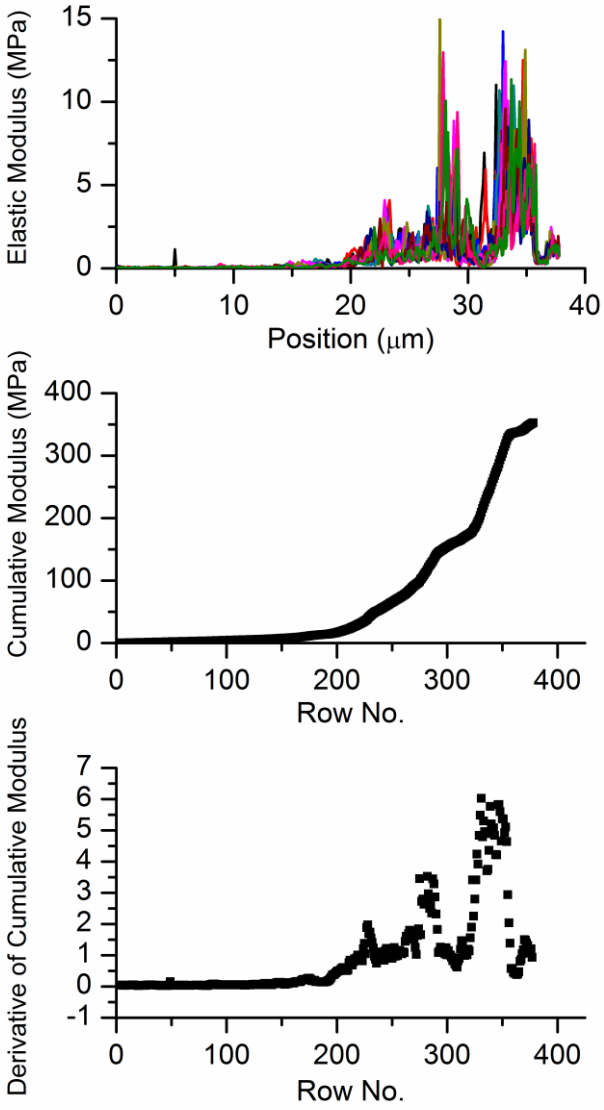

Figure 6.6. a) Plot of the elastic modulus with respect to the vertical position of the AFM indentation measurement with each curve representing the x axis location. The plots show a transition from low elastic modulus dermis from position 0 to higher elastic modulus values of the epidermis towards the edge of the sample. b) Cumulative elastic modulus plot, where the elastic modulus of each row as averaged and the cumulative elastic modulus plotted to highlight the transition point between dermis and epidermis. c) The derivative with respect to position of the cumulative elastic modulus to confirm the transition from dermis to epidermis.

Figure 6.6a shows a relatively low elastic modulus starting from within the dermis that significantly increases in value. The cumulative modulus in Figure 6.6b highlights the inflection lying beyond position 240, which corresponds to an epidermal thickness of approximately 24.0 μm. In conjunction the plotting the positional variation in the elastic modulus, a plot of derivative of the cumulative modulus with respect to position was produced to visualise the transition point between the epidermis and the dermis, as shown in Figure 6.6c.

The transition from dermis to epidermis allows an average elastic modulus for each phase to be calculated. Data points from line 0 to line 240 were used to define the dermis volume and a numerical average was used to give the elastic modulus for the dermis. The ratio of the number of data points taken for the average dermal elastic modulus over the total number of data points is used to provide the fraction of dermis for each AFM data set. The average elastic modulus of the epidermis is determined by the average elastic modulus of the remaining points in the data set. The average epidermal and dermal elastic modulus curves describing the Voigt and Reuss composite modulus behaviour can be constructed by taking an average value for the elastic modulus of the epidermis and dermis across all of the samples measured and calculating the composite elastic modulus for a given volume fraction of epidermis present. The average V-R bounding curves are shown in Figure 6.7 along with the composite elastic modulus of whole skin calculated from each individual AFM data set.

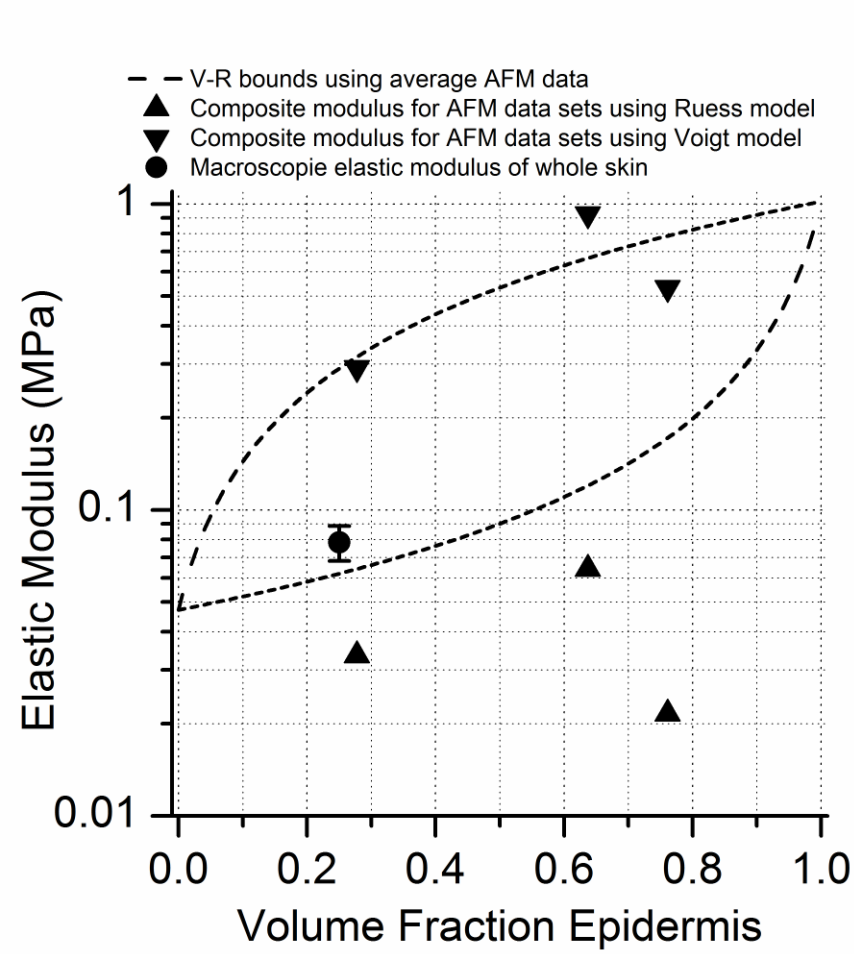

Figure 6.7. Elastic modulus versus volume fraction of epidermis plot indicating the variation between the average V-R bounds, the composite modulus calculated from the AFM elastic modulus measurements and the macroscopic measurement of whole skin.

The average V-R bound curves and composite elastic modulus values for the cryosection samples shown in Figure 6.7 illustrate that the V-R bounds are not suitable for estimating the composite modulus of skin from the AFM data sets. The V-R model predicts composite elastic modulus values for the AFM data sets that fall outside of the average V-R bound limits and display no dependence on volume fraction of epidermis. The poor prediction of elastic modulus for skin using Voigt-

Reuss bounds are derived from continuous fibre reinforced two phase composite materials where perfect stress transfer occurs between the fibres and the matrix (Hull and Clyne, 1996) and the force is longitudinal or transverse to the fibre direction resulting in an isostrain or isostress condition respectively, which is not the case within the structure of skin. Thus, the poor prediction of skin macroscopic mechanical properties using Voigt-Reuss approaches is perhaps expected. Hashin-Shtrikman bounds provide more general bounds for materials of arbitrary phase geometry (Hashin and Shtrikman, 1963). The Hashin-Shtrikman (H-S) bounds are derived in terms of the bulk modulus and the shear modulus. These additional parameters are calculated using the same average elastic modulus values used to calculate the Voigt-Reuss (V-R) bounds. The bulk and shear moduli are calculated for an AFM data set from Equation 6.7 and Equation 6.8 using values for the Poisson's ratio of 0.49, 0.499, and 0.4999 and then computing the H-S bounds, with Figure 6.8 detailing the plot of the bounds with the varying Poisson's ratio. Values of Poisson's ratio close to $\nu = 0.5$ are used as a boundary condition as $\nu = 0.5$ would cause the bulk modulus of each phase to tend to unity. Little deviation between the bounds when the Poisson's ratio is varied is observed in Figure 6.8 so that remaining calculations were carried out assuming a Poisson's ratio of 0.499.

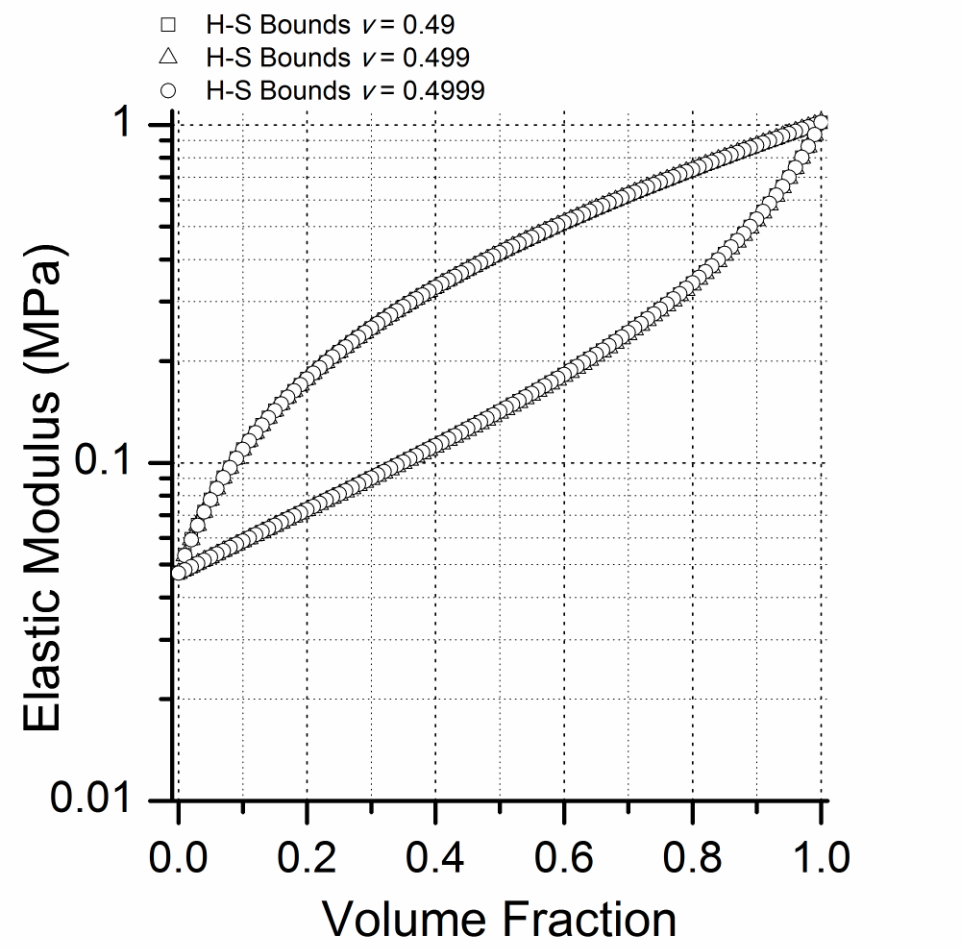

Figure 6.8. Elastic modulus versus volume fraction plot of a defined elastic modulus material with the composite modulus calculated using the H-S bounds illustrating little effect of varying the Poisson's ratio between 0.49 and 0.4999.

The functions describing the composite modulus as a function of volume fraction of epidermis were constructed using Equation 6.11 and Equation 6.12 as well as average elastic moduli of epidermis and dermis for all the cross section samples measured. The function describing the H-S bounds is plotted in Figure 6.9 alongside the data points representing the calculated lower bound for the individual AFM data sets and the macroscopic experimental measurements. The V-R bounds are also represented along with the data points showing the composite modulus calculated

from the Reuss model using the average modulus values for the epidermis and the dermis within each AFM data set.

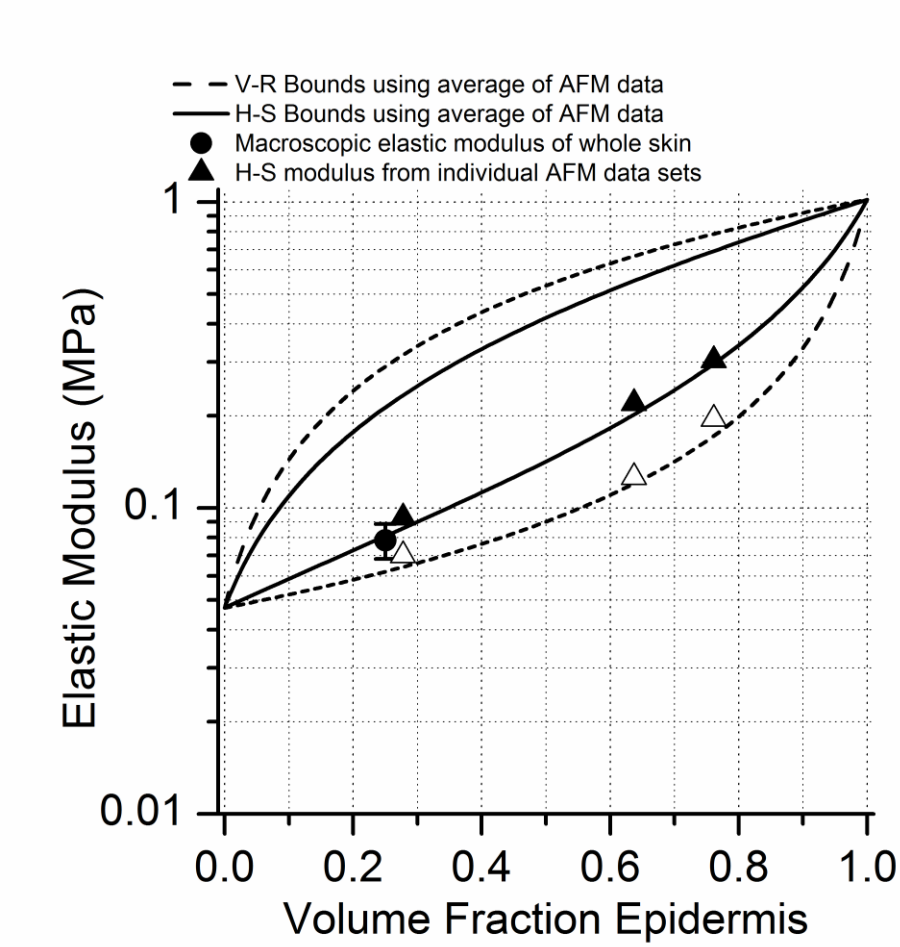

Figure 6.9. Elastic modulus versus volume fraction of epidermis plot for the H-S bounds applied to the average dermis and epidermis elastic modulus values from the AFM force-displacement measurements. Good agreement between the AFM measurements, the prediction from the H-S bounds and the macroscopic result is found. The V-R composite modulus for the average AFM data is also shown as the open triangles with the values still not representative of the macroscopic measurement.

Figure 6.9 shows agreement between the curve describing the lower H-S bound and the data points calculated from the individual AFM data sets with an R-squared value of 0.998. Additionally, the macroscopic measurement of the elastic modulus whole skin falls on the curve of the predicted composite elastic modulus. Comparatively, the V-R bounds also provide a good fit to the individual data points, R-squared value of 0.991. However the Reuss model underestimates the composite modulus of whole skin when compared to the experimental measurement of whole skin. This result indicates that the bulk mechanics of skin can be predicted through the measurement small volumes and the application analytical models, although through the application of the Hashin-Shtrikman estimation there is a loss of the spatial distribution of the elastic modulus data as averages of the epidermis and dermis must be taken. In order to include all of the spatial data information, more complex computational methods through finite element analysis were employed.

6.3.1 Finite Element Analysis

The FEA of a mechanically homogenous material was conducted in order to validate the boundary conditions being applied. Two materials of different elastic modulus were analysed, with the difference in elastic modulus being two orders of magnitude, 10 kPa and 1 MPa. These values of elastic modulus are of a similar order of magnitude to observations in the mouse tail cross sections for the dermis and the epidermis. The FEA provided an elastic modulus of 9.987 kPa and 1.00001 MPa for the homogenous 10 kPa and 1 MPa samples respectively, which gives an indication that the applied boundary conditions are suitable for analysing the elastic modulus of the sample under a compressive deformation. With the validation of a homogenous material satisfied, analysis of a two phase composite sample was conducted in order

to interpret how the FEA package describes composite materials. The results of the analysis of the elastic modulus of three composites with varying compositions of two phases are shown in Table 6.1. Included in Table 6.1 for comparison are the predicted composite moduli using the Reuss model and the Hashin-Shtrikman lower bound. The elastic moduli are displayed in Figure 6.10 as a plot against the volume fraction of the stiffer phase in addition to the functions describing the Reuss model and the H-S lower bound.

Table 6.1. Comparison of the predicted composite elastic modulus values using various methods with the finite element analysis result.

Fraction of 1 MPa phase	FEA elastic modulus (MPa)	H-S predicted elastic modulus (MPa)	Reuss predicted elastic modulus (MPa)
1	1.00001	1	1
0.8	0.072137	0.097127	0.048077
0.5	0.022719	0.033357	0.019802
0.2	0.013568	0.015954	0.012469
0	0.009987	0.01	0.01

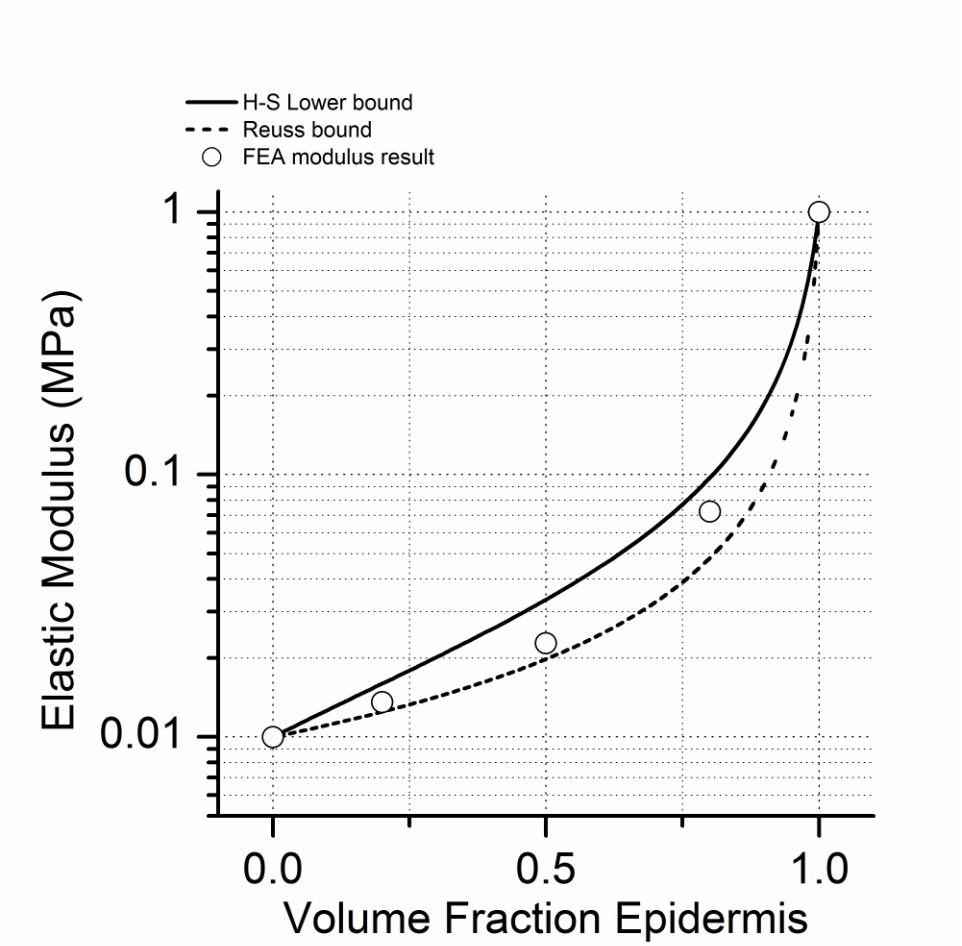

Figure 6.10. Skin elastic modulus results from the FEA of a predefined composite material illustrating that the finite element results fall between the V-R and H-S bounds for the composite elastic modulus.

The data in Table 6.1 and in Figure 6.10 show that the FEA is resulting in elastic modulus values that lie between the Reuss and H-S bounds. The elastic modulus of the validation mesh falling within the two sets of bounds indicates the boundary conditions applied to the model are sufficient.

Three FEA meshes were produced using the AFM data sets from the analysis of the cross sectioned mouse tail skin. The meshes produced included all the individual

elastic moduli from each point within the data set. The results of the FEA to determine the composite elastic modulus of the whole sample are shown in Figure 6.11 alongside the Reuss and H-S bounds from the average modulus of the dermis and epidermis.

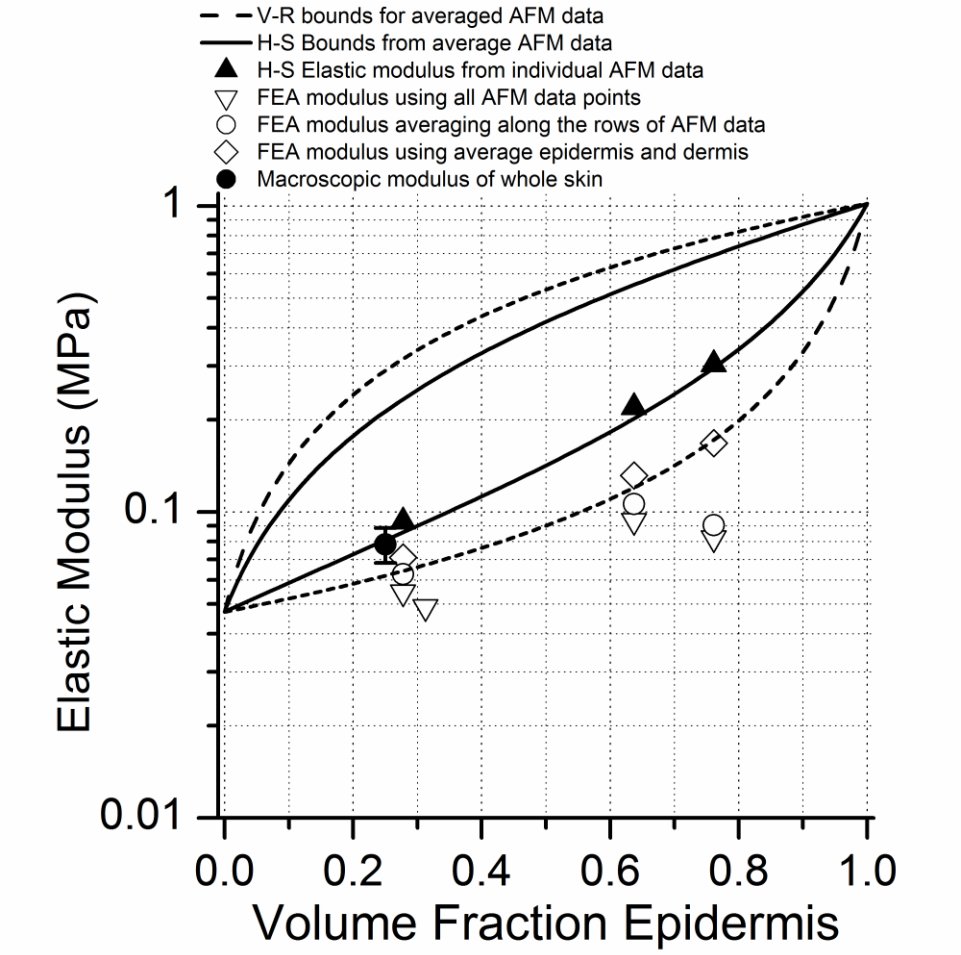

Figure 6.11. Plot of the results of the FEA from the meshes based on the AFM measurements. The results show FEA output that is significantly lower than the H-S and V-R models regardless of mesh complexity.

The open triangles represent the elastic modulus using the entire AFM data set and results in elastic moduli that are significantly lower than the Reuss model. The low

value of elastic modulus can be explained by the presence of significantly softer regions relative to the remainder of the mesh, as these regions will have greater deformations at much smaller loads. Therefore the applied deformation will be localised within these soft regions resulting in an analysis that is not inclusive of the entirety of the sample but rather a small percentage, so the elastic modulus value expressed from this model is not representative of the whole sample.

The main variations of the elastic modulus of skin occur through the thickness from the epidermis to the dermis. To maintain these variations in elastic modulus, while improving the FEA model, the average elastic modulus value was calculated along each row of the mesh. The average elastic modulus for the row was then assigned each element of that the row and the FEA was repeated. The elastic modulus values resulting from the FEA of the averaged row samples are shown in Figure 6.11 as the open circles. Figure 6.11 indicates a slight elastic modulus increase for rows compared to point considerations, but the contribution of the entire sample is not being included in the analysis. The model was simplified further by using only the overall average elastic modulus values for the epidermis and dermis as the material property inputs. For each sample the same number of elements, volume fraction, and dimension of the mesh were consistent and the FEA was conducted again.

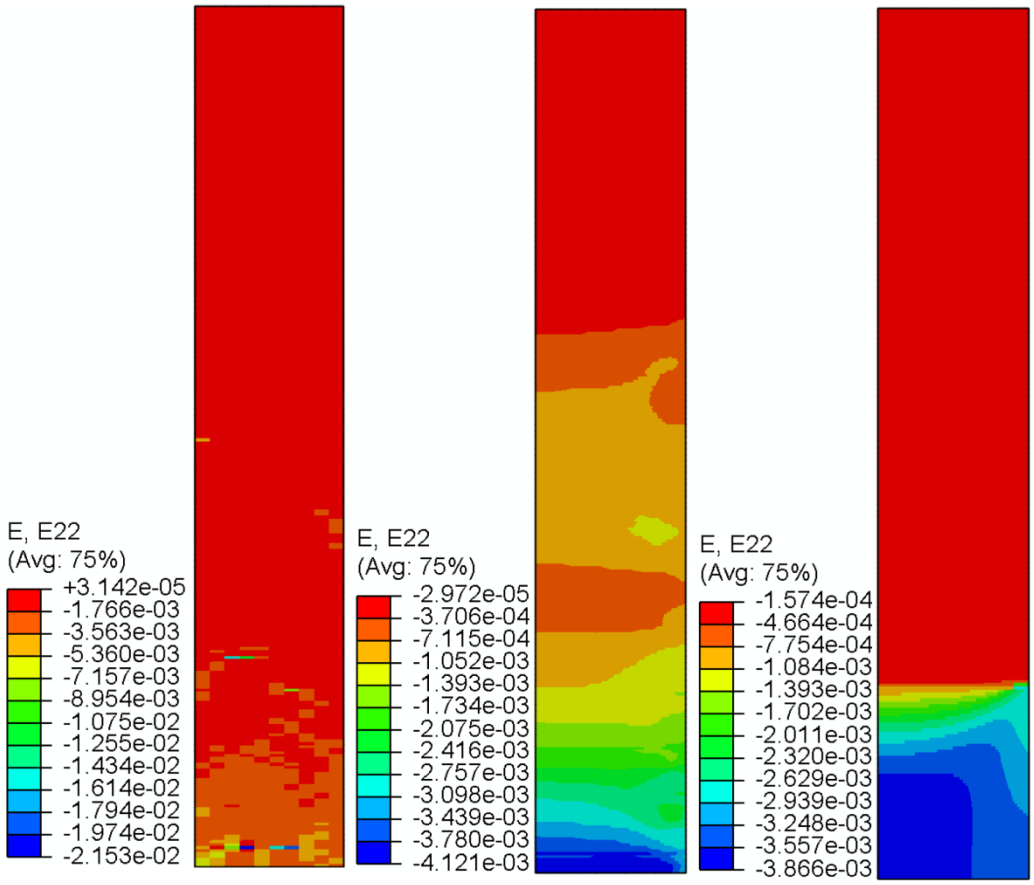

Figure 6.12. FEA result of the strain in the direction of the applied deformation. (left) the mesh using all of the AFM elastic modulus measurements where specific regions are displaying significantly higher deformation than the surrounding regions. (middle) the mesh using the average row value of elastic modulus and (right) the mesh using an average elastic modulus for the dermis and epidermis.

The effect of simplifying the model components can be seen in the overall strain in the direction of the applied deformation. Within the E22 deformation, as shown in Figure 6.12 for all three model types, the distribution of deformation behaviour is lost through the simplification of the elements to average elastic modulus values. The model including all of the individual elastic modulus data displays the regions where significant deformation is occurring relative to the surrounding region, further

highlighting the effect of the distribution of mechanical properties on the overall elastic modulus. Averaging across the rows of the mesh reduces the effect of the spatial distribution of the elastic modulus, with the maximum strain in the E22 direction being an order of magnitude lower when compared to the previous model. The simplification of the model to a two phase system further reduces the effect of location deformations. The reduction in the deformation of single elements by removing the spatial variation results in an increase in the composite elastic modulus of the model.

The elastic modulus results of the FEA with the simplified two phase models are represented by the open diamonds in Figure 6.11. The position of these results on the plot shows an increase in the calculated elastic modulus of the bulk sample and additionally the sample with a volume fraction of 0.76 shows a significant increase in elastic modulus. Although the FEA elastic modulus values lie within the Reuss bound, the values are still significantly lower than the macroscopic measurement and the H-S bound. The progressive simplification of the model and the resulting increase in elastic modulus indicates that the model is sensitive to the variations in mechanical properties distributed throughout the mesh. The relatively small volume being considered in the FEA compared to the macroscopic sample may be a contributing factor within the FEA resulting in an underestimation of the elastic modulus of a bulk sample. Asymmetric distributions of soft regions throughout a small volume would be compensated in a larger volume by surrounding stiffer regions but the soft regions are free to deform within a small volume sample. The volume of the sample was therefore considered as a parameter that could be used to improve the accuracy of the model.

Plotting the difference in elastic modulus between the predicted modulus from the Hashin-Shtrikman bounds and the modulus calculated from the FEA, for each of the cross section samples, against the total sample volume for each mesh is shown in Figure 6.13. The volume was taken as $V = \pi r^2 h$ from the axisymmetric model construction of the sample mesh. A fourth data set was produced by reducing the sample volume of the AFM data set with an epidermis volume fraction of 0.27 in order to further understand if there is a relationship between the total sample volume and the difference between the H-S model and the FEA.

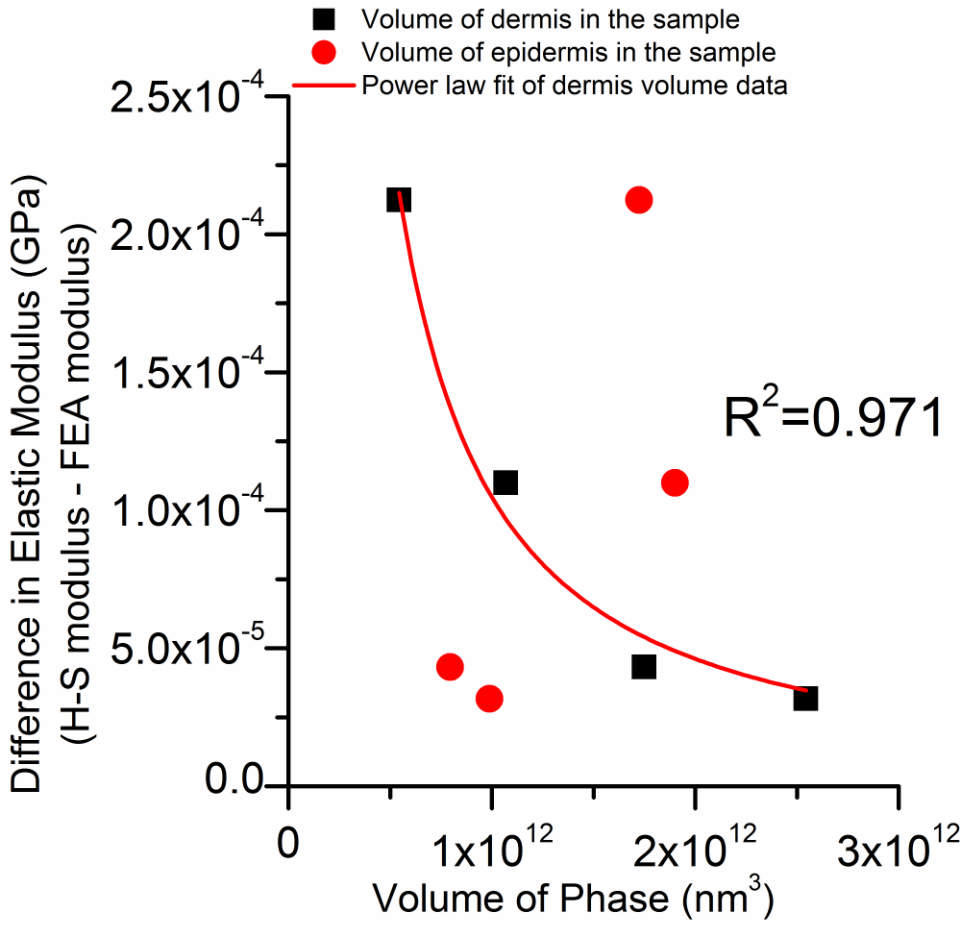

Figure 6.13. Plot of the difference in elastic modulus between the H-S model and the FEA result versus the total volume of each phase (epidermis and dermis) present in the mesh. Dependence between the difference in elastic modulus and the total volume of dermis is observed but little effect of the volume of the epidermis on the elastic modulus result is found.

Figure 6.13 indicates that there is no relationship between the total sample volume and the difference in the elastic modulus. The FEA results showed that the majority of the sample deformation was occurring within the region of the model representing the dermis. Plotting the difference in elastic modulus against the volume of the dermis within each sample, as shown in Figure 6.13, displays an effect of the volume

of the dermis on the elastic modulus produced from the FEA. Additionally, a similar plot of the volume of the epidermis against the difference in elastic modulus displays no correlation as represented by the red data points in Figure 6.13. No correlation between the difference in elastic modulus and the total volume of the sample or volume of the epidermis indicates that these two factors are not contributing to the resulting elastic modulus, where the volume of the dermis is shown to have a clear impact on the result of the FEA. The trend relating the volume of the dermis to the difference in the elastic modulus can therefore be used to calibrate the FEA model.

A power law function can be used to describe the trend between the volume of the dermis and the difference in elastic modulus, with the regression fit shown in Figure 6.13, with a corresponding adjusted R^2 of 0.971 given by,

$$c = 1.652 \times 10^{10} \cdot x^{-1.183} \qquad \text{Equation 6.17}$$

where c represents the difference in elastic modulus and x the volume of the dermis within the sample. The calibration factor for the FEA is calculated using Equation 6.17 based on the volume of the dermis and then added to the FEA elastic modulus using $E_a = E_0 + c$, where E_a is the initial FEA elastic modulus, c is the calibration factor based on the function of the total sample volume, and E_a is the calibrated FEA result. The physical representation of this calibration factor suggests that as the volume of the dermis tends to infinitely large volumes, the value of the calibration will approach zero, while as the volume of the dermis approaches zero the calibration function will increase and at a volume of zero the function breaks down. This asymptotic behaviour is appropriate as the model is assuming a two phase composite system where a zero dermis volume causes an invalid composite system, as the composite modulus cannot be predicted based on a one phase model.

Figure 6.14 shows the calibrated elastic modulus values against the H-S prediction with the plot showing the improvement in the elastic modulus from the FEA. The volume based correction factor improves the FEA result such that the elastic modulus values lie on the H-S curve predicting the composite elastic modulus of whole skin. This result indicates that there is a large contribution of the volume of the sample on the elastic modulus calculated from the finite element software. The larger sample volume therefore provides a FEA elastic modulus closer to the H-S bounds. Each individual measurement in smaller sample volumes provide a greater effect on the overall analysis such that a single uncharacteristically soft region could have a disproportionate effect on the calculated overall composite modulus. In the case for larger sample volumes, the individual regions are less likely to have an effect on the bulk mechanics and the FEA is more representative of the bulk system.

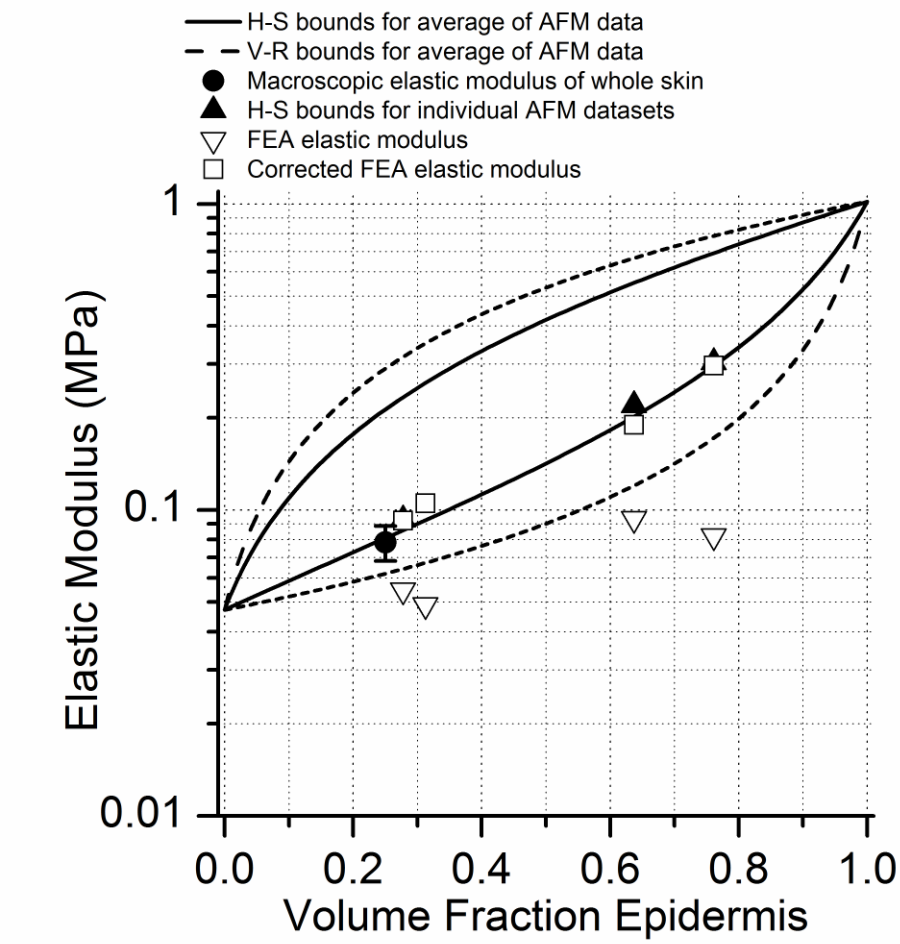

Figure 6.14. Plot of the elastic modulus versus volume fraction of epidermis indicating that the FEA model can be calibrated to the elastic modulus of whole skin from nanoscale AFM measurements.

The macroscopic indentation showing the whole skin elastic modulus lie on the H-S bound alongside the corrected FEA modulus, indicating this model can be used to predict the composite bulk elastic modulus under nanoscale deformations from the individual nanoscale AFM measurements. However, it should be noted that these results are only applicable to the linear elastic region of skin and are not representative of mechanical behaviour at higher strains. Subjecting skin to higher strains results in a non-linear response, which has been shown in this chapter using

flat punch indentation. This model also demonstrates the potential for using finite element analysis to predict the effect of local changes in the elastic modulus on the mechanics of the overall system within a specific range of nanoscale linear elastic deformation. For example, the local changes in a tissue could be due to disease or wounding that alter the mechanical properties of tissue at the nanoscale. These changes in elastic modulus could be substituted into the FEA model and used to predict the overall isotropic linear elastic modulus of skin in an altered state when sufficient samples may not be available for experimental testing.

6.4 Conclusions

Indentation measurements were conducted on whole skin samples from mouse tail at low strains to determine the macroscopic mechanical properties. High spatial resolution mechanical measurements of whole skin cryosections were used to predict the composite material behaviour using the Voigt-Reuss and Hashin-Shtrikman bounds. The elastic modulus predicted from the small volume measurements using the two-phase Hashin-Shtrikman bound agreed with the macroscopic mechanical measurements recorded. Finite element analysis was used to evaluate a complex multi-phase composite material with the computed elastic modulus showing a dependence on the volume of the soft dermis phase present within the model. Finite element analysis using a calibration gave an elastic modulus that showed good agreement with the experimental macroscopic result from small scale testing.

Chapter 7 – Electrospinning and cell culture

7.1 Introduction

The ability to quantify the spatial mechanical properties of skin has been demonstrated in previous chapters. This information provides an opportunity to consider the suitability of appropriate tissue scaffolds that can provide mechanical properties that mimic those of the native tissue. Polycaprolactone (PCL) is a common synthetic biodegradable polyester that has become commonly used in tissue culture scaffolds and is a candidate biomaterial in skin applications, and proposed in this chapter as a mechanical analogue to skin (Franco et al., 2011; Ghasemi-Mobarakeh et al., 2008; Kim, 2008; Tan and Teoh, 2007). PCL has been FDA approved for use in clinical applications such as slow release drug delivery and as a suture material (Woodruff and Hutmacher, 2010). PCL has a long degradation time period with bulk PCL having a total degradation period between 2-3 years (Nair and Laurencin, 2007). Processing PCL through electrospinning methods, where PCL is produced as fibres with diameter control from sub-micron to many microns, provides a potential method for constructing a suitable tissue engineering scaffold. PCL has been routinely electrospun into fibres by preparing solutions of the bulk polymer using a range of solvents including chloroform, dimethylformaide (DMF)/tetrahydrofuran

(THF), dichloromethane (DCM), trifluoroethanol (TFE), hexaflouro-2-propanol (HFP) and acetic acid/formic acid solutions (Bordes et al., 2010; Charitidis, 2011; Croisier et al., 2012; Denis et al., 2014; Gautam et al., 2013; Ghasemi-Mobarakeh et al., 2008; Liu et al., 2010; Zhang et al., 2005). The concentration of PCL in solution can range from 10-40 wt/v% (Cipitria et al., 2011). Electrospun scaffolds of PCL have been used for *in vitro* cell culture research using many different cell types including, but not limited to, human dermal fibroblasts (Zhang et al., 2005), mouse lung fibroblasts (Cipitria et al., 2011), and human epidermal keratinocytes (Chong et al., 2007). PCL scaffolds have also been developed for skin regeneration using dermal fibroblasts (Chandrasekaran et al., 2011).

One of the drawbacks of using PCL as a cell culture scaffold is the hydrophobic nature of the material. Hydrophobicity results in poor wetting behaviour and can lead to limited cell adhesion, affecting the viability of the structure as a cell culture scaffold (Zhang et al., 2005). The hydrophobic behaviour of PCL can be overcome by surface treating the polymer after electrospinning. Surface treatments generally used to alter the PCL surface chemistry are plasma treatment, chemical treatment, deposition of common ECM proteins, or combining bioactive components into the electrospun fibre network (Cipitria et al., 2011). PCL can also be combined with other synthetic or natural polymers to alter the properties of the fibres such as further improve the biocompatibility, change the degradation rate, or effect the surface wetting properties of the fibres depending on the requirements of the fibre. PCL is commonly combined with collagen, gelatin, or other biodegradable polyesters such as PLA (Cipitria et al., 2011) to define the degradation properties. Combining PCL with gelatin when electrospinning scaffolds improves the overall biocompatibility of the scaffold because gelatin is derived from collagen. Gelatin also has the effect

improving the liquid droplet wetting properties of electrospun scaffold. Ghasemi-Mobarakeh *et al.* have shown that the addition of gelatin, at a ratio of [70:30] (PCL/gelatin) with PCL in the electrospinning solution reduced the water contact angle from 120˚ on a scaffold of composed of only PCL, to 32˚ on the PCL/gelatin composite scaffold. The contact angle was further reduced to complete wetting, or 0˚, using a PCL/gelatin ratio of [50:50] (Ghasemi-Mobarakeh et al., 2008).

PCL/gelatin composites have been used frequently for developing a dermal replacement or wound dressing as both PCL and gelatin are biocompatible and affordable materials (Chong et al., 2007; Gümüşderelioğlu et al., 2011). The addition of gelatin or collagen to the electrospun fibre increases the biodegradation rate as shown by Gümüşderelioğlu *et al.,* and demonstrated a 20% loss in weight after 7 days, in PBS at 37˚C, of a PCL/gelatin scaffold compared to the PCL scaffold, which showed a negligible loss in weight (Gümüşderelioğlu et al., 2011). The increase in biodegradation rate is promising for a dermal substitute that can be remodelled and ultimately replaced by naturally produced extra cellular matrix material. Many of the studies conducted used scaffolds comprising of fibres with a diameter of 200-400 nm (Chong et al., 2007; Duan et al., 2013) and did not quantify the fibroblast migration into the scaffold. Increasing the electrospun fibre diameter could result in a larger pore size and promote further cell migration into the scaffold.

The mechanical properties of PCL/gelatin (50:50) scaffolds have been reported to lie in the 1.2-1.6 MPa range, when tested in dry conditions by uniaxial tension (Duan et al., 2013). Critically, the elastic modulus of electrospun PCL scaffold has not been assessed throughout the cell culture or within a hydrated environment as the presence of the cell culture environment may impact the mechanical properties of the scaffold (Duan et al., 2013). The mechanical properties of a PCL/gelatin scaffold therefore

require characterisation to understand the spatial changes in the mechanical environment at the nanoscale, with AFM indentation a suitable technique that provides mechanical information spatially. AFM indentation also provides mechanical evaluation of both the individual fibres and entire scaffold to ensure the properties of the scaffold are similar to the measured modulus values of a hydrated dermis. The elastic modulus is also obtainable *in vitro* by AFM indentation, and allows for analysis of the effects of biodegradation on the mechanical stability of the scaffold and any contribution of the cultured cells on the mechanics of the system.

The complex three dimensional microenvironment that fibroblasts are exposed to within the dermis is key to understanding the behaviour and activity of the cells (Lo et al., 2000; Rehfeldt et al., 2007; Saez et al., 2005; Solon et al., 2007). The introduction of a 3D environment leads to a significant change in cellular behaviour when compared with a flat 2D in vitro environment (Cukierman et al., 2001). Fibroblast migration, proliferation and signalling have shown marked differences *in vitro* when compared to a 3D cell derived matrix (CDM) and a flattened 2D CDM (Green and Yamada, 2007).Specifically, Green et al. showed human primary fibroblasts cultured in a 3D CDM had a proliferation rate that was double the rate of human fibroblasts cultured on a fibronectin substrate, and that cell migration within the 3D environment was more persistent and migrated at a higher velocity. Mesenchymal stem cell fate has also been shown to be directly influenced by the mechanical environment used to culture stem cells (Engler et al., 2006). The stiffness of the microenvironment or ECM is therefore critical in determining the behaviour of the cell and is expected to vary according to the 3D organization found in the dermis. CDMs provide an interesting platform for investigating the effects of a 3D environment on cellular behaviour as these naturally produced structures mimic the

in vivo characteristics of the stromal tissue present in the dermis (Ishikawa et al., 1997; Kutys et al., 2013). In situ analysis of the 3D microenvironment is important to understand the variations that may exist in the mechanical properties of different tissue culture scaffolds.

This chapter aims to further extend the mechanical analysis techniques established in the previous chapters. The link between the nanoscale mapping of mechanical properties to the bulk mechanics of a heterogeneous material has been developed and is extended here to investigate the mechanical properties of a tissue scaffold. The bulk material properties of a CDM/scaffold biocomposite can be estimated by using AFM spatial mechanical mapping over a small volume of the material to determine the suitability of engineered scaffolds as mechanical analogues to skin.

7.2 Materials and Methods

7.2.1Polymer Solutions

Polycaprolactone pellets (Sigma Aldrich, UK) with an average molecular number of 80,000 and type A gelatin from porcine skin (gel strength 300, Sigma Aldrich, UK) were used as the polymer base for the electrospun scaffolds. The polymer solutions used in this work were formed with a combination of acetic acid (glacial, Sigma Aldrich, UK) and formic acid (reagent grade, Sigma Aldrich, UK) as the solvent at a ratio of 9:1 (Acetic acid/Formic Acid). Acetic acid dissolves both PCL and gelatin separately, but combining the PCL and gelatin solutions lead to partial precipitation of the gelatin. The addition of formic acid aids in the dissolution of the gelatin into solution and decreases the apparent viscosity of the solution, which is important in allowing electrospinning of the solution. Acetic acid and formic acid were selected

over other solvents, such as hexafluoroisopropanol and trifluoroethanol, to reduce the risk of residual toxic solvent being released from the electrospun scaffolds during the cell culturing process. The polymer solutions of PCL and gelatin are prepared separately and mixed under forced agitation using a magnetic stirring bar until no particulates of the base polymer are observed within the solutions. The polymer solutions were prepared in two weight percentage concentrations of 15.5 w/w% and 17.5 w/w%. The gelatin solution was then added to the PCL solution to form a PCL/gelatine solution at a ratio of 8:2 (PCL/gelatin).

7.2.2Electrospinning

Electrospinning was used to generate the desired nanofibre scaffold. Electrospinning is the process that applies an electric field to a polymer solution under constant pressure to form a charged jet of polymer. The polymer jet is then drawn towards a collector substrate by the force of the electric field. Solid polymer fibres are produced as the solvent of the polymer solution evaporates during deposition as a random nonwoven sheet onto a collector substrate (Doshi and Reneker, 1995; Reneker and Chun, 1996).

A custom built electrospinning setup using a single needle in a vertical orientation was used and is schematically shown in Figure 7.1.

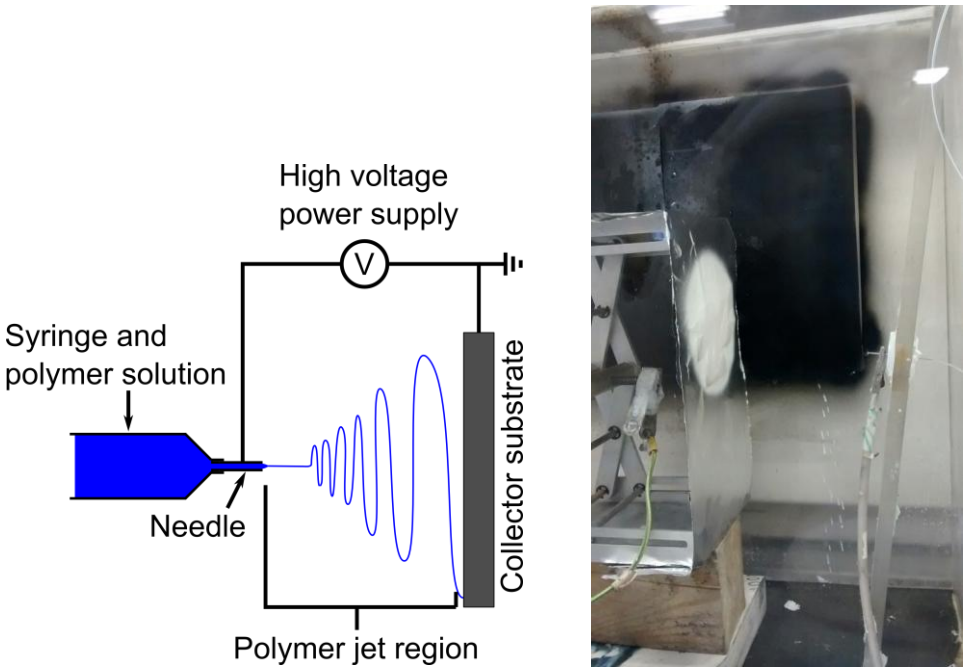

Figure 7.1. (Left) Schematic of the electrospinning setup where the polymer solution is fed through a needle at a controlled rate and the voltage is applied directly to the needle with a metallic ground collector plate. (Right) Photo of the electrospinning setup with the sample target on the left and the needle on the right. The distance between the needle and the target is approximately 20 cm.

A horizontal electrospinning setup was used to avoid the possibility of any solution droplets falling from the needle onto the electrospun fibre mat and dissolving regions of the fibres (Blackwood et al., 2008; Cipitria et al., 2011; Li et al., 2002).

The polymer solution was supplied at a constant flow rate of polymer solution to the needle through PTFE tubing from a syringe pump (Genie, Kent Scientific, UK) located outside of the electrospinning chamber. High voltage was applied between the needle and the target substrate, typically square sheets of aluminium, by directly attaching the voltage supply (FC Series, Glassman High Voltage Inc., USA/EU)

between the needle and the target. The substrate used in this work was an aluminium sheet approximately 15 cm x 15 cm x 0.1 mm. Each polymer solution required a specific set of electrospinning parameters including the applied voltage, flow rate, and total time of electrospinning that are shown below in Table 7.1. The two different solution concentrations were electrospun for at least 2 hours in order to produce relatively thick (>0.5 mm) scaffolds that would not deform when removed from the aluminium substrate.

Table 7.1. Electrospinning working conditions applied to two PCL/gelatin polymer solutions used for tissue scaffolds.

Polymer Solution	**Working Distance (cm)**	**Applied Voltage (kV)**	**Flow Rate (mL/hr)**	**Relative Humidity**
15.5 w/w%	~20	~23.0	1.0	~25%
17.5 w/w%	~20	~23.0	1.0	~22%

The electrospinning process typically produces nanometre sized fibres in a dense nonwoven network. The nanofibre network produced was difficult to observe using light microscopy as the fibre dimensions are approaching the diffraction limit of optical microscopy. Therefore, scanning electron microscopy (SEM) was employed as the imaging technique for characterising the electrospun scaffolds.

The scaffolds are produced from polymers, which only contain low atomic number elements (carbon, oxygen, hydrogen, nitrogen and sulphur) that do not yield many secondary electrons when exposed to the electron beam of the SEM. A gold/palladium coating was applied to the surface of the scaffold in order to improve

the electron yield without distorting the dimensions of the polymer fibres using an Agar Auto Sputter Coater (Agar Scientific, UK). The Ag/Pd coating was sputtered onto the surface and was approximately 4 nm thick. Imaging of the scaffolds was conducted using SEM with an accelerating voltage of 5 kV, 3.5 spot size, and a working distance of 10 mm. Images were captured using secondary electrons at several different magnifications in order to observe the topography and dimensions of the fibres produced. For quantification of the fibre diameter, six images taken at 20,000x magnification of random areas of the scaffold were captured for each scaffold and at least 50 individual fibres were measured per image, providing a distribution of the fibre diameter across the scaffold. The individual fibre diameters were measured using ImageJ (NIH, USA) by counting the number of pixels across the width of the fibre perpendicular to the long axis of the fibre and using the calibration scale of the SEM image to convert the number of pixels into a length in micrometres.

7.2.3Cell culture

The cell culturing and maintenance of the cells was carried out by Georgios Theocharidis at the Centre for Cell Biology and Cutaneous Research, Barts and the London School of Medicine and Dentistry, Queen Mary University of London. Human foreskin dermal fibroblast HCA2 cell line immortalised with human telomerase reverse transcriptase (hTeRT) were cultured in T75 polystyrene culture flasks with Dulbecco's Modified Eagle's Medium (DMEM) containing GlutaMAX^{TM} (Gibco, Invitrogen, Paisley, UK), 10% fetal bovine serum (FBS) (labtech.com, Uckfield, UK) and 1% penicillin and streptomycin (Gibco, Invitrogen) at 37°C in a humidified atmosphere of 5% CO_2/95% air (Stephens et al., 2004). The

culture medium was changed every two to three days and the cells were passaged at 70 to 80% confluency.

Polystyrene cloning rings were attached to the scaffold surface to ensure that fibroblasts only attached to one surface of the scaffold during cell seeding. An illustration of the positioning of the rings and seeded cells is shown in Figure 7.2.

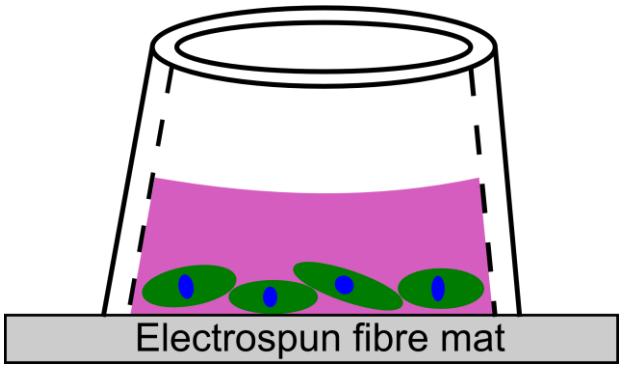

Figure 7.2. Illustration of the cloning rings used to confine the cell seeding to one surface of the electrospun scaffold. The green regions denote the cell area with the nuclei coloured blue. The pink region represents the cell culture media contained within the cloning ring.

The cloning rings were attached to the scaffolds by depositing a thin layer of petroleum based grease and pressing the ring onto the scaffold surface. The rings deformed the edge of the scaffold where pressure was applied to ensure adhesion between the rings and the scaffold. However this region of deformed scaffold edge was not considered when any further analysis was conducted.

The scaffolds and cloning rings were sterilised prior to seeding the cells to the scaffold surface. The sterilisation process is outlined in Table 7.2 and all the steps were carried out in a sterile laminar flow cabinet. This process is necessary as the cell culture environment should be free of any external contamination that may have an effect on the behaviour of the cells or cause an infection of the culture. After the sterilisation process was complete, the scaffolds were stored in a 12 well cell culture plate in PBS sealed with parafilm at 4˚C until the cells culture studies were initiated.

Table 7.2. Sterilisation protocol applied to the electrospun fibre scaffolds prior to seeding fibroblasts onto the scaffold surface.

Procedure	**Time**
UV light exposure	30 min
100% Ethanol	30 min
Air dry	30 min
Wash with PBS	3x

HCA2 dermal fibroblasts were plated at a density of 60,000 cells per well and cultured overnight in 37°C, 5% CO_2 to achieve full confluency by next day. Media supplemented with 50 μg/ml ascorbic acid (L-ascorbic acid, Sigma-Aldrich) was added and subsequently changed every two days. Cells were cultured for 7 days to create their own ECM structures, which serves as a tissue scaffold analogue (Cukierman et al., 2001; Ishikawa et al., 1997). The addition of ascorbic acid promotes the synthesis of collagen by fibroblasts in culture (Murad et al., 1983). Scaffolds were removed and prepared for mechanical analysis following the 7 day

culture procedure. The scaffolds were cross sectioned using the procedure outlined in Chapter 3, with the cryosections cut to a thickness of 10 µm. Cross-sectioned scaffolds provided a surface of the electrospun scaffold with the addition of the CDM, where both layers and the interface between them could be mechanically probed using AFM. Six samples were produced for cell culture and the experiment of producing CDM on electrospun scaffolds was repeated three times for both of the electrospun scaffolds using PCL/gelatin concentrations of 15.5 w/w% and 17.5 w/w%,.

The CDM could not be differentiated with clarity using optical microscopy due to the thickness of the electrospun scaffold so immunofluorescence microscopy was employed as the method for observing the CDM. Fibronectin (FN) was selected as the primary protein for identifying the thickness of the CDM as FN is produced throughout the CDM by fibroblasts (Cukierman et al., 2001). Cryosectioned samples were first fixed using 4% PFA in PBS for 10 min at room temperature and then rinsed in PBS. Permeabilisation of the sections was then conducted using a 0.2% triton X-100 (Sigma Aldrich, UK) solution for 10 minutes and then rinsed in PBS. The samples were subsequently incubated with a blocking buffer of 4% bovine serum albumin (Sigma Aldrich, UK) for 1 hour at room temperature and further incubated with the primary antibody overnight at 4˚C in a humidified chamber. The primary antibody used was anti-fibronectin extracted from a rabbit (Sigma Aldrich, UK). The samples were rinsed several times in PBS and incubated in the secondary antibody solution, Alexa Fluor 555 goat anti-rabbit (Life Technologies, UK), for 1 hour at room temperature in a dark environment. Samples were further stained with Alexa Fluor 488 phalloidin (Life Technologies, UK) and DAPI (Sigma Aldrich, UK) to highlight the F-actin cytoskeleton and the nucleus respectively to identify the

regions of the samples comprised of cells. Samples were then rinsed in PBS three times followed by one rinse of distilled water and a cover slide was attached using polyvinylalcohol based Mowiol mounting media. Images of the CDMs were acquired on a Leica MM DM4000 microscope using MetaMorph software at 10x and 20x magnifications. The thickness of the CDM was identified as the region of the fluorescence image where the FN staining was present and quantified using ImageJ. The ImageJ line tool was used to manually measure the thickness of the CDM. For each PCL/gelatin concentration, three samples were imaged and six images of random areas across the samples were acquired. For each of the six images, at least 50 measurements of the CDM thickness were conducted

Degradation of the PCL and resultant dimensional changes to the electrospun nanofibres was assessed using SEM. Portions of the scaffold were incubated in cell culture media at 37˚C for 7 days without the addition of cells. At days 1, 4, and 7 separate Samples were removed and prepared and imaged using SEM to measure the diameter of the fibres within the scaffold. For each section of scaffolds, 6 images were taken at 20,000x magnification and 30 fibres were measured per image. We note that the same image evaluation method was used to define both the initial electrospun fibre diameter and variation of fibre diameter due to degradation, thus allowing comparisons to be made.

The elastic modulus of the cryosectioned electrospun fibre mat with CDM was analysed using the in situ AFM indentation technique established in Chapter 5. V-shaped Si_3N_4 AFM probes (Bruker, EU) with a spring constant between 0.01 $N.m^{-1}$ and 0.5 $N.m^{-1}$ were used for imaging and AFM indentation. The AFM probe was positioned over a random area of the cross section and a 50 µm by 50 µm area was imaged using contact mode. The edge of the sample was included within the imaging

area to ensure the entirety of the CDM was included. A continuous section within the imaged area was selected to perform AFM indentation over with dimensions of 5 µm by 10-15 µm where the long dimension was orthogonal to the electrospun/CDM interface. The AFM indentations were conducted over the entire CDM and into the electrospun fibre mat. The indentations were spaced at 100 nm intervals along the long dimension and 500 nm intervals along the short dimension. The indentations were performed with a tip velocity of 2 $\mu m.s^{-1}$ with the indentation depth limited to 300 nm. The force-displacement curves conducted on the cryosection samples showed no evidence of probe tip to sample adhesion during the unloading curve. Therefore, the curve fitting analysis outlined in Chapter 3 was applied to the force-displacement curves to determine the elastic modulus electrospun fibre/CDM composite.

7.3 Results and Discussion

The electrospinning process was successfully used to produce nonwoven nanofibre substrates using two different weight percent polymer solutions. Continuous fibres were produced without the presence of any significant geometric defects such as beading, ribbon-like structures or fibre splitting. Figure 7.3 shows a representative SEM micrograph of fibres produced from each polymer solution. Larger fibre diameters spun from the higher polymer concentration solution can be observed qualitatively in Figure 7.3, with SEM micrographs used to quantify the average diameter of the fibres produced from each polymer solution. The distribution of fibre diameters is shown in Figure 7.4.

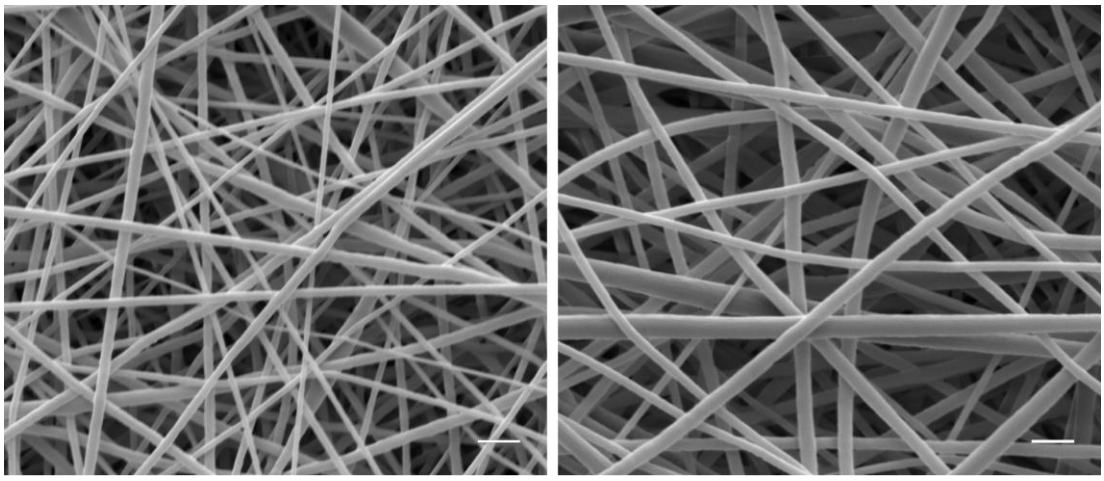

Figure 7.3. SEM micrograph of the (left) fibres electrospun from the 15.5 w/w% solution and (right) fibres electrospun from the 17.5 w/w% solution providing increased fibre diameter. Scale bar 1 µm.

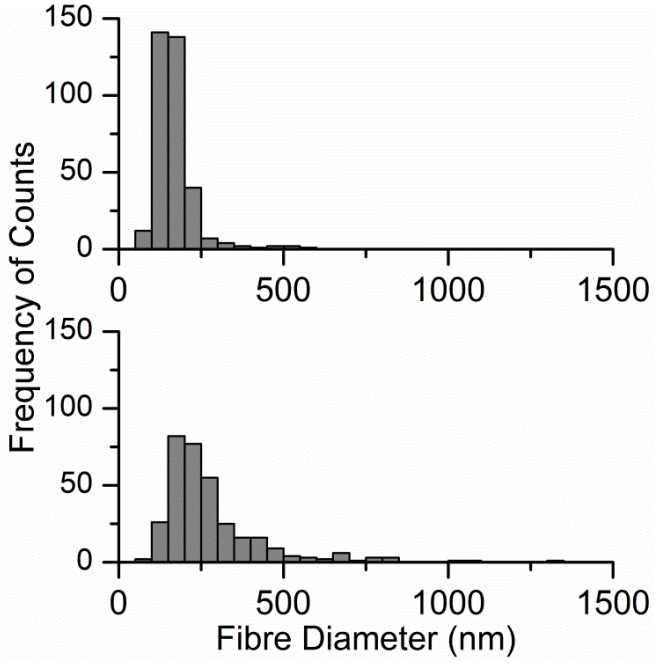

Figure 7.4. Histogram of the frequency of counts for the fibre diameter of each polymer solution with the (top) 15.5 w/w% solution showing a narrower distribution of fibre diameters when compared to the n = 350 (bottom) 17.5 w/w% polymer solution n = 333.

The electrospinning of the 15.5 w/w% PCL/gelatin solution resulted in a mean fibre diameter of 167.1 nm ± 63.69 nm (mean ± standard deviation, n = 350), and the 17.5 w/w% PCL/gelatin solution resulted in a mean diameter of 280.7 nm ± 159.5 nm (mean ± standard deviation, n = 333). The fibre distributions shown in Figure 7.4 and the mean values of the fibre diameter indicate a difference between the fibres produced from the two polymer solutions, with the difference in the mean fibre diameter being statistically significant (Student's T-Test, $p < 0.01$). The distribution and the standard deviations indicate that the 17.5 w/w% solution, while resulting in larger diameter fibres, also provide a wider distribution of fibre diameters. The increase in fibre diameter is expected to be due to the increase in the weight percent of polymer present in the electrospinning solution as all other electrospinning conditions remained constant throughout the production of the fibre scaffolds.

The degradation behaviour of the fibres is shown in Figure 7.5, with fibres exposed to the cell culture environment produced at the same time as the fibres initially measured by SEM. The degradation was measured as the change in the mean fibre diameter over the course of 7 days, which was the same time period selected for the culturing of fibroblasts for the production of a CDM. The changes in the value of the mean fibre diameter are shown in Table 7.3. The 17.5 w/w% fibres showed an overall decrease in diameter and the 15.5 w/w% appears to remain at a constant diameter, but over the 7 days there was no significant change in the mean fibre diameter in either the 15.5 w/w% or 17.5 w/w% fibre mats. Indeed, minimal changes in fibre diameter were expected, as observed, as bulk PCL is reported to take up to several years to significantly degrade (Nair and Laurencin, 2007). The work here adds gelatin to the PCL but this appears to have little effect as no initial increased degradation behaviour of the fibres is observed in Figure 7.5 or Table 7.3.

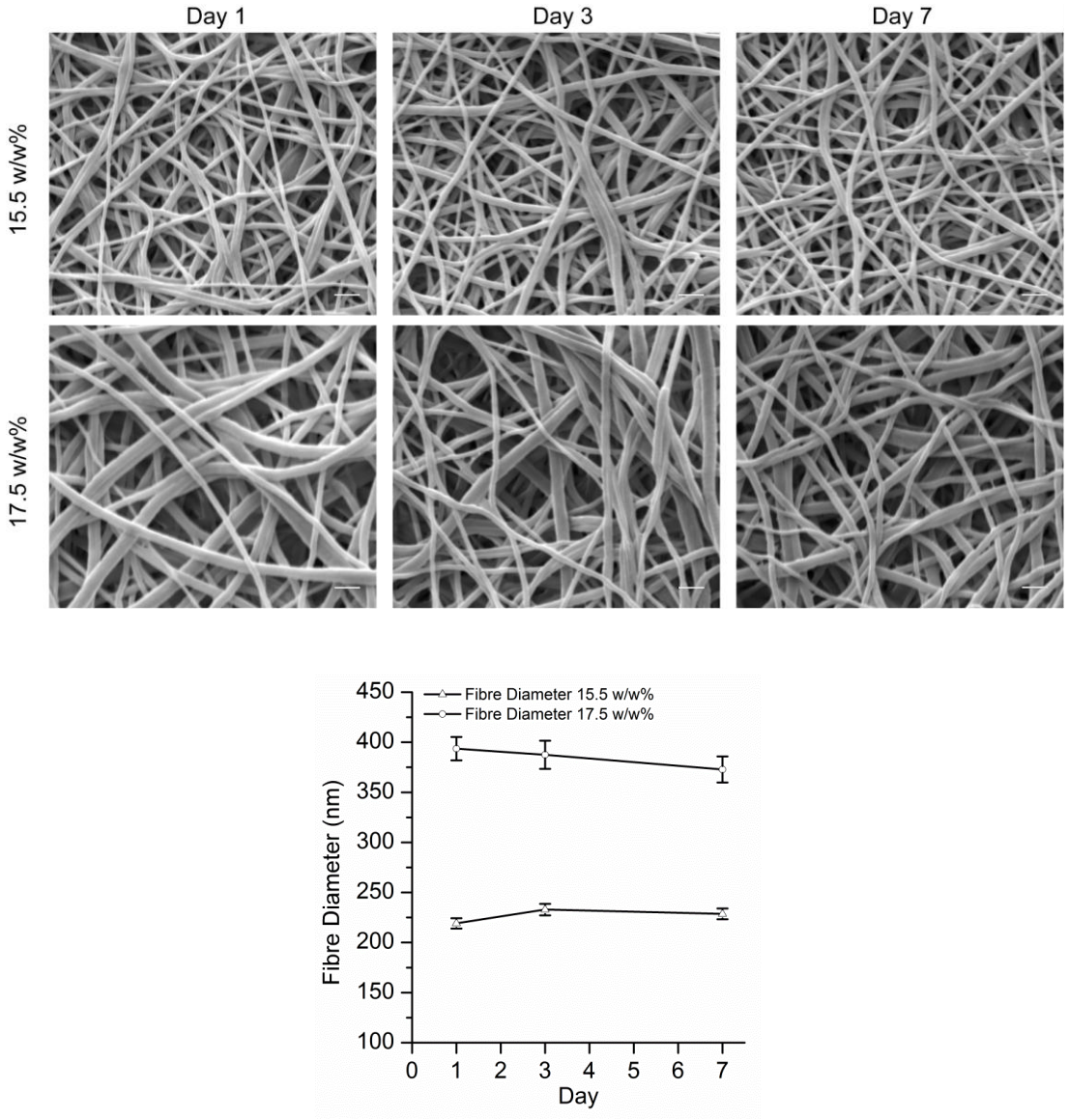

Figure 7.5. (Top) SEM images showing the effect of the cell culture environment on the structure of the nanofibre scaffold after 1, 3 and 7 days, scale bar 1 µm. (Bottom) quantitative analysis of the fibre diameter versus time with the error bars showing standard error of mean ($n \geq 30$ for each time point), with the open circles showing fibres spun from the 17.5 w/w% solution and the open triangles showing fibres spun from 15.5 w/w% solution.

Table 7.3. Fibre diameters for each polymer solution shown as mean ± standard error of mean.

	Day 1	**Day 3**	**Day 7**
15.5 w/w% Fibre diameter (nm)	219.2 ± 5.175	232.9 ± 5.778	228.6 ± 5.432
17.5 w/w% Fibre diameter (nm)	393.6 ± 11.62	387.5 ± 14.12	372.8 ± 12.96

A qualitative change between the initial state of the fibres, when observed before incubation in cell culture media, and the fibres observed after 24 hours of incubation can be considered in Figure 7.5 despite no significant change in the diameter of the fibres over the 7 day period recorded in Table 7.3. Fibres exposed to the cell culture environment appeared curved and bend in Figure 7.5, compared to the control fibres, which appear straight and non-deformed. The lack of significant change in the fibre diameter over the duration of the cell culture time period indicates that a stable fibre scaffold has been produced and can be used to evaluate the effect of nanofibre diameter on the extracellular matrix produced by fibroblasts.

The culturing of fibroblasts on a nanofibre scaffold was carried out in order to produce an engineered biological sample that could be evaluated mechanically at the nanoscale using AFM techniques. The CDM produced by the fibroblasts over the culturing period was observed by fluorescence microscopy, with a representative image of the cross sections of the fibre scaffold and CDM shown in Figure 7.6. The region of each cross section with the higher fluorescence intensity is the fibronectin

staining that was used to define the thickness of the CDM. All of the images captured displayed autofluorescence of the fibre scaffold so thresholding of the images was conducted prior to evaluation of the CDM thickness, as shown by the binary images in Figure 7.6. The CDM thickness was quantified and the results are shown in Figure 7.7. Thicker fibres produced from the 17.5 w/w% polymer solution resulted in an overall increase in the mean thickness of the CDM when compared to the CDM thickness on the fibres produced from the 15.5 w/w% polymer solution (Student's T-Test, $p < 0.001$, N = 3). The composition of the fibre mats electrospun from the two PCL/gelatin solutions are the same, with the ratio of PCL/gelatin constant at 8:2, so the variation in the CDM thickness is expected to be from the effect of the diameter of the fibres within the scaffold or the mechanical properties of the scaffold. Additionally, each scaffold showed no evidence of significant migration of the cells into the scaffold indicating that the spacing between the fibres is not sufficient to allow cell mobility throughout the scaffold.

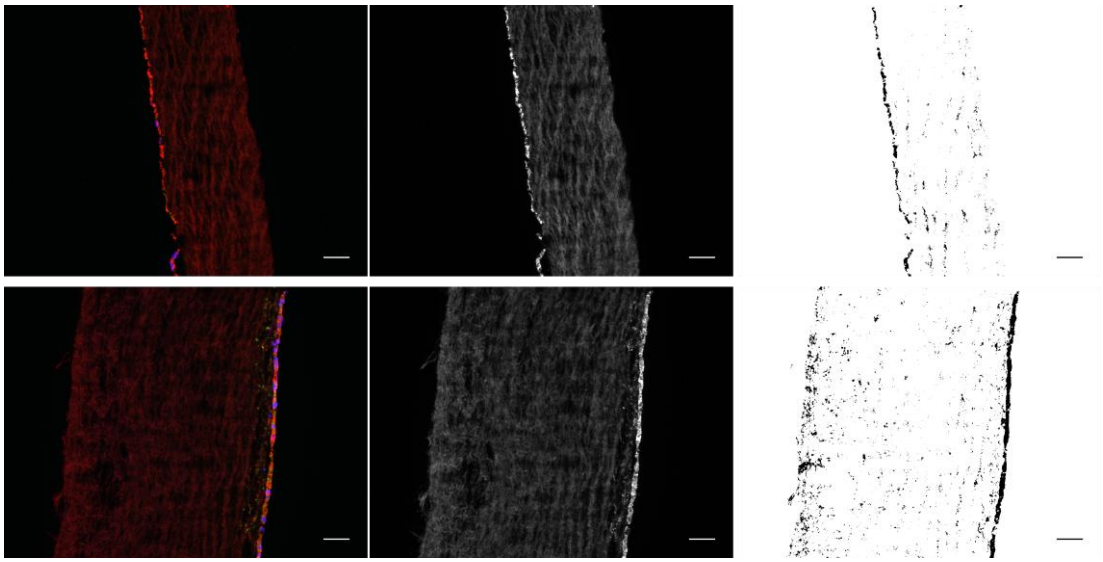

Figure 7.6. Immunofluorescence staining for fibronectin (red), phalloidin (green) and DAPI (blue) of the (top) 15.5 w/w% fibre scaffold with CDM and of the (bottom) 17.5 w/w% fibre scaffold showing the difference in overall thickness of the nanofibre scaffold. Scale bar 100 µm.

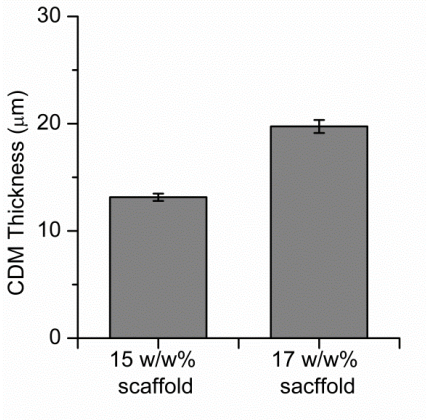

Figure 7.7. Bar chart of the CDM thickness in µm as measured from the fibronectin staining, represented as mean ± standard error of mean. (n = 220 for each bar)

The CDMs were also observed by SEM to evaluate the surface morphology with secondary electron images shown in Figure 7.8. The SEM images showed the CDM

deposited as a continuous layer on the nanofibre scaffold. The cracked regions within the SEM image are likely due to the dehydration process used during sample preparation. At higher magnifications, evidence of fibroblasts and CDM located beneath the some of the nanofibres of the scaffold is found, suggesting some degree of penetration of the cells into the scaffold although this penetration is not of a large enough magnitude to be observed using optical microscopy techniques.

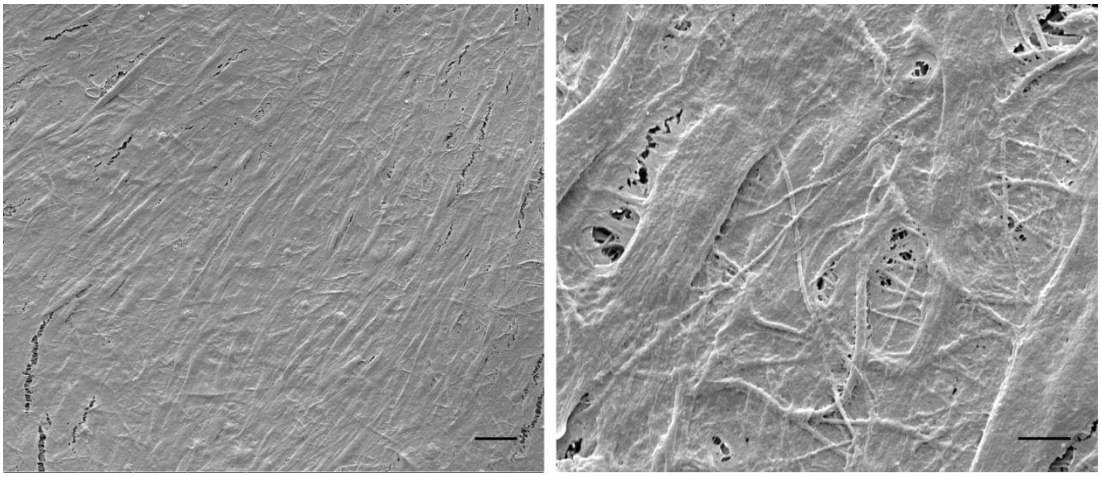

Figure 7.8. SEM images of the CDM deposited on the electrospun nanofibre scaffold. Scale bar (left) 20 μm and (right) 5 μm.

Fibroblasts at the surface and within the nanofibre scaffold provide a region of interest to examine tissue mechanical behaviour. Specifically, the use of electrospun fibres to promote tissue growth also requires replication of mechanical properties found in the native tissue that is being replaced. This region can therefore be characterised using the AFM techniques that were employed to measure the elastic modulus of the whole skin cryosections. Typical AFM height images of the cryosections for the CDM and scaffold samples are shown in Figure 7.9.

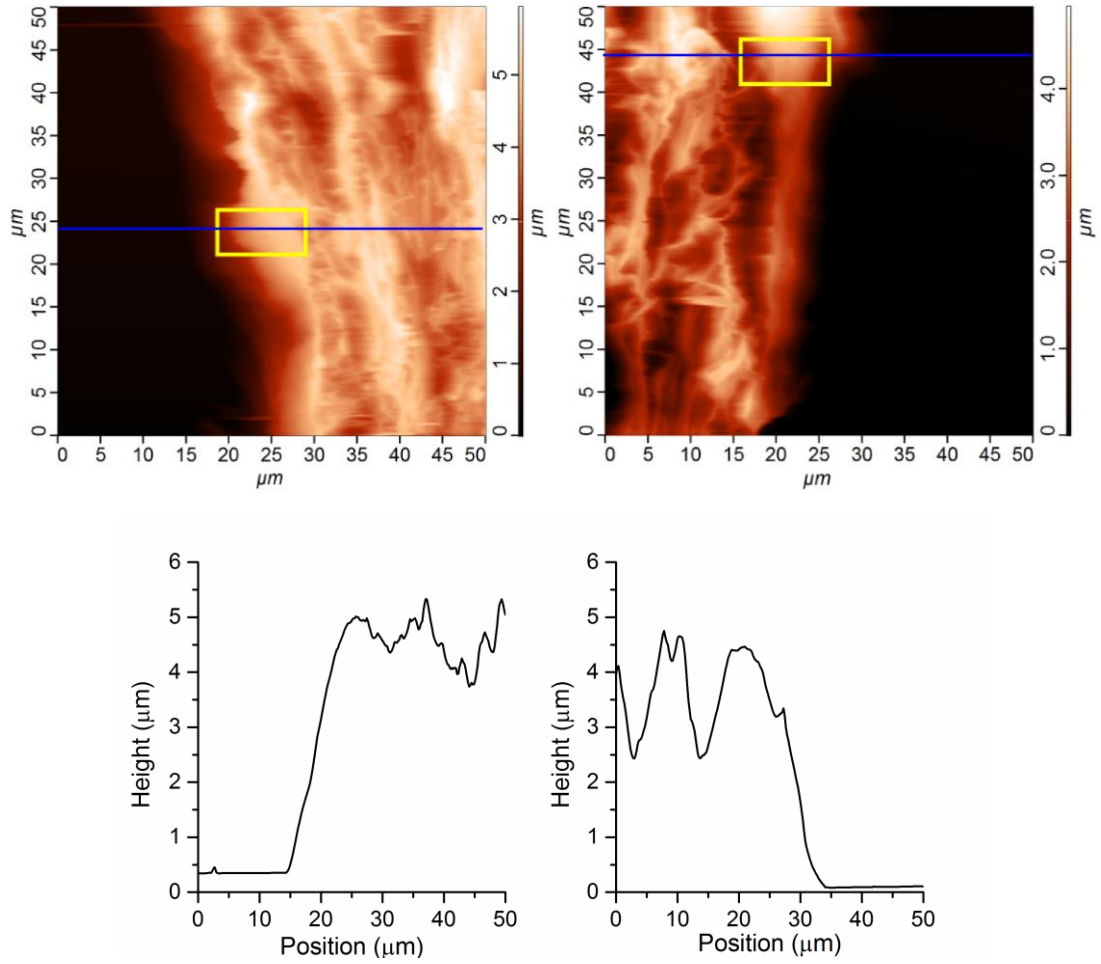

Figure 7.9. (Top) AFM height images captured in low set point contact mode of the cryosections of (left) CDM deposited on the scaffold electrospun from the 15.5 w/w% solution and (right) showing the CDM deposited on the scaffold electrospun from the 17.5 w/w% solution. The yellow box indicates the regions selected for mechanical analysis using AFM indentation. (Bottom) AFM line scans corresponding to the blue lines in the above AFM height images. Within the line scans there is a clear drop off between the cryosection and the glass slide.

The AFM height images in Figure 7.9 correlate with the SEM images in Figure 7.8, such that the CDM region appears continuous along the surface of the scaffold. The mechanical analysis conducted only considered the continuous regions of the sample,

highlighted in Figure 7.9, as performing nanoindentations in the porous fibrous would deform the fibres in a complex manner, such as fibre bending or AFM tip sliding into spaces between the fibres, requiring non-continuum mechanical analysis not considered here.

AFM-based nanoindentation of the regions shown in Figure 7.9 produced force-displacement curves indicated in Figure 7.10.

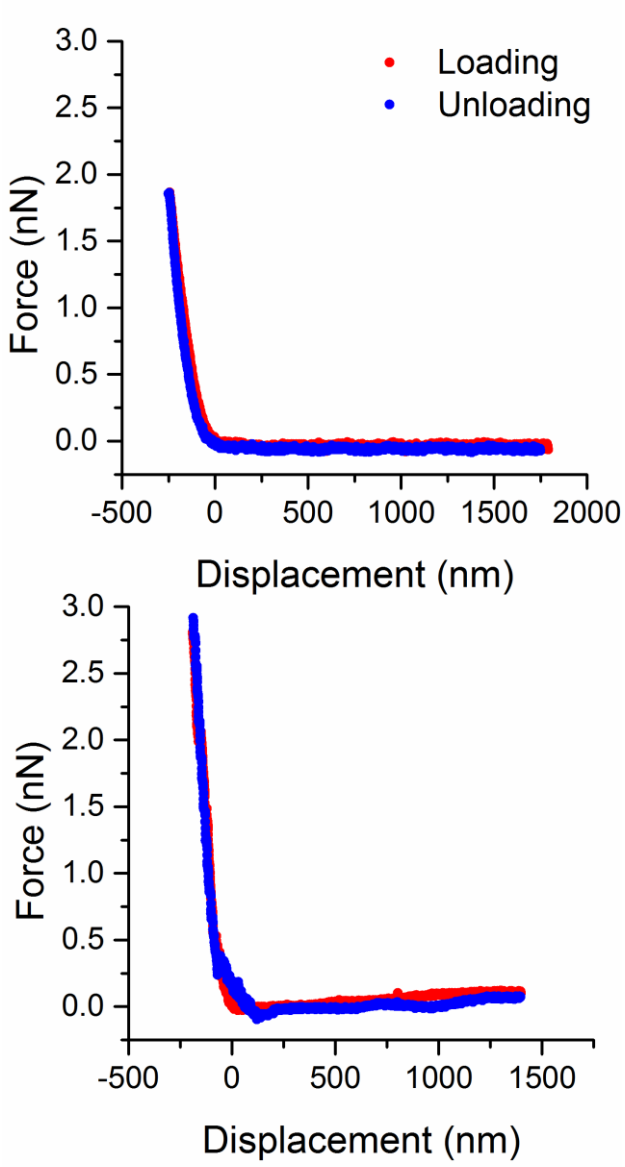

Figure 7.10. Sample force-displacement curves conducted on (top) CDM and (bottom) nanofibre regions.

The force-displacement curves in Figure 7.10 showed elastic behaviour through the loading curve being retraced by the unloading curve for force-displacement curves conducted on CDM and fibre regions of the cryosectioned CDM/fibre composite samples. The lack of observed adhesion forces between the indenting AFM tip and

sample allowed for the Hertzian contact mechanics to be applied to the analysis of the force-displacement curves. The force-displacement curves were analysed using the methodology previously applied in Chapter 5 to the cryosections of mouse tail skin and the elastic modulus was extracted at each point, resulting elastic modulus distribution maps as shown in Figure 7.11 each scaffold fibre diameter.

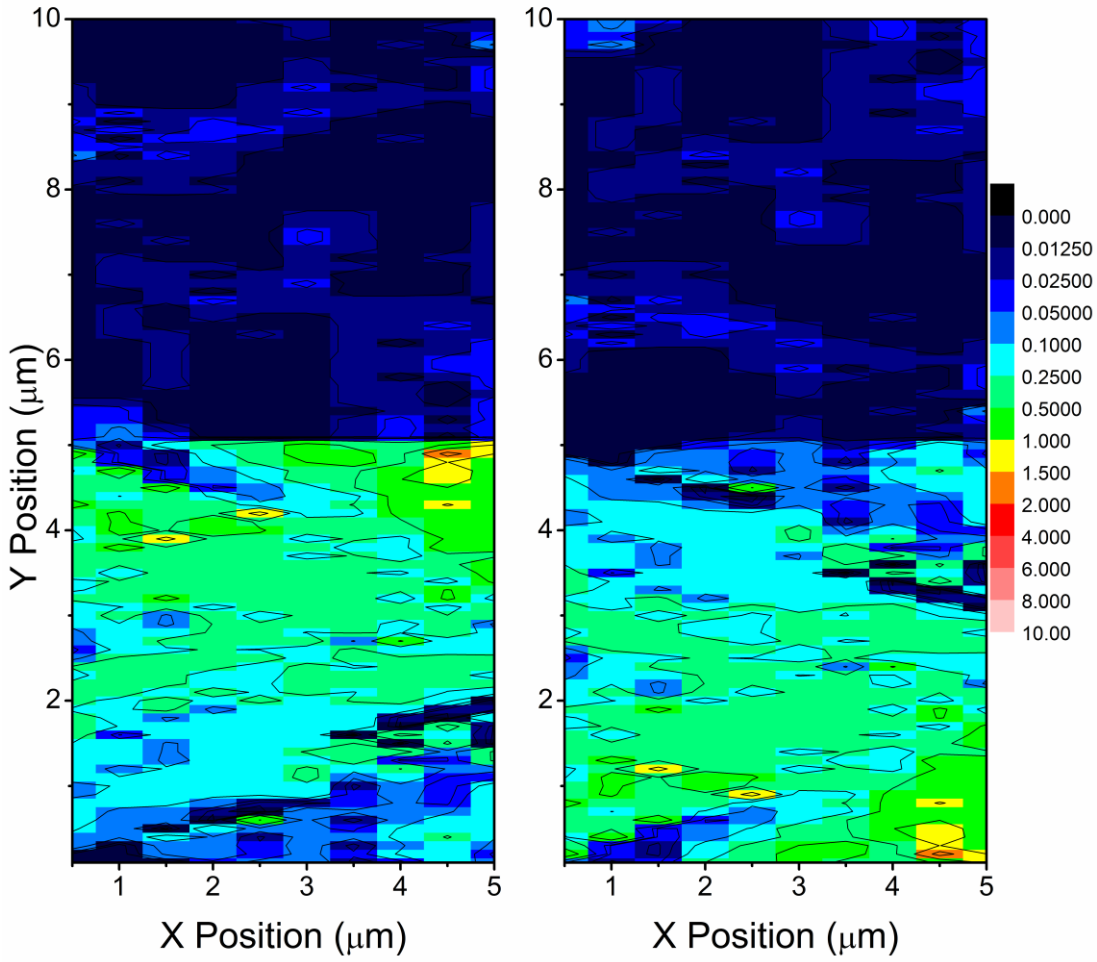

Figure 7.11. Elastic modulus distribution map of the interface between the (top) CDM and (bottom) electrospun scaffold from the corresponding highlighted regions of Figure 7.9. (Left) shows a elastic modulus map of the fibre scaffold electrospun from the 15.5 w/w% solution and (right) shows the CDM deposited on a scaffold electrospun from the 17.5 w/w% solution. The colouration scale is in MPa.

The elastic modulus distribution maps shown in Figure 7.11 both display two distinct regions, which represent the stiffer fibres and softer CDM. The interface between the fibre region and the CDM is not completely discrete, with the CDM observed to integrate into the electrospun fibrous network. Qualitatively, the elastic modulus maps display elastic moduli ranging between 0.25 MPa and 1.5 MPa for the smaller and larger fibre diameters respectively, indicating a similarity in stiffness for both both fibre scaffolds. Quantitative analysis of the data in Figure 7.10 gives an elastic modulus for the fibres electrospun from the 17.5 w/w% solution as 876.5 kPa ± 855.9 kPa (mean ± standard deviation) whereas the fibres electrospun from the 15.5 w/w% solution have an elastic modulus of 548.8 kPa ± 483.6 kPa (mean ± standard deviation). Comparing the average elastic modulus of the fibre regions provides an indication that the larger fibres diameters spun from the higher concentration polymer solution give higher elastic modulus values, but this result is not significant ($p > 0.1$) with a large degree of variation in the values for each of the fibre scaffolds. At a material level, individual electrospun fibres have been shown to increase their elastic modulus with decreasing fibre diameter due to enhance polymer chain orientation (Stachewicz et al., 2012). Such literature suggests that fibres spun from 15.5 w/w% solutions would be expected to give higher elastic modulus values, which is not observed here. The higher elastic modulus of the larger diameter fibres thus indicates that the AFM approach is not testing the mechanical properties of the single fibres by indentation to give an elastic modulus. Indeed, geometric effects are perhaps a stronger influence on the recorded mechanical response under the action of the indenting AFM tip and can be simply examined using a fibre bending analysis. Specifically, a fibre modelled as a beam that is deflecting under an applied load from

an AFM tip gives a bending deflection, δ, for a concentrated load, P, on a fixed fibre described as (Stachewicz et al., 2012)

$$\delta = \frac{PL^3}{192EI} \quad \text{Equation 7.1}$$

$$I = \frac{\pi d^4}{64} \quad \text{Equation 7.2}$$

where I is the moment of inertia of the cross sectional area of the beam, L the length, d the diameter of fibre and E the elastic modulus of the fibre material.

The peak stiffness (P/δ) of six force-displacement curves recorded within the fibrous regions of the composites produced from the 15.5 w/w% and 17.5 w/w% solutions were measured. The average peak stiffness for the 15.5 w/w% fibres was calculated to be 0.01163 nN/nm and 0.01789 nN/nm for the 17.5 w/w% fibres. The higher peak stiffness of the fibres from the 17.5 w/w% polymer solution compared to the 15.5 w/w% polymer solution indicates that the geometry of the fibres is influencing the mechanical response of the material. The difference in elastic modulus between the fibres produced from the two different polymer solutions required measurement of the individual fibre diameter and length. The average fibre diameter was previously measured after 7 days of incubation in cell culture media in this chapter by SEM, resulting in an average diameter of 228.6 nm ± 5.432 nm for the 15.5 w/w% fibres and 372.8 nm ± 12.96 nm for the 17.5 w/w% fibres. The average length between fibre connections was also measured using SEM and the ImageJ line tool with the appropriate image calibration. The average fibre length for the 15.5 w/w% was found to be 749.8 nm ± 184.1 nm and 851.1 nm ± 236.6 nm for the 17.5 w/w% fibres. The elastic modulus of the individual fibres was then predicted according to Equation 7.1 using the average fibre length, average fibre diameter, and the average peak stiffness.

The elastic modulus of the 15.5 w/w% fibres was predicted to be 1.408 GPa and 189.2 MPa for the 17.5 w/w% fibres. The difference between the predicted elastic modulus of the fibres using the beam bending theory against the elastic modulus measured using AFM force-displacement curves therefore indicates that the geometry is indeed effecting the measured mechanical response of the fibrous region of the composite.

The force-displacement measurements on the CDM of each nanofibre scaffold resulted in an elastic modulus of 121.5 kPa ± 141.9 kPa (mean ± standard deviation) for the fibre scaffold electrospun from the 17.5 w/w% solution and 67.88 kPa ± 62.05 kPa for the fibre scaffold electrospun from 15.5 w/w% solution. Plotting a histogram of each distribution of elastic modulus, Figure 7.12, shows that the two CDMs have peaks in the number of counts at similar elastic modulus values.

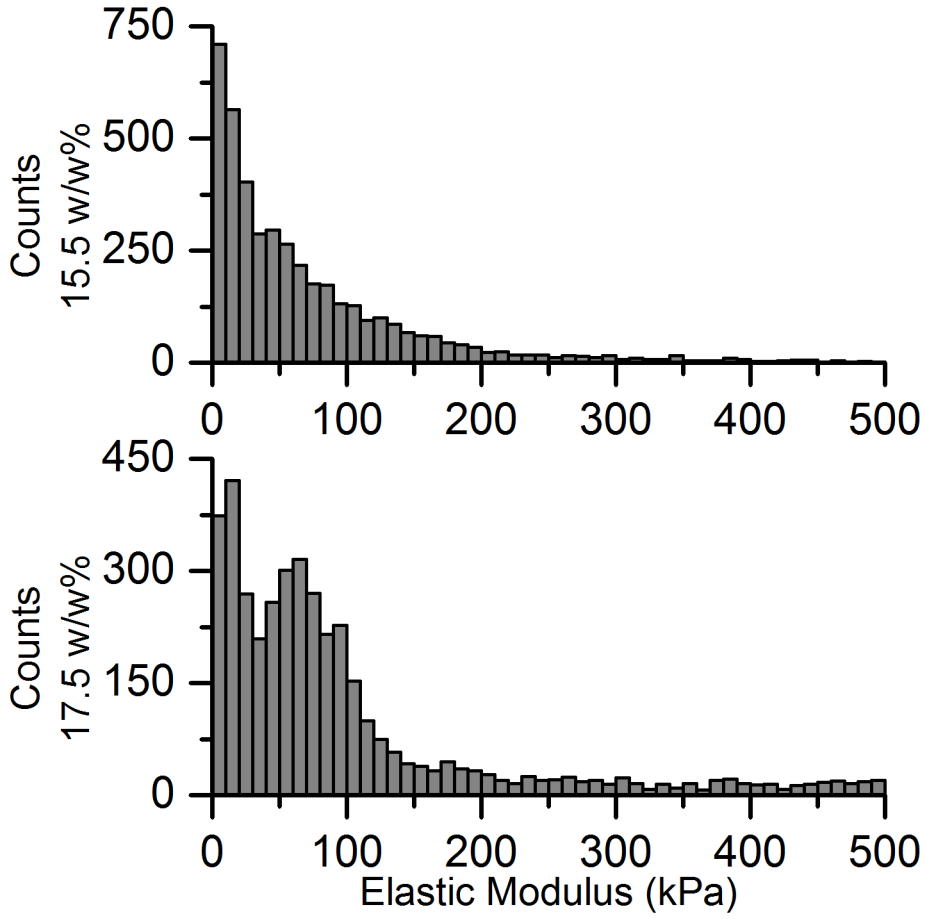

Figure 7.12. Truncated elastic modulus distribution histograms showing the frequency of counts from the measured elastic modulus for CDM deposited on fibrous scaffolds electrospun from a (top) 15.5 w/w% polymer solution (n = 4250) and a (bottom) 17.5 w/w% polymer solution (n = 4750).

Figure 7.12 indicates a wider distribution of elastic modulus for fibres spun from a higher concentration polymer solution when compared to the lower concentration solution, which was previously indicated earlier in this chapter by the standard deviation associated with the mean value of the elastic modulus. Comparison of the two distributions using the average elastic modulus from each CDM produced (n = 7 for the two different polymer solution) by the Mann-Whitney U-test gives a *p*-value

of 0.4540 indicating that there is no significant difference between the two distributions. The similarity between the two distributions can also be observed by plotting the density functions, as shown in Figure 7.13, highlighting little significant difference in the location of the peaks. The results of the frequency of counts for the elastic modulus and the density function plots indicate that the elastic modulus of the CDM is independent of the nanofibre diameter of the scaffold. The lack of dependence between the CDM mechanics and the mechanical properties of the nanofibres, as displayed in Figure 7.13 through the overlapping distributions of elastic modulus, indicates that the substrate mechanics are not having an effect on the mechanical properties of the CDM. The substrate does have an effect on the rate at which the CDM is produced, as shown in Figure 7.7 displaying the CDM thickness for each substrate after 7 days of cell culture. The increased rate of CDM production can be assumed by the overall thickness that was previously measured by the fibronectin staining after the full culturing time period.

Additionally, the elastic modulus distribution display peaks between 10 kPa to 30 kPa in Figure 7.13 for the CDM on both the smaller and larger fibre diameter scaffolds is lower than the previously measured values of elastic modulus for the dermis reported in Chapters 4 and 5 of approximately 44 kPa. The reduced elastic modulus of the CDM compared to the dermis could be contributed to the fact that the CDM is only produced from fibroblasts, and not all of the components of the dermis are present resulting in a CDM structure that is less stable than the dermis. Integrating the low elastic modulus CDM within a higher elastic modulus electrospun fibre scaffold produced a composite system comprised of two phases, with the CDM as the matrix phase and the electrospun fibres as the reinforcement phase. The volume fraction of each phase can be adjusted to tailor the overall

mechanics of the composite system. The relatively high average elastic modulus of the fibres scaffold, approximately 500 kPa to 800 kPa, combined with the low average elastic modulus CDM, approximately 50 kPa to 100 kPa, provides a range of mechanics that can be tailored to mimic that of the whole skin mechanics modelled in Chapter 6.

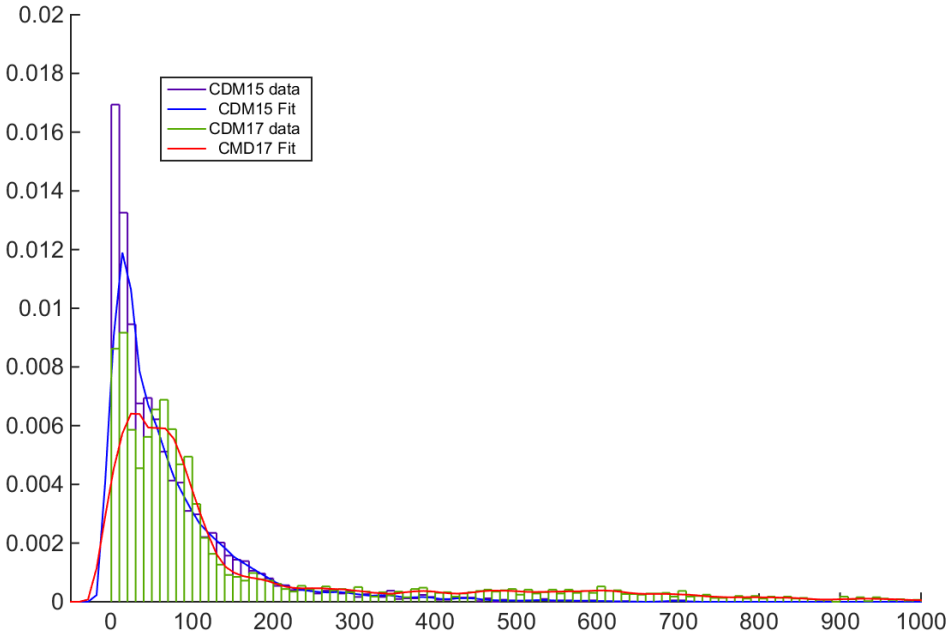

Figure 7.13. Probability density function plots of the distribution of elastic modulus values for each CDM sample. With CDM15 showing the elastic modulus data measured from the CDMs deposited on 15.5 w/w% scaffolds and CDM17 the elastic modulus data for the 17.5 w/w% scaffolds.

The volume fraction of fibres/CDM present within the composite system influences the overall mechanical response. The variation in elastic modulus of the fibre/CDM

composite as a function of fibre volume fraction must be understood to see if the composite system mimics the mechanical behaviour of whole skin. The elastic modulus on the cryosection samples of the CDM and nanofibre scaffold can be analysed using the analytical techniques previously employed in Chapter 6. The Hashin-Shtrikman (H-S) bounds were applied with the average elastic modulus of the CDM and the elastic modulus of the fibres used to represent the two phases. Therefore, two composite systems were evaluated based on the two fibre scaffolds used in cell culture. A composite elastic modulus was calculated for each CDM/scaffold sample and plotted against the volume fraction of fibres present within the measured area, as shown in Figure 7.14. To compare the predicted elastic modulus of the CDM/scaffold samples to the whole skin mechanics, the H-S bound calculated in Chapter 6 for whole skin as a function of epidermal volume fraction was included in Figure 7.14.

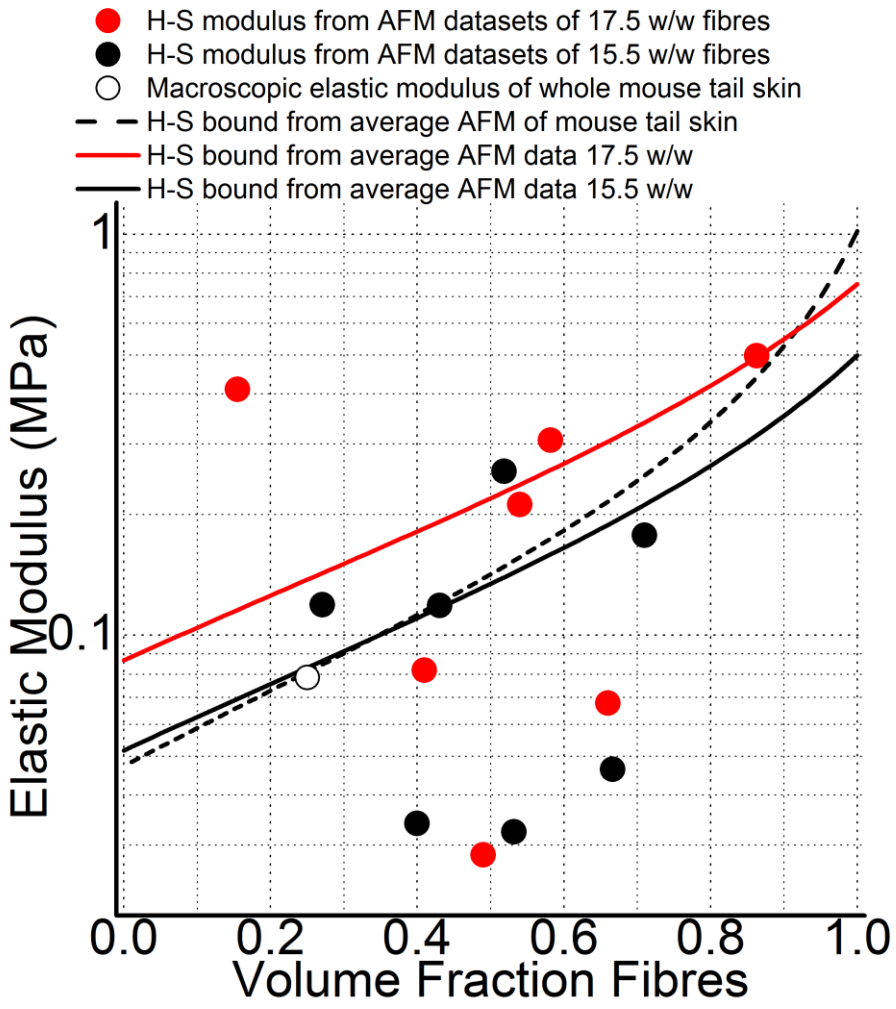

Figure 7.14. Variation of elastic modulus with volume fraction of fibres for the calculated composite modulus of the CDM/scaffold composite material. The solid curves are generated from the average values of the measured elastic modulus for the CDM and the electrospun scaffold. The dashed line represents the composite modulus curve for whole skin.

The scatter of the data points for both the fibres spun from 15.5 w/w% and 17.5 w/w% solutions indicate that the elastic modulus of the samples vary significantly and no clear trend observed with increasing fibre volume fraction. Combining all of

the elastic modulus data of the CDM and the measured elastic modulus for each fibre scaffold continuous H-S curves were produced to model the two composite systems. The curves in Figure 7.14 indicate that the elastic modulus of the composites show a continuous increase with fibre volume. The H-S bound produced from the elastic modulus data of the 17.5 w/w% fibre scaffold was consistently higher when compared to the composite using the fibres from the 15.5 w/w% polymer solution. The consistently higher composite elastic modulus produced from the thicker fibres of the 17.5 w/w% solution results from the higher elastic modulus when the fibre region of the cross section samples was measured by AFM indentation when compared to the measured elastic modulus of the fibrous region of the 15.5 w/w% solution.

Examining the continuous H-S bound curves in Figure 7.14 for the composites produced with fibres spun from 15.5 w/w% solution and the curve describing the whole skin shows that the linear elastic mechanics of whole skin could potentionally be mimicked by the composite system for volume fraction of fibres between 0.1 and 0.9. The samples produced using fibres spun from a 15.5 w/w% polymer solution resulted in a composite with similar elastic modulus values to whole skin. Furthermore, the macroscale mechanical measurement of whole skin carried out in Chapter 6, denoted by the open circle in Figure 7.14, which measured an elastic modulus of 78.4 kPa with an epidermal volume fraction of 0.25 can be replicated by a composite produced using a 0.22 volume fraction of fibres spun from a 15.5 w/w% polymer solution. These results indicate that a mechanical analogue to whole skin is produced by combining CDMs and electrospun fibres produced from a 15.5 w/w% polymer solution.

The composite modulus serves as a method for estimating the composition required if the CDM/scaffold was used as a mechanical substitute for whole skin. The CDMs produced here do not penetrate into the nanofibre scaffold, so two distinct layers are formed, as seen in the immunofluorescence images of Figure 7.6 . An ideal dermal analogue composite system would consist of a nanofibre network completely embedded within a CDM matrix. The nanofibre scaffold would provide a mechanically robust framework while the CDM would be a highly biocompatible material and over time the nanofibre scaffold would degrade and be replaced by new extracellular matrix material. The lack of penetration into the scaffold is due to the spacing between the nanofibres, approximately 5 μm if the assumption that the fibre spacing is taken as 10 times the fibre diameter of a random nonwoven fibre mat, which is smaller than the size of the fibroblasts thus preventing migration into the scaffold. The spacing between the fibres would increase with increasing fibre diameter (Lowery et al., 2010) and the 17.5 w/w% polymer solution produced consistent fibres with the largest diameter using a solvent of acetic acid and formic acid. Further increasing the spacing between the fibres would in turn allow cell penetration into the fibre scaffold and greater integration of the CDM within the fibre scaffold.

7.4 Conclusions

Electrospun polymer fibre mats were fabricated for use as a cell culture scaffold with fibroblasts used to deposit a cell derived matrix within the scaffold. The composite electrospun scaffold and cell derived matrix were mechanically evaluated at high spatial resolution using AFM indentation as established in the previous chapter, with

results indicating that the geometry and material properties of the electrospun scaffold do not influence the mechanical properties of the cell derived matrix. However, the total volume of matrix deposited within the scaffold was found to increase when the scaffold was comprised of larger diameter fibres. Scaffolds composed of larger diameter fibres with a higher individual fibre stiffness resulted in increased CDM deposition. Established two-phase composite material theories were applied and showed that the mechanical properties of the scaffold and CDM are comparable to the mechanical properties of mouse whole skin. These results indicate that the scaffold/CDM composite material could potentially be used as a mechanical analogue to whole skin. The evaluation of the small scale spatial variations in mechanical properties of engineered biocomposites were also shown to estimate macroscopic linear isotropic elastic modulus and thus link multi-length scale mechanical behaviour within a complex biological system.

Chapter 8 – Conclusions and Future Work

8.1 Summary of the thesis

In the first chapter the rationale behind the research into the spatial variations in the mechanical properties of skin at the nanoscale was established. The work produced for the thesis was outlined and the overall objects of the study were defined. Chapter 2 provided a comprehensive review of the current state of the literature regarding the mechanical properties of skin at the macroscale and the micro/nanoscale. The structure and composition of skin were summarized, and the importance of the structure on the mechanical response was reviewed. The mechanical properties of materials were also discussed and the benefits of nanoindentation for analysis of small volumes highlighted. The function and ability of AFM to analyse the surface of materials at the nanoscale was outlined along with the analytical methods that can be applied to use AFM as a tool for probing the mechanical properties at the nanoscale. The literature review particularly focused on the current gap in knowledge regarding the link between the mechanical behaviour observed at the nanoscale to the observations recorded during macroscopic testing. The review of the literature

provided the reasoning for investigating the relationship between nanoscale and macroscale mechanics of skin.

Chapter 3 discussed the AFM setup and the testing methodology applied in order to measure the elastic modulus of skin at the nanoscale within a hydrated environment. A range of sample preparation methods applied to mouse tail skin were considered so that the dermal surface of skin was exposed by mechanically peeling off the epidermal layers. Individual layers of skin exposed through cross sectioning at cryogenic temperatures were used to mechanically test the variations in spatial mechanical properties. The calibration of AFM cantilevers was outlined along with the data processing required to extract elastic modulus information from AFM force-displacement measurements. The AFM force-displacement measurements were validated using agarose gels of known elastic modulus to establish the AFM elastic modulus measurements are both precise and accurate.

The AFM force-displacement measurement technique outlined in Chapter 3 was applied to dermal tissue samples from mouse tail skin in Chapter 4 to establish the mechanical properties of the dermis at the nanoscale and draw comparisons to the literature values. The dermal samples were also subjected to treatment of cryoprotective agents and a freeze thaw cycle in order to determine the effects of the freezing and thawing process on the elastic modulus of mouse tail skin. The data recorded from AFM force-displacement measurements indicated that there was no effect on the elastic modulus of the tissue as a result of the freezing and thawing process, thus indicating that mechanical properties of samples frozen to cryogenic temperatures, cross sectioned and thawed would be consistent with the initial freshly excised state.

In Chapter 5, the AFM force-displacement technique was used to map the elastic modulus of through thickness whole skin cryosections to characterise the spatial variations in mechanical properties. The elastic modulus of the dermal region of the mouse tail skin was found to have little variation whereas a gradual increase in the elastic modulus was observed within the epidermis. The outermost layers of the epidermis displayed the highest elastic modulus values. The gradient of elastic modulus within the epidermis was attributed to the stratification process keratinocytes undergo during terminal differentiation. The elastic modulus information for the dermal region of the cryosection samples was compared to the measurements conducted on the dermal explant samples and indicated that the resulting change in sample orientation had no impact on the measured elastic modulus. The lack of variation between the two sample orientations indicates an isotropic response of the dermis at the nanoscale. This isotropic response was attributed to the material properties of the dermis at the nanoscale being dominated by the soft ground substance matrix of the dermis with the stiff collagen fibril network providing mechanical stabilisation. A mechanism where loads applied at the nanoscale are insufficiently large to deform the collagen fibrils but instead displace the collagen network within the ground substance matrix was proposed. The spatial mapping through the thickness of skin provided mechanical information for the different layers of skin and the ability to extract whole skin mechanical properties from these values was studied in the subsequent chapter.

Chapter 6 focused on exploring the link between the spatial variations of the elastic modulus of whole skin to the overall mechanical properties of whole skin as measured at the macroscale. Large scale indentations of whole skin were conducted using a 1 mm indenter at low strains to record elastic modulus values using a similar

loading condition to the AFM force-displacement curves. Theories to predict the elastic modulus of composite materials were applied to the elastic modulus maps described in Chapter 5 to evaluate the whole skin elastic modulus from a small volume of material. A two phase Hashin-Shtrikman model, when applied to the AFM elastic modulus maps, showed good agreement between the elastic modulus of whole skin predicted from the nanoscale measurements and the direct large scale macroscopic measurement of whole skin. The use of a two phase model constructed from nanoscale measurements meant that the spatial resolution and distribution of mechanical properties was lost within the analysis. Therefore, finite element analysis was used to construct an analytical model from the elastic modulus maps. The whole skin linear elastic modulus from the finite element analysis showed a strong dependence on the total volume of the dermis within the sample. Calibrating the model against the volume of the dermis resulted in accurate prediction of the whole skin elastic modulus consistent with the macroscopic mechanical tests.

In Chapter 7, the established experimental and analytical techniques of the thesis were applied to an engineered biocomposite material composed of an electrospun nanofibre scaffold and a cell derived matrix (CDM) produced by dermal fibroblasts. Measurement of the elastic modulus of the CDM and electrospun scaffold indicated that the structure and material properties of the nanofibres had little effect on the mechanical properties of the CDM but influenced the total amount of CDM produced, indicating that the geometry and structural properties of a tissue scaffold may be more important than the elastic modulus. Analysis of the CDM/nanofibre composite also showed that overall elastic modulus was similar to the whole skin elastic modulus. The similarity of the elastic modulus values shows that the biocomposite system could serve as a mechanical analogue to whole skin.

8.2 Future Work

The work presented in this thesis provides a novel method for analysing the mechanical behaviour of materials and relating the nanoscale mechanical properties to the bulk macroscale properties. This method of material analysis provides a tool that is not limited to the characterisation of biological materials and could be applied to a broad scope of materials. Within the biological material regime, many opportunities of future work are expected, with one avenue being extending the finite element analysis to provide a platform for evaluating the effect of abnormal tissue regions, such as diseased states or wounded regions, within skin and predicting the resulting effect on the bulk mechanical properties of the tissue. This could be achieved by either performing AFM force-displacement measurements on through thickness sections of tissue samples containing the alternate state skin and generating a finite element model from the mechanical measurements as was conducted in Chapter 6. The second potential avenue would be to modify the existing finite element model to incorporate regions of the mesh with mechanical properties measured from alternate tissue states if through thickness sections were unavailable. Both of these methods would provide a platform for predicting the mechanical response of alternate tissue states at the macroscale. The AFM technique also shows promise as a method to provide experimental data uses to predict bulk mechanical properties of a tissue. Such an approach may be useful where sample volume is insufficient to conduct more traditional large scale testing such as uniaxial tension.

8.3 Major Findings of the Thesis

The thesis provides a systematic approach to exploring the mechanical properties of skin. The major findings of this work that perhaps extend the research field beyond current understand can be defined as:

- A freezing and thawing process required to prepare skin samples via cross sectioning at cryogenic temperatures was found to have no effect on the measured elastic modulus of the dermis of mouse tail skin. Sectioning methods while retaining inherent skin mechanical properties was therefore developed.

- Nanoscale mechanical measurements of the dermis displayed isotropic behaviour in response to a change in the direction of the applied load.

- The spatial variation in the elastic modulus of skin was observed at the nanoscale. The dermis displayed a consistent elastic modulus while the epidermis exhibited a gradient from the softer basal layers to the stiff outer cornified layers.

- The low strain isotropic linear elastic modulus of whole skin was estimated from nanoscale measurements of small volumes of skin using a two phase Hashin-Shtrikman model. Finite element analysis was implemented to calculate elastic modulus values of the whole skin from high spatial resolution elastic modulus measurements of through thickness skin when

nanoscale deformations were applied and linear isotropic elastic behaviour was assumed.

- The spatial variation in a biocomposite composed of nanofibres and cell derived matrix was accurately measured and the elastic modulus of the CDM shown to be independent of the material properties of the scaffold material. However, the geometry of the scaffold directly influenced the overall production of CDM.

- Composite material theories directly applied to the nanofibre/CDM biocomposite estimated the bulk tissue mechanical properties and indicated the potential suitability of the composite as a mechanical analogue to tissue. This result combined with the latter highlight suggests the importance of scaffold geometry once a mechanical analogue to the tissue is achieved.

References

Achterberg, V.F., Buscemi, L., Diekmann, H., Smith-Clerc, J., Schwengler, H., Meister, J.-J., Wenck, H., Gallinat, S., Hinz, B., 2014. The nano-scale mechanical properties of the extracellular matrix regulate dermal fibroblast function. J. Invest. Dermatol. 134, 1862–72. doi:10.1038/jid.2014.90

Albrecht, T.R., Akamine, S., Carver, T.E., Quate, C.F., 1990. Microfabrication of Cantilever Styli for the Atomic Force Microscope. J. Vac. Sci. Technol. a-Vacuum Surfaces Film. 8, 3386–3396.

Alsteens, D., Dupres, V., Yunus, S., Latgé, J.-P., Heinisch, J.J., Dufrêne, Y.F., 2012. High-resolution imaging of chemical and biological sites on living cells using peak force tapping atomic force microscopy. Langmuir 28, 16738–44. doi:10.1021/la303891j

Andriani, F., Margulis, A., Lin, N., Griffey, S., Garlick, J.A., 2003. Analysis of microenvironmental factors contributing to basement membrane assembly and normalized epidermal phenotype. J. Invest. Dermatol. 120, 923–931.

Ashcroft, G.S., Yang, X., Glick, a B., Weinstein, M., Letterio, J.L., Mizel, D.E., Anzano, M., Greenwell-Wild, T., Wahl, S.M., Deng, C., Roberts, a B., 1999. Mice lacking Smad3 show accelerated wound healing and an impaired local inflammatory response. Nat. Cell Biol. 1, 260–266. doi:10.1038/12971

Bakhach, J., 2009. The cryopreservation of composite tissues: Principles and recent advancement on cryopreservation of different type of tissues. Organogenesis 5, 119–126. doi:10.4161/org.5.3.9583

Bar, G., Brandsch, R., Whangbo, M.H., 1998. Effect of viscoelastic properties of polymers on the phase shift in tapping mode atomic force microscopy. Langmuir 14, 7343–7348.

Bar, G., Thomann, Y., Brandsch, R., Cantow, H.J., Whangbo, M.H., 1997. Factors affecting the height and phase images in tapping mode atomic force microscopy. Study of phase-separated polymer blends of poly(ethene-co-styrene) and poly(2,6-dimethyl-1,4-phenylene oxide). Langmuir 13, 3807–3812.

Bastatas, L., Martinez-Marin, D., Matthews, J., Hashem, J., Lee, Y.J., Sennoune, S., Filleur, S., Martinez-Zaguilan, R., Park, S., 2012. AFM nano-mechanics and calcium dynamics of prostate cancer cells with distinct metastatic potential. Biochim. Biophys. Acta-General Subj. 1820, 1111–1120.

Baust, J.G., Gao, D., Baust, J.M., 2009. Cryopreservation: An emerging paradigm change. Organogenesis 5, 90–96. doi:10.4161/org.5.3.10021

Beard, J.D., Guy, R.H., Gordeev, S.N., 2013. Mechanical tomography of human corneocytes with a nanoneedle. J. Invest. Dermatol. 133, 1565–71. doi:10.1038/jid.2012.465

Bhardwaj, N., Kundu, S.C., 2010. Electrospinning: A fascinating fiber fabrication technique. Biotechnol. Adv. 28, 325–347. doi:10.1016/j.biotechadv.2010.01.004

Binnig, G., Quate, C., Gerber, C., 1986. Atomic force microscope. Phys. Rev. Lett. 56, 930 – 933.

Blackwood, K. a, McKean, R., Canton, I., Freeman, C.O., Franklin, K.L., Cole, D., Brook, I., Farthing, P., Rimmer, S., Haycock, J.W., Ryan, A.J., MacNeil, S., 2008. Development of biodegradable electrospun scaffolds for dermal replacement. Biomaterials 29, 3091–104. doi:10.1016/j.biomaterials.2008.03.037

Blanpain, C., Fuchs, E., 2009. Epidermal homeostasis: a balancing act of stem cells in the skin. Nat Rev Mol Cell Biol 10, 207–217.

Böl, M., Ehret, A.E., Leichsenring, K., Ernst, M., 2015. Tissue-scale anisotropy and compressibility of tendon in semi-confined compression tests. J. Biomech. 48, 1092–1098. doi:10.1016/j.jbiomech.2015.01.024

Bordes, C., Fréville, V., Ruffin, E., Marote, P., Gauvrit, J.Y., Briançon, S., Lantéri, P., 2010. Determination of poly(epsilon-caprolactone) solubility parameters: application to solvent substitution in a microencapsulation process. Int. J. Pharm. 383, 236–43. doi:10.1016/j.ijpharm.2009.09.023

Bowes, W.M., Russell, L.T., Suter, G.T., 1984. Mechanics of engineering materials. Wiley, New York.

Braun, K.M., Niemann, C., Jensen, U.B., Sundberg, J.P., Silva-Vargas, V., Watt, F.M., 2003. Manipulation of stem cell proliferation and lineage commitment: visualisation of label-retaining cells in wholemounts of mouse epidermis. Development 130, 5241–5255. doi:10.1242/dev.00703

Bravo, D., Rigley, T.H., Gibran, N., Strong, D.M., Newman-Gage, H., 2000. Effect of storage and preservation methods on viability in transplantable human skin allografts. Burns 26, 367–378.

Burgeson, R.E., Christiano, A.M., 1997. The dermal-epidermal junction. Curr. Opin. Cell Biol. 9, 651–658.

Burnham, N. a, Chen, X., Hodges, C.S., Matei, G. a, Thoreson, E.J., Roberts, C.J., Davies, M.C., Tendler, S.J.B., 2002. Comparison of calibration methods for atomic-force microscopy cantilevers. Nanotechnology 14, 1–6. doi:10.1088/0957-4484/14/1/301

Butt, H.J., Cappella, B., Kappl, M., 2005. Force measurements with the atomic force microscope: Technique, interpretation and applications. Surf. Sci. Rep. 59, 1–152.

Callister, W., Rethwisch, D., 2007. Materials science and engineering: an introduction, Materials Science and Engineering. doi:10.1016/0025-5416(87)90343-0

Candi, E., Schmidt, R., Melino, G., 2005. The cornified envelope: a model of cell death in the skin. Nat Rev Mol Cell Biol 6, 328–340.

Cappella, B., Dietler, G., 1999. Force-distance curves by atomic force microscopy. Surf. Sci. Rep. 34, 1–104.

Chakravarti, S., Magnuson, T., Lass, J.H., Jepsen, K.J., LaMantia, C., Carroll, H., 1998. Lumican regulates collagen fibril assembly: Skin fragility and corneal opacity in the absence of lumican. J. Cell Biol. 141, 1277–1286. doi:10.1083/jcb.141.5.1277

Chan, B.P., Leong, K.W., 2008. Scaffolding in tissue engineering: General approaches and tissue-specific considerations. Eur. Spine J. 17. doi:10.1007/s00586-008-0745-3

Chandrasekaran, A.R., Venugopal, J., Sundarrajan, S., Ramakrishna, S., 2011. Fabrication of a nanofibrous scaffold with improved bioactivity for culture of human dermal fibroblasts for skin regeneration. Biomed. Mater. 6, 015001. doi:10.1088/1748-6041/6/1/015001

Charitidis, C.A., 2011. Nanoscale Deformation and Nanomechanical Properties of Polydimethylsiloxane (PDMS). Ind. Eng. Chem. Res. 50, 565–570.

Charras, G.T., Horton, M. a, 2002. Determination of cellular strains by combined atomic force microscopy and finite element modeling. Biophys. J. 83, 858–879. doi:10.1016/S0006-3495(02)75214-4

Chen, F., Zhang, W., Wu, W., Jin, Y., Cen, L., Kretlow, J.D., Gao, W., Dai, Z., Wang, J., Zhou, G., Liu, W., Cui, L., Cao, Y., 2011. Cryopreservation of tissue-engineered epithelial sheets in trehalose. Biomaterials 32, 8426–8435.

Chong, E.J., Phan, T.T., Lim, I.J., Zhang, Y.Z., Bay, B.H., Ramakrishna, S., Lim, C.T., 2007. Evaluation of electrospun PCL/gelatin nanofibrous scaffold for wound healing and layered dermal reconstitution. Acta Biomater. 3, 321–30. doi:10.1016/j.actbio.2007.01.002

Cipitria, A., Skelton, A., Dargaville, T.R., Dalton, P.D., Hutmacher, D.W., 2011. Design, fabrication and characterization of PCL electrospun scaffolds—a review. J. Mater. Chem. 21, 9419. doi:10.1039/c0jm04502k

Cleveland, J.P., Manne, S., Bocek, D., Hansma, P.K., 1993. Nondestructive method for determining the spring constant of cantilevers for scanning force microscopy. Rev. Sci. Instrum. 64, 403–405. doi:10.1063/1.1144209

Clifford, C. a., Seah, M.P., 2005. Quantification issues in the identification of nanoscale regions of homopolymers using modulus measurement via AFM nanoindentation. Appl. Surf. Sci. 252, 1915–1933. doi:10.1016/j.apsusc.2005.08.090

Corr, D.T., Gallant-Behm, C.L., Shrive, N.G., Hart, D.A., 2009. Biomechanical behavior of scar tissue and uninjured skin in a porcine model. Wound Repair Regen. 17, 250–259.

Courtney, T.H., 2005. Mechanical Behavior of Materials: Second Edition. Waveland Press.

Coutinho, A.R.S., Mendes, C.M., Caetano, H.V.A., Nascimento, A.B., Oliveira,

V.P., Hernandez-Blazquez, F.J., Sinhorini, I.L., Visintin, J.A., Assumpcao, M.E.O., 2007. Morphological changes in mouse embryos cryopreserved by different techniques. Microsc. Res. Tech. 70, 296–301.

Crichton, M.L., Chen, X., Huang, H., Kendall, M.A.F., 2013. Elastic modulus and viscoelastic properties of full thickness skin characterised at micro scales. Biomaterials 34, 2087–2097.

Crichton, M.L., Donose, B.C., Chen, X., Raphael, A.P., Huang, H., Kendall, M.A.F., 2011. The viscoelastic, hyperelastic and scale dependent behaviour of freshly excised individual skin layers. Biomaterials 32, 4670–4681.

Croisier, F., Duwez, a-S., Jérôme, C., Léonard, a F., van der Werf, K.O., Dijkstra, P.J., Bennink, M.L., 2012. Mechanical testing of electrospun PCL fibers. Acta Biomater. 8, 218–24. doi:10.1016/j.actbio.2011.08.015

Cross, S.E., Jin, Y.-S., Tondre, J., Wong, R., Rao, J., Gimzewski, J.K., 2008. AFM-based analysis of human metastatic cancer cells. Nanotechnology 19, 384003. doi:10.1088/0957-4484/19/38/384003

Cui, W., Cheng, L., Hu, C., Li, H., Zhang, Y., Chang, J., 2013. Electrospun poly(L-lactide) fiber with ginsenoside rg3 for inhibiting scar hyperplasia of skin. PLoS One 8, e68771. doi:10.1371/journal.pone.0068771

Cukierman, E., Pankov, R., Stevens, D.R., Yamada, K.M., 2001. Taking cell-matrix adhesions to the third dimension. Science (80-.). 294, 1708–1712. doi:10.1126/science.1064829

D'Agostino, R.B., Belanger, A., D'Agostino Sr., R.B., D'Agostino Jr., R.B., 1990. A Suggestion for Using Powerful and Informative Tests of Normality. Am. Stat.

Delaine-Smith, R.M., Burney, S., Balkwill, F.R., Knight, M.M., 2016. Experimental validation of a flat punch indentation methodology calibrated against unconfined compression tests for determination of soft tissue biomechanics. J. Mech. Behav. Biomed. Mater. 60, 401–415. doi:10.1016/j.jmbbm.2016.02.019

Delalleau, A., Josse, G., Lagarde, J.-M., Zahouani, H., Bergheau, J.-M., 2006. Characterization of the mechanical properties of skin by inverse analysis combined with the indentation test. J. Biomech. 39, 1603–10. doi:10.1016/j.jbiomech.2005.05.001

Denis, P., Dulnik, J., Sajkiewicz, P., 2014. Electrospinning and Structure of Bicomponent Polycaprolactone/Gelatin Nanofibers Obtained Using Alternative Solvent System. Int. J. Polym. Mater. Polym. Biomater. 64, 354–364. doi:10.1080/00914037.2014.945208

Devireddy, R., Neidert, M., Bischof, J.C., Tranquillo, R.T., 2003. Cryopreservation of collagen-based tissue equivalents. I. Effect of freezing in the absence of cryoprotective agents. Tissue Eng. 9, 1089 – 1100.

Dimitriadis, E.K., Horkay, F., Maresca, J., Kachar, B., Chadwick, R.S., 2002. Determination of elastic moduli of thin layers of soft material using the atomic force microscope. Biophys. J. 82, 2798–2810.

Diridollou, S., Patat, F., Gens, F., Vaillant, L., Black, D., Lagarde, J.M., Gall, Y., Berson, M., 2000. In vivo model of the mechanical properties of the human skin under suction. Ski. Res. Technol. 6, 214–221.

Doerner, M., Nix, W., 1986. A method for interpreting the data from depth-sensing indentation instruments. J. Mater. Res. 1, 601 – 609.

Doshi, J., Reneker, D.H., 1995. Electrospinning Process and Applications of Electrospun Fibers. J. Electrostat. 35, 151–160.

Drake, B., Prater, C.B., Weisenhorn, A.L., Gould, S.A.C., Albrecht, T.R., Quate, C.F., Cannell, D.S., Hansma, H.G., Hansma, P.K., 1989. Imaging Crystals, Polymers, and Processes in Water with the Atomic Force Microscope. Science (80-.). 243, 1586–1589.

Duan, H., Feng, B., Guo, X., Wang, J., Zhao, L., Zhou, G., Liu, W., Cao, Y., Zhang, W.J., 2013. Engineering of epidermis skin grafts using electrospun nanofibrous gelatin/ polycaprolactone membranes. Int. J. Nanomedicine 8, 2077–84. doi:10.2147/IJN.S42384

Eastwood, M., Mudera, V.C., McGrouther, D. a., Brown, R. a., 1998. Effect of precise mechanical loading on fibroblast populated collagen lattices: Morphological changes. Cell Motil. Cytoskeleton 40, 13–21. doi:10.1002/(SICI)1097-0169(1998)40:1<13::AID-CM2>3.0.CO;2-G

Elmoazzen, H.Y., Elliott, J.A.W., McGann, L.E., 2005. Cryoprotectant equilibration in tissues. Cryobiology 51, 85–91.

Engler, A.J., Sen, S., Sweeney, H.L., Discher, D.E., 2006. Matrix elasticity directs stem cell lineage specification. Cell 126, 677–89. doi:10.1016/j.cell.2006.06.044

Evans, N.D., Oreffo, R.O.C., Healy, E., Thurner, P.J., Man, Y.H., 2013. Epithelial mechanobiology, skin wound healing, and the stem cell niche. J. Mech. Behav. Biomed. Mater. 28, 397–409. doi:10.1016/j.jmbbm.2013.04.023

Fang, M., Goldstein, E.L., Turner, a. S., Les, C.M., Orr, B.G., Fisher, G.J., Welch, K.B., Rothman, E.D., Banaszak Holl, M.M., 2012. Type i collagen D-spacing in fibril bundles of dermis, tendon, and bone: Bridging between nano- and micro-level tissue hierarchy. ACS Nano 6, 9503–9514. doi:10.1021/nn302483x

Foutz, T.L., Stone, E.A., Abrams, C.F., 1992. Effects of freezing on mechanical properties of rat skin. Am. J. Vet. Res. 53, 788–792.

Franco, R.A., Nguyen, T.H., Lee, B.-T., 2011. Preparation and characterization of electrospun PCL/PLGA membranes and chitosan/gelatin hydrogels for skin bioengineering applications. J. Mater. Sci. Mater. Med. 22, 2207–18. doi:10.1007/s10856-011-4402-8

Fuchs, E., Green, H., 1980a. Changes in keratin gene expression during terminal differentiation of the keratinocyte. Cell 19, 1033–1042. doi:10.1016/0092-8674(80)90094-X

Fuchs, E., Green, H., 1980b. Changes in Keratin Gene-Expression during Terminal

Differentiation of the Keratinocyte. Cell 19, 1033–1042.

Fuchs, E., Raghavan, S., 2002. Getting under the skin of epidermal morphogenesis. Nat Rev Genet 3, 199–209.

Fuller, B.J., 2004. Cryoprotectants: the essential antifreezes to protect life in the frozen state. Cryo Letters 25, 375–88.

Gahagnon, S., Mofid, Y., Josse, G., Ossant, F., 2012. Skin anisotropy in vivo and initial natural stress effect: a quantitative study using high-frequency static elastography. J. Biomech. 45, 2860–5. doi:10.1016/j.jbiomech.2012.08.032

García, R., Perez, R., 2002. Dynamic atomic force microscopy methods. Surf. Sci. Rep. 47, 197 – 301.

Gąsior-Głogowska, M., Komorowska, M., Hanuza, J., Mączka, M., Zając, a, Ptak, M., Będziński, R., Kobielarz, M., Maksymowicz, K., Kuropka, P., Szotek, S., 2013. FT-Raman spectroscopic study of human skin subjected to uniaxial stress. J. Mech. Behav. Biomed. Mater. 18, 240–52. doi:10.1016/j.jmbbm.2012.11.023

Gaucher, S., Elie, C., Verola, O., Jarraya, M., 2012. Viability of cryopreserved human skin allografts: effects of transport media and cryoprotectant. Cell Tissue Bank. 13, 147–155.

Gautam, S., Dinda, A.K., Mishra, N.C., 2013. Fabrication and characterization of PCL/gelatin composite nanofibrous scaffold for tissue engineering applications by electrospinning method. Mater. Sci. Eng. C. Mater. Biol. Appl. 33, 1228–35. doi:10.1016/j.msec.2012.12.015

Gavara, N., Chadwick, R.S., 2012. Determination of the elastic moduli of thin samples and adherent cells using conical atomic force microscope tips. Nat. Nanotechnol. 7, 733–6. doi:10.1038/nnano.2012.163

Ge, G., Han, D., Lin, D., Chu, W., Sun, Y., Jiang, L., Ma, W., Wang, C., 2007. MAC mode atomic force microscopy studies of living samples, ranging from cells to fresh tissue. Ultramicroscopy 107, 299–307.

Geerligs, M., van Breemen, L., Peters, G., Ackermans, P., Baaijens, F., Oomens, C., 2011. In vitro indentation to determine the mechanical properties of epidermis. J. Biomech. 44, 1176–1181.

Gelse, K., Pöschl, E., Aigner, T., 2003. Collagens - Structure, function, and biosynthesis. Adv. Drug Deliv. Rev. 55, 1531–1546. doi:10.1016/j.addr.2003.08.002

Ghasemi-Mobarakeh, L., Prabhakaran, M.P., Morshed, M., Nasr-Esfahani, M.-H., Ramakrishna, S., 2008. Electrospun poly(epsilon-caprolactone)/gelatin nanofibrous scaffolds for nerve tissue engineering. Biomaterials 29, 4532–9. doi:10.1016/j.biomaterials.2008.08.007

Giannini, S., Buda, R., Di Caprio, F., Agati, P., Bigi, A., De Pasquale, V., Ruggeri, A., 2008. Effects of freezing on the biomechanical and structural properties of human posterior tibial tendons. Int. Orthop. 32, 145–151. doi:10.1007/s00264-006-0297-2

Giessibl, F.J., 2003. Advances in atomic force microscopy. Rev. Mod. Phys. 75, 949–983.

Goldsmith, L.A., 1991. Physiology, biochemistry, and molecular biology of the skin.

Grant, C.A., Brockwell, D.J., Radford, S.E., Thomson, N.H., 2008. Effects of hydration on the mechanical response of individual collagen fibrils. Appl. Phys. Lett. 92, 2006–2009. doi:10.1063/1.2937001

Grant, C.A., Twigg, P.C., Tobin, D.J., 2012. Static and dynamic nanomechanical properties of human skin tissue using atomic force microscopy: effect of scarring in the upper dermis. Acta Biomater. 8, 4123–9. doi:10.1016/j.actbio.2012.06.042

Green, J.A., Yamada, K.M., 2007. Three-dimensional microenvironments modulate fibroblast signaling responses. Adv. Drug Deliv. Rev. 59, 1293–8. doi:10.1016/j.addr.2007.08.005

Greenwood, J. a., 2007. On the DMT theory. Tribol. Lett. 26, 203–211. doi:10.1007/s11249-006-9184-7

Greenwood, J. a., 1997. Adhesion of elastic spheres. Proc. R. Soc. A Math. Phys. Eng. Sci. 453, 1277–1297. doi:10.1098/rspa.1997.0070

Groves, R.B., Coulman, S. a, Birchall, J.C., Evans, S.L., 2013. An anisotropic, hyperelastic model for skin: experimental measurements, finite element modelling and identification of parameters for human and murine skin. J. Mech. Behav. Biomed. Mater. 18, 167–80. doi:10.1016/j.jmbbm.2012.10.021

Gümüşderelioğlu, M., Dalkıranoğlu, S., Aydın, R.S.T., Cakmak, S., 2011. A novel dermal substitute based on biofunctionalized electrospun PCL nanofibrous matrix. J. Biomed. Mater. Res. A 98, 461–72. doi:10.1002/jbm.a.33143

Haga, H., Sasaki, S., Kawabata, K., Ito, E., Ushiki, T., Sambongi, T., 2000. Elasticity mapping of living fibroblasts by AFM and immunofluorescence observation of the cytoskeleton. Ultramicroscopy 82, 253–258.

Hansma, P.K., Cleveland, J.P., Radmacher, M., Walters, D.A., Hillner, P.E., Bezanilla, M., Fritz, M., Vie, D., Hansma, H.G., Prater, C.B., Massie, J., Fukunaga, L., Gurley, J., Elings, V., 1994. Tapping Mode Atomic-Force Microscopy in Liquids. Appl. Phys. Lett. 64, 1738–1740.

Hashin, Z., Shtrikman, S., 1963. A variational approach to the theory of the elastic behaviour of multiphase materials. J. Mech. Phys. Solids. doi:10.1016/0022-5096(63)90060-7

Heinisch, J.J., Lipke, P.N., Beaussart, A., El Kirat Chatel, S., Dupres, V., Alsteens, D., Dufrêne, Y.F., 2012. Atomic force microscopy - looking at mechanosensors on the cell surface. J. Cell Sci. 125, 4189–95. doi:10.1242/jcs.106005

Hollister, S.J., 2005. Porous scaffold design for tissue engineering. Nat. Mater. 4, 518–24. doi:10.1038/nmat1421

Howard, D., Buttery, L.D., Shakesheff, K.M., Roberts, S.J., 2008. Tissue

engineering: Strategies, stem cells and scaffolds. J. Anat. 213, 66–72. doi:10.1111/j.1469-7580.2008.00878.x

Huang, Z., Zhou, D., Ren, Q., 2010. Nonlinear anisotropic composite biomechanical modeling of human skin. J. Shanghai Jiaotong Univ. 15, 363–367. doi:10.1007/s12204-010-1017-z

Hubbell, J.A., 1995. Biomaterials in tissue engineering. Biotechnology. (N. Y). 13, 565–576. doi:10.1038/nbt0695-565

Hull, D., Clyne, T.W., 1996. An introduction to composite materials. Cambridge University Press, Cambridge; New York.

Hutmacher, D., 2001. Scaffold design and fabrication technologies for engineering tissues—state of the art and future perspectives. J. Biomater. Sci. Polym. Ed. 12, 107–124. doi:10.1163/156856201744489

Hutter, J.L., Bechhoefer, J., 1993. Calibration of Atomic-Force Microscope Tips. Rev. Sci. Instrum. 64, 1868–1873.

Ishikawa, O., Kondo, a, Okada, K., Miyachi, Y., Furumura, M., 1997. Morphological and biochemical analyses on fibroblasts and self-produced collagens in a novel three-dimensional culture. Br. J. Dermatol. 136, 6–11. doi:DOI 10.1111/j.1365-2133.1997.tb08738.x

Jachowicz, J., McMullen, R., Prettypaul, D., 2007. Indentometric analysis of in vivo skin and comparison with artificial skin models. Ski. Res. Technol. 13, 299–309. doi:10.1111/j.1600-0846.2007.00229.x

Jandt, K.D., 2001. Atomic force microscopy of biomaterials surfaces and interfaces. Surf. Sci. 491, 303–332.

Janz, F.D.L., Debes, A.D.A., Cavaglieri, R.D.C., Duarte, S.A., Romão, C.M., Morón, A.F., Zugaib, M., Bydlowski, S.P., 2012. Evaluation of distinct freezing methods and cryoprotectants for human amniotic fluid stem cells cryopreservation. J. Biomed. Biotechnol. 2012, 649353. doi:10.1155/2012/649353

Johnson, K., Greenwood, J., 1997. An adhesion map for the contact of elastic spheres. J. Colloid Interface Sci. 192, 326 – 333.

Johnson, K.L., 1997. Adhesion and friction between a smooth elastic spherical asperity and a plane surface. Proc. R. Soc. London Ser. a-Mathematical Phys. Eng. Sci. 453, 163–179.

Kadler, K.E., Holmes, D.F., Trotter, J. a, Chapman, J. a, 1996. Collagen fibril formation. Biochem. J. 316 (Pt 1, 1–11.

Karlsson, J.O., Toner, M., 1996. Long-term storage of tissues by cryopreservation: critical issues. Biomaterials 17, 243–56.

Khan, A., Philip, J., Hess, P., 2004. Young's modulus of silicon nitride used in scanning force microscope cantilevers. J. Appl. Phys. 95, 1667–1672. doi:10.1063/1.1638886

Khatyr, F., Imberdis, C., Vescovo, P., Varchon, D., Lagarde, J.M., 2004. Model of the viscoelastic behaviour of skin in vivo and study of anisotropy. Ski. Res. Technol. 10, 96–103. doi:10.1111/j.1600-0846.2004.00057.x

Kierszenbaum, A.L., Tres, L., 2015. Histology and Cell Biology: An Introduction to Pathology: . Saunders.

Kim, G.H., 2008. Electrospun PCL nanofibers with anisotropic mechanical properties as a biomedical scaffold. Biomed. Mater. 3, 025010. doi:10.1088/1748-6041/3/2/025010

Kubo, K., Kuroyanagi, Y., 2004. Development of a cultured dermal substitute composed of a spongy matrix of hyaluronic acid and atelo-collagen combined with fibroblasts: cryopreservation. Artif. Organs 28, 182–8.

Kumbar, S.G., Nukavarapu, S.P., James, R., Nair, L.S., Laurencin, C.T., 2008. Electrospun poly(lactic acid-co-glycolic acid) scaffolds for skin tissue engineering. Biomaterials 29, 4100–7. doi:10.1016/j.biomaterials.2008.06.028

Kurland, N.E., Drira, Z., Yadavalli, V.K., 2012. Measurement of nanomechanical properties of biomolecules using atomic force microscopy. Micron 43, 116–128.

Kutys, M.L., Doyle, A.D., Yamada, K.M., 2013. Regulation of cell adhesion and migration by cell-derived matrices. Exp. Cell Res. 319, 2434–2439. doi:10.1016/j.yexcr.2013.05.030

Lavker, R.M., 1979. Structural alterations in exposed and unexposed aged skin. J. Invest. Dermatol. doi:10.1111/1523-1747.ep12532763

Lavker, R.M., Zheng, P.S., Dong, G., 1987. Aged skin: a study by light, transmission electron, and scanning electron microscopy. J. Invest. Dermatol. 88, 44s–51s.

LeBleu, V.S., MacDonald, B., Kalluri, R., 2007. Structure and function of basement membranes. Exp. Biol. Med. 232, 1121–1127.

Lee, S.M., 1993. Handbook of composite reinforcements. VCH, New York.

Lévy, R., Maaloum, M., 2001. Measuring the spring constant of atomic force microscope cantilevers: thermal fluctuations and other methods. Nanotechnology. doi:10.1088/0957-4484/13/1/307

Levy-Mishali, M., Zoldan, J., Levenberg, S., 2009. Effect of scaffold stiffness on myoblast differentiation. Tissue Eng. Part A 15, 935–44. doi:10.1089/ten.tea.2008.0111

Li, W.-J., Laurencin, C.T., Caterson, E.J., Tuan, R.S., Ko, F.K., 2002. Electrospun nanofibrous structure: a novel scaffold for tissue engineering. J. Biomed. Mater. Res. 60, 613–21.

Liao, S., Li, B., Ma, Z., Wei, H., Chan, C., Ramakrishna, S., 2006. Biomimetic electrospun nanofibers for tissue regeneration. Biomed. Mater. 1, R45–53. doi:10.1088/1748-6041/1/3/R01

Limpert, E., Stahel, W.A., Abbt, M., 2001. Log-normal Distributions across the

Sciences: Keys and Clues. Bioscience 51, 341–352. doi:10.1641/0006-3568(2001)051[0341:LNDATS]2.0.CO;2

Lin, D.C., Dimitriadis, E.K., Horkay, F., 2007a. Robust strategies for automated AFM force curve analysis - I. Non-adhesive indentation of soft, inhomogeneous materials. J. Biomech. Eng. Asme 129, 430–440. doi:10.1115/1.2720924

Lin, D.C., Dmitriadis, E.K., Horkay, F., 2007b. Robust strategies for automated AFM force curve Analysis-II: Adhesion-influenced indentation of soft, elastic materials. J. Biomech. Eng. Asme 129, 904–912.

Lin, D.C., Horkay, F., 2008. Nanomechanics of polymer gels and biological tissues: A critical review of analytical approaches in the Hertzian regime and beyond. Soft Matter 4, 669–682.

Liu, X., Lin, T., Fang, J., Yao, G., Zhao, H., Dodson, M., Wang, X., 2010. In vivo wound healing and antibacterial performances of electrospun nanofibre membranes. J. Biomed. Mater. Res. A 94, 499–508. doi:10.1002/jbm.a.32718

Lo, C.M., Wang, H.B., Dembo, M., Wang, Y.L., 2000. Cell movement is guided by the rigidity of the substrate. Biophys. J. 79, 144–52. doi:10.1016/S0006-3495(00)76279-5

Love, A.E.H., 1939. Boussinesq's problem for a rigid cone. Q. J. Math. 10, 161–175. doi:10.1093/qmath/os-10.1.161

Lowery, J.L., Datta, N., Rutledge, G.C., 2010. Effect of fiber diameter, pore size and seeding method on growth of human dermal fibroblasts in electrospun poly(epsilon-caprolactone) fibrous mats. Biomaterials 31, 491–504. doi:10.1016/j.biomaterials.2009.09.072

Lulevich, V., Yang, H., Isseroff, R.R., Liu, G., 2010. Single cell mechanics of keratinocyte cells. Ultramicroscopy 110, 1435–1442. doi:10.1016/j.ultramic.2010.07.009

Maccarana, M., Kalamajski, S., Kongsgaard, M., Magnusson, S.P., Oldberg, A., Malmström, A., 2009. Dermatan sulfate epimerase 1-deficient mice have reduced content and changed distribution of iduronic acids in dermatan sulfate and an altered collagen structure in skin. Mol. Cell. Biol. 29, 5517–28. doi:10.1128/MCB.00430-09

MacNeil, S., 2007. Progress and opportunities for tissue-engineered skin. Nature 445, 874–880. doi:10.1038/nature05664

Magonov, S.N., Reneker, D.H., 1997. Characterization of polymer surfaces with atomic force microscopy. Annu. Rev. Mater. Sci. 27, 175–222.

Manne, J., Markova, M., Siracusa, L.D., Jimenez, S. a., 2013. Collagen content in skin and internal organs of the Tight Skin mouse: An animal model of scleroderma. Biochem. Res. Int. doi:10.1155/2013/436053

Mathur, A.B., Collinsworth, A.M., Reichert, W.M., Kraus, W.E., Truskey, G.A., 2001. Endothelial, cardiac muscle and skeletal muscle exhibit different viscous and elastic properties as determined by atomic force microscopy. J. Biomech.

34, 1545–1553.

McClintock, F.A., Argon, A.S., 1966. Mechanical Behavior of Materials, Addison-Wesley Series in Metallurgy and Materials. Addison-Wesley.

McKee, C.T., Last, J. a, Russell, P., Murphy, C.J., 2011. Indentation versus tensile measurements of Young's modulus for soft biological tissues. Tissue Eng. Part B 17, 155–64. doi:10.1089/ten.TEB.2010.0520

Melling, M., Pfeiler, W., Karimian-Teherani, D., Schnallinger, M., Sobal, G., Zangerle, C., Menzel, E.J., 2000. Differential scanning calorimetry, biochemical, and biomechanical analysis of human skin from individuals with diabetes mellitus. Anat. Rec. 259, 327–333. doi:10.1002/1097-0185(20000701)259:3<327::aid-ar90>3.0.co;2-g

Murad, S., Tajima, S., Johnson, G.R., Sivarajah, S., Pinnell, S.R., 1983. Collagen synthesis in cultured human skin fibroblasts: effect of ascorbic acid and its analogs. J. Invest. Dermatol.

Nachar, N., 2008. The Mann-Whitney U: A Test for Assessing Whether Two Independent Samples Come from the Same Distribution. Tutor. Quant. Methods Psychol. 4, 13–20.

Nair, L.S., Laurencin, C.T., 2007. Biodegradable polymers as biomaterials. Prog. Polym. Sci. 32, 762–798. doi:10.1016/j.progpolymsci.2007.05.017

Neidert, M., Devireddy, R., Tranquillo, R.T., Bischof, J.C., 2004. Cryopreservation of collagen-based tissue equivalents. II. Improved freezing in the presence of cryoprotective agents. Tissue Eng. 10, 23 – 32.

Newton, H., Fisher, J., Arnold, J., Pegg, D., 1998. Permeation of human ovarian tissue with cryoprotective agents in preparation for cryopreservation. Hum. Reprod. 13, 376–380.

Ní Annaidh, A., Bruyère, K., Destrade, M., Gilchrist, M.D., Maurini, C., Otténio, M., Saccomandi, G., 2012a. Automated estimation of collagen fibre dispersion in the dermis and its contribution to the anisotropic behaviour of skin. Ann. Biomed. Eng. 40, 1666–78. doi:10.1007/s10439-012-0542-3

Ní Annaidh, A., Bruyère, K., Destrade, M., Gilchrist, M.D., Otténio, M., 2012b. Characterization of the anisotropic mechanical properties of excised human skin. J. Mech. Behav. Biomed. Mater. 5, 139–48. doi:10.1016/j.jmbbm.2011.08.016

Noorlander, M.L., Melis, P., Jonker, A., Van Noorden, C.J.F., 2002. A quantitative method to determine the orientation of collagen fibers in the dermis. J. Histochem. Cytochem. 50, 1469–1474. doi:10.1177/002215540205001106

Notbohm, J., Poon, B., Ravichandran, G., 2012. Analysis of nanoindentation of soft materials with an atomic force microscope. J. Mater. Res. 27, 229–237. doi:10.1557/jmr.2011.252

O'Brien, F.J., 2011. Biomaterials & scaffolds for tissue engineering. Mater. Today 14, 88–95. doi:10.1016/S1369-7021(11)70058-X

Oliver, W., Pharr, G., 1992. An improved technique for determining hardness and elastic modulus using load and displacement sensing indentation experiments. J. Mater. Res. 7, 1564 – 1583.

Osawa, T., Onodera, M., Feng, X.Y., Nozaka, Y., 2003. Comparison of the thickness of basement membranes in various tissues of the rat. J. Electron Microsc. (Tokyo). 52, 435–440.

Ottenio, M., Tran, D., Ní Annaidh, A., Gilchrist, M.D., Bruyère, K., 2014. Strain rate and anisotropy effects on the tensile failure characteristics of human skin. J. Mech. Behav. Biomed. Mater. doi:10.1016/j.jmbbm.2014.10.006

Oyen, M.L., Cook, R.R., 2009. A practical guide for analysis of nanoindentation data. J. Mech. Behav. Biomed. Mater. 2, 396–407.

Pailler-Mattei, C., Bec, S., Zahouani, H., 2007. In vivo measurements of the elastic mechanical properties of human skin by indentation tests. Med. Eng. Phys. 30, 599–606. doi:10.1016/j.medengphy.2007.06.011

Pan, H., Jiang, H., Chen, W., 2006. Interaction of dermal fibroblasts with electrospun composite polymer scaffolds prepared from dextran and poly lactide-co-glycolide. Biomaterials 27, 3209–20. doi:10.1016/j.biomaterials.2006.01.032

Pasch, J., Schiefer, A., Heschel, I., Rau, G., 1999. Cryopreservation of keratinocytes in a monolayer. Cryobiology 39, 158–168.

Petrie, R.J., Gavara, N., Chadwick, R.S., Yamada, K.M., 2012. Nonpolarized signaling reveals two distinct modes of 3D cell migration. J. Cell Biol. 197, 439–55. doi:10.1083/jcb.201201124

Poumay, Y., Pittelkow, M.R., 1995. Cell density and culture factors regulate keratinocyte commitment to differentiation and expression of suprabasal K1/K10 keratins. J. Invest. Dermatol. doi:10.1111/1523-1747.ep12612810

Powell, H.M., Boyce, S.T., 2009. Engineered human skin fabricated using electrospun collagen-PCL blends: morphogenesis and mechanical properties. Tissue Eng. Part A 15, 2177–87. doi:10.1089/ten.tea.2008.0473

Powell, H.M., Supp, D.M., Boyce, S.T., 2008. Influence of electrospun collagen on wound contraction of engineered skin substitutes. Biomaterials 29, 834–43. doi:10.1016/j.biomaterials.2007.10.036

Prockop, D.J., Kivirikko, K.I., 1995. COLLAGENS : Molecular for Therapy. Proteins.

Pulkkinen, L., Uitto, J., 1998. Hemidesmosomal variants of epidermolysis bullosa. Exp. Dermatol. 46–64.

Purslow, P.P., Wess, T.J., Hukins, D.W., 1998. Collagen orientation and molecular spacing during creep and stress-relaxation in soft connective tissues. J. Exp. Biol. 201, 135–142.

Radmacher, M., Fritz, M., Hansma, P.K., 1995. Imaging Soft Samples with the Atomic-Force Microscope - Gelatin in Water and Propanol. Biophys. J. 69,

264–270.

Rehfeldt, F., Engler, A.J., Eckhardt, A., Ahmed, F., Discher, D.E., 2007. Cell responses to the mechanochemical microenvironment - Implications for regenerative medicine and drug delivery. Adv. Drug Deliv. Rev. 59, 1329–1339.

Reneker, D.H., Chun, I., 1996. Nanometre diameter fibres of polymer, produced by electrospinning. Nanotechnology 7, 216–223. doi:10.1088/0957-4484/7/3/009

Ryu, H.S., Joo, Y.H., Kim, S.O., Park, K.C., Youn, S.W., 2008. Influence of age and regional differences on skin elasticity as measured by the Cutometer®. Ski. Res. Technol. 14, 354–358. doi:10.1111/j.1600-0846.2008.00302.x

Sader, J.E., 1995. Parallel Beam Approximation for V-Shaped Atomic-Force Microscope Cantilevers. Rev. Sci. Instrum. 66, 4583–4587.

Sader, J.E., Chon, J.W.M., Mulvaney, P., 1999. Calibration of rectangular atomic force microscope cantilevers. Rev. Sci. Instrum. 70, 3967–3969. doi:10.1063/1.1150021

Sader, J.E., Larson, I., Mulvaney, P., White, L.R., 1995. Method for the calibration of atomic force microscope cantilevers. Rev. Sci. Instrum. 66, 3789–3798. doi:10.1063/1.1145439

Sader, J.E., White, L., 1993. Theoretical-Analysis of the Static Deflection of Plates for Atomic-Force Microscope Applications. J. Appl. Phys. 74, 1–9.

Saez, A., Buguin, A., Silberzan, P., Ladoux, B., 2005. Is the mechanical activity of epithelial cells controlled by deformations or forces? Biophys. J. 89, L52–4. doi:10.1529/biophysj.105.071217

Sakai, S., Yamanari, M., Lim, Y., Nakagawa, N., Yasuno, Y., 2011. In vivo evaluation of human skin anisotropy by polarization-sensitive optical coherence tomography. Biomed. Opt. Express 2, 2623–31. doi:10.1364/BOE.2.002623

Sen, S., Subramanian, S., Discher, D.E., 2005. Indentation and adhesive probing of a cell membrane with AFM: Theoretical model and experiments. Biophys. J. 89, 3203–3213. doi:10.1529/biophysj.105.063826

Shi, S.-R., Liu, C., Pootrakul, L., Tang, L., Young, A., Chen, R., Cote, R.J., Taylor, C.R., 2008. Evaluation of the value of frozen tissue section used as “gold standard” for immunohistochemistry. Am. J. Clin. Pathol. 129, 358–66. doi:10.1309/7CXUYXT23E5AL8KQ

Shimizu, H., 2007. Shimizu’s Textbook of Dermatology. 中山書店.

Silver, F.H., Freeman, J.W., DeVore, D., 2001. Viscoelastic properties of human skin and processed dermis. Ski. Res. Technol. 7, 18–23.

Silver, F.H., Siperko, L.M., Seehra, G.P., 2003. Mechanobiology of force transduction in dermal tissue. Ski. Res. Technol. 9, 3–23.

Simpson, C.L., Patel, D.M., Green, K.J., 2011. Deconstructing the skin:

cytoarchitectural determinants of epidermal morphogenesis. Nat Rev Mol Cell Biol 12, 565–580. doi:http://www.nature.com/nrm/journal/v12/n9/suppinfo/nrm3175_S1.html

Sirghi, L., Ponti, J., Broggi, F., Rossi, F., 2008. Probing elasticity and adhesion of live cells by atomic force microscopy indentation. Eur. Biophys. J. with Biophys. Lett. 37, 935–945.

Sirghi, L., Rossi, F., 2006. Adhesion and elasticity in nanoscale indentation. Appl. Phys. Lett. 89, 243118. doi:10.1063/1.2404981

Smalls, L.K., Wickett, R.R., Visscher, M.O., 2006. Effect of dermal thickness, tissue composition, and body site on skin biomechanical properties. Ski. Res. Technol. 12, 43–49.

Sneddon, I.N., 1948. Boussinesq's problem for a rigid cone. Math. Proc. Cambridge Philos. Soc. 44, 492–507. doi:10.1093/qmath/os-10.1.161

Solon, J., Levental, I., Sengupta, K., Georges, P.C., Janmey, P. a, 2007. Fibroblast adaptation and stiffness matching to soft elastic substrates. Biophys. J. 93, 4453–61. doi:10.1529/biophysj.106.101386

Stachewicz, U., Bailey, R.J., Wang, W., Barber, A.H., 2012. Size dependent mechanical properties of electrospun polymer fibers from a composite structure. Polymer (Guildf). 53, 5132–5137. doi:10.1016/j.polymer.2012.08.064

Stephens, P., Grenard, P., Aeschlimann, P., Langley, M., Blain, E., Errington, R., Kipling, D., Thomas, D., Aeschlimann, D., 2004. Crosslinking and G-protein functions of transglutaminase 2 contribute differentially to fibroblast wound healing responses. J. Cell Sci. 117, 3389–3403. doi:10.1242/jcs.01188

Suhodolčan, L., Brojan, M., Kosel, F., Drobnič, M., Alibegović, A., Brecelj, J., 2013. Cryopreservation with glycerol improves the in vitro biomechanical characteristics of human patellar tendon allografts. Knee Surg. Sports Traumatol. Arthrosc. 21, 1218–25. doi:10.1007/s00167-012-1954-1

Suvarna, S.K., Layton, C., Bancroft, J.D., 2013. Bancroft's Theory and Practice of Histological Techniques,Expert Consult: Online and Print,7: Bancroft's Theory and Practice of Histological Techniques, Churchill Livingstone. Churchill Livingstone Elsevier.

Tan, P.S., Teoh, S.H., 2007. Effect of stiffness of polycaprolactone (PCL) membrane on cell proliferation. Mater. Sci. Eng. C 27, 304–308. doi:10.1016/j.msec.2006.03.010

Tasheva, E.S., Koester, A., Paulsen, A.Q., Garrett, A.S., Boyle, D.L., Davidson, H.J., Song, M., Fox, N., Conrad, G.W., 2002. Mimecan/osteoglycin-deficient mice have collagen fibril abnormalities. Mol. Vis. 8, 407–415. doi:v8/a48 [pii]

Tobin, D.J., 2006. Biochemistry of human skin--our brain on the outside. Chem. Soc. Rev. 35, 52–67. doi:10.1039/b505793k

Venkatasubramanian, R.T., Grassl, E.D., Barocas, V.H., Lafontaine, D., Bischof, J.C., 2006. Effects of freezing and cryopreservation on the mechanical

properties of arteries. Ann. Biomed. Eng. 34, 823–32. doi:10.1007/s10439-005-9044-x

Venugopal, J.R., Zhang, Y., Ramakrishna, S., 2006. In vitro culture of human dermal fibroblasts on electrospun polycaprolactone collagen nanofibrous membrane. Artif. Organs 30, 440–6. doi:10.1111/j.1525-1594.2006.00239.x

Verbeken, G., Verween, G., De Vos, D., Pascual, B., De Corte, P., Richters, C., De Coninck, A., Roseeuw, D., Ectors, N., Rose, T., Jennes, S., Pirnay, J.-P., 2012. Glycerol treatment as recovery procedure for cryopreserved human skin allografts positive for bacteria and fungi. Cell Tissue Bank. 13, 1–7.

Vexler, A., Polyansky, I., Gorodetsky, R., 1999. Evaluation of skin viscoelasticity and anisotropy by measurement of speed of shear wave propagation with viscoelasticity skin analyzer. J. Invest. Dermatol. 113, 732–739. doi:10.1046/j.1523-1747.1999.00751.x

Villalba, R., Benitez, J., DeNoLowis, E., Rioja, L.F., GomezVillagran, J.L., 1996. Cryopreservation of human skin with propane-1,2-diol. Cryobiology 33, 525–529.

Wang, X., Paloheimo, K.-S.K.-S., Xu, H., Liu, C., 2010. Cryopreservation of Cell/Hydrogel Constructs Based on a New Cell-assembling Technique. J. Bioact. Compat. Polym. 25, 634–653. doi:10.1177/0883911510382571

Weisenhorn, A.L., Hansma, P.K., Albrecht, T.R., Quate, C.F., 1989. Forces in Atomic Force Microscopy in Air and Water. Appl. Phys. Lett. 54, 2651–2653. doi:10.1063/1.101024

Weisenhorn, A.L., Maivald, P., Butt, H.J., Hansma, P.K., 1992. Measuring adhesion, attraction, and repulsion between surfaces in liquids with an atomic-force microscope. Phys. Rev. B 45, 226–232.

Wickett, R.R., Visscher, M.O., 2006. Structure and function of the epidermal barrier. Am. J. Infect. Control 34, S98–S110.

Williams, J.A., Dwyer-Joyce, R.S., 2000. Contact Between Solid Surfaces. Mod. Tribol. Handb. 1, 121–162. doi:doi:10.1201/9780849377877.ch3\n10.1201/9780849377877.ch3

Wong, C.P., Bollampally, R.S., 1999. Thermal conductivity, elastic modulus, and coefficient of thermal expansion of polymer composites filled with ceramic particles for electronic packaging. J. Appl. Polym. Sci. 74, 3396–3403. doi:10.1002/(SICI)1097-4628(19991227)74:14<3396::AID-APP13>3.0.CO;2-3

Woodruff, M.A., Hutmacher, D.W., 2010. The return of a forgotten polymer—Polycaprolactone in the 21st century. Prog. Polym. Sci. 35, 1217–1256. doi:10.1016/j.progpolymsci.2010.04.002

Wu, H.W., Kuhn, T., Moy, V.T., 1998. Mechanical properties of l929 cells measured by atomic force microscopy: Effects of anticytoskeletal drugs and membrane crosslinking. Scanning 20, 389–397.

Wu, Y., Chen, L., Scott, P.G., Tredget, E.E., 2007. Mesenchymal stem cells enhance

wound healing through differentiation and angiogenesis. Stem Cells 25, 2648–2659. doi:10.1634/stemcells.2007-0226

Yang, S., Leong, K.-F., Du, Z., Chua, C.-K., 2004. The Design of Scaffolds for Use in Tissue Engineering. Part I. Traditional Factors. Http://Dx.Doi.Org/10.1089/107632701753337645 7, 679–689.

Zahouani, H., Pailler-Mattei, C., Sohm, B., Vargiolu, R., Cenizo, V., Debret, R., 2009. Characterization of the mechanical properties of a dermal equivalent compared with human skin in vivo by indentation and static friction tests. Ski. Res. Technol. 15, 68–76. doi:10.1111/j.1600-0846.2008.00329.x

Zhang, Y., Ouyang, H., Lim, C.T., Ramakrishna, S., Huang, Z.-M., 2005. Electrospinning of gelatin fibers and gelatin/PCL composite fibrous scaffolds. J. Biomed. Mater. Res. B. Appl. Biomater. 72, 156–65. doi:10.1002/jbm.b.30128

Zhou, Y., Yang, D., Chen, X., Xu, Q., Lu, F., Nie, J., 2008. Electrospun water-soluble carboxyethyl chitosan/poly(vinyl alcohol) nanofibrous membrane as potential wound dressing for skin regeneration. Biomacromolecules 9, 349–54. doi:10.1021/bm7009015

Zhu, X., Cui, W., Li, X., Jin, Y., 2008. Electrospun Fibrous Mats with High Porosity as Potential Scaffolds for Skin Tissue Engineering. Biomacromolecules 9, 1795–1801.

Zieger, M. a, Tredget, E.E., McGann, L.E., 1996. Mechanisms of cryoinjury and cryoprotection in split-thickness skin. Cryobiology 33, 376–389. doi:10.1006/cryo.1996.0038

Zieger, M.A.J., Tredget, E.E., Sykes, B.D., McGann, L.E., 1997. Injury and protection in split-thickness skin after very rapid cooling and warming. Cryobiology 35, 53–69.

Zillikens, D., Giudice, G.J., 1999. BP180 type XVII collagen: its role in acquired and inherited disorders or the dermal-epidermal junction. Arch. Dermatol. Res. 291, 187–194.

Appendix

Characterisation of AFM Probe Tip

A SEM image of the AFM cantilevers, MLCT type (Bruker, EU), used throughout the thesis is shown in Appendix Figure 1. The SEM image shows that the AFM cantilever cannot be represented by the parallel beam approximation or any other simplified geometry. Appendix Figure 2 displays an SEM image of a typical AFM probe tip prior to using the probe for any scanning. The opening angle of the tip is approximately 37°, which indicates a half-tip opening angle of 18.5°.

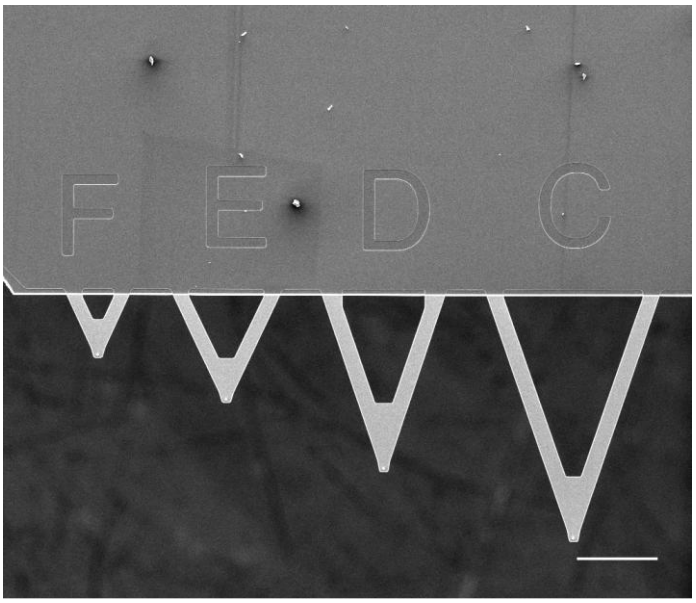

Appendix Figure 1. SEM image of AFM cantilevers used. Scale bar, 100 µm

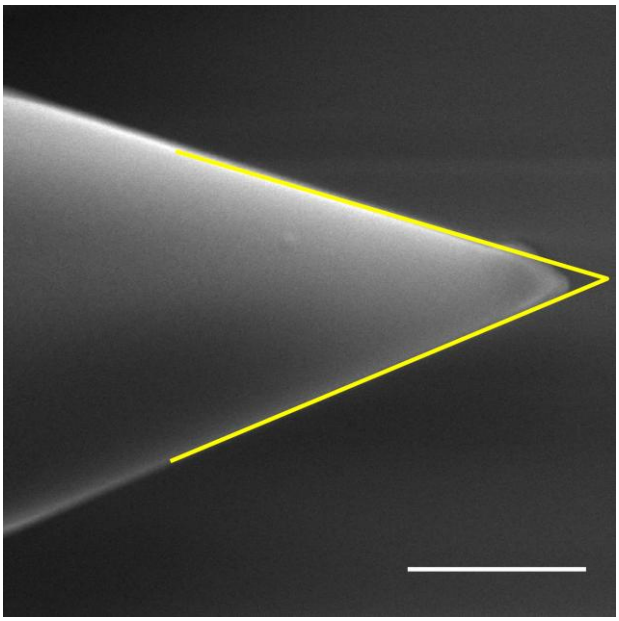

Appendix Figure 2. SEM image of AFM probe tip with the opening angle of the probe highlighted in yellow. The opening angle of the imaged tip is approximately 37°. Scale bar, 1 µm.

Mechanical Testing of Agarose Gels

The unconfined compression testing of agarose gels was undertaken by Dr. Robin Delaine-Smith, at the School of Engineering and Materials Science, Queen Mary, University of London, following the testing methodology described in Delaine-Smith et al. 2016 (Delaine-Smith et al., 2016), and is briefly described here.

Unconfined compression testing was performed using a screw-driven MTS synergie 100 (MTS Systems, USA) using a 50 N load cell and a 7 mm diameter stainless steel plate, throughout testing the gel samples were submerged in PBS at room temperature. The schematic of the testing set up is shown in Appendix Figure 3.

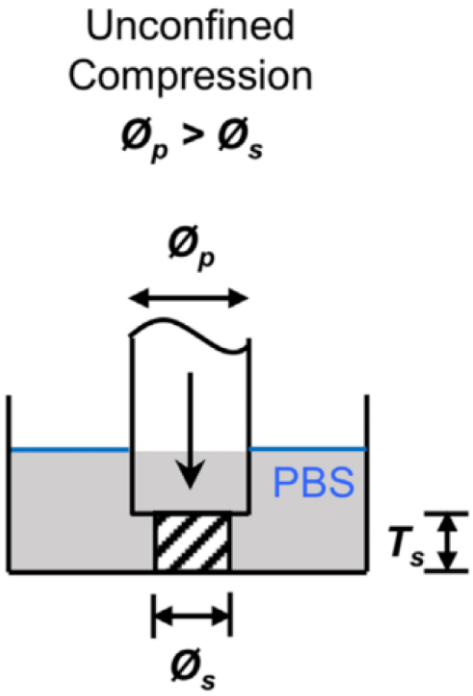

Appendix Figure 3. Schematic of the experimental setup for unconfined compression of agarose gels. With $Ø_p$ being the diameter of the plate, $Ø_s$ the diameter of the sample, and T_s the thickness of the sample. Figure adapted from (Delaine-Smith et al., 2016).

The gels were loaded to 20% strain at a rate of 1% strain per second and held at 20% strain for 3 minutes. The loading phase was followed by an unloading phase at a rate of 1% strain per second until the sample reached 0% strain. The mechanical properties of the gels was calculated from the stress vs strain curves, with an example curve shown in Appendix Figure 4. The elastic modulus was determined by taking the slope between 2.5% strain and 7.5% strain of the loading curve. A total of n = 6 samples were measured for each gel concentration.

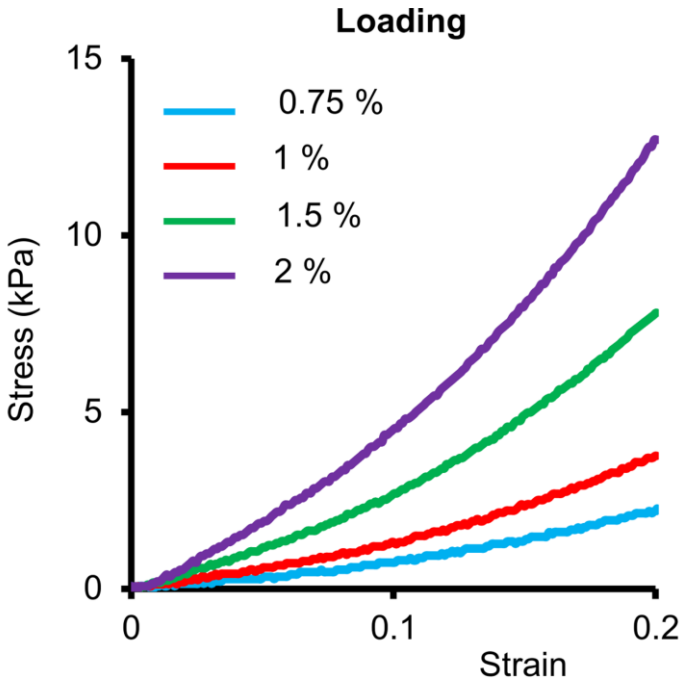

Appendix Figure 4. Representative stress vs strain curves for the unconfined compression of agarose gels to 20% strain. It should be noted that for this work the agarose gels used are represented by the 1% (red) and 1.5% (green) curves. Figure adapted from (Delaine-Smith et al., 2016)

Force-Displacement Curves Dermal Explant Samples

Sample force-displacement curves are shown below in Appendix Figure 5 for the highlighted boxes of Figure 4.5. The force-displacement curves highlight the differences between the extreme high and low elastic modulus values found within the data set. Despite the difference in elastic modulus, each curve still displays the shape that can be fit to Equation 4.2 to determine the elastic modulus.

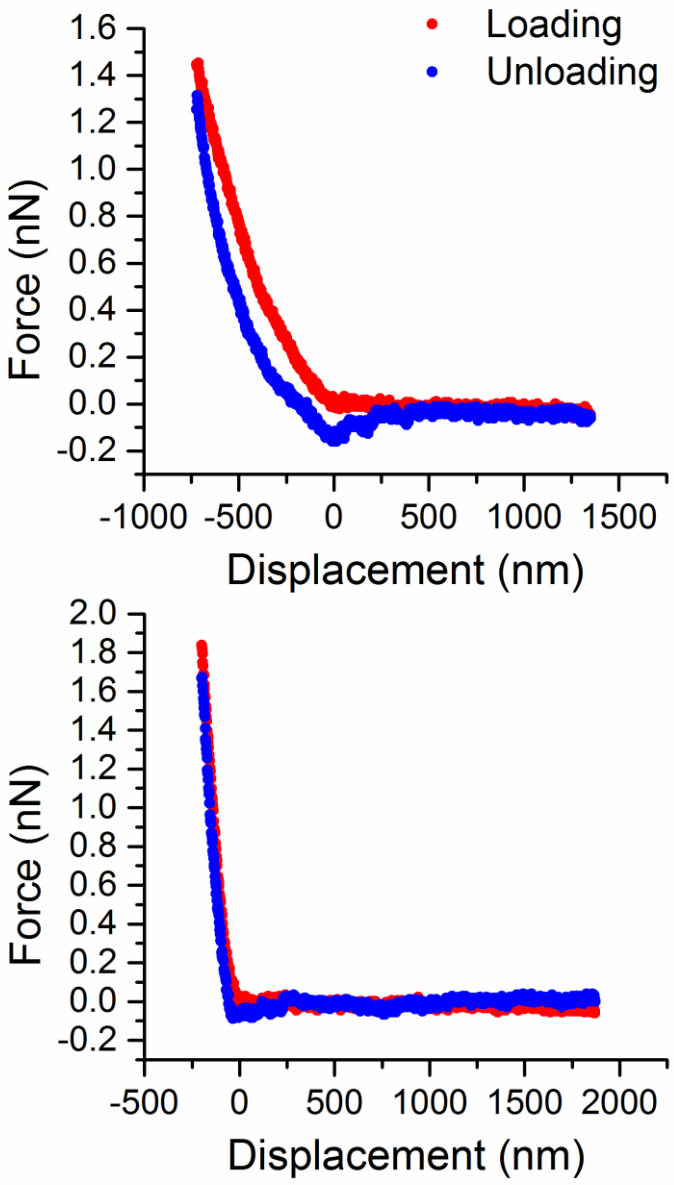

Appendix Figure 5. Force-displacement curves for the highlighted boxes of Figure 4.5. The (top) curve represents a significantly low elastic modulus value compared to the mean of the data set. And the (bottom) curve is a significantly high elastic modulus value point.

Haematoxylin and Eosin Staining Protocol

The following protocol was used when conducting Haematoxylin and Eosin (H&E) staining on cryosections throughout the thesis:

Slides were first mounted within a stainless steel staining rack and then subjected to the following procedure in order:

Solution	Time
Distilled Water	3 minutes
Haematoxylin (Gill's 1x, Sigma Aldrich UK)	5 minutes
Tap water (running)	5 minutes
Acid Alcohol (1% HCl in 70% EtOH)	Dipped 3-5 times
Tap water (running)	3-5 minutes
Eosin Y (Sigma Aldrich, UK)	2 minutes
Tap water (Running)	3-5 minutes
70% EtOH	2 minutes
90% EtOH	2 minutes
100% EtOH	2 minutes
100% EtOH	2 minutes
100& Xylene	2 minutes
100% Xylene	2 minutes

After the final xylene rinse, cover slides were mounted using DPX mounting media (Sigma Aldrich, UK) and left to dry for 12 hours.